Microstructure Evolution and Phase Transformation of Welded Metastable Beta-Titanium Alloy (Ti-5Al-5V-5Mo-3Cr)

Yuan Tao

A thesis submitted to
Auckland University of Technology
in fulfilment of the requirements for the degree of
Doctor of Philosophy (PhD)

2016

School of Engineering, Computer and Mathematical Sciences
Auckland University of Technology

I hereby declare that this submission is my own work and that, to the best of my knowledge and belief, it contains no material previously published or written by another person (except where explicitly defined in the acknowledgements), nor material which to a substantial extent has been submitted for the award of any other degree or diploma of a university or other institution of higher learning.

Signed _____ Date_____

Acknowledgements

Firstly, I would like to express my sincere gratitude to my advisor Assoc. Professor Tim Pasang for giving me the opportunity to study my PhD at Auckland University of Technology. With the deepest appreciation I would like to thank him for his continuous support, vast knowledge, patience, motivation, encouragement and great sense of humour.

Next I would like to thank my co-advisor, Prof. Zhan Chen for his guidance with my work, and generous suggestions on my writing and presentations.

I would specially like to thank Patrick Conor for being my mentor on the Scanning Electron Microscopy operation. He has taught me so much on fractography analysis and given me great advice on my sample preparation.

Many thanks to all workshop staff: Mark Masterton, Ross Jamieson, Jim Crossen, Yan Wang, Makirai Henry for access to the laboratory and research facilities, help and guidance in the experimental work and Dr. Shanghai Wei for the TEM analysis.

I appreciate the support, discussions and advice from my colleagues and friends Mana, Nurul, Doddy, Mahros, and Kurosh. Their friendship and encouragement have made my life brighter in the past three years.

Last but not least, my sincere appreciation goes to my family: my parents who have been supporting me spiritually and financially over the years; my grandparents for forgiving me for not being there on their last days; and the final appreciation goes to my husband Richard for believing in me and occasionally helping out with the house chores.

Publications

Pasang, T., Tao, Y., Sabol, J.C., Misiolek, W. Z., Kamiya, O., & Kudo, G. (2013). Welding characteristics of a new titanium alloy for aerospace applications. International Symposium on Green Manufacturing and Applications, Hawaii.

Pasang, T., Sánchez, J. M., Tao, Y., Amaya-Vázquez, M. R., Botana, F. J., Sabol, J. C., Misiolek,W. Z., & Kamiya, O. (2013). Comparison of Ti-5Al-5V-5Mo-3Cr welds performed by LBW, EBW and GTAW. *Procedia Engineering* 63: 397-404.

Tao, Y., Chen, Z. W., Conor, P. (2013). Microstructure evolution and phase transformation of welded metastable beta-Titanium alloy (Ti-5Al-5V-5Mo-3Cr-0.5Fe). Proceedings of the NZ Conference of Chemical and Materials Engineering 2013. New Zealand.

Pasang, T., Tao, Y., Kamiya, O., Miyano, Y., & Kudo, G. (2014). Research on various welding methods on aerospace titanium alloys: Collaboration between Akita University and Auckland University of Technology. *International Journal of the Society of Materials Engineering for Resources*, *20*(1), 35-39.

Table of Contents

List of Figures

Abstract

Ti-5Al-5V-5Mo-3Cr (Ti5553, in wt%) is a recently developed metastable β titanium alloy, specifically designed to replace Ti-10V-2Fe-3Al (VT22) in the manufacture of large airplane components. The studies of Ti5553 have drawn the attention of many researchers. Ti5553 shows reasonable weldability and can be welded autogenously (without filler metal). Most of the previous studies were directed at forged material behaviour. There is still a lack of understanding of the microstructure evolution and the phase transformation in regards both similar and dissimilar welded material.

The main part of this study investigates the microstructure evolution and phase transformation of Ti5553-Ti5553 similar weldment upon various post weld heat treatment (PWHT). The microstructure analysis was carried out by optical, scanning electron microscopy (SEM) and electron transmission microscopy (TEM). Microstructural results show that the weld zone in Ti5553 can retain the β phase in the as-welded condition. SEM micrographs reveal the different morphology and growth rate of the α precipitation at 500℃ and 600℃ ageing temperature. TEM results in the fusion zone (FZ) area of an as-welded (AW) specimen show the diffraction patterns of the ω phase. This ω phase was retained as athermal ω_a which formed during cooling from the welding process. All evidence proved that ω_a in the weld zone improved the precipitation rate. However, there was no evidence for an isothermal ω at a 500℃ ageing temperature.

The volume fraction and size of α precipitates have a major influence on hardness and tensile strength. At around 30mins of ageing time at either temperature, the α platelets reached an equilibrium of precipitation and hence had the highest volume fraction which resulted in the highest tensile strength. Increasing the ageing time resulted in the α laths coarsening, especially for samples aged at 600℃. The coarsened α laths caused a decrease in hardness. However, changes in tensile strength were not significant. Most of the fractures occurred in the FZ. Fractographic analysis showed dimple rupture via microvoid coalescence for all tensile tested pieces.

Investigation on AW dissimilar welding Ti5553-Ti64 and Ti5553-CPTi suggested that Ti5553 is weldable to the most common titanium alloys (Ti64 & CPTi) and with reasonable tensile strength. All fractures occurred at the low-strength area. Hardness

profiles indicated higher hardness in the FZ. Electron probe micro-analysis (EPMA) was employed to investigate material flow in the melt pool.

Chapter 1. Introduction

1.1 Titanium alloys and titanium welding

1.1.1 Introduction

Titanium (symbol Ti, atomic number 22) is the fourth most abundant structural metal (9th most plentiful element) in the Earth's crust, which was first discovered in Cornwall (U.K.) by the mineralogist and chemist William Gregor in 1791 (Leyens & Peters, 2003; Lütjering & Williams, 2007). The name of titanium came from Greek mythology – specifically the divine beings called Titan. It was first extracted from ilmenite sands ($FeTiO_3$) also known as 'black sand.' Ninety five percent of titanium ore is destined for refining into titanium dioxide (TiO_2). The extraction process is expensive, so as the development of cost-effective titanium production technology grew rapidly, the titanium market escalated dramatically. In order to satisfy future industrial demands, enhancing the properties of titanium alloys is becoming crucial.

Titanium is usually known as an aerospace material for its outstanding properties, such as high strength to density ratio, corrosion resistance, fatigue and high crack resistance, and so on. It is as strong as steel but only has approximately 60% of the density of steel. Titanium also has a relatively high melting point (1668℃). The working temperature for commercial titanium alloys is between 538℃ to 595℃ (Donachie, 2000). Titanium has high corrosion resistance in most environments. It is also non-toxic, and resists human body fluids, which makes it an outstanding material for both the chemical and biomaterial fields (Caron & Staley, 1997). High durability has made titanium more popular for jewellery making, particularly titanium rings. Titanium can be alloyed with many elements such as iron, aluminium, vanadium, and others to meet different industrial requirements.

Although titanium was first discovered in the 1790s, it did not become widely used until the 1900s. Over the years, many researchers have dedicated themselves to improving the production of titanium and its properties. In the 1950s, numerous large companies started early titanium industry developments. Since then global titanium production has been increasing expeditiously. Titanium industry shipments from the U.S. from early 1950 to

the present have risen from 800,000 kg to 35.8 million kg per year (Froes, 2015). After the end of the Cold War, titanium alloys became one of the most desired materials for commercial use aircraft structures and engines due to its high strength to weight ratio. By the late 1990s, a record 27 million kg of mill products were being shipped per year in the United States, with 15% of titanium being used on Boeing 777's landing gear, Ti-10V-2Fe-3Al for the main landing gear and Ti-15V-3Cr-3Al-3Sn for ducts, fittings, and nut clips; beta-21S was used for weight saving, volume constraints, operating temperatures and compatibility with polymeric composites and corrosion resistance. After 2001, a new alloy was developed by Allegheny Technologies Incorporated Wah Cheng, Ti-4Al-2.5V-1.5Fe which had many of the characteristics of the Ti-6Al-4V alloy, but it was cold workable (Froes, 2015). Between 2003 and 2007 with the creation of the Airbus A380, Joint Strike Fighter F-35 and Boeing 787, the U.S. mill production reached a new record of 35.8 million kg per year, with the addition of the new Boeing 787 using in excess of 20%, including the high strength and high toughness Ti-5Al-5V-5Mo-3Cr alloy in the landing gear, wing structure and nacelle area (Froes, 2015). Production did decrease subsequently in 2008 and 2009 with the global recession and banking crisis, when during that time two new alloys were made: (Ti-6Al-2Fe-0.1Si) and (Ti-6.8Mo-4.5Fe-1.5Al). Demand increased again during the 2010-2014 time period with large titanium purchases for the Airbus A380, military JSF35, and Boeing 787 (Froes, 2015). Titanium use in both engines and airframes is increasing.

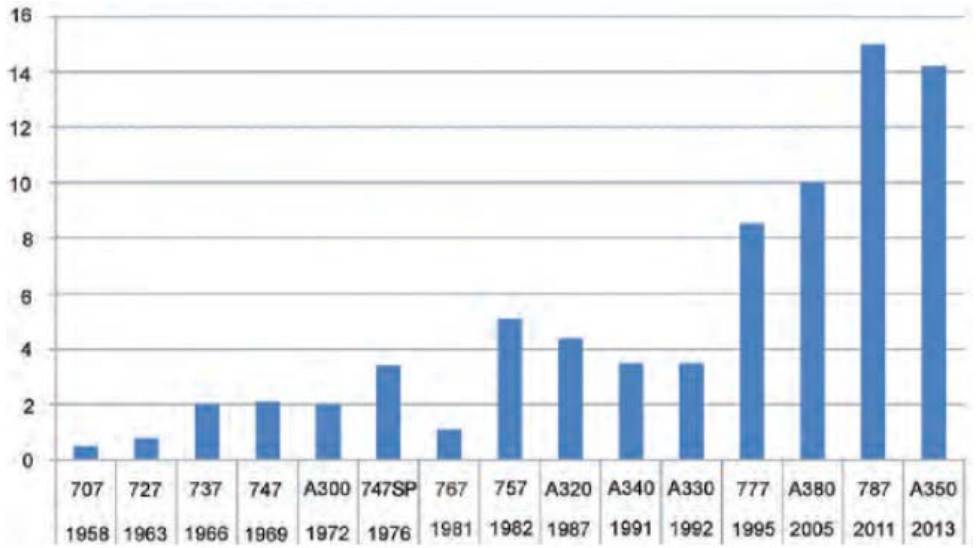

Figure 1.1. Growth in titanium use as a percentage of total gross empty weight on Boeing and Airbus aircraft (Froes, 2015)

1.1.2 Titanium alloy classification

Titanium is an allotropic element, which means it can exhibit more than one crystal structure in different temperature ranges. The stability of each phase depends on the chemical composition of the alloy, temperature range and cooling rate. The transformation from one phase to another is called allotropic transformation. The temperature when the transformation happens is called the transus temperature. In general, titanium exhibits hexagonal closed-packed (HCP) crystal structure (alpha) at low temperature, and body-centred cubic (BCC) crystal structure (beta) at high temperature. The atomic structures of HCP and BCC titanium are schematically shown in Figure 1.2. The atomic distance for the ideal HCP structure is $a = 0.295nm$, ratio c/a= 1.587. The atomic distance for the ideal BCC structure is $a = 0.332nm$.

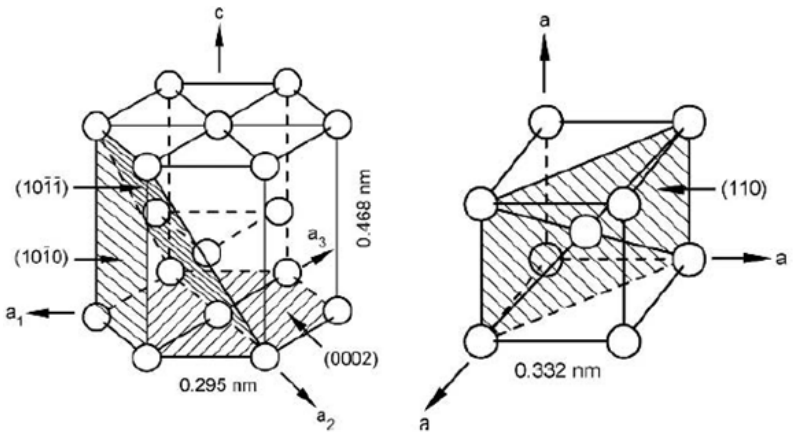

Figure 1.2. HCP and BCC crystal structure (Leyens & Peters, 2003)

Nevertheless, the properties of titanium alloys are fundamentally determined by their chemical composition. Based on the present phase at room temperature, titanium alloys in general can be categorised as alpha (α), alpha-beta (α+β), and beta (β) alloys (Leyens & Peters, 2003; Lütjering & Williams, 2007). Based on their influence on the stability of these phases, these elements are known as: α-stabilizer, β-stabilizer and neutral additions. Some of the major interstitial and substitution alloying elements are shown in Table 1.1. The effects of alloying elements on the phase diagrams of titanium alloys are illustrated in Figure 1.3.

<table>
<tr><th colspan="2">Effect on structure</th><th>Possible alloying element in titanium</th><th colspan="2">Example alloys</th></tr>
<tr><td colspan="2" rowspan="2">α stabilizer</td><td rowspan="2">Aluminium (Al)
Gallium (Ga)
Germanium (Ge)
Lanthanum (La)
Cerium (Ce)
Oxygen (O)
Nitrogen (N)
Carbon (C)</td><td>α and near α</td><td>$\alpha + \beta$</td></tr>
<tr><td>Grade (1, 4, 6)
Ti0.3Mo0.8Ni
Ti5Al2.5Sn
Ti8Al1Mo1V
TIMTETAL 685</td><td>Ti6Al4V
Ti6Al4V2Sn
Ti6Al2Sn4Zr6Mo</td></tr>
<tr><td rowspan="3">β stabilizer</td><td>β isomorphous</td><td>Vanadium (V)
Niobium (Nb)
Tantalum (Ta)
Molybdenum (Mo)
Rhenium (Rh)</td><td colspan="2">Metastable β and β</td></tr>
<tr><td>β eutectoid</td><td>Copper (Cu)
Silver (Ag)
Gold (Au)
Indium (In)
Bismuth (Bi)
Chromium (Cr)
Tungsten (W)
Manganese (Mg)
Iron (F)
Cobalt (Co)
Nickel (Ni)
Uranium (U)
Hydrogen (H)
Silicon (Si)</td><td colspan="2" rowspan="2">SP 700
Beta III
Beta C
Ti10V2Fe3Al
Ti5Al5Mo5V3Cr
Ti13V11Cr3Al
Ti8Mo8V2Fe3Al
Ti15V3Cr3Al3Sn</td></tr>
<tr><td colspan="2">Neutral addition</td><td>Zirconium (Zr)
Hafnium (Hf)
Tin (Sn)</td></tr>
</table>

Table 1.1. Classification of the major alloying elements in titanium (Froes, 2015)

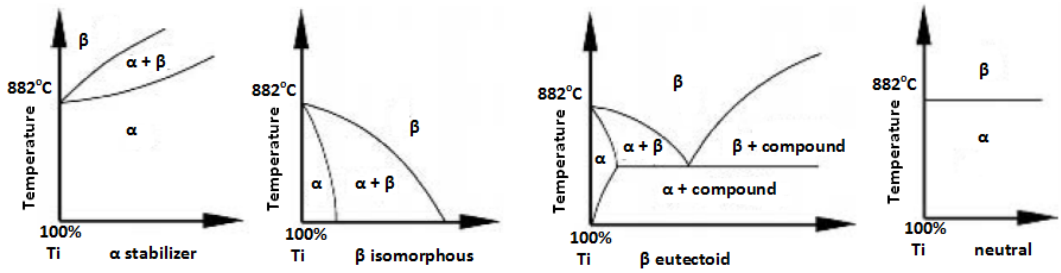

Figure 1.3. Effect of alloying elements on phase diagrams of titanium alloys (Lütjering & Williams, 2007)

(i) α-stabilizer and α, near α alloys

α-stabilizers, as the name suggests, are soluble in the α phase and increase the temperature in which the alpha phase exists (Froes, 2015). Aluminium (Al) is probably the most effective commercial α-strengthening element, because it is the only common α-stabilizer that has large solubility in both the α and β phase (Lütjering & Williams, 2007). As shown in Table 1.1, other substitutional and interstitial α-stabilizers include Ga, Ge, O, N, C, and so on. For example, in order to increase the strength of pure titanium, oxygen is usually added to produce several different grades of titanium. The maximum amount of α-stabilizer is expressed as in Eq. 1.1 (Donachie, 2000; Messler R. W., 2004):

$$Al.Eq. = 1.0(wt.\%)Al + 0.17(wt.\%)Zr + 0.33(wt.\%)Sn \leq 8 \qquad \text{Eq. 1.1}$$

One typical example is the titanium-aluminium system. The binary Ti-Al phase diagram is shown in Figure 1.4. For instance, the amount of Al should not exceed wt8% in order to avoid the embrittlement intermediate phase-Ti_3Al (Froes, 2015). In industry, the content of Al is normally limited to 6%wt to avoid the appreciable amount of Ti_3Al (Donachie, 2000).

The definition of α and near α alloys are disputable. Alloys containing α-stabilizers does not make them α alloys. One of the descriptions designates the type of alloy by the phases present near room temperature. The common applications for α alloys are the chemical and process engineering industries such as biomedical joint replacement and bone plate surgeries due to their excellent corrosion resistance and high deformability (Leyens & Peters, 2003). In general, titanium α alloys have slightly less corrosion resistance than pure titanium, but higher strength. They also have very good weldability. However, heat

treatment cannot be used to improve mechanical properties for α alloys since only a single phase exists.

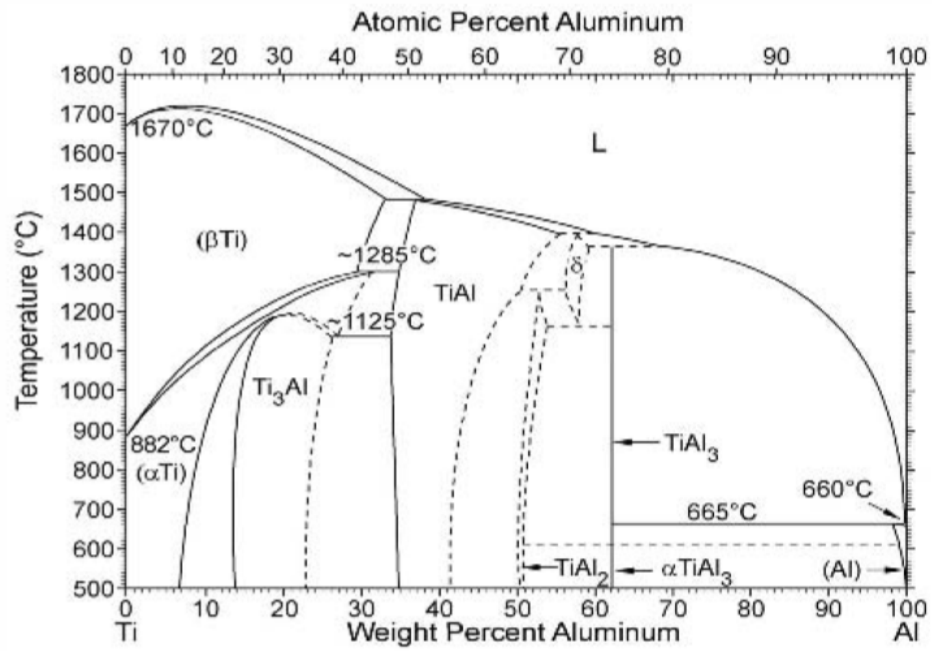

Figure 1.4. The titanium-aluminium phase diagram (Lütjering & Williams, 2007)

(ii) $\alpha + \beta$ alloys

Both $\alpha + \beta$ alloys are designed to allow both hexagonal alpha and BCC beta phases to exist at room temperature. This group of alloys contains aluminium and substantial amounts of beta-isomorphous elements such as Molybdenum or Vanadium which give $\alpha + \beta$ alloys excellent stability at high temperature and stress (Froes, 2015). They have a good combination of strength and ductility, higher strength than CP Ti and α alloys. They also have reasonable weldability depending on the amount of beta stabilizer they contain and are heat treatable. One of the most common commercial uses of $\alpha + \beta$ alloys is Ti6Al4V which makes up over more than 50% of all titanium alloys in today's titanium market, especially in the aerospace industry (Leyens & Peters, 2003). Other high strength and high toughness $\alpha + \beta$ alloys such as Ti6-2-4-6 were designed for gas turbine engines.

(iii) β-stabilizer and β alloy

β-stabilizer elements promote a beta phase and lower the beta transus temperature. Alloys with sufficient β-stabilizer that can retain a beta phase at room temperature from annealing conditions are designated as a β alloy. The β-stabilizers are further subdivided as β isomorphous elements and β eutectoid forming elements. The binary phase diagrams are shown as Figure 1.5. The most commonly used β-stabilizers include V, Mo, Nb, Cr, Fe and Si. Other possible β-stabilizers have a very limited usage. The stability of the β alloy is described by Moly Equivalent (Mo_{eq}), which normally requires a minimum of 10.0 to stabilize the β alloy upon quenching (Bania, 1994; Donachie, 2000).

$$Mo_{eq.} = 1.0(wt.\%Mo) + 0.67(wt.\%V) + 0.44(wt.\%W) + 0.28(wt.\%Nb) + 0.22(wt.\%Ta) + 2.9(wt.\%Cr) \ldots - \ 1.0(wt.\%Al) \quad \text{Eq. 1.2}$$

As shown in Figure 1.5, both metastable and stable beta alloys are located outside of the martensite start (Ms) line, which means these alloys do not form martensite upon quenching. A more detailed description of the beta alloys phase transformation will be further discussed in the next chapter. The applications of metastable/stable beta alloys have increased exponentially over the last few decades. Alloys such as Ti-5-5-5-3, Ti-10-2-3, and Beta C can be hardened by precipitation due to a necessary amount of beta phase to achieve an extremely high strength and high toughness. The retained fully beta BCC structure increases ductility which leaves reasonable room for a reduction of ductility after heat treatment. Beta alloys are generally weldable, although not as superior as those of α or $\alpha + \beta$ alloys. Most applications of beta alloys are for aircraft components.

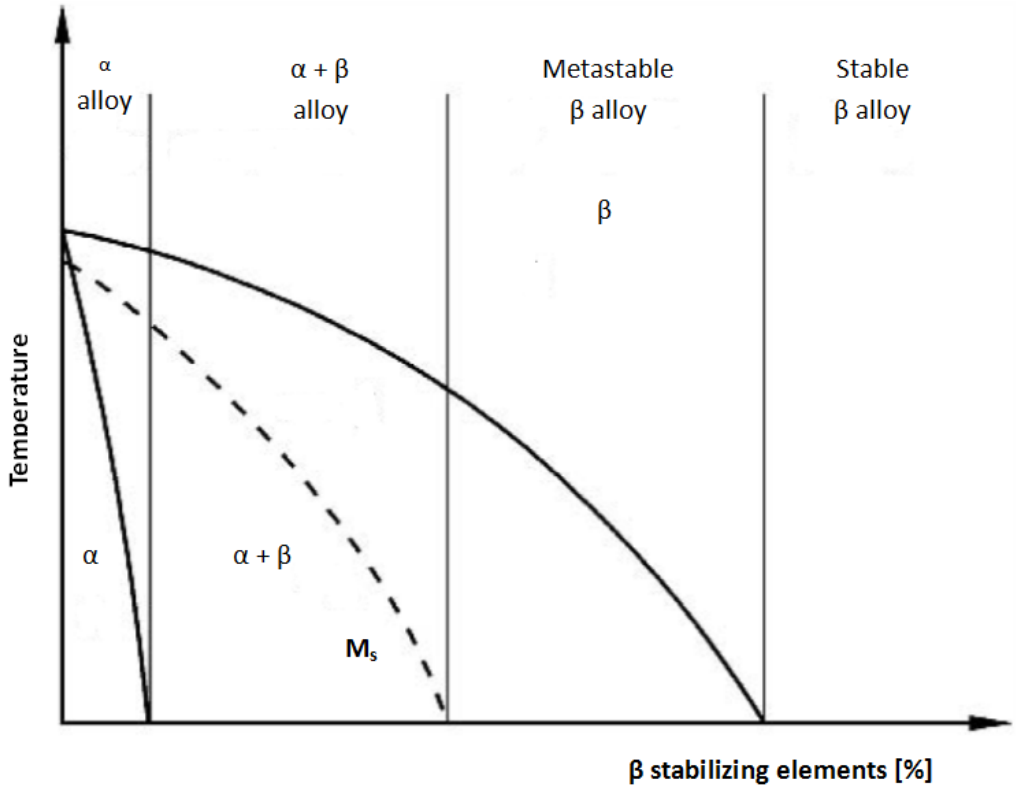

Figure 1.5. Pseudo-binary β-isomorphous phase diagram of titanium with indications of regions pertaining to α alloys, $\alpha + \beta$ alloys, metastable β alloys, and stable β alloys (Lütjering & Williams, 2007)

1.2 Background of Ti5553 and application

Ti-5Al-5V-5Mo-3Cr (Ti5553, in wt%) is a recently developed metastable β titanium alloy which was specifically designed to replace Ti-10V-2Fe-3Al (VT22) for large airplane components (Shariff T. et al., 2012). Ti-10V-2Fe-3Al was primarily designed by Russia for its high strength and toughness applications at temperatures up to 315℃ and tensile strength of 1241 MPa (Chandler, 1996). The alloy also possesses the best hot die forgability of any commercial titanium alloy and is suitable for near net shape forging applications and isothermal forging. In order to provide weight savings over steel, the primary components of aircraft landing gear that is forged by Ti10V2Fe3Al saves approximately 270kg per aircraft (Leyens & Peters, 2003). Compared to Ti10V2Fe3Al, Ti-5Al-5V-5Mo-3Cr has better deep hardenability, which means larger parts can be forged in one. For instance, the landing gear "Bogie Beam" (Figure 1.6) for large airlines is made from two pieces of Ti10V2Fe3Al, with Ti5553 it can be forged as one component.

The β-stabilizers in Ti5553 suppress the β transus temperature to an average value of 856^{o}C (Fanning, 2005). The typical ageing temperatures are 560^{o}C and 677^{o}C (Fanning, 2005). Compared to the most commonly used titanium alloy Ti64, Ti5553 is lighter, has higher strength and better cycle fatigue crack propagation and can be processed at lower temperatures (Shariff T. et al., 2012). Ti5553 can achieve strengths of up to 1517MPa being treated with heat (ChenY., Du Z., Xiao S., Xu L., & Tian J., 2014). However, in order to achieve such high strength, Ti5553 can become too brittle to be applied in industry. Also, Ti5553 has slightly higher thermal conductivity (approximately 10W/m/^{o}C at 100^{o}C, 15W/m/^{o}C at 600^{o}C) than Ti64, but it does not change the fact that like other titanium alloys, Ti5553 is difficult to machine (Wagner, Baili, Dessein, & Lallement, 2010). A metastable β-alloy such as Ti5553 does not go through martensitic transformation upon quenching to room temperature. After heat treatment and ageing at the proper temperature, very fine α phase platelets precipitate in the β-matrix, which means this alloy can be hardened to much higher yield stress levels (Bania, 1994; Lütjering & Williams, 2007).

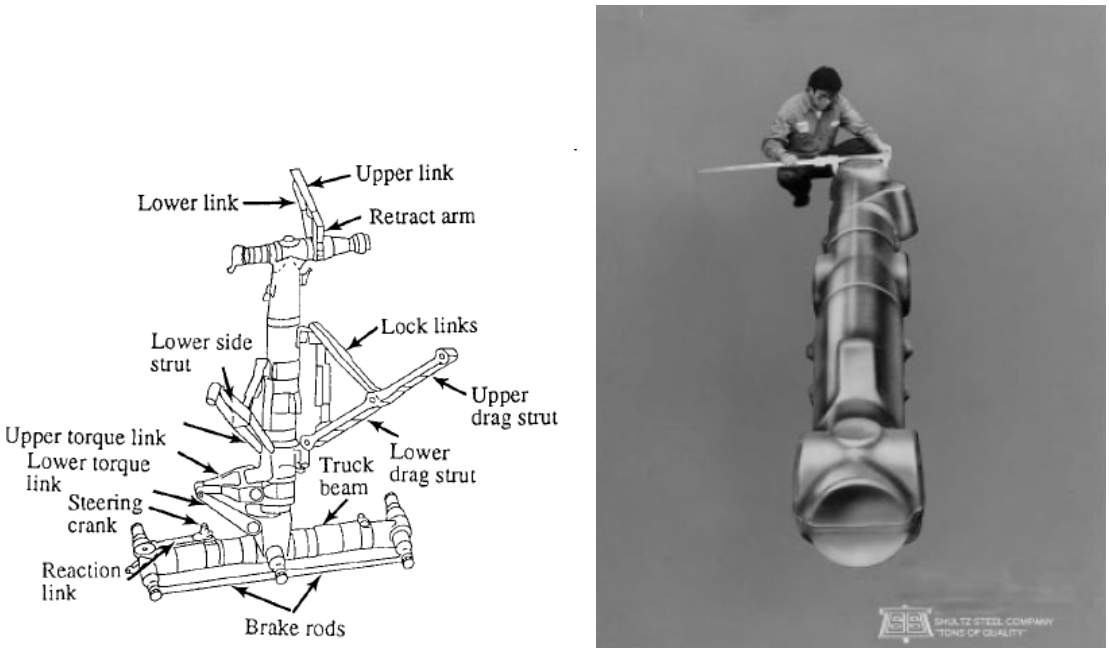

Figure 1.6. Main landing gear of the Boeing 777 of forged Ti10V2Fe3Al parts and “Bogie Beam” (Leyens & Peters, 2003)

1.3 Titanium fusion welding

Unalloyed titanium and α alloys have excellent weldability. Some titanium alloys such as Ti5Al2.5Sn, Ti6Al2Sn4Zr2Mo require an annealed condition. Titanium alloys with a higher content of β stabilizer makes the welding more difficult than those with less β stabilizer content alloys. This is because alloying elements such as molybdenum (Mo) reduces long-term elevated-temperature strength and enhances the embrittlement effect (Davis J. R, 2012). The weldability, along with the other main characteristics of the titanium alloy family are illustrated in Figure 1.7 (Donachie, 2000). So far, Ti5553 shows reasonable weldability and can be welded autogenously (without filler metal).

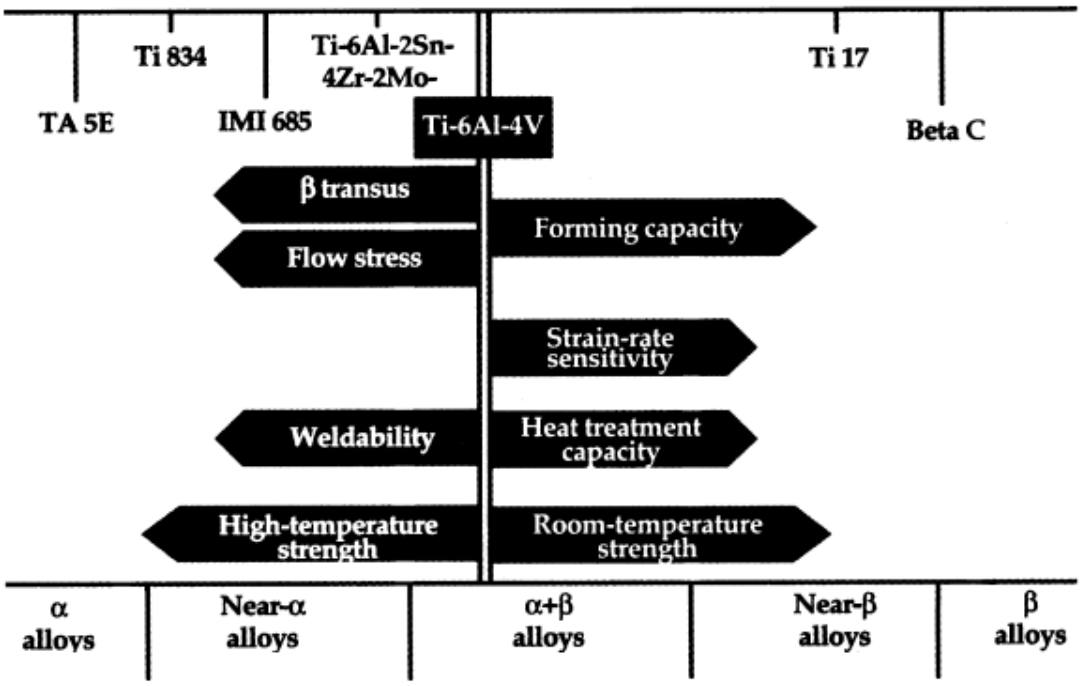

Figure 1.7. Main characteristics of different titanium alloy family groupings (Donachie, 2000)

1.3.1 Welding method

Gas-Tungsten Arc Welding (GTAW) also known as Tungsten-Inert Gas (TIG) is one of the most common welding methods for titanium. GTAW uses a non-consumable tungsten electrode to create an arc to a workpiece accompanied by a shielding gas to protect the electrode, as shown schematically in Figure 1.8. The power source supplies a constant current via a tungsten electrode to produce electrical energy. The shielding gas goes

through the nozzle directly toward the weld pool to protect it from the air. GTAW is usually used to weld thin sections of non-ferrous metals with a filler metal. However, in order to avoid the complication of microstructure, an autogenous welding method was employed which means no filler material was used for joining. Due to its high reactivity with oxygen and hydrogen behaviour, titanium requires sufficient shielding gas, such as argon or helium during GTAW.

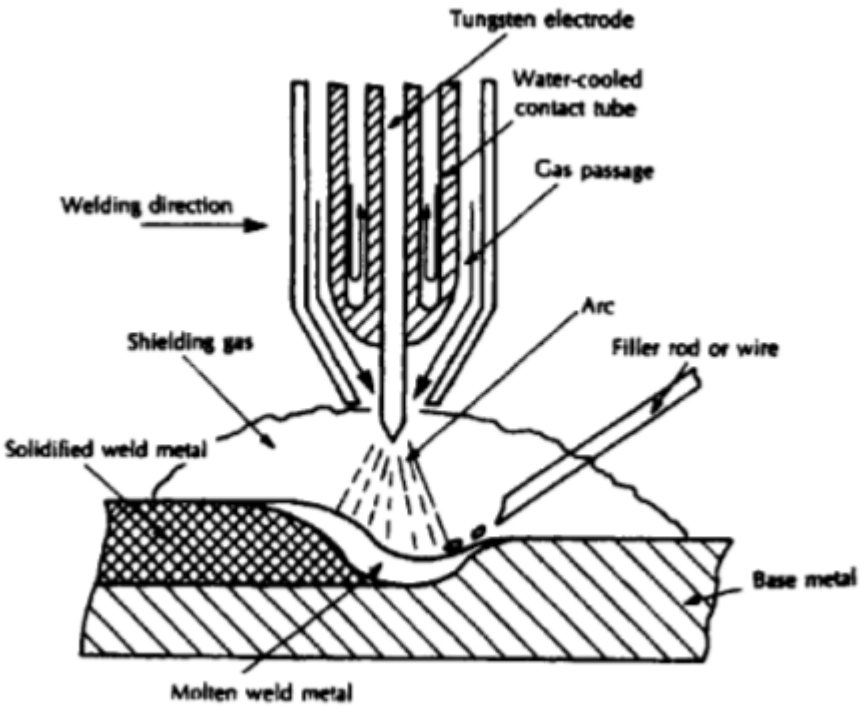

Figure 1.8. Schematic drawing of Gas Tungsten Arc Welding (Messler R. W., 2004)

1.3.2 General macrostructure and microstructure of fusion welding

In the macroscopic aspect of weld solidification, the shape of a joint is affected by the heat input, heat flow, travel speed, and so on. Figure 1.9 (a) is a schematic drawing of a typical single groove butt joint. In general, there are three distinct regions of a weldment due to the interaction of the heat source and the workpiece. These regions, as shown in Figure 1.9 (b), are named as: the fusion zone (FZ) or weld zone, where it is associated with melting and re-solidification; the heat-affected zone (HAZ), which is not melted but affected by the heat source; and the unaffected base metal (BM). The FZ is where the weld or joint is formed. The HAZ can be further subdivided into the partially melted zone

(PMZ) and true heat-affected zone (THAZ). However, some alloys have a very narrow solidification temperature range and the PMZ is hardly observed.

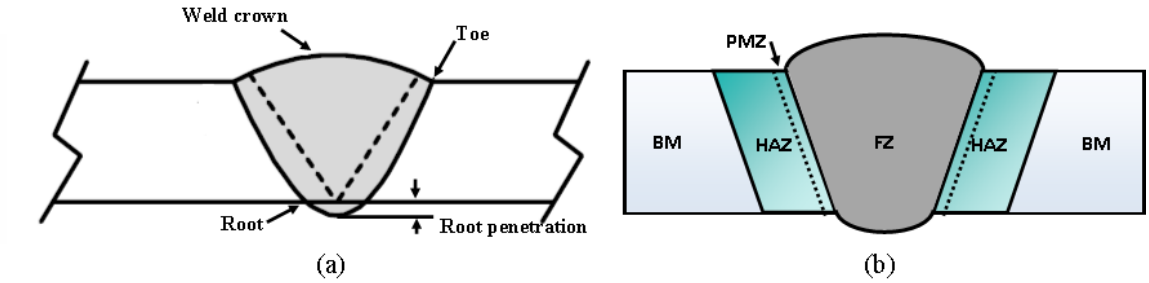

Figure 1.9. Schematic drawing of a butt joint (a), and illustration of zones in a single groove weld (b)

1.3.3 Basic solidification concepts

The grain structure of a weldment can significantly affect the mechanical properties after welding. Therefore, some basic concepts of nucleation and solidification are necessary to be reviewed to understand the formation of the grain structure. When melted metal starts to solidify, the solute atoms are rearranged during solidification. The factor that affects the redistribution of the atoms depends on the thermodynamics, diffusion, undercooling, fluid flow, and so on. The thermodynamic factor is present as a phase diagram which indicates the location of Solid-liquid (S/L) interface (Kou S., 2003). As shown in Figure 1.10, four typical solidification modes are demonstrated: (a) planar, (b) cellular, (c) columnar dendritic, and (d) equiaxed dendritic (Kou S., 2003). The formation of this grain structure is related to the degree of constitutional supercooling which occurs during solidification. A high constitutional supercooling promotes an equiaxed dendritic structure.

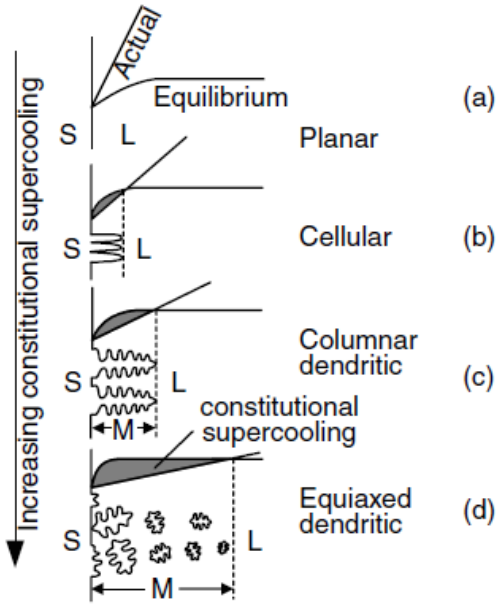

Figure 1.10. Effect of constitutional supercooling on the solidification mode (Kou S., 2003)

Chapter 2. Objective

The objective of this PhD research is to study and characterise the microstructure evolution of welded Ti-5Al-5V-5Mo-3Cr (Ti5553) upon post-weld heat treatment (PWHT), to analyse the phase transformation and process of precipitation hardening, and furthermore, to understand the influence on its mechanical properties.

Although some researchers have studied Ti5553 previously, there is still a lack of understanding about how fusion welded Ti5553 behaves upon heat treatment. This research may explore more applications in industry by analysing the behaviour of welded Ti5553 upon heat treatment considering the relationship to its mechanical properties.

In this research study, the methods of analysis include:

1) Revealing the microstructure (phase and grain structure) of similar (Ti5553-Ti5553) and dissimilar (Ti5553-CPTi & Ti5553-Ti64) weldments in an as-welded condition.
2) Characterising the microstructure of similar weldments upon a series of controlled Post Weld Heat Treatment (PWHT).
3) The use of transmission electron microscope (TEM) to analyse the $\beta \rightarrow \omega$ and $\beta \rightarrow \alpha$ phase transformation. Identify ω and α particles to understand their role during precipitation hardening.
4) Study the influence on weldments and optimise the mechanical properties by hardness and tensile testing.

Chapter 3. Literature review

3.1 Phases of titanium

The metallurgical phases present in titanium have a huge impact on their properties. These phases can be designed and altered by heat treatment. In other words, in order to improve the properties of alloys, mastering the ability to control the distribution, size and morphology of the phases is essential. Phase transformations do not occur instantaneously. The final structure depends on the heating/cooling rate and heat treatment temperature and time.

In general, the phases present in titanium alloys are categorised as equilibrium phases and metastable phases. The equilibrium phases concern the α and β phases where the metastable phases involve $\alpha', \alpha^{"}, \omega, and\ \beta^{"}$. The stability of present phases is essentially related to the alloying elements, temperature, pressure and cooling rate. The temperature when the β/α transformation occurs is called β transus temperature (T_β). Typically, T_β for pure commercial titanium which is $882℃$, T_β for Ti64 is $995℃$ and $856℃$ for Ti5553 (Lütjering & Williams, 2007). The major phase transformation in titanium is known by four types: $\beta \rightarrow \alpha$ diffusional transformation, $\beta \rightarrow \alpha'$ or $\beta \rightarrow \alpha^{"}$ martensitic transformation, $\beta \rightarrow \omega$ shuffle transformation, and $\beta \rightarrow \beta'$ phase separation (Lütjering & Williams, 2007). For Ti5553 alloy, the phase transformation study is focused on $\beta \rightarrow \alpha$ diffusional transformation and $\beta \rightarrow \omega$ shuffle transformation. Ti5553 alloy does not form martensite upon quenching, however it is possible to form athermal ω_a precipitates during cooling to room temperature after welding. Figure 3.1 shows the temperature range for ω precipitation in the Ti5553 alloy, where C_c is the critical minimum level of beta stabilizer content, and C_s is the stabilizer concentration of stable beta alloy (Bania, 1994; Leyens & Peters, 2003; Lütjering & Williams, 2007). The crystallographic orientation relationship of the transformation from the BCC β phase to the HCP α phase is described as a Burgers relationship (Lütjering & Williams, 2007):

$$(\mathbf{110})_{\boldsymbol{\beta}} \,||\, (\mathbf{0002})_{\boldsymbol{\alpha}}$$

$$[\mathbf{1\bar{1}1}]_{\boldsymbol{\beta}} \,||\, [\mathbf{11\bar{2}0}]_{\boldsymbol{\alpha}}$$

As mentioned in the introduction, according to this relationship, a BCC crystal can transform into 12 hexagonal variants with different orientations. Both diffusional

transformation and martensitic transformations obey the Burgers relationship in respect to the parent β crystal (Lütjering & Williams, 2007).

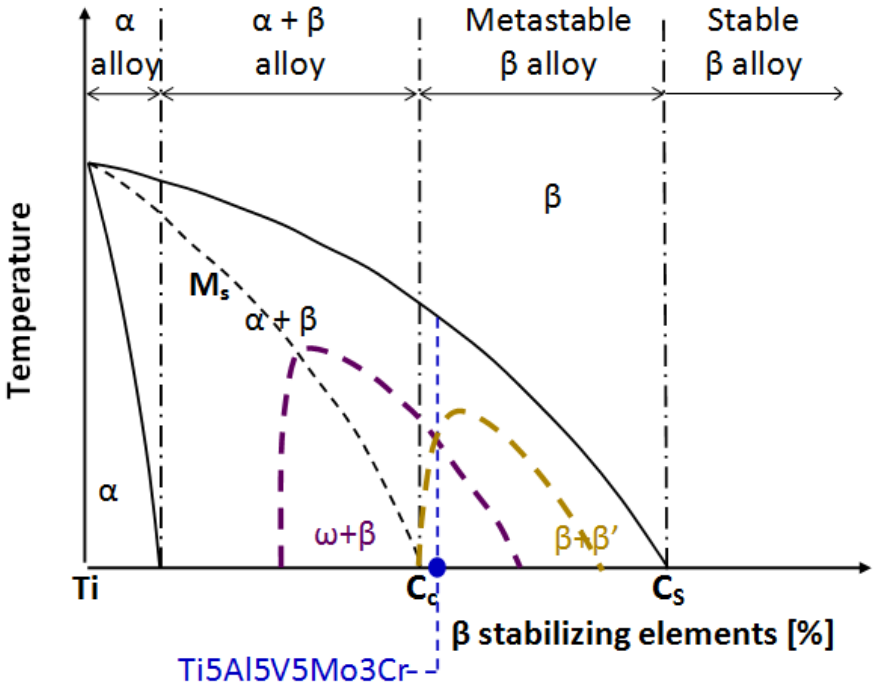

Figure 3.1. Schematic drawing of a pseudo-binary β-isomorphous phase diagram of titanium system indicating the area of various precipitates for Ti5553 (Lütjering & Williams, 2007)

3.1.1 $\beta \rightarrow \alpha$ diffusional transformation

Depending on the cooling rate and composition of the alloys, the BCC β phase can transform to the HCP α phase undergoing conventional nucleation and growth or a martensitic structure during phase transformation (Leyens & Peters, 2003; Lütjering & Williams, 2007). The conventional nucleation and growth is the result of a slow cooling rate from the β phase field into the α+β phase field, which usually leads to a lamellar structure (Leyens & Peters, 2003; Lütjering & Williams, 2007). Figure 3.2 is the lamellar $\alpha + \beta$ microstructure of Ti6Al4V after slow cooling from the β phase. During continued cooling, the precipitated crystal (i.e. α plates) nucleates at the interface boundary of another crystal, where the composition of the precipitated crystal differs from the matrix; the process of this diffusional transformation is called sympathetic nucleation and growth which is illustrated as Figure 3.4 (Branch & Section, 1995; Froes, 2015; Menon & H. I. Aaronson, 1987).

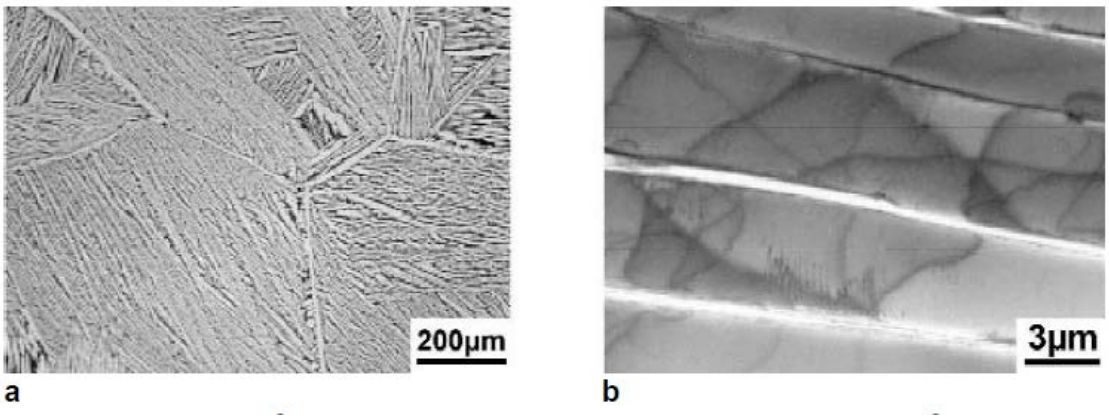

Figure 3.2. Lamellar microstructure of slowly cooled Ti6Al4V: (a) optical microscope image (b) TEM (Lütjering & Williams, 2007)

This type of transformation strictly obeys the Burgers relationship and the flat surface of the α plate is parallel to $(\bar{1}100)_\alpha$ and $(\bar{1}12)_\beta$ planes, shown as Figure 3.3 (Lütjering & Williams, 2007). As the slow cooling continues, the α phase carries on to nucleate and grow into a β grain as parallel plates which separate the prior β matrix into layers. This mixture has the same Burgers variant and is named an α colony. These α colonies continue growing until they reach other colonies with a different orientation (Lütjering & Williams, 2007).

When the temperature drops to T_β, the alpha phase stars to nucleate on multiple sites, although the very first nucleates prefer β boundaries. With an increase in the cooling rate, the size of the α colonies and the thickness of the single α plates become smaller. Colonies can also nucleate on the boundaries of other colonies when they cannot fill the whole grain. A common microstructure is known as “basket weave” or “Widmanstatten” structure. This type of structure is due to the new α plates which grow almost perpendicular to an existing boundary of the α colony to minimise the overall elastic strains (Lütjering & Williams, 2007).

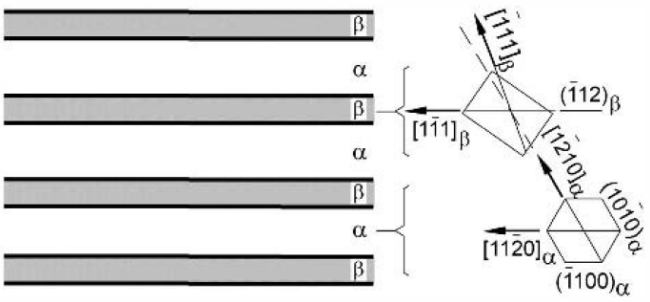

Figure 3.3. Crystallographic relationship between α plates and β matrix within an α colony (Lütjering & Williams, 2007)

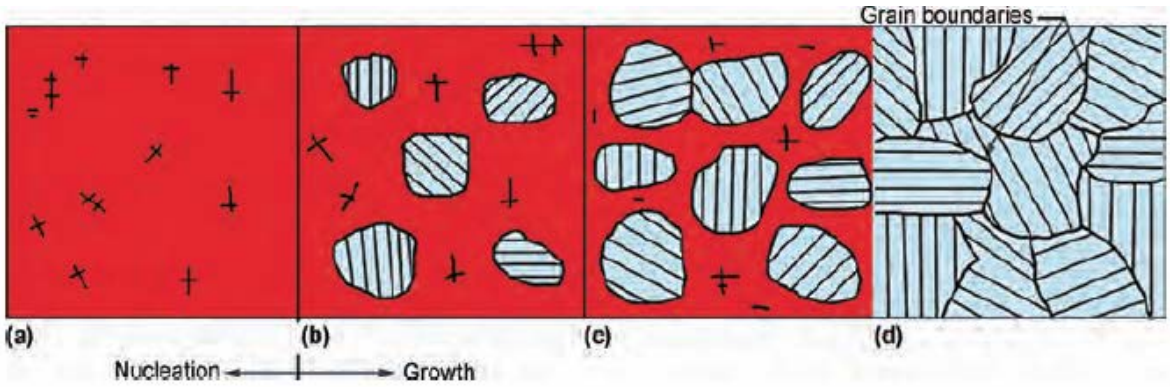

Figure 3.4. Schematic drawing of nucleation and diffusional growth (Froes, 2015)

3.1.2 $\beta \rightarrow \alpha'$ or $\beta \rightarrow \alpha^{"}$ martensitic transformation

The Ti5553 alloy does not have a martensitic transformation. As illustrated in the pseudo phase diagram Figure 3.1, the Ti5553 is located in a region outside of the martensitic start temperature (Ms). Nevertheless, it is necessary to review the process of this transformation. The transformation of martensite involves the cooperative movement of atoms by a shear type process resulting in a homogeneous transformation from a beta phase to an alpha phase (Lütjering & Williams, 2007). This type of transformation is difussionless. Based on morphologies, martensites can be characterised as massive martensite and "acicular" martensite. Both the two types have hexagonal crystal structures that are designated as alpha prime (α'). Massive martensite has a large irregular region and only occurs in pure titanium and its alloys with a very high Ms temperature. Acicular martensite is a mixture of α lath with a thickness of 0.5-1μm (Lütjering & Williams, 2007). By increasing the solute content, the hexagonal crystal structure distorts and loses its hexagonal structure. This type of distorted martensite is described as orthorhombic martensite, known as α''(Lütjering & Williams, 2007). Apart from the alloying elements, the morphologies of martensite highly depend on the heating temperature and cooling methods. Martensite in titanium can be obtained by either quenching or applying an external stress (Duerig & Williams, 1984).

An example of a martensitic transformation of annealed Ti6Al-4V is shown as Figure 3.5. Image (b) and (c) demonstrates the microstructure of Ti64 that has been air cooled and water quenched from above the β transus temperature; (d) and (e) are the ones that are air cooled and water quenched from below the β transus temperature. At 1065℃, the

material is 100% β. Air cooling from this temperature results in a combination of a transformed β (acicular α) and a prior β grain boundaries microstructure with air cooling. Fast cooling, such as by water quenching from this temperature, results in a mixture of an α' (martensite) matrix with a β and prior β grain. Below the β transus temperature (955℃ in this case) the material presents an $\alpha + \beta$ phase. Air cooled material presents a mixture of primary α grain in a matrix of transformed β which contains acicular α. A fast cooling rate produces equiaxed primary α in a matrix of α' (martensite) (Donachie, 2000).

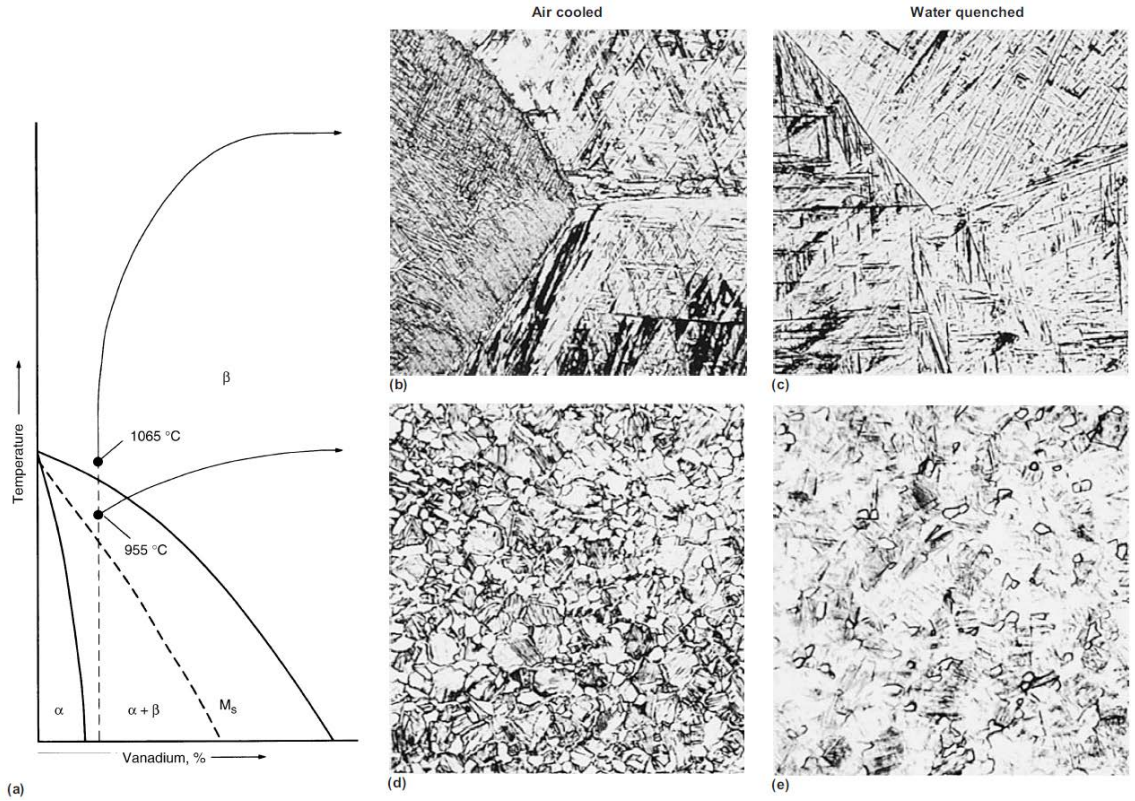

Figure 3.5. Microstructure of annealed $\alpha + \beta$ Ti-6Al-4V with different cooling methods from different temperatures. (a) Pseudo phase diagram, (b) Acicular α with prior β grain boundaries, (c) Martensite with β and prior β grain boundaries, (d) Grains of primary α in a matrix of transformed β containing acicular α, (e) Equiaxed primary α in a matrix of α' (martensite) (Donachie, 2000)

3.1.3 $\beta \rightarrow \omega$ shuffle transformation

In certain metastable and stable β alloys, a metastable by-product omega-phase (ω) coexists depending on the thermal condition, cooling rate and deformation capacity at room temperature. The omega phase was first discovered by X-ray diffraction by Frost in

1954 and later on observed via transmission electron microscopy (Hickman, 1969). This $\beta \rightarrow \omega$ phase transformation involves a shear displacement in the <111> direction of the BCC lattice (Duerig & Williams, 1984; Lütjering & Williams, 2007). The name shuffle suggests this type of transformation involves a small movement of atoms within the cell which results in the formation of an interface between the transformed and parent phase which causes the changes in symmetry and structure. A schematic drawing of $\beta \rightarrow \omega$ transformation is shown as Figure 3.6. The transformation could be incomplete with trigonal symmetry or complete with hexagonal symmetry (Lütjering & Williams, 2007).

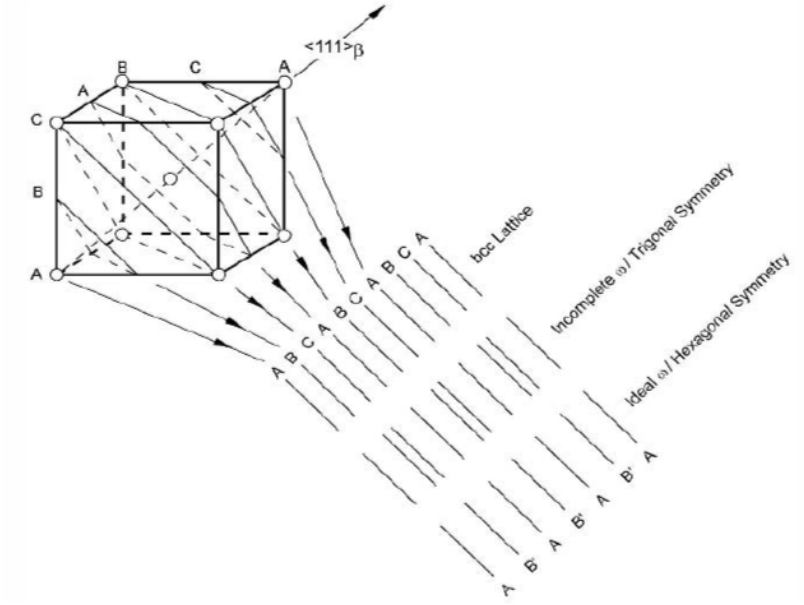

Figure 3.6. Schematic drawing of $\beta \rightarrow \omega$ transformation (Lütjering & Williams, 2007)

In general, ω particles appear as two morphologies: ellipsoidal with a long axis and cuboidal with a flat surface, shown as Figure 3.7 (Lütjering & Williams, 2007). The difference in morphologies depend on the precipitate/matrix misfit (Lütjering & Williams, 2007). In low misfit systems such as Ti-Mo, ω particles are ellipsoidal, and for high misfit systems like Ti-V and Ti-Fe, ω particles tend to be cuboidal. Omega particles without any deformation appear as a spheroid morphology with the lattice parameters of a=4.60 $\dot{A}$ and c=2.82 $\dot{A}$ (Ohmori, Ogo, Nakai, & Kobayashi, 2001; Sukedai, Yoshimitsu, Matsumoto, Hashimoto, & Kiritani, 2003). The orientation relationship between β and ω and the lattice parameters of the ω structure can be expressed as:

$(0001)_\omega // (111)_\beta$ and $< 11\bar{2}0 >_\omega // < 011 >_\beta$;

$a_\omega = \sqrt{2} a_\beta \; and \; c_\omega = (\sqrt{3}/2) a_\beta$. Eq. 3. 1

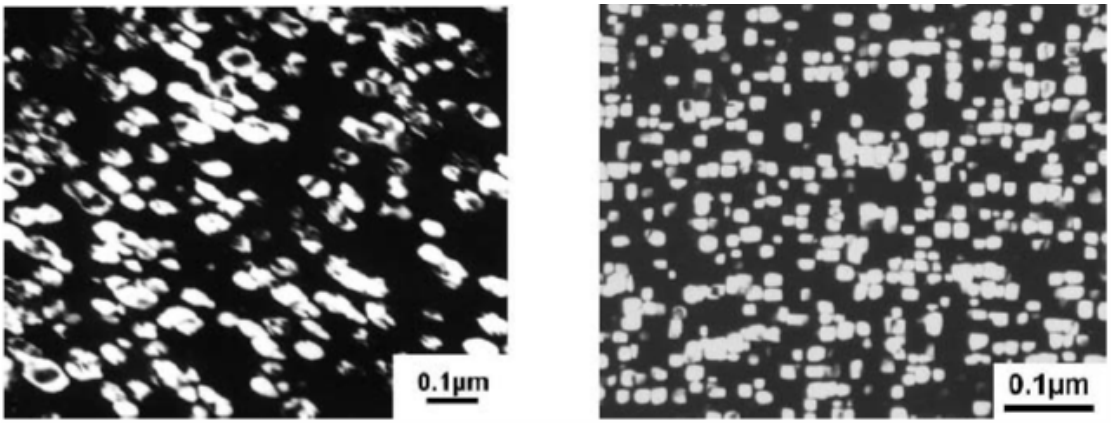

Figure 3.7. Dark field TEM image of ellipsoidal ω precipitates in Ti-16Mo aged for 48hrs at 450℃ and cuboidal ω precipitates in Ti-8Fe aged for 4hrs at 400℃ (Lütjering & Williams, 2007)

There are three conditions known to form a ω-phase, for example during rapid cooling, ageing and deformation at room temperature (Hickman, 1969):

(i) The omega phase formed upon rapid cooling is known as athermal ω_a. This type of omega has been suggested to be a precursor to the martensitic reaction. Athermal ω has a trigonal symmetry structure which is likely to form in heavily β stabilized alloys during rapid cooling. However, for rapid cooling conditions, depending on the alloy type, the ω phase is not guaranteed to be observed. For instance, hexagonal α' and orthorhombic α" could appear first in some rapidly quenched specimens. However, reheating these alloys above the Ms temperature can result in omega precipitation (Hickman, 1969; Leibovitch & Rabinkin, 1980).

(ii) The omega phase formed during ageing is called isothermal ω_{iso}. During ageing the ω phase precipitation is induced at an ageing temperature between an α nose and an Ms point. Isothermal ω exhibits hexagonal symmetry. An isothermal ω-phase can sometimes be the nucleation site for an α-phase. For example, continuing to age after the ω-phase formation induces an equilibrium α-phase (Hickman, 1969). As shown in Figure 3.8, S. Nag demonstrated in his work of Ti5553, the α particles started to nucleate as a sharp tail from the prior ellipsoidal ω precipitates (Leibovitch & Rabinkin, 1980; Nag S., 2008; Nag et al., 2009).

(iii) The last condition of ω-phase formation is highly dependent on the alloying elements. Deformation such as that in the tensile test at room temperature, has shown to produce ω-phase particles in certain titanium β-alloys (Hickman, 1969; Leibovitch & Rabinkin, 1980). In this PhD study, athermal ω_a and isothermal ω_{iso} will be investigated.

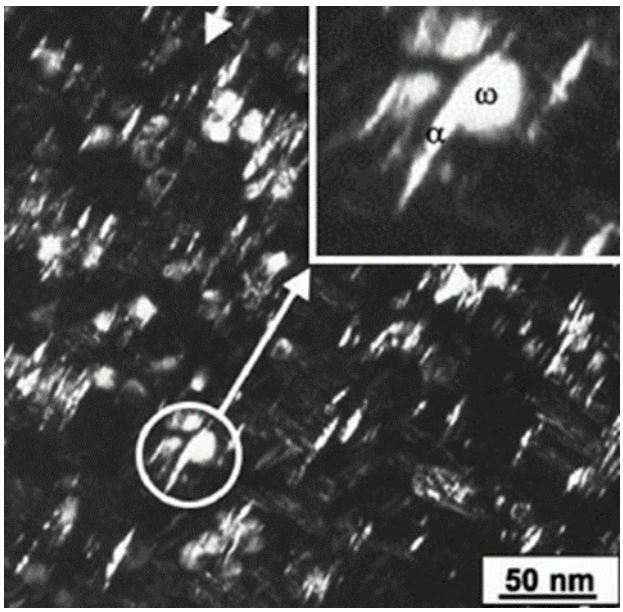

Figure 3.8. Dark field TEM image of $\omega_a \rightarrow \alpha$ transformation (Nag et al., 2009)

The ω phase particle has been cited by various researchers in causing the brittleness of the metastable β-alloy and this will be investigated in the study. Apart from promoting an α phase nucleation, the reason for ω phase raising much interest is that, from the mechanical properties point of view, ω particles cause large increases in strength but also cause a large reduction in ductility.

3.1.4 $\beta \rightarrow \beta'$ phase separation

$\beta \rightarrow \beta'$ phase separation exists when there is a high concentration of β stabilizers. Both phases have BCC crystal structures and different lattice parameters. Both ω and β' are coherent and are the result of shear displacement caused by the moving dislocations (Lütjering & Williams, 2007). Such precipitations are usually avoided due to localised slip bands which can cause early crack nucleation and low ductility (Lütjering & Williams, 2007). Thus ageing and step ageing treatments are usually involved in order to precipitate α phase and use ω and β' as nucleation sites.

3.2 Precipitation hardening (age hardening)

Precipitation hardening (also known as age hardening), is a heat treatment technique to achieve a desired physical effect for some alloys by forming uniformly dispersed small particles within the original phase matrix. Many structural alloys such as titanium, aluminium, magnesium and nickel can use this technique to increase yield strength. As shown in Figure 3.9, precipitation hardening normally includes two steps of heat treatment: (i) the solution treatment in which the alloy is heated to a temperature (T_s) to form a homogenous single-phase solution, followed by rapid cooling (quenching) results in a stable material by preventing the creation of lattice defects; and (ii) ageing the supersaturated solid solution heated to a designated temperature (T_2) for a certain amount of time (Callister & Rethwisch, 2013). The solution treatment and ageing is normally known as STA. Quenching or rapid cooling prevents the formation of any second phase. The precipitation formed during ageing results in a substantial strengthening effect.

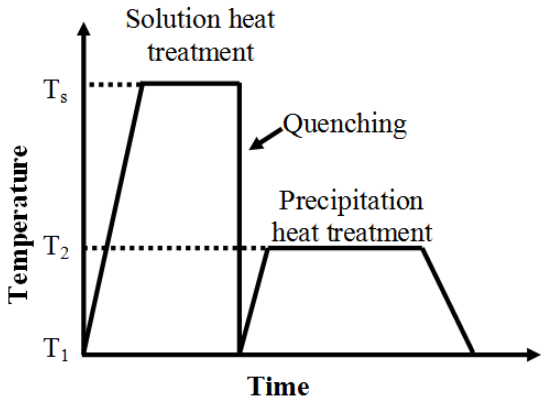

Figure 3.9. Schematic drawing of temperature vs. time showing solution and precipitation heat treatments for precipitation hardening

The hardening mechanism of precipitation can be explained by the modulus mismatch (changes of dislocation energy) and the size of precipitate particles (Ardell, 1985). During ageing, the alloys must be kept at an elevated temperature for a period of time to allow second phase particles to form within the original phase. The newly formed impurity particles are usually extremely small and uniformly distributed. It can take a few hours to allow precipitation to take place. The precipitates act as obstacles that impede the movement of dislocations. The size and the number of precipitates increases as the precipitation proceeds, and consequently, those impurity particles increase the strength and hardness of the alloys. Before the precipitate particles reach their critical size, as the ageing time increases the size of the precipitate particles also increase, causing more difficulty in cutting through. When the precipitate particles reach their critical size, a

longer ageing time results in large, spread-out ineffective precipitates and causes dislocation which tends to bowing around the particle (Orowan Loop), which results in a decrease in material strength (Grote & Antonsson, 2009).

To obtain a higher degree of alloy hardness, sometimes a two-step ageing treatment is introduced for titanium β alloys. This ageing process involves: (i) solution heat treatment and quenching, (ii) first step ageing at a lower temperature to obtain slight precipitation, and (iii) full precipitation of the α phase at a higher temperature. Some of the precipitates formed in first-step ageing serve as precipitation nuclei during second-step ageing (Kuroda, Matsuda, & Iwagi, 2017). Kuroda et al. have reported that the volume fraction of the α phase increased 9% during second-step ageing. The hardness has increased from 470Hv to 530Hv (Kuroda et al., 2017).

3.3 Literature review on precipitation hardening for Ti5553 and similar beta titanium alloys

Wrought Ti5553 requires solution heat treatment and quenching before precipitation hardening. The as-welded metastable/stable β-alloys, in general, exhibit a moderate strength and hardness. However, via a series of controlled thermal treatments, optimised mechanical properties can be achieved by controlling the phase transformation and microstructure. One of the advantages of a post weld heat treatment (PWHT) of metastable and stable β titanium alloys during the heat treatment, α-phase particles precipitate in the β-matrix as very fine, undeformed platelets (Leyens & Peters, 2003; Lütjering & Williams, 2007). Smaller particles with large density and homogenous distribution result in a higher volume fraction. Thereby, metastable/stable β-alloys have the potential to achieve much higher yield stress than α+β alloys (Leyens & Peters, 2003; Lütjering & Williams, 2007). An interesting phenomenon that has drawn many researchers' attention is during phase transformation; a by-product ω-phase particle is formed. It is a metastable phase which is normally found below 500^{o}C (Giosa R. P., 2009) and at a high temperature or under rapid quenching conditions where the ω-phase is either dissolved or never appears upon certain conditions (Giosa R. P., 2009; Hickman, 1969). The formation range of the ω-phase on the phase diagram is shown in Figure 3.1. There are different theories about ω-phase formation and disappearance. In some literature, ω-phase particles are believed to be the nucleation site of the α-phase (Harper, 2004). However, whether all ω particles transform into α is still contentious.

Clement et al. (Clement, Lenain, & Jacques, 2007) studied the effects of heat treatment of Ti5553 and Ti-LCB alloys and observed different amounts of α-phase precipitation. After ageing at 500℃ for 1 hour, the new grains are described by Clement et al. as a combination of fine α precipitation and residual β. The original β matrix is completely transformed at this temperature. With further nucleation at 700℃, the α-phase precipitation forms a film which almost completely covers the original β matrix. The appearance of an athermal ω phase is demonstrated in Figure 3.10. Clement et al. explained the difference in presence of the ω phase which is related to the contents of aluminium in each titanium alloy. A titanium alloy with higher aluminium can delay or suppress the ω precipitation (Harmon & Troiano, 1961). Thus Ti-LCB with 1.5 wt% Al shows more clearly ω precipitation as shown by the diffraction patterns in Figure 3.10.

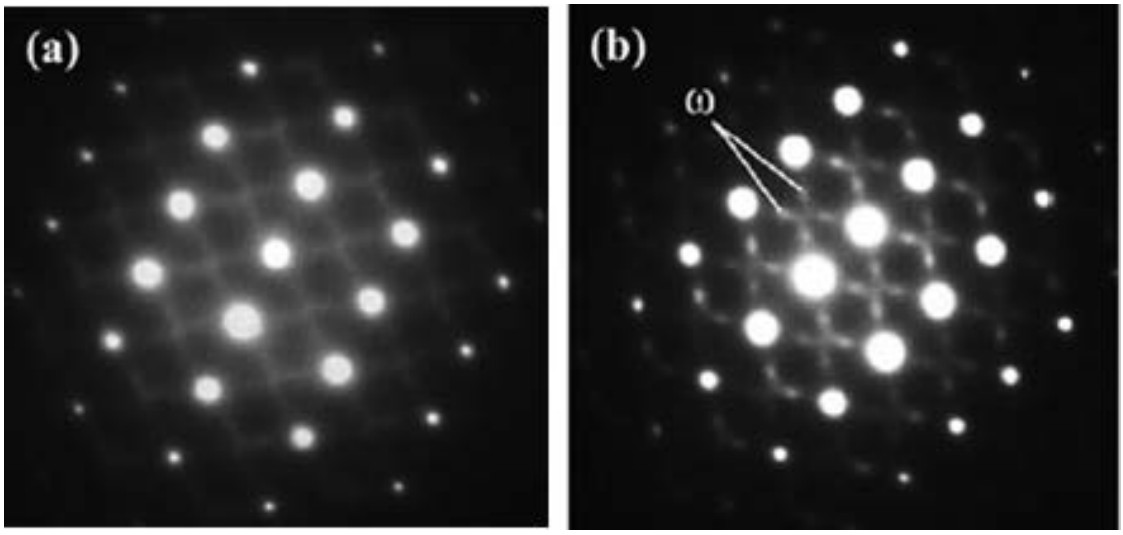

Figure 3.10. Selected area diffraction (SAD) in [110] zone direction of aged (a) Ti5553 and (b) Ti-LCB. Specimens were quenched from 800℃. (Clement et al., 2007)

Similar to the research done by Clement et al., Ohmori et al. (Ohmori et al., 2001) studied the effects of ω-phase precipitation on phase transformation of the metastable beta alloy Ti-9.87V-1.78Fe-3.20Al and recorded a more detailed thermal treatment experiment and results. The forged titanium alloy bar was solution treated at 1000^{o}C for 10mins followed by various ageing treatments. Firstly, an accelerated martensitic plate formation was observed when the specimen was aged isothermally at 250^{o}C for 30sec. However, when holding at this temperature for 1min, the formation of martensite α" was found to be suppressed. Fine ω-phase particles growing rapidly was observed when holding the ageing temperature at 300^{o}C for 100mins. When ageing the specimen isothermally at 350^{o}C, both coarse ω and α particles could be seen in the β matrix, as demonstrated in

Figure 3.11. Ohmori et al. also reported that at 600ºC ω-phase particles were not found. Instead, α" martensite was nucleated from the α laths which suggested that ω-phase precipitation did not promote α" formation or provide the nucleation site for martensitic transformation (Ohmori et al., 2001). Furthermore, they concluded that the ω-phase was only precipitated at temperatures between 200ºC to 400ºC.

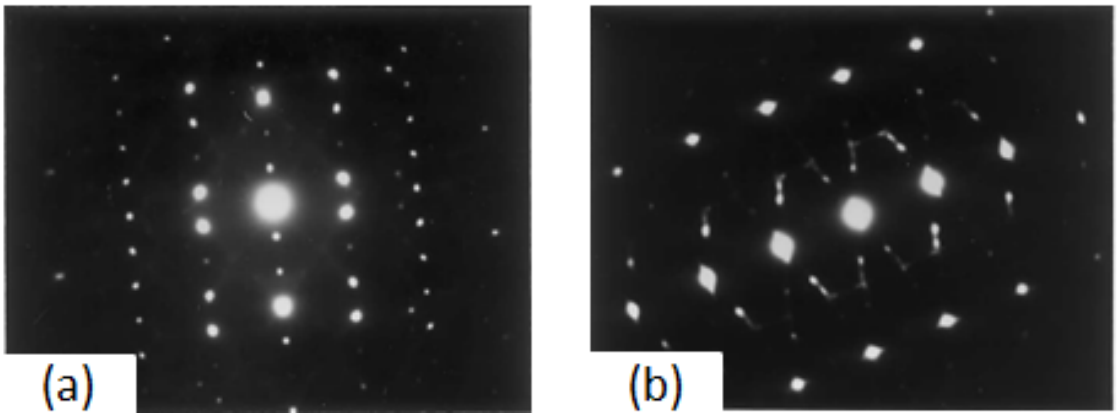

Figure 3.11. Selected area electron diffraction pattern (SAD): (a) held at 300℃ for 100mins; (b) held at 350 ℃ for 10mins (Ohmori et al., 2001)

Nag et al. (Nag S., 2008; Nag et al., 2009) investigated the role of ω precipitation in a T5553 alloy. Samples were solution treated above the β-transus temperature followed by water quenching and isothermal ageing at various temperatures from 30 mins to 4 hours. After solution treatment, an athermal ω-phase was formed. These athermal ω-phase particles provided nucleation sites for fine α precipitation during isothermal ageing. For the same thermal treatment conditions followed by different cooling methods, ageing at 600ºC for 4 hours followed by slow furnace cooling showed coarser intragranular α than those formed from water quenching. In the as-quenched condition, TEM evidence proved the existence of β+ω+α, Figure 3.12. After ageing isothermally at 350ºC for 2 hours, the dark field TEM images showed the changes in size and morphologies of ω and α precipitation which proved to be a coarser spherical and lenticular shape respectively (Nag et al., 2009). At a higher ageing temperature, they reported that the ω precipitation dissolved at 400ºC and the α precipitation appeared to be more coarsened (Nag et al., 2009).

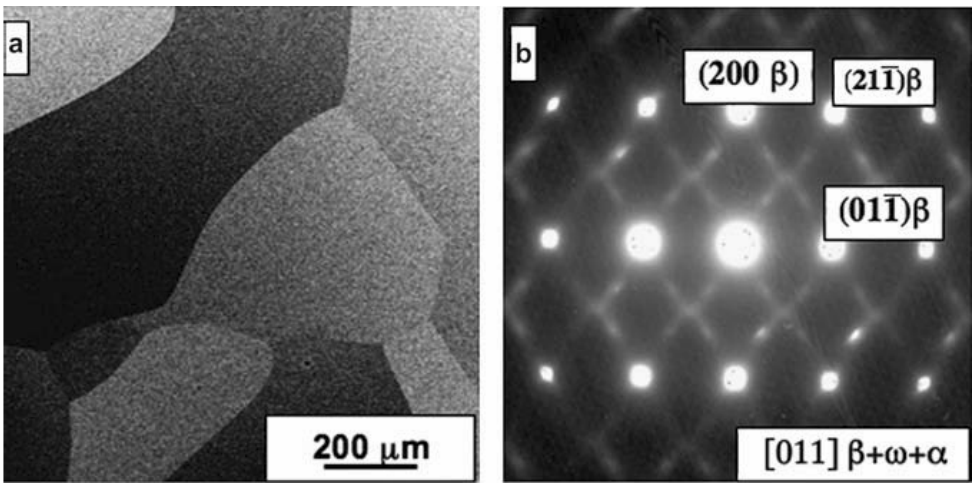

Figure 3.12. TEM results of Ti5553 as-quenched condition: (a) Backscattered image indicates equiaxed β grain; (b) SAD indicates ω precipitates within β grain (Nag et al., 2009)

Researchers such as Bhattacharjee et al. (Bhattacharjee et al., 2008) and Du et al. (Du Z. et al., 2014) have done some work in regard to the influence of the microstructure to mechanical properties of beta titanium alloys after heat treatment. Although the original condition of studied material is different, some of the research methods were employed in this PhD work.

In Bhattacharjee's (Bhattacharjee et al., 2008) study on forged beta titanium alloy Ti-10V-4.5Fe-3Al, the work was focused on the relationship between the volume fraction of β grains after thermal treatment and tensile behaviour. According to their results, the yield strength obeys the Hall-Petch relationship which is $\delta_y = \delta_i + \frac{k}{\sqrt{d}}$ which means the tensile strength decreases as the β grain size increases. The grain size increases as the solution treatment temperature increases. The thermal conditions and tensile test results are presented in Table 3.1. TEM results indicate very fine athermal ω phase precipitation after solution treatment. Compared to their previous work, unlike Ti-10V-2Fe-3Al, there is no stress induced martensitic transformation during the tensile test (Bhattacharjee et al., 2008).

Temperature (ºC)	820	900	1100	1200
Grain size (μm)	158±11	189±11	235±16	866±17
Yield strength (MPa)	778	770	763	710
UTS (MPa)	814	811	801	723
Total elongation (%)	23.1	22.2	18.8	6.0

Table 3.1. Tensile properties of Ti-10V-4.5Fe-3Al alloy (Bhattacharjee et al., 2008)

Du et al. (Du Z. et al., 2014) studied the effect of heat treatment on the microstructure and mechanical properties of Ti-3.5Al-5Mo-6V-3Cr-2Sn-0.5Fe. They investigated the relationship between volume fraction of α phase particles and mechanical properties after various thermal treatments. Du suggested the mechanical properties of a β alloy can be greatly improved by a two-step heat treatment which included a homogenized matrix by solution treatment at around β-transus temperature and then strengthening the alloy by precipitating fine α-phase particles at lower temperatures (Du Z. et al., 2014). They concluded that heat treatment can improve strength but decrease ductility by precipitating a secondary α phase. With a higher ageing temperature, strength decreases. This is because as the ageing temperature increases, the volume fraction of the secondary α is reduced (i.e. the size of the secondary α is bigger).

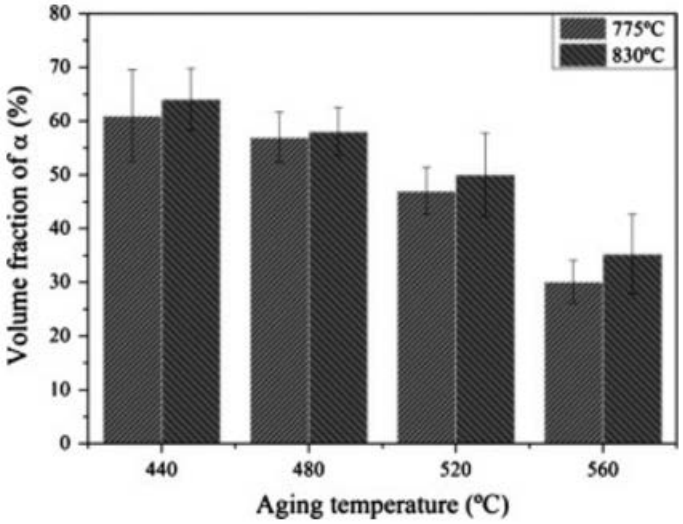

(a)

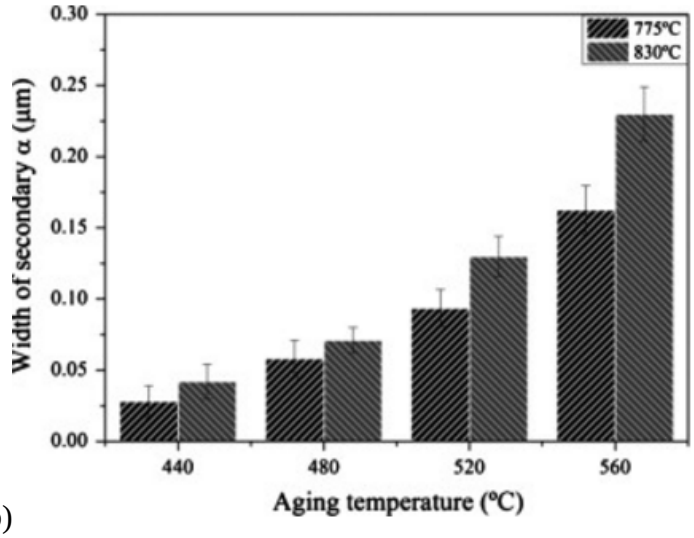

(b)

Figure 3.13. Volume fraction and width of secondary α as a function of ageing temperature: (a) volume fraction of α, (b) width of secondary α (Du Z. et al., 2014)

3.4 Literature review on fracture surface

The slip systems for the BCC crystal structure are up to 48 systems (Leyens & Peters, 2003; Lütjering & Williams, 2007). For titanium alloys, the BCC crystal structure has a 12 slip system, and the HCP crystal structure has 3 slip systems. The slip systems of BCC and HCP titanium are shown in Table 3.2 (Leyens & Peters, 2003; Lütjering & Williams, 2007).

Crystal Structure	Slip Plane	Number of Plane	Slip Direction	Number of Direction	Number of Slip System
BCC	{110}	6	$< \bar{1}11 >$	2	12
HCP	{0001}	1	$< 11\bar{2}0 >$	3	3

Table 3.2. Slip planes and slip direction in BCC β phase and hexagonal α phase (Leyens & Peters, 2003; Lütjering & Williams, 2007)

Study of fracture surface and crack propagation is important because the fracture surface shows evidence of the loading history, analyses the material quality and records the failure history. Before examining the tested pieces, the principle of fracture modes and the atlas of fractographs need to be reviewed. This literature review will help to characterise the fracture surface appearance, identify the weldment flaws, and understand the mechanism associated with the fracture modes.

Before revealing the fracture modes, the first thing that needs to be classified is the fracture loading mode. As illustrated in Figure 3.14, there are three basic types of fracture loading modes: Mode I fracture – opening mode where the tensile stress applied in the normal direction to the plane of the crack; Mode II fracture – sliding mode where a shear stress applied parallel to the plane of the crack in a normal direction to the crack front; Mode III fracture – tearing mode where the shearing stress applied parallel to the plane of the crack in the direction parallel to the crack front (Handbook, 1987; Sun, Rao, & Chen, 2013). These three loading modes depend on the loading direction and relative motion of the mating fracture surfaces (Handbook, 1987). The fracture paths are known as transgranular (through the grains) and intergranular (along the grain boundaries), as shown in Figure 3.15.

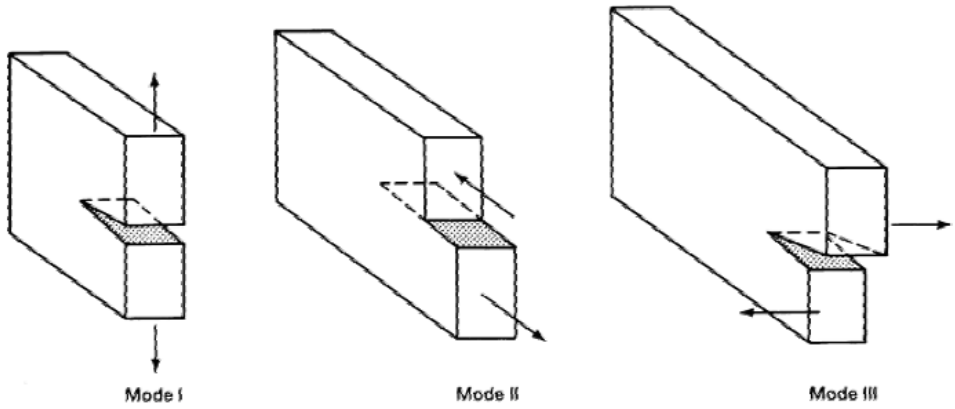

Figure 3.14. Three fracture loading modes: Mode I fracture; Mode II fracture; Mode III fracture (Handbook, 1987)

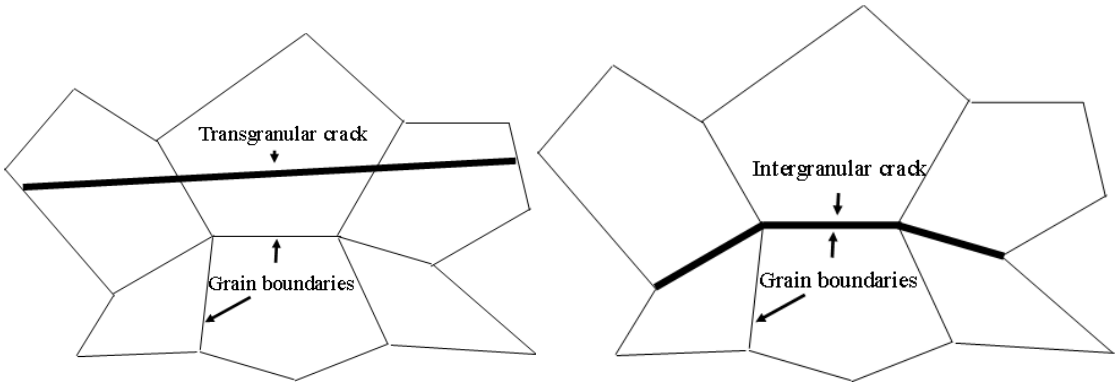

Figure 3.15. Schematic drawing of transgranular crack, intergranular crack and grain boundaries

There are four basic fracture modes: (i) dimple rupture, (ii) cleavage, (iii) fatigue and (iv) decohesive rupture (Handbook, 1987). Dimple rupture is the most common for metals. The process of this failure is called microvoid coalescence (Handbook, 1987). The morphology of dimples are shown in Figure 3.16, being affected by the principal loading direction and plasticity of the material. When the material is under a uniaxial tensile load, the dimples are presented as an equiaxed shape with a closed rim. For shearing and tearing the loading direction, the fracture surface appears as elongated dimples with open ends. Where fractures are caused by a tear load, the dimples have the same direction for the top and bottom surfaces of the mating faces. Where fractures are caused by a shear load, the dimples have the opposite direction on the mating surface. The size of dimples is influenced by the number and distribution of microvoids.

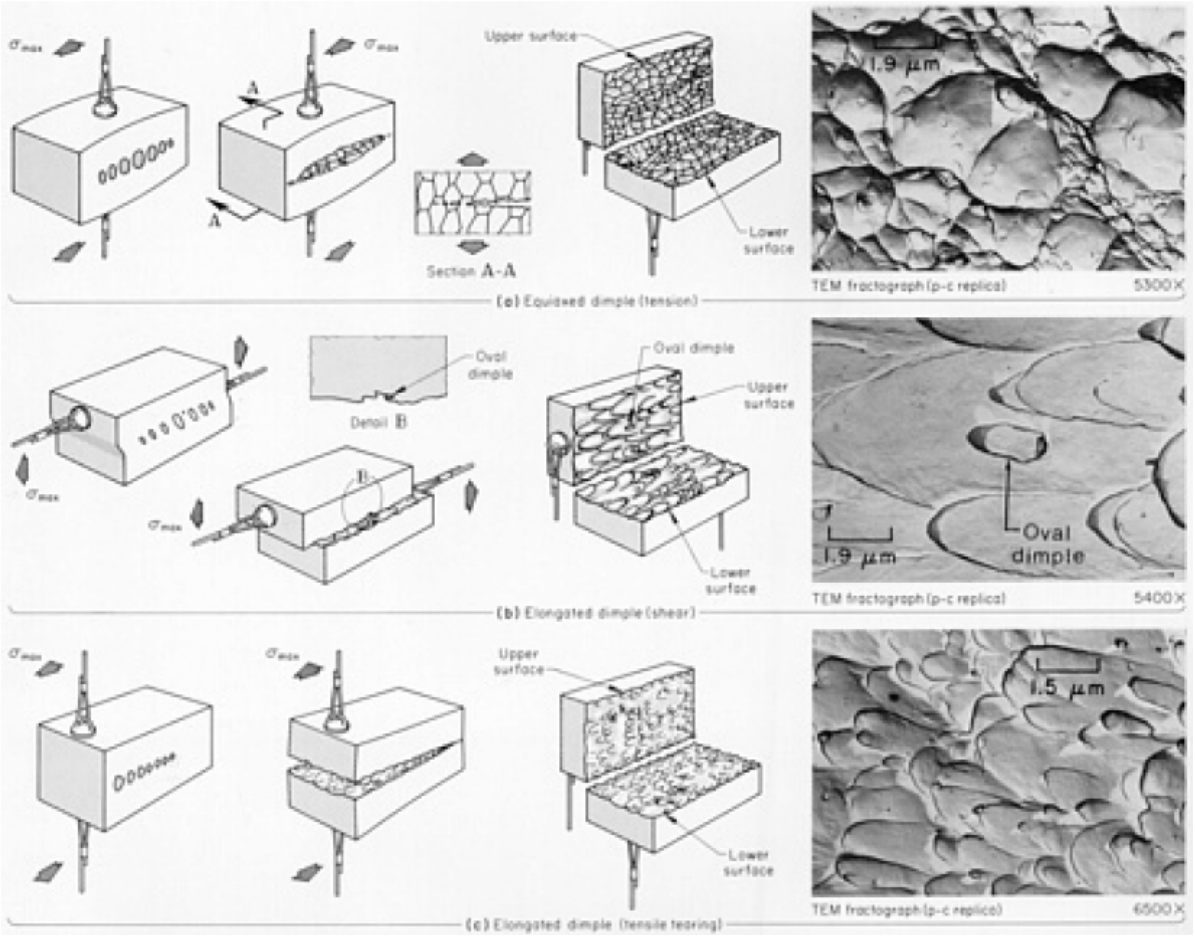

Figure 3.16. Shapes of dimples formed by microvoid coalescence (a) equiaxed dimples formed by tension, (b) elongated dimples in opposite direction on mating surface that are formed by shear force, (c) elongated dimples with the same direction on the mating surface that are formed by tensile tearing (Handbook, 1987)

Cleavage fracture is a brittle form of fracture that occurs by breaking atomic bonds along crystallographic planes. Theoretically, ideal cleavage fractures contain parallel transgranular plans. However, due to imperfections in crystal lattice orientation, such as grain and sub-grain boundaries, dislocation and so on that affect the cleavage propagation, most of the engineering alloys have river patterns, cleavage steps, feather markings, chevron patterns and tongues (Handbook, 1987). Figure 3.17 demonstrates examples of cleavage fracture with the above cleavage features. However, it is not common to see cleavage in titanium fractures.

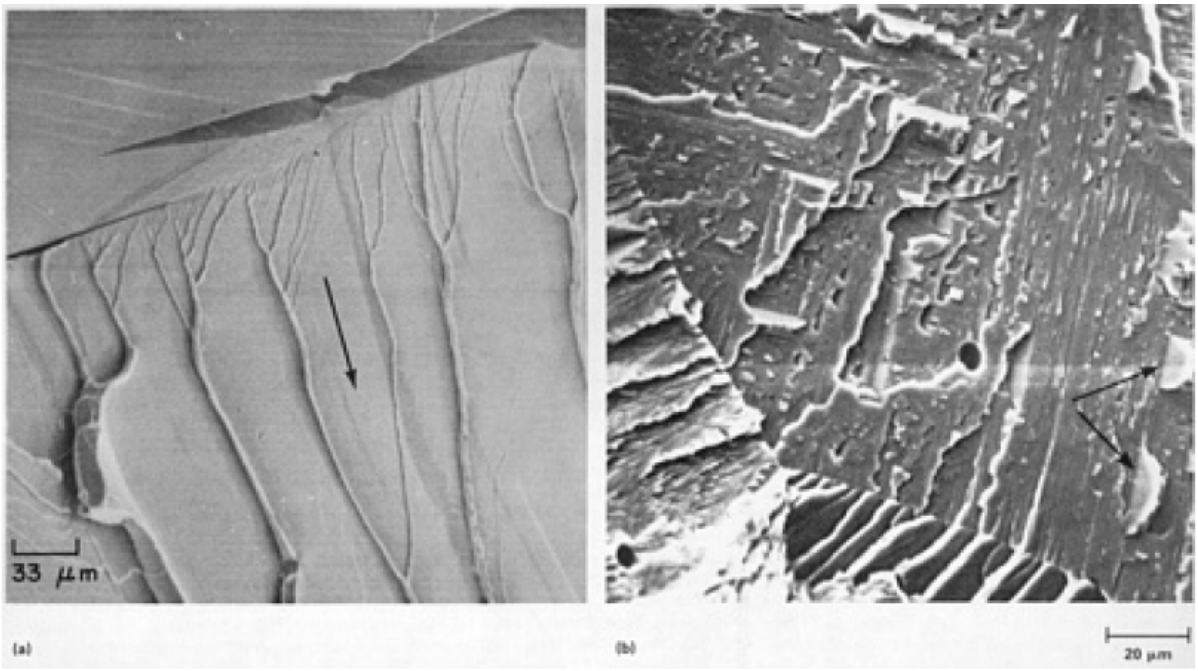

Figure 3.17. (a) Fractured by impact that contains a twist boundary, cleavage steps, and river patterns in an Fe-0.01C-0.24Mn-0.02Si alloy. (b) Tongues (arrows) on the surface of a 30% Cr steel weld metal (Handbook, 1987)

Fatigue mechanism is not studied in this PhD research. However, it is good to have a brief review about fatigue fractures since fatigue is commonly found in titanium alloys, particularly in aerospace applications. A fatigue fracture is a result of cyclic loading. The stress is not high enough to cause a sudden fracture but the cyclic load produces layers of cracks with a very small distance in each loading cycle. The ASM classifies fatigue fracture in three stages: stage I fatigue, where crack is initiated by the active slip system in the metal which is influenced by microstructure and stress (Handbook, 1987). Cracks follow crystallographic planes and are redirected at grain boundaries. At stage II fatigue, cracks are propagated and exhibit crack-arrest marks known as fatigue striations (Handbook, 1987). Stage III fatigue is where the fatal failure occurs. The example fractography images are present as in Figure 3.18.

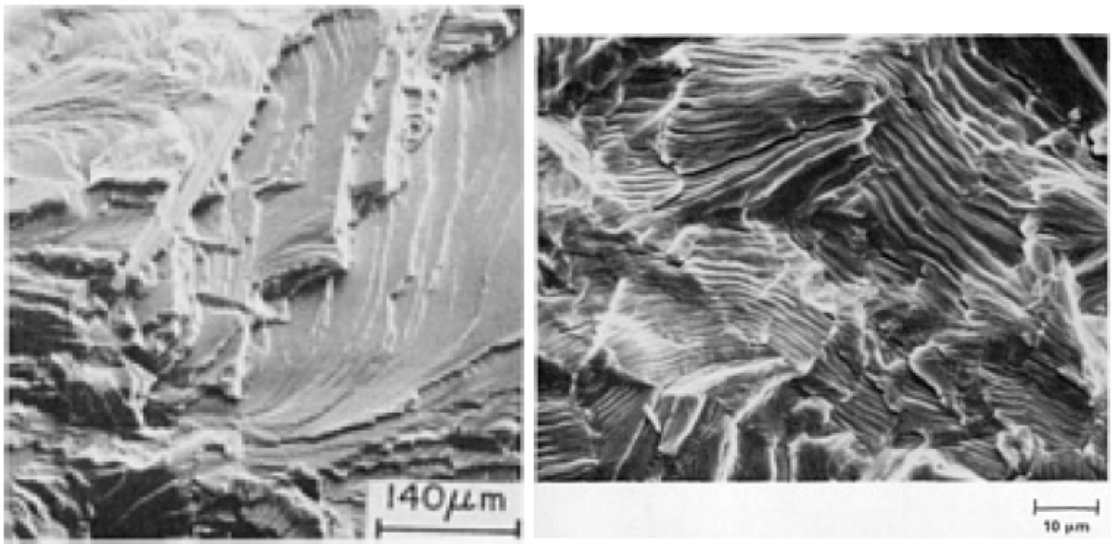

Figure 3.18. Fatigue crack growth and striations on the fracture surface of Ti-6Al-2Sn-4Zr-2Mo-0.1Si and CP Ti specimens (Handbook, 1987)

A decohesive rupture is the result of a reactive environment or a unique microstructure which involves the weakening of atomic bonds and a reduction in surface energy (Handbook, 1987). The rupture only happens along grain boundaries which usually contain elements such as hydrogen, sulfur, phosphorus, and so on, causing a reduction of cohesive strength and promoting decohesive rupture. The schematic illustration of decohesive rupture is shown in Figure 3.19.

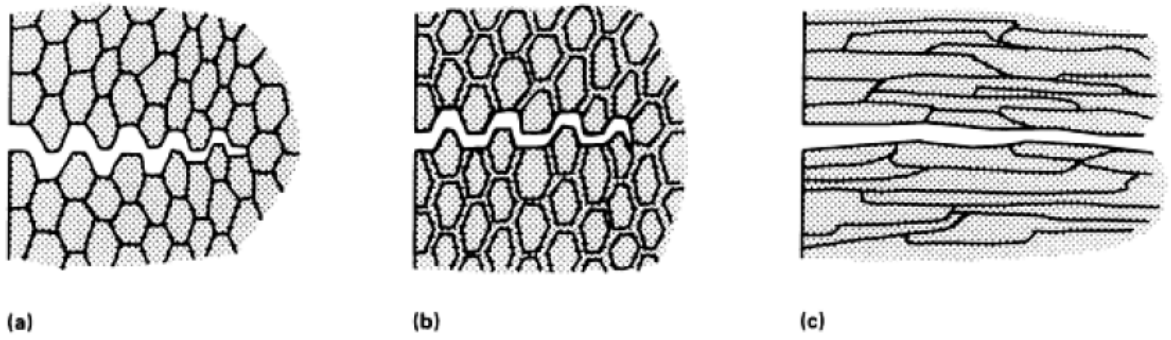

Figure 3.19. Decohesive rupture along grain boundaries (Handbook, 1987)

Chapter 4. Experimental methods

4.1 Introduction

This chapter discusses the methodology used in the research study, including: the techniques used in sample preparation, the welding procedure and details of welding parameters, design of heat treatment and the equipment employed in the analysis. An autogenous fusion welding technique was applied throughout the welding experiments which means no filler metal was added. A metallurgical examination and analysis were employed, using optical microscopy, a scanning electron microscopy and transmission electron microscopy. The mechanical properties examination was carried out by engaging hardness and tensile tests.

4.2 Materials and welding methods

The composition of titanium Ti5553, CP Ti and Ti64 alloys used in this PhD research are displayed in Table 4.1. The main alloy, Ti5553 is essentially Ti-5Al-5V-5Mo-3Cr. This study investigates similar welding of Ti5553-Ti5553 as well as some of the features in the dissimilar welding of Ti5553-Ti64 and Ti5553-CPTi. Gas Tungsten Arc Welding (GTAW/TIG) was the major welding technique that was employed in this study. All samples were butt welded autogenously (without filler material) with full penetration. Occasionally, bead on plate (BOP), also with full penetration, was performed for metallurgical examination. Thoriated tungsten was used as the electrode material. The welding parameters are shown in Table 4.2.

Laser Beam Welding (LBW) was performed to a lesser extent. LBW was conducted at the Japan Welding Research Institute (JWRI), Osaka University, Japan with a power of 2-3kW, travelling speed of 100mm/sec. Argon gas shielding was used at 20-30L/min.

	Ti	**Al**	**V**	**Mo**	**Cr**	**Fe**	**C**	**O**	**N**
CP Ti	Bal.	0.16	<0.01	<0.01	<0.01	0.22	0.01	0.28	0.01
Ti64	Bal.	6.08	3.85	<0.01	0.02	0.17	0.02	0.05	<0.01
Ti5553	Bal.	5.03	5.10	5.06	2.64	0.38	0.01	0.14	<0.01

Table 4.1. Composition of titanium alloys used in this study (wt.%)

A cleaning process is essential in the welding preparation to minimise the reaction of titanium with air, moisture, grease, and so on. Before welding, the weld joints and adjacent areas were washed with non-chlorinated solvents such as acetone to remove all the grease and dirt. Lint-free cloths were used to remove any remaining residue. During welding, a trailing purge kit was used to provide sufficient shielding gas over the weld bead to ensure the joint is cooled below its critical temperature before exposing it to the atmosphere.

Welding method	Welding current	Voltage	Amperage	Welding speed	Shielding gas	Gas flow rate
GTAW	DC electrode negative	$\approx 10V$	$20 - 70Amp$	$\approx 162\ mm\ per\ min$	Pure argon gas	Welding torch = 14-15 LPM Purge = 8-10 LPM

Table 4.2. Welding parameters for GTAW

4.3 Thermal treatment condition

For a Ti5553-Ti5553 as-welded (AW) specimen, the solution treatment of this near-β alloy is usually conducted below the β transus temperature ($\approx 860℃$), and the suitable ageing temperature is in the range of 566-677^{o}C (Nyakana, Fanning, & Boyer, 2005). Based on the literature, ageing at 500℃ and 600℃ have been chosen as the post welding heat treatment (PWHT) temperatures. The cooling method is air cooling for all heat-treated specimens. A solution heat treated process was carried out for comparison. The ageing time and temperature has been designed and is shown in Table 4.3.

Specimen	**Solution Treatment**	**PWHT condition**
Ti5553-Ti5553 (BoP and butt joint)	--	Ageing at 500^{o}C for 5min, 15min, 30min, 2hrs, 3hrs, 4hrs, 8hrs followed by air cooling
Ti5553-Ti5553 (BoP and butt joint)	--	Ageing at 500^{o}C for 8hrs followed by ageing at 800^{o}C

		for 15min, 30min, 2hrs followed by air cooling
Ti5553-Ti5553 (BoP and butt joint)	--	Ageing at 600^{o}C for 5min, 15min, 30min, 2hrs, 3hrs, 4hrs, 8hrs followed by air cooling
Ti5553-Ti5553 (BoP and butt joint)		Ageing at 600^{o}C for 8hrs followed by ageing at 800^{o}C for 15min, 30min, 2hrs followed by air cooling
Ti5553-Ti5553	ST ~ 800℃ for 30mins followed by water quenching	Ageing at 500^{o}C for 15mins 30min, 2hrs, 4hrs followed by air cooling
Ti5553-Ti5553	ST ~ 800℃ for 30mins followed by water quenching	Ageing at 600^{o}C for 15mins 30min, 2hrs, 4hrs followed by air cooling

Table 4.3. PWHT conditions for Ti5553 similar weldments

4.4. Description of experimental methods and equipment

4.4.1 Sample preparation: mechanical polishing and etching method

(i) Mechanical grinding and polishing

Metallurgical samples for SEM and microscopy were prepared according to ASM standards. Test pieces were prepared by precision cutting using a Struers Lotom-3 abrasive saw and a Buehler slow cutting machine. Selected specimens were mounted by a Struers LoboPress-3 metallurgical mounting machine with 20N force, under 180^{o} for 6mins, followed by 3mins of cooling. PolyFast phenoic hot mounting resin with carbon filler was used for hot mounting.

Mechanical preparation for metallographic examination of titanium alloys is difficult due to their low grinding and polishing rates. For titanium alpha and near alpha alloys, a mechanical grinding procedure can cause the test piece work to harden and induce deformation twinning (Vander Voort, 1999). A planar grinding procedure was performed

with 180-, 500-, 1200- and 2400-grit SiC paper carried out by a Metaserv rotary grinder. Mechanical polishing used a 6μm diamond suspension (DP) and a 1μm standard colloidal silica suspension (OP-S) and was carried out with a Struers TegraPol 21 automatic metallurgical polishing machine. Finally, polished samples were cleaned using a Techspan ultrasonic cleaner with 95% ethanol.

(ii) Etching

All samples for metallurgical examination were etched by Kroll's reagent: 93% H_2O + 2%HF+5% HNO_3 (Sabol, Pasang, Misiolek, & Williams, 2012).

4.4.2 Optical microscope (OM)

An Olympus BX51M optical microscope was used for the low magnification microstructure observation. Images were captured by charge coupled devices and recorded with a ScopePhoto system. The magnifications used for microstructure examination were 50x, 100x, 200x and 1000x. The macrographs taken near the fracture area after tensile testing was carried out by an Olympus LG-PS2 with 10 times the magnification.

4.4.3 Scanning Electron Microscopy (SEM)

A Hitachi SU-70 Schottky field emission scanning electron microscope (SEM) was employed for high magnification microstructure image and fracture surface analysis. An Energy Dispersive Spectrometer (EDS) was used for basic chemical analysis via the integration of the Noran System 7 (NSS). An Electron Probe Micro-Analysis (EPMA) was carried out in the Japan Welding Research Institute (JWRI), Osaka University, to analyse the composition of a dissimilar weldment.

4.4.4 Transmission Election Microscopy (TEM)

For a phase transformation analysis, a transmission election microscope (TEM) was employed. Since the particle size of α and ω can be fairly small, a conventional microscope cannot fullfill the investigation. The idea of using TEM is to expose the

existing particles with high resolution images and diffraction patterns in selected areas to reveal the present phases. A Tecnai^{TM} F20 scanning/transmission electron microscope (S/TEM) coupled with a Gatan Digital Micrograph, were employed for the phase transformation analysis. The Tecnai F20 has an X-TWIN lens and high brightness field emission electron gun. The system can be used to analyse elemental compositions down to the sub-nanometer range, while having the best high resolution imaging and diffraction data in an uncorrected S/TEM and high tilt range, automation and dynamic focus adjustment. This analysis used a wide range of techniques including high resolution scanning S/TEM, diffraction, chemical analysis and 3D tomography.

The procedure to prepare TEM foils is summarised as follows.

1). The fusion zone of welded Ti5553 was cut into $6\text{mm} \times 20\text{mm}$ rectangular test pieces.

2). The test pieces were manually ground to approximately 50-80μm thin foils. The foils were then cut into 3mm diameter round chips.

3). All TEM specimens were prepared by using twin-jet electrolytic thinning in 10% H_2SO_4 + 90% CH_3OH solution at -40℃ (Bhattacharjee et al., 2008).

4). TEM was operated with 200kV and analysis was carried out by using a Gatan Digital Micrograph.

4.4.5 Hardness testing

An LM800AT tester was used for the Vickers microhardness test. The purpose of the test is to investigate the hardness profile of the as-welded and PWHT samples. The applied load was 300gf with 10sec dwell time**.** The tested specimens were the same samples that were used for metallurgical work.

4.4.6 Tensile testing

Tensile testing was carried out with a Tinius Olesen testing machine with 3mm/min position rate and a 25mm extensometer for the elongation measurement. The dimension of the dog-bone shaped specimen is illustrated as in Figure 4.1.

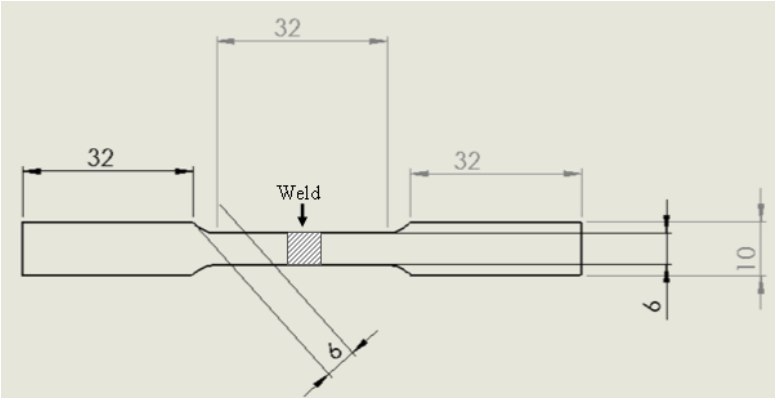

Figure 4.1. Dimension of a dog-bone shaped specimen

Chapter 5. Microstructure evolution and phase transformation with heat treatment

5.1 Introduction

This chapter discusses the microstructure evolution and phase transformation of Ti5553 and a similar weldment upon various post weld heat treatment (PWHT). The microstructure analysis was carried out by an optical microscope and scanning electron microscope (SEM). An advanced phase transformation analysis is carried out by transmission electron microscope (TEM). The purpose of this study is to investigate the growth of the α precipitates and the role of the ω phase during heat treatment.

5.2 Microstructure of as-received Ti5553

Microstructure of the as-received Ti5553 is demonstrated in three planes (horizontal, longitudinal and transverse), as shown in Figure 5.1. The welding direction is the same as the horizontal direction. The microstructure of the base metal is observed via an optical microscope and presented in Figure 5.2. A low magnification image indicated that the base material was in the as-rolled condition. High magnification images reveal a typical α+β microstructure, where α particles with an average size of 2-3μm are distributed within the β matrix.

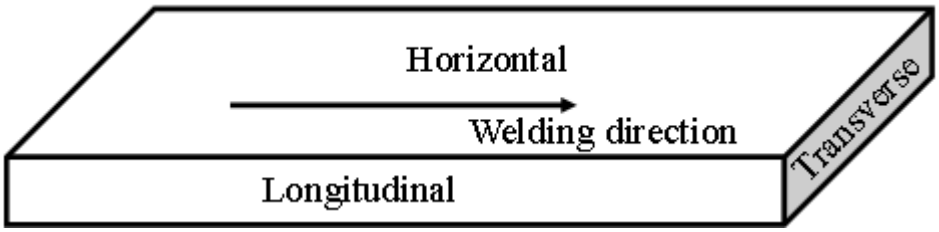

Figure 5.1. Three planes of as-received Ti5553 and the welding direction

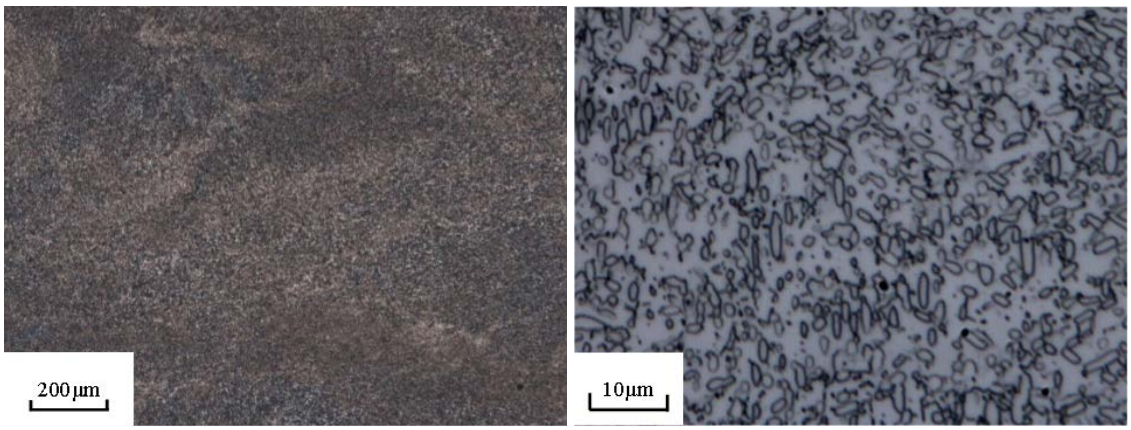

Horizontal plane

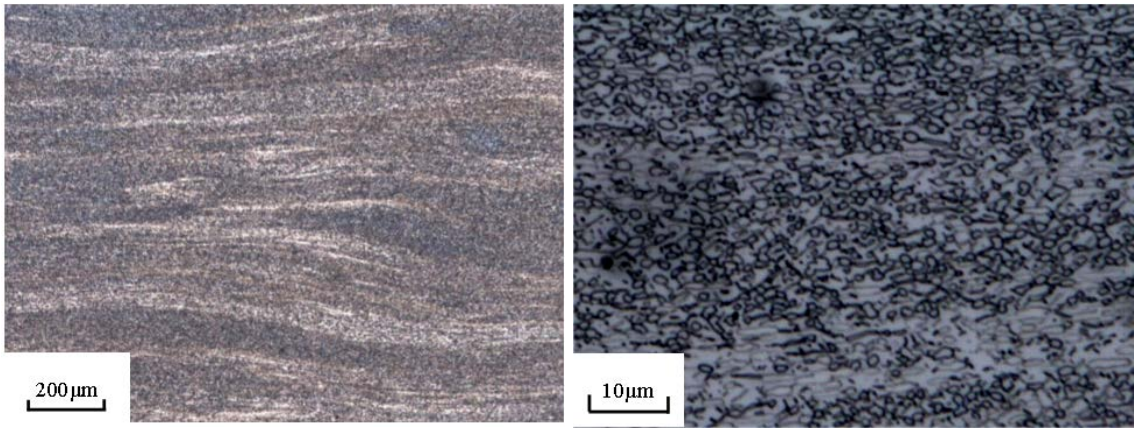

Longitudinal plane

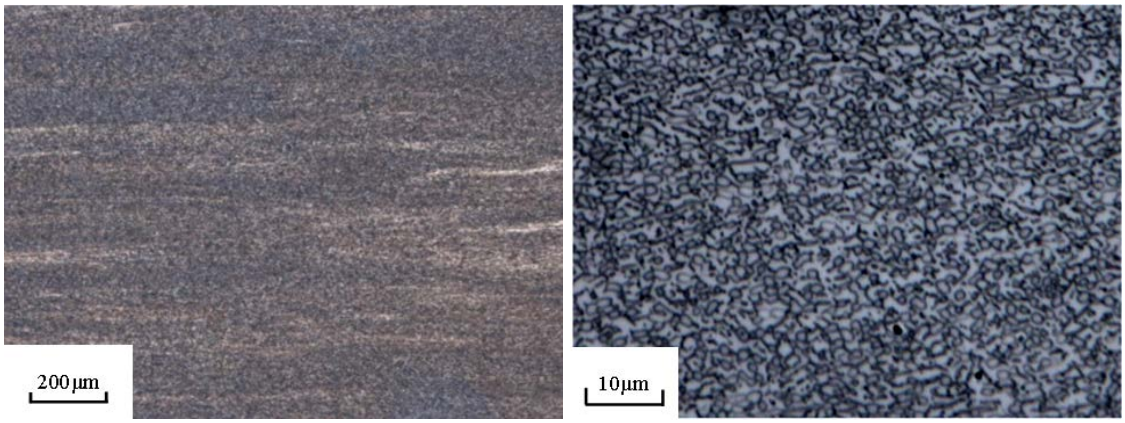

Transverse plane

Figure 5.2. Microstructures of the as-rolled Ti5553 in 50x and 1000x magnifications of horizontal, longitudinal and transverse planes

5.3 Physical metallurgy in as-welded condition

In this section, a few microstructure observations in the as-welded (AW) condition are discussed. Since the workpieces were welded autogenously (no filler added), the fusion zone is formed by the melting and re-solidification of the Ti5553 alloy only. GTAW and LBW samples are used to discuss the similarities and differences between the two metallurgical results. The top view of Ti5553 workpieces after welding are shown in Figure 5.3.

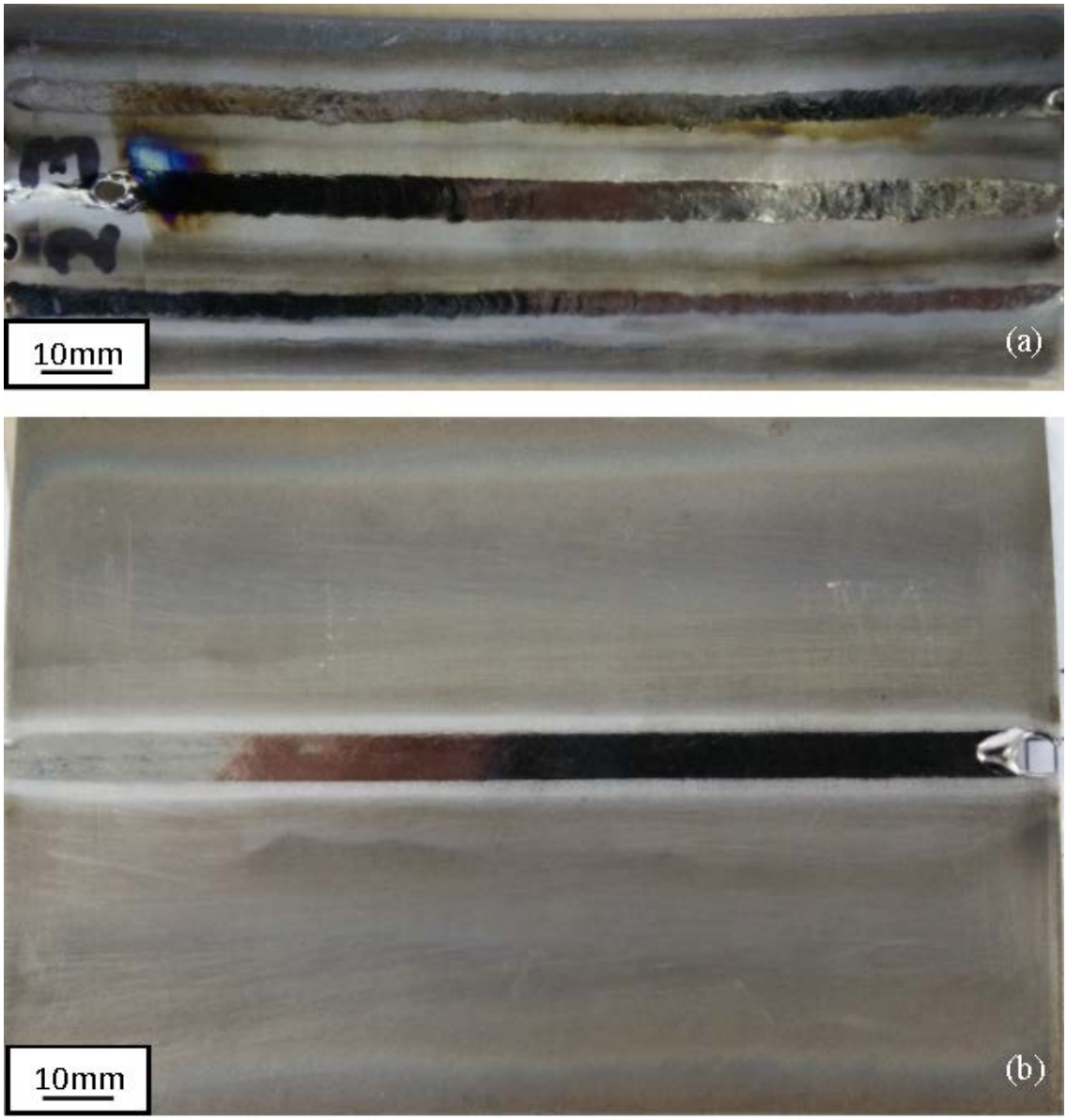

Figure 5.3. Top view of GTAW weldments: (a) bead on plate (BOP), (b) butt joint

The shape of the weld zone normally depends on the energy intensity of the welding method, the traveling speed and the thickness of the workpiece. In the macroscopic point

of view, as presented in the first images of Figure 5.4 & 5.5, due to the high intensity of the heat source and fast welding travel speed, the LBW has a much smaller crown size (approximately 2mm) than the GTAW (approximately 6mm). The LBW weld also has a very narrow HAZ because of the smaller size of heat source and high power of density; hence low heat input. The base metal of Ti5553 at the fusion line provided the growth site. Unlike casting, weld solidification does not require a nucleation site (Lampman, 1997). Solidification occurs at an initial stage proceeded by rapid atom deposition from a molten weld pool on an adjacent HAZ (Lampman, 1997; Kou S., 2003). Growth starts by arranging atoms without changing the existing crystallographic orientation which results in a continuity of grain growth. Such grain structure is known as epitaxial growth which is commonly seen in Ti5553 similar welds. Epitaxial growth often occurs in autogenous welding. The crystallographic orientation of the HAZ grains at the weld interface continue into the weld fusion zone (Lampman, 1997). In the microscopic aspects, both the GTAW and the LBW are predominantly occupied by a columnar dendritic structure in the FZ. Three types of grain boundaries were observed in the FZ. They are:

(i) Solidification sub-grain boundaries (SSGB) which are the boundaries that separate dendrites. These SSGB are low-angle ($<5^{o}$) boundaries which have low misorientation and dislocation density because the sub-grains favour growth along the crystallographic direction, which is $<100>_{\beta}$ for BCC metals (Lippold, 2015).

(ii) Solidification grain boundaries (SGB). These grain boundaries are the intersections that separate a group of sub-grains with the same growth direction and orientation. SGBs are high-angle boundaries that have high angular misorientation which result in a network of dislocations along the boundary. SGBs can also be formed by the redistribution of solute alloying elements such as Vanadium (V) (Lippold, 2015).

(iii) Migrated grain boundaries (MGB). MGB is a migrated boundary of SGB. These boundaries are high-angle boundaries which carry the same crystallographic misorientation of the parent SGB. MGB usually occurs in single phase weld metals because the crystallographic components of the second phase act like “pins” which restrain the movement of the SGB. Thus, filler wire is normally used for preventing grain migration. The MGB often occurs in reheating or multipass welding (Corbacho, Suarez, & Molleda, 1998; Lippold, 2015). A MGB has been reported in other welded metastable titanium alloys. Baeslack et al. (Baeslack III, Liu, & Paskell, 1993; Baeslack

III, Liu, Barbis, Schley, & Wood, 1993) reported the cause of grain migration was due to the poor correlation between the “liquated” grain boundary (LGB) and the MGB. This caused an occurrence of beta grain migration limited HAZ liquation.

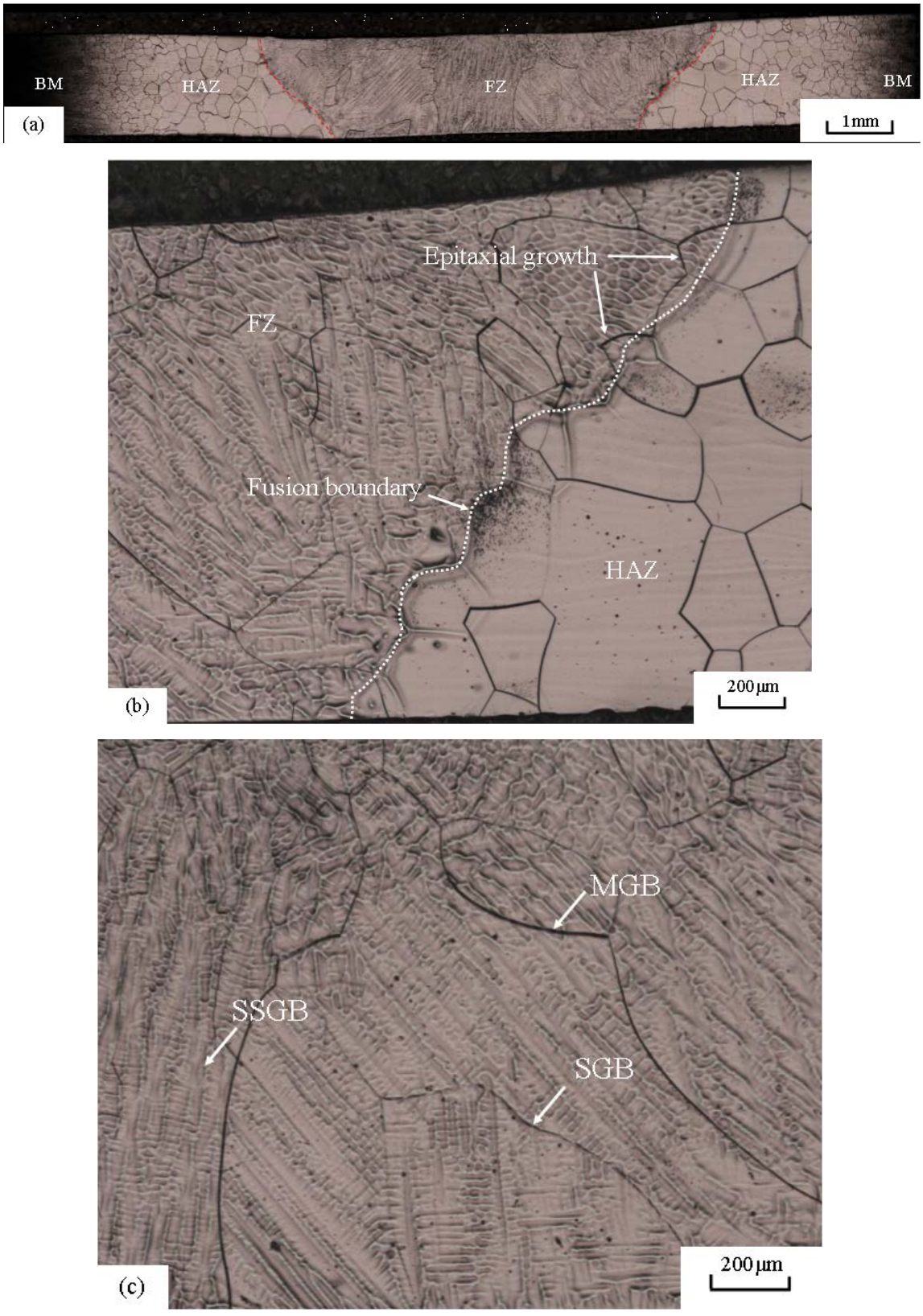

Figure 5.4. Microstructure of as-welded Ti5553 with a GTAW: (a) low magnification micrograph of the FZ, HAZ and BM, (b) FZ, HAZ, fusion boundary and epitaxial growth, and (c) FZ and three types of grain boundaries

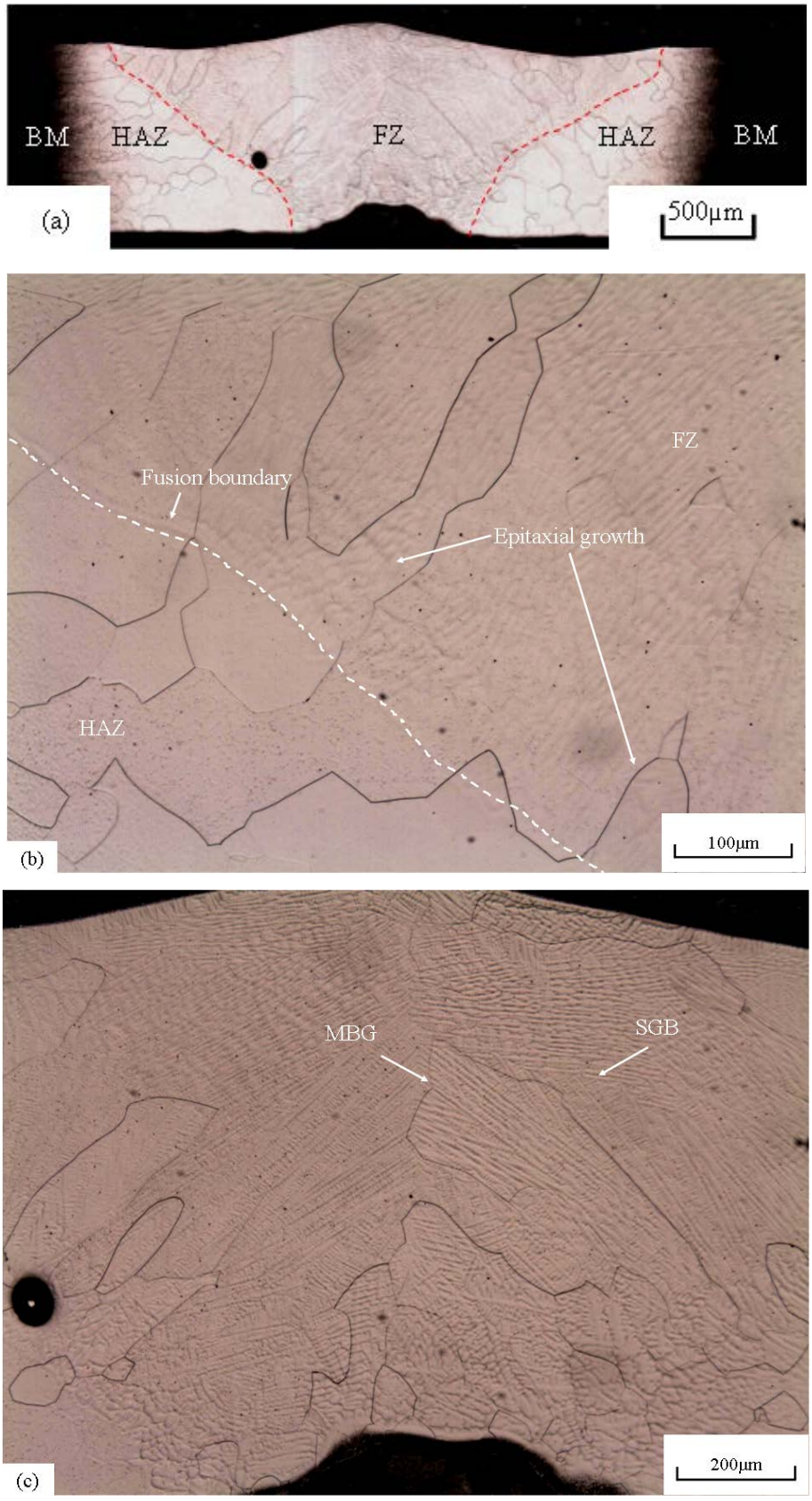

Figure 5.5. Microstructure of as-welded Ti5553 with LBW: (a) low magnification micrograph of the FZ, HAZ and BM, (b) FZ, HAZ, fusion boundary and epitaxial growth, and (c) FZ and two types of grain boundaries

A higher welding speed such as an LBW and an EBW (i.e. lower heat input), resulted in a smaller size of crown, smaller weld pool and also a finer dendritic structure. This observation is proved by the differences in dendrite arm spacing (DAS). As shown in Figure 5.6, the GTAW has larger primary and secondary DAS than the LBW specimen. The primary DAS (λ_1) of the GTAW is almost twice as big as the LBW and the secondary DAS (λ_2) of the GTAW is nearly three times the size of the DAS of the LBW.

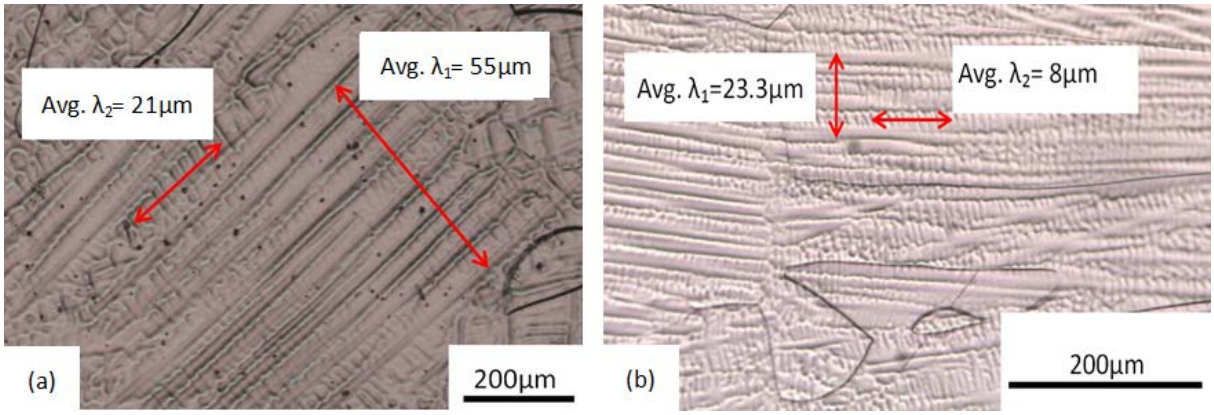

Figure 5.6. Dendrite arm spacing comparison in which the λ_1 and λ_2 are primary and secondary DAS respectively: (a) GTAW; (b) LBW

The HAZ showed large equiaxed grains near the fusion boundaries which became smaller towards the base metal. Epitaxial growth can be found at the fusion boundaries. Along the fusion boundary, the solidification mode was cellular growth.

5.4 Physical metallurgy in post weld heat treatment conditions (PWHT)

The overall weld zone of Ti5553 after a PWHT retains its columnar microstructure. Previous reports in the literature on thermal treatment of wrought Ti5553 alloys suggested that the ideal temperature for this alloy is around 500℃ (Chen Y., et al., 2014; Fanning, 2005). In order to accomplish the goal of optimising the mechanical property of welded Ti5553, experimental heat treatments were carried out at 500℃ and 600℃. Microstructure examinations were carried out by optical microscope (OM), SEM and TEM.

5.4.1 Metallurgy in PWHT at 500℃ ageing condition

1) 5 minutes at 500 ℃: precipitation has not taken place. No evidence of nucleation was found by OM or SEM. This is also confirmed by the hardness results (described later in Section 6.2). However, very fine, small parts of sub-grain (SG) were observed. These fine SG provided α nucleation sites and promoted precipitation. Some dark spots were observed in the FZ. However, higher magnification of SEM images showed some of them were believed to be the possible growth site for the SG, the rest of them were etch pits. The amount of these newly formed SG was low and they were scattered throughout the FZ. Thus, at this stage, there was no significant change to the microstructure.

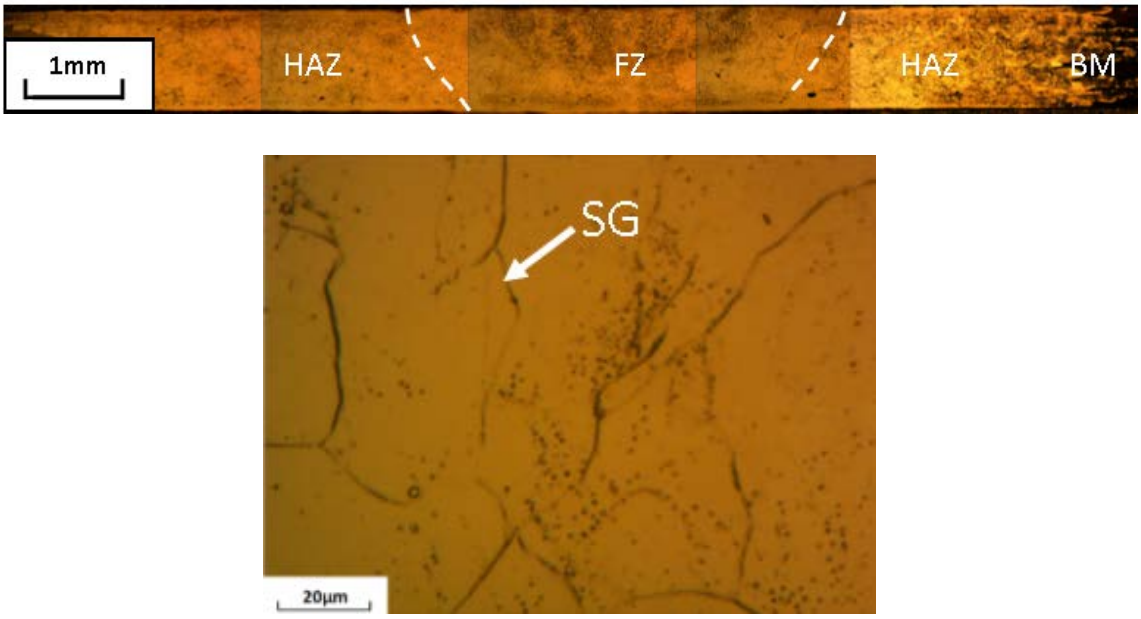

Figure 5.7. Optical micrographs of overall weld profile and FZ of welded Ti5553 aged at 500℃ for 5mins

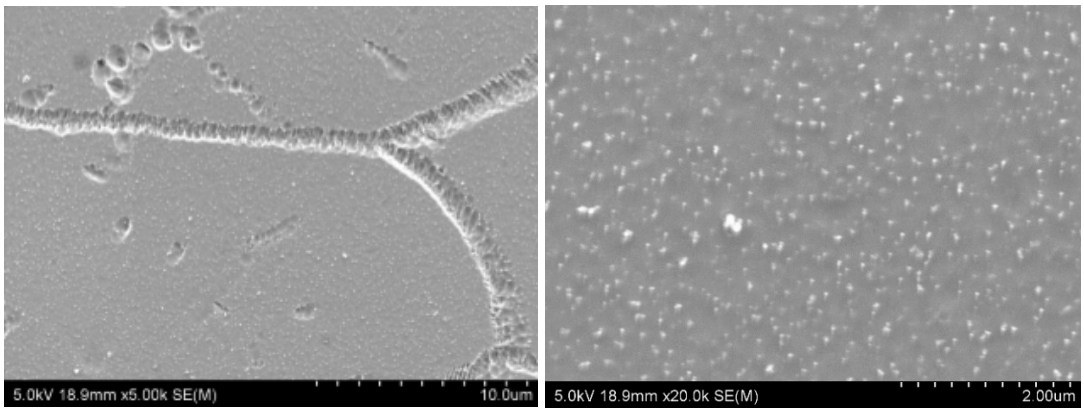

Figure 5.8. SEM micrographs of FZ of welded Ti5553 aged at 500℃ for 5mins

2) 15 minutes at 500℃: optical micrographs exposed unevenly etched colour. The dark area revealed localised α precipitation within the retained β matrix. SEM micrographs show that at the current stage, most of those α particles start to precipitate on the grain boundaries and the newly formed sub-grain structure (SG) within the β matrix. Those α particles are rather small with a low density. Precipitation near the grain boundaries grew distinctly faster than inside the grains. Furthermore, the SG became coarser. Due to the inhomogeneous distribution of the α particles, local hardness has been altered. A tensile test also showed a little improvement at this stage. The mechanical properties will be discussed later in Chapter 6.

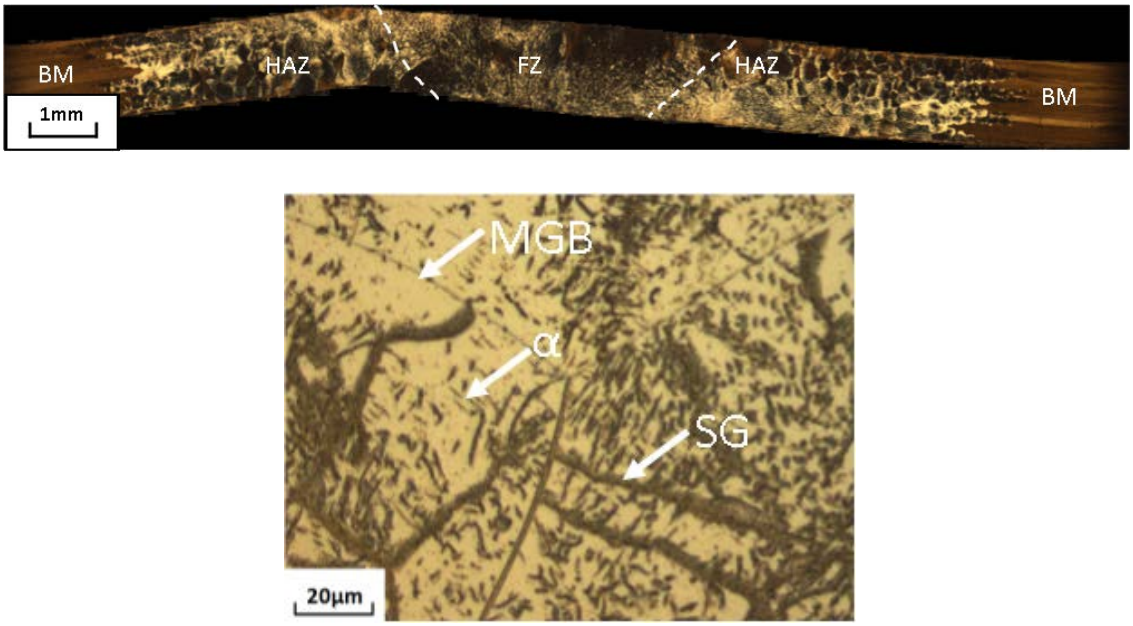

Figure 5.9. Optical micrographs of overall weld profile and FZ of welded Ti5553 aged at 500℃ for 15mins

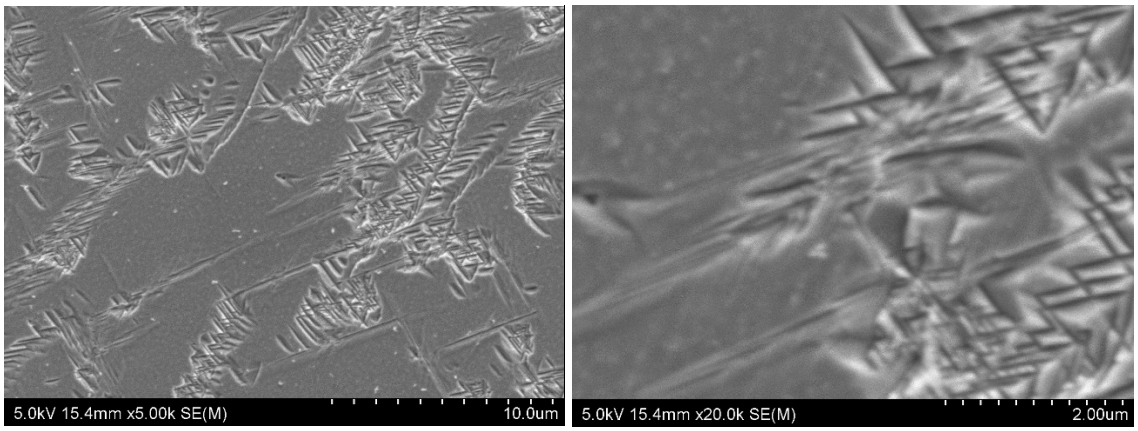

Figure 5.10. SEM micrographs of FZ of welded Ti5553 aged at 500℃ for 15mins

3) 30 minutes at 500 ℃ : optical micrographs revealed a homogeneous distribution of α precipitation in the FZ and HAZ adjacent fusion boundaries. The slightly different etched colour near the BM indicated the different precipitation rates of α particles. As the ageing time increases, SG continue to coarsen. SEM micrographs reveal a high volume fraction of fine α platelets. The average length and thickness of α laths were 1.83μm and 0.02 μm respectively. The distribution of fine α platelets was uniform.

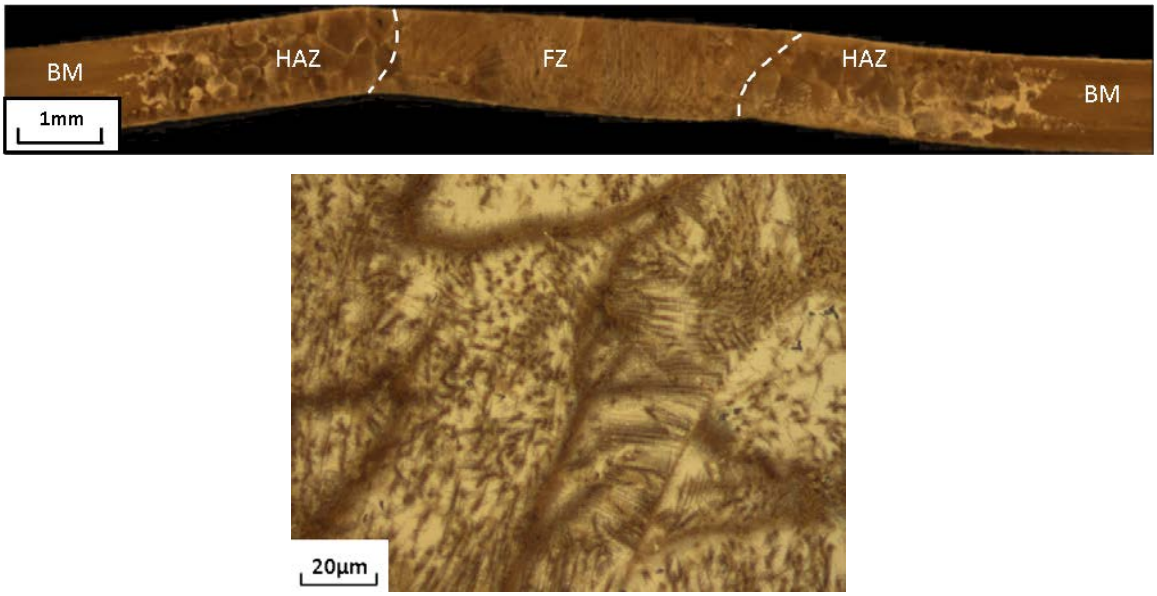

Figure 5.11. Optical micrographs of overall weld profile and FZ of welded Ti5553 aged at 500℃ for 30mins

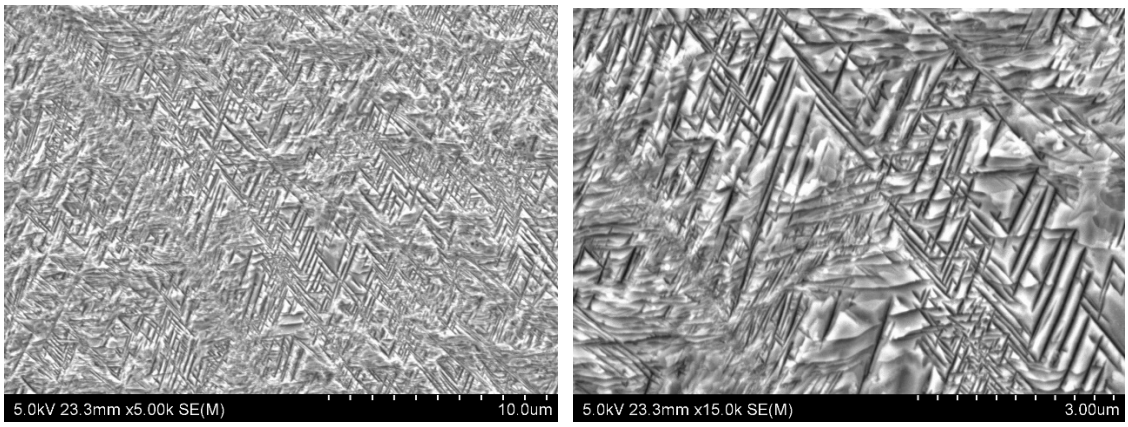

Figure 5.12. SEM micrographs of FZ of welded Ti5553 aged at 500℃ for 30mins

4) 2 hours at 500℃: optical micrographs showed an even etched colour over the weldment. During this period, the α phase was completely covered prior to the β matrix. It indicated a homogeneous distribution of the α precipitation. The morphology of the α precipitation at 500℃ for 2hrs became larger. The average length and width of α laths is 2.59μm and 0.04μm. A high magnification SEM image showed an acicular microstructure adjacent to the grain boundary that was arranged in fine laths.

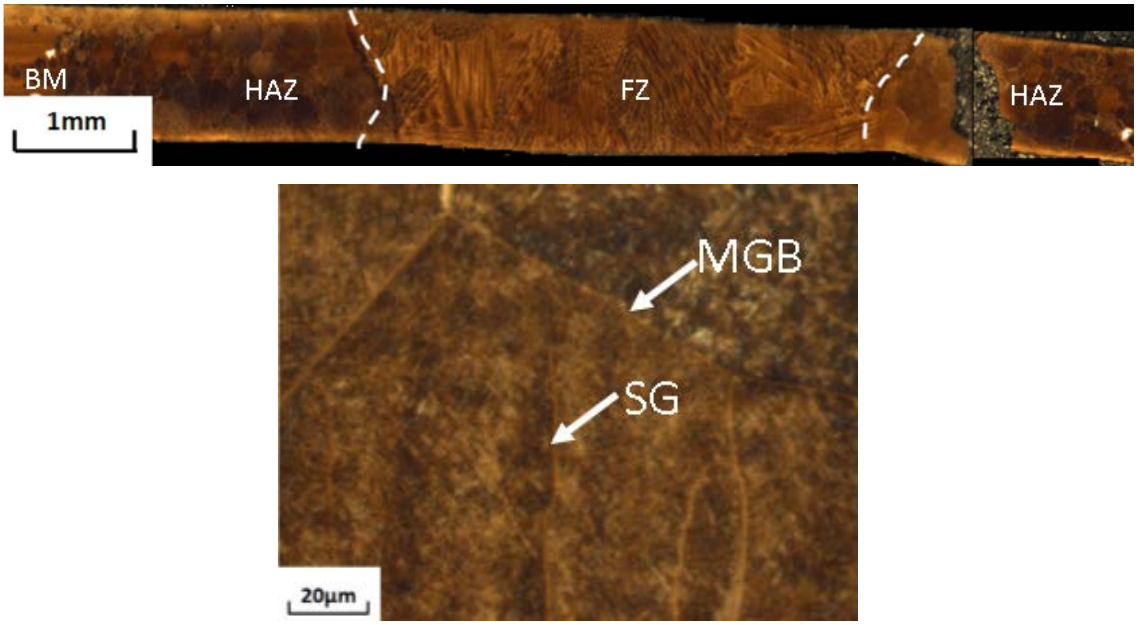

Figure 5.13. Optical micrographs of overall weld profile and FZ of welded Ti5553 aged at 500℃ for 2hrs

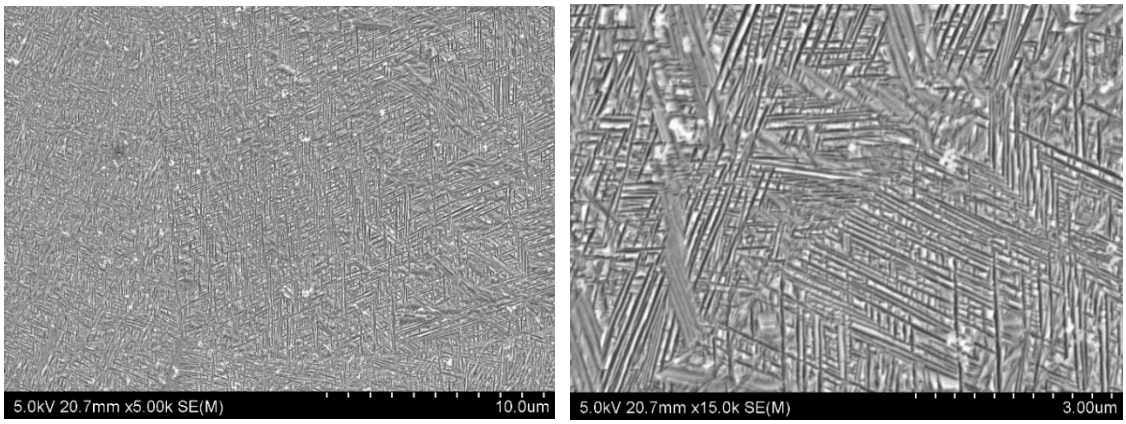

Figure 5.14. SEM micrographs of FZ of welded Ti5553 aged at 500℃ for 2hrs

5) 3 hours at 500 ℃ : continuous growth of α particles was observed. The optical micrographs of the specimen showed an even etched colour over the workpiece which indicated a homogeneous distribution of the α precipitation. The SEM micrograph exposed the average length of an α precipitation was similar to the sample that was aged at the same temperature for 2hrs. However, the average thickness of the α lath increases to 0.07µm which is almost double the size of the previous condition.

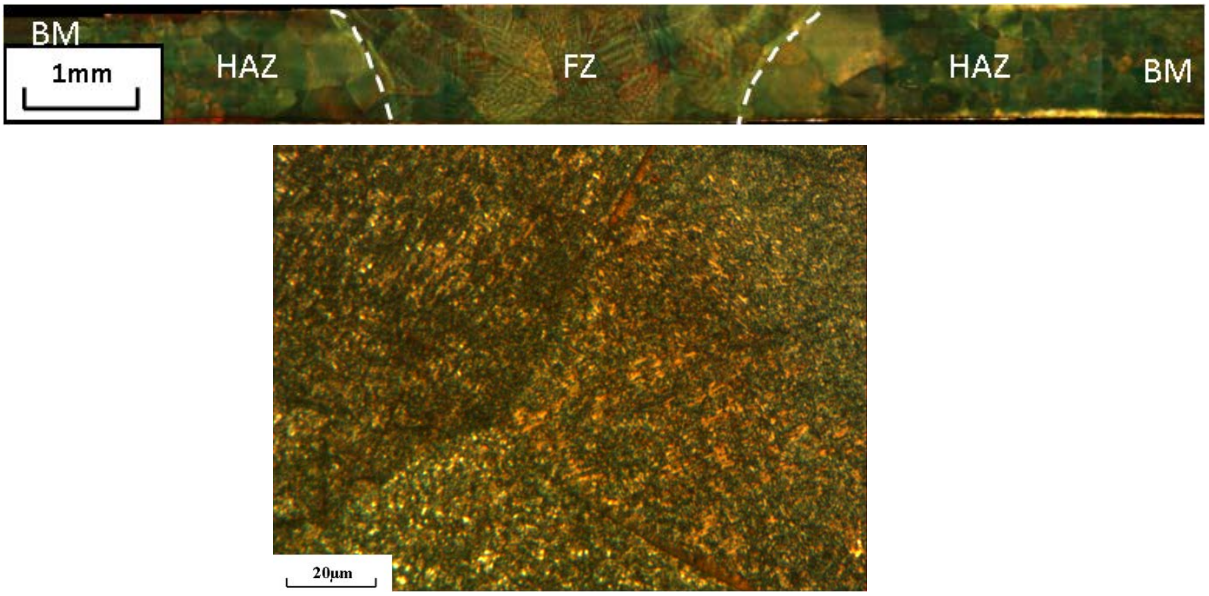

Figure 5.15. Optical micrographs of overall weld profile and FZ of welded Ti5553 aged at 500℃ for 3hrs

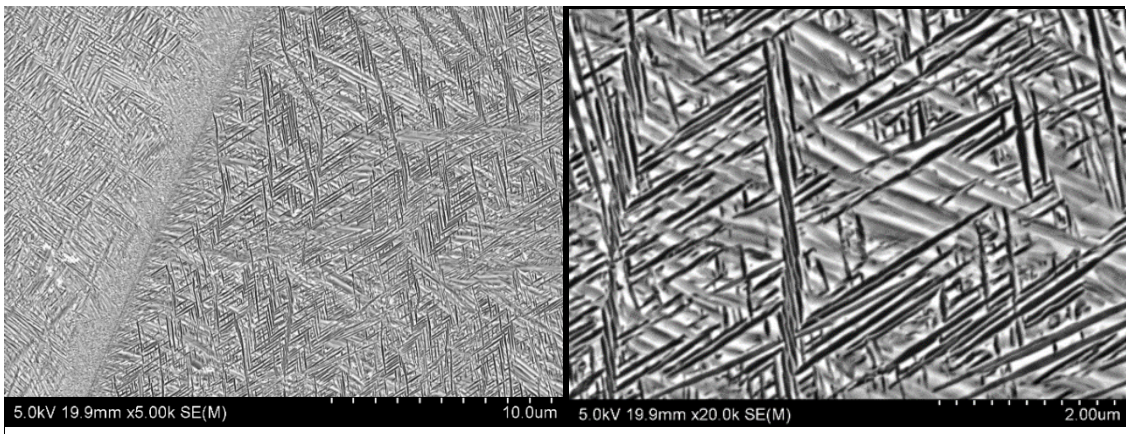

Figure 5.16. SEM micrographs of FZ of welded Ti5553 aged at 500℃ for 3hrs

6) 4 hours at 500℃: no significant differences compared to 3hrs at 500℃. The SEM results show that the average length of the α lath has slightly increased. However, the thickness of the increase of the α lath is not much different compared to those aged for 3hrs.

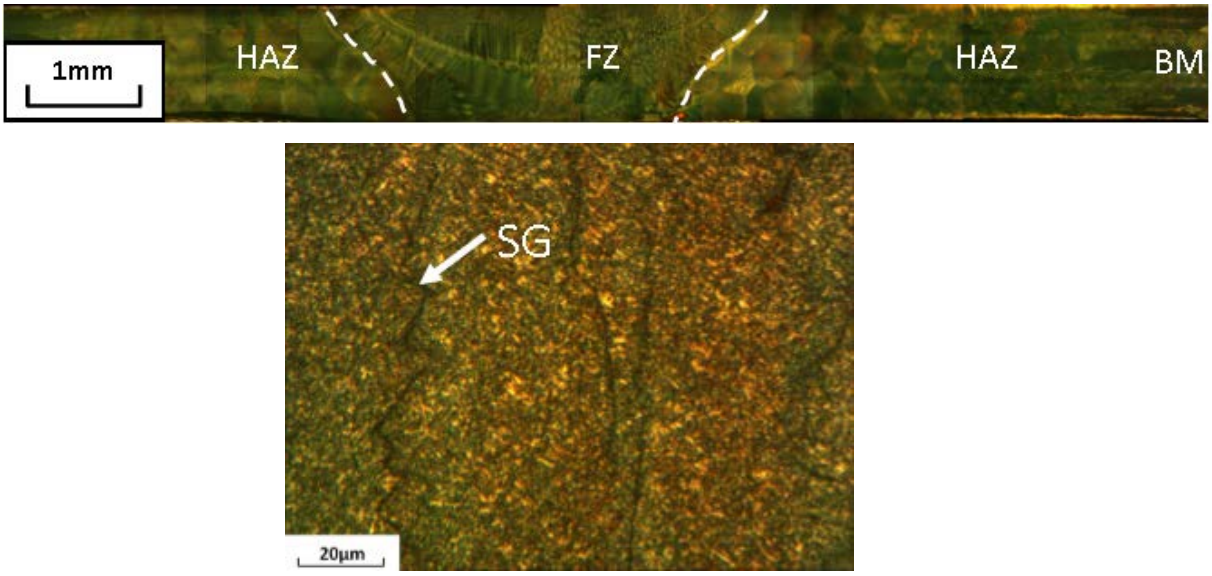

Figure 5.17. Optical micrographs of overall weld profile and FZ of welded Ti5553 aged at 500℃ for 4hrs

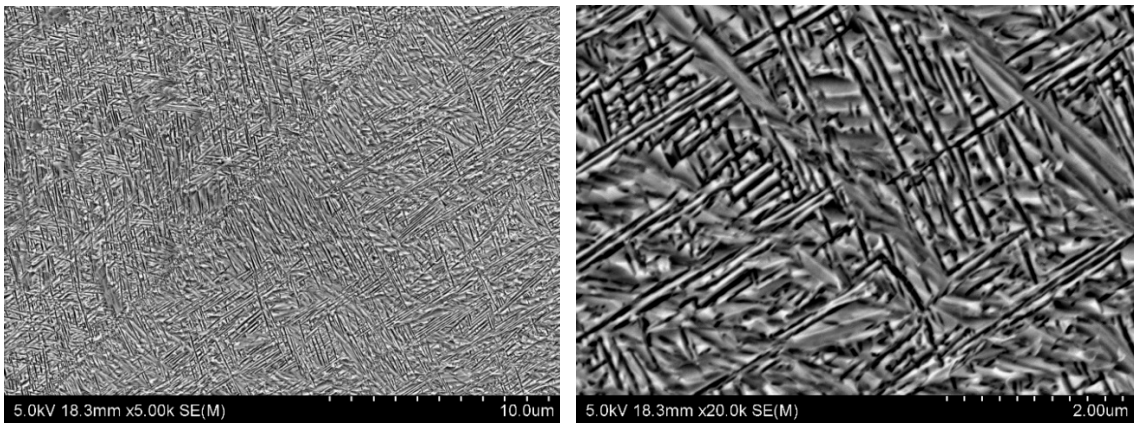

Figure 5.18. SEM micrographs of FZ of welded Ti5553 aged at 500℃ for 4hrs

7) 8 hours at 500℃: significant coarsening of the SG structure was observed. The SEM results indicate there was no significant change in the average length of the α lath. However, the average thickness of the α lath has almost doubled in those of 4hrs. This indicates that the α precipitation may have reached its equalibrium at 4hrs of ageing.

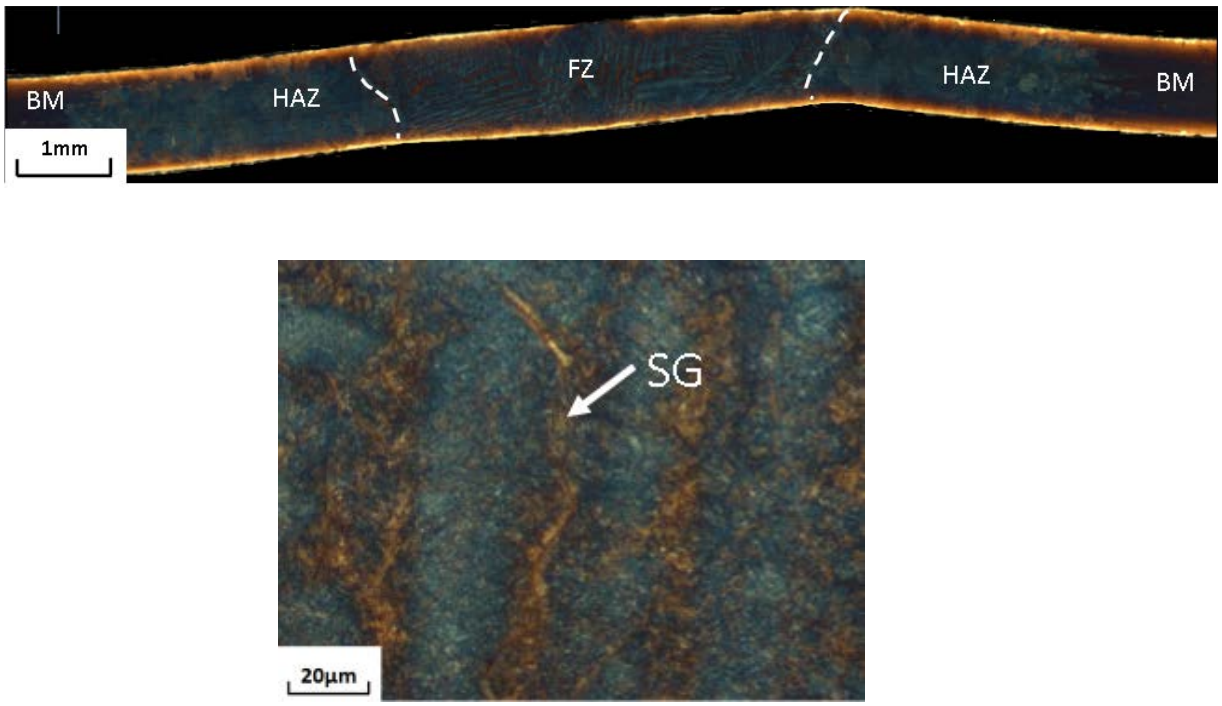

Figure 5.19. Optical micrographs of overall weld profile and FZ of welded Ti5553 aged at 500℃ for 8hrs

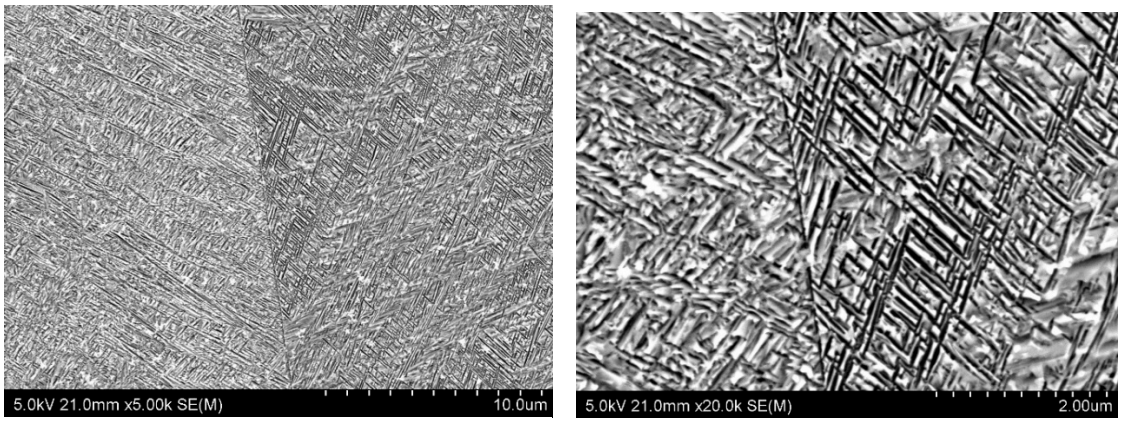

Figure 5.20. SEM micrographs of FZ of welded Ti5553 aged at 500℃ for 8hrs

5.4.2 Metallurgy in PWHT at 600℃ ageing condition

1) 5 minutes at 600℃: showed distinct differences compare to the sample aged at 500℃ for 5mins. For the same amount of ageing time, the α particles had already started to nucleate in the weld zone at a temperature of 600℃. The different colour area of the optical micrograph illustrated the inhomogeneity of the α particle distribution causing localised hardening. The SEM image also indicated the early stage of the α lath that grew heavily near the grain boundaries and some open spaces within the β matrix.

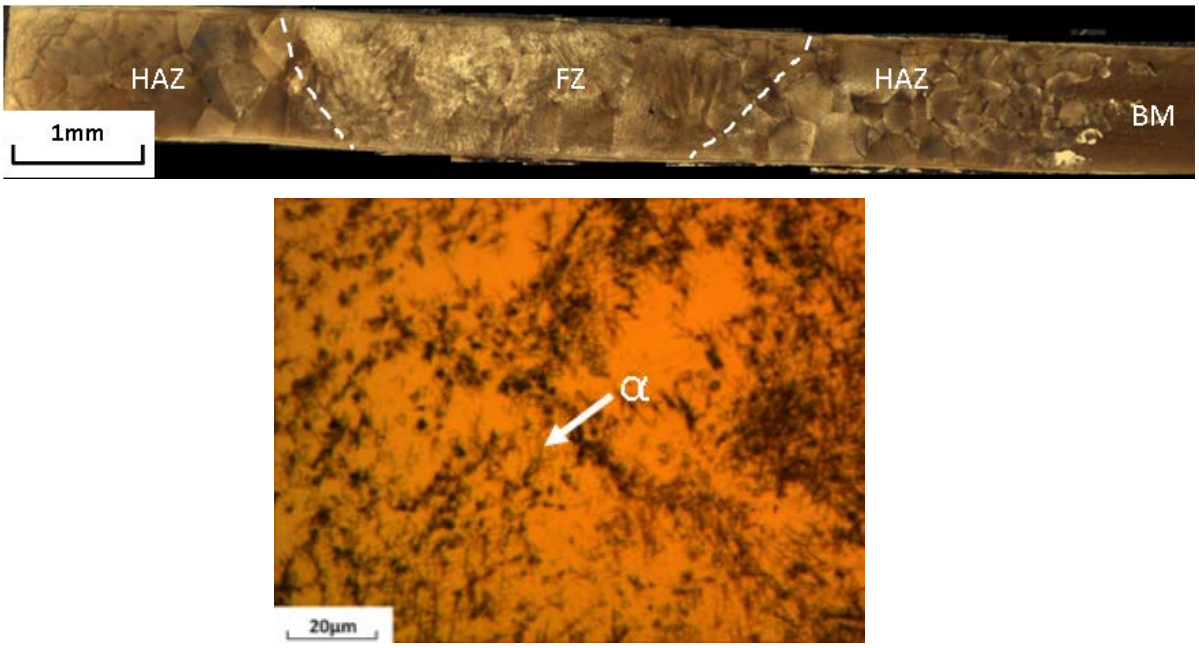

Figure 5.21. Optical micrographs of overall weld profile and FZ of welded Ti5553 aged at 600℃ for 5mins

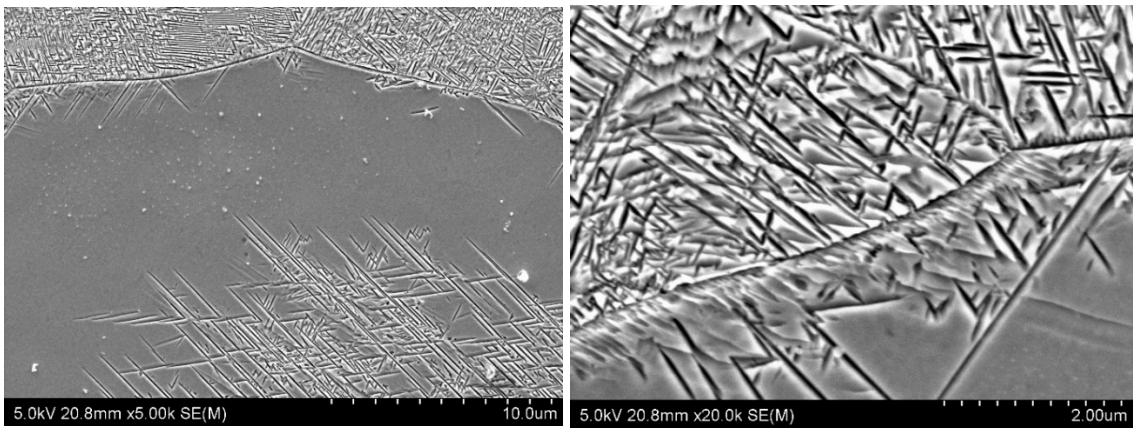

Figure 5.22. SEM micrographs of FZ of welded Ti5553 aged at 600℃ for 5mins

2) 15 minutes at 600℃: distinct appearance compared to the sample that was aged at 500℃ for 15mins. For the same amount of time, ageing at 600℃ has a much faster precipition rate than at 500℃. Optical micrographs indicated a fully covered α phase over the FZ and HAZ which means the α particles have already nucleated within the β matrix. The SEM image clearly showed α lath.

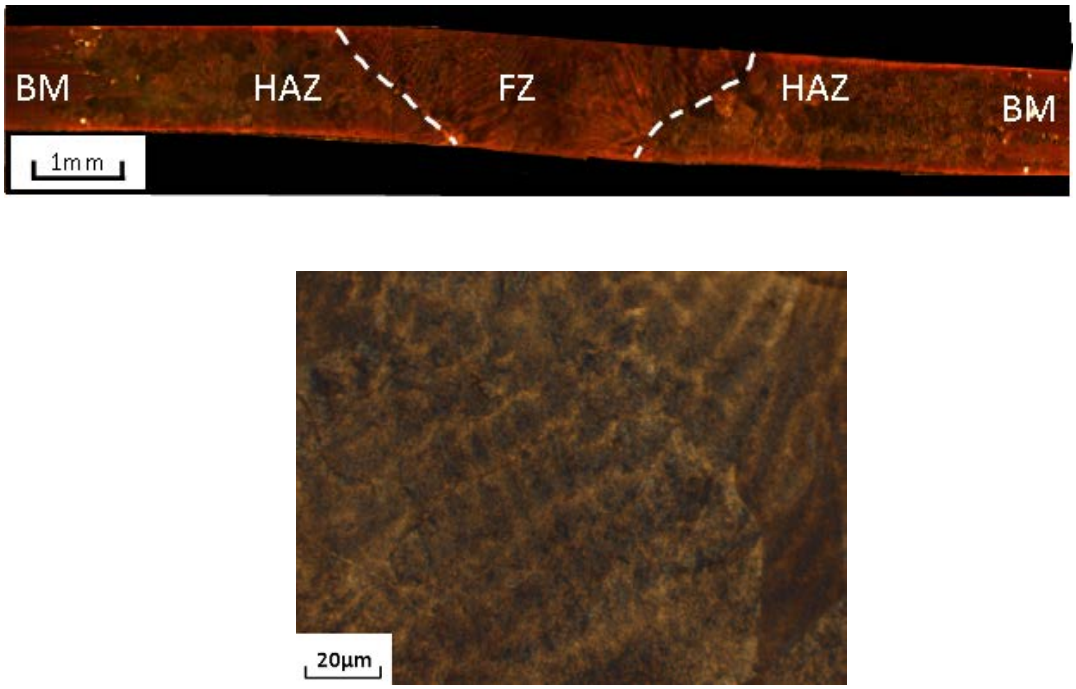

Figure 5.23. Optical micrographs of overall weld profile and FZ of welded Ti5553 aged at 600℃ for 15mins

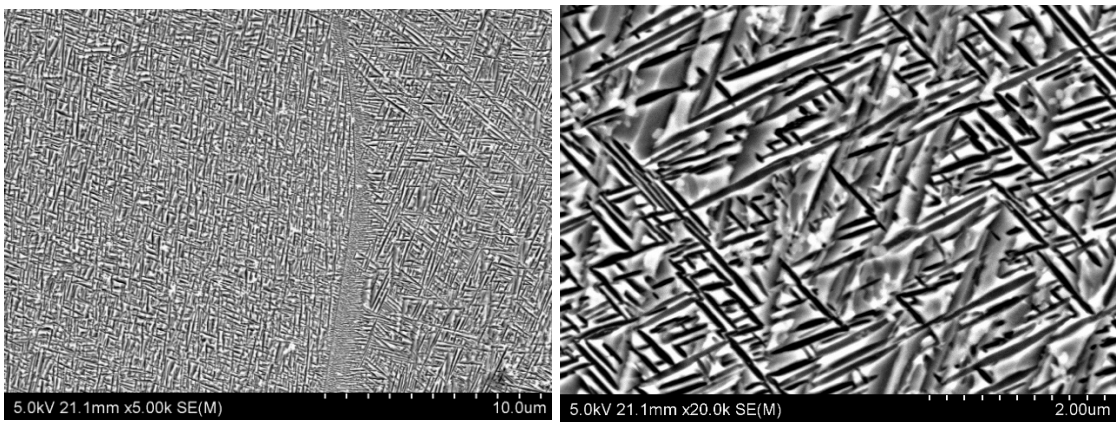

Figure 5.24. SEM micrographs of FZ of welded Ti5553 aged at 600℃ for 15mins

3) 30 minutes at 600℃: homogenous distribution of the α precipitation revealed by optical microscope. They are observed not only in the FZ but also in the HAZ and BM. SEM micrographs show a different morphology of the α laths. The average length of α laths is 0.9μm which is only half the length of the specimen that was aged at 500℃ for 30mins. However, the average thickness of α laths is 0.05μm which results in a similar average area for ageing at 500℃ and 600 ℃. This phenomenon explains the resemblance in mechanical properties.

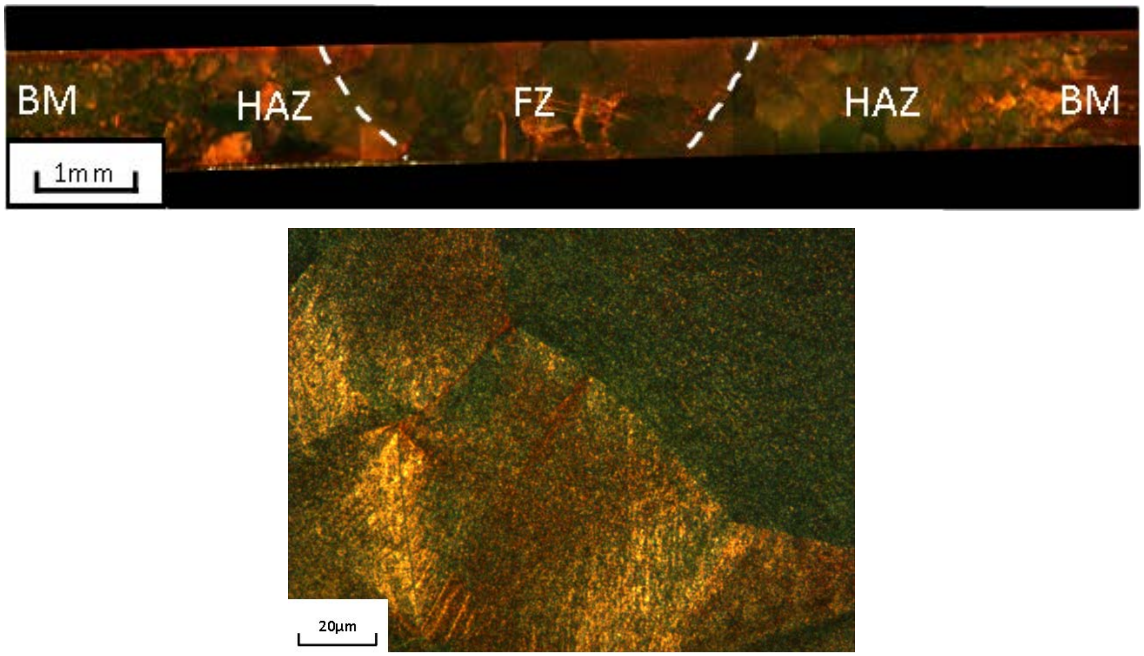

Figure 5.25. Optical micrographs of overall weld profile and FZ of welded Ti5553 aged at 600℃ for 30mins

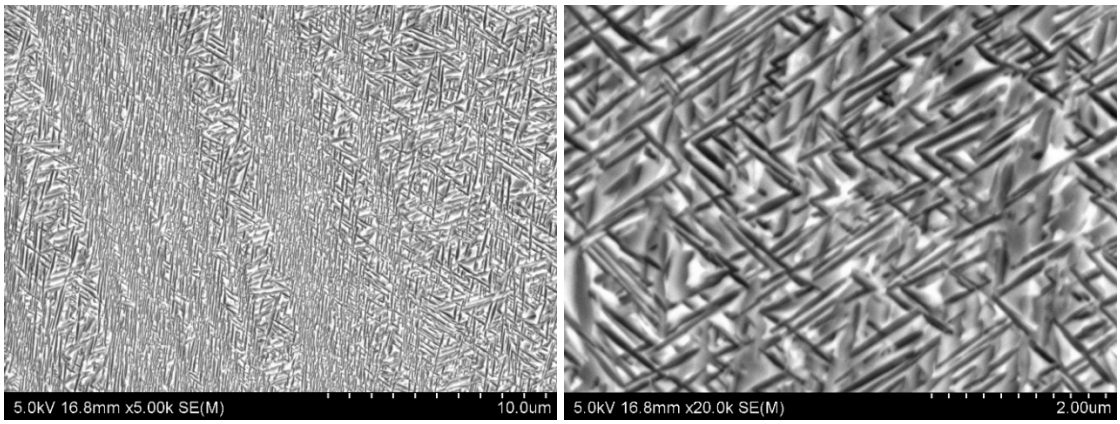

Figure 5.26. SEM micrographs of FZ of welded Ti5553 aged at 600℃ for 30mins

4) 2 hours at 600℃: optical micrographs revealed a coarsened microstructure. The average length of α laths is 2.9μm which has significantly increased from the previous condition. The thickness of the α laths also coarsens to 0.09μm.

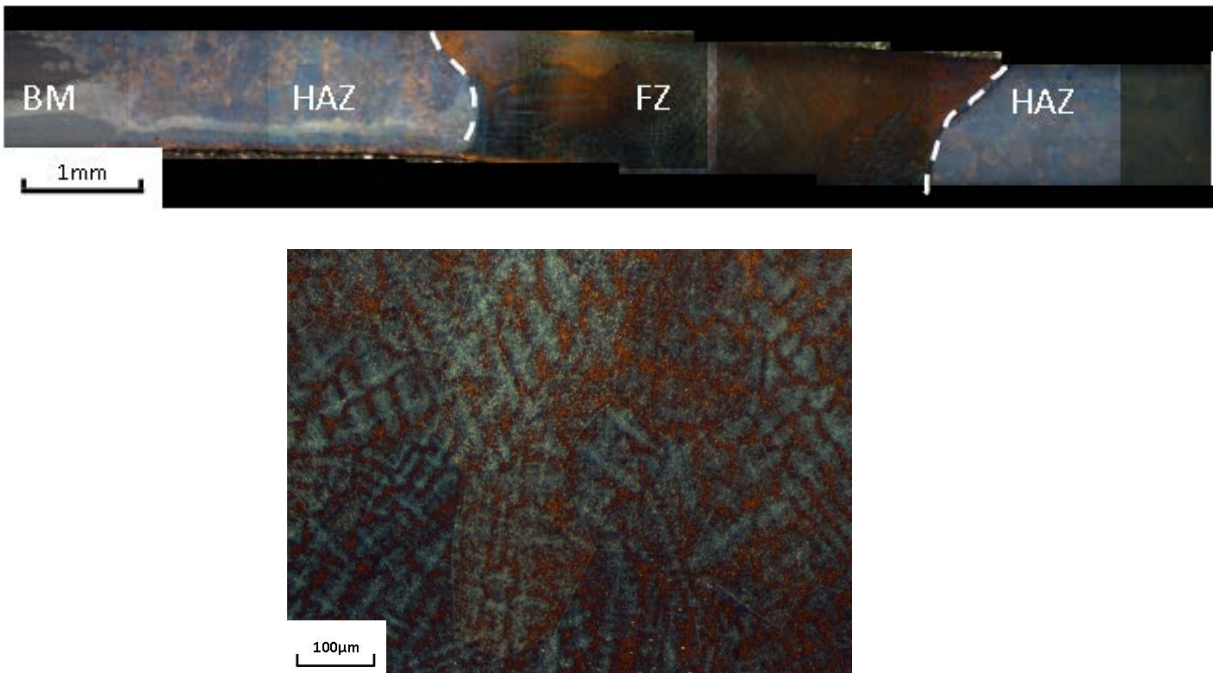

Figure 5.27. Optical micrographs of overall weld profile and FZ of welded Ti5553 aged at 600℃ for 2hrs

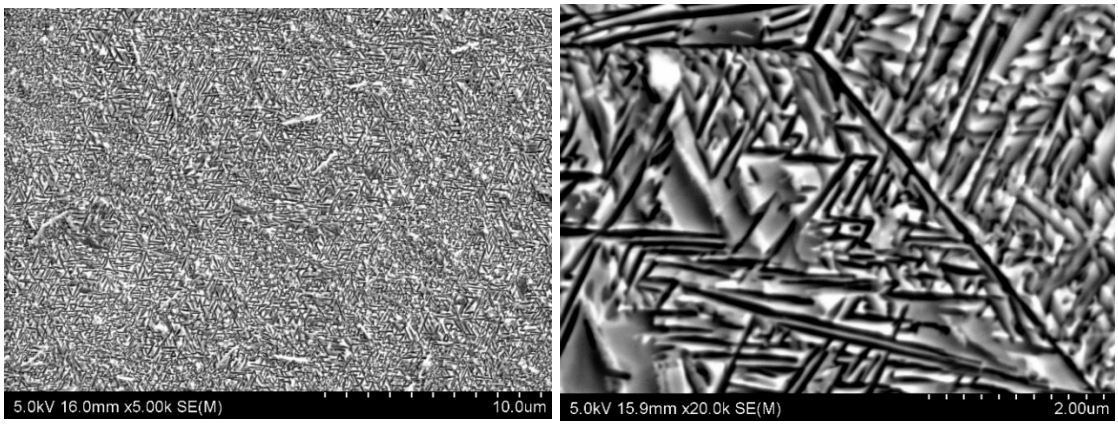

Figure 5.28. SEM micrographs of FZ of welded Ti5553 aged at 600℃ for 2hrs

5) 3 hours at 600℃: no significant differences compared with those aged for 2hrs. The average length of α laths is 3μm which is similar to the previous condition. However, the thickness of α laths continues to increase and has an average value of 0.11μm.

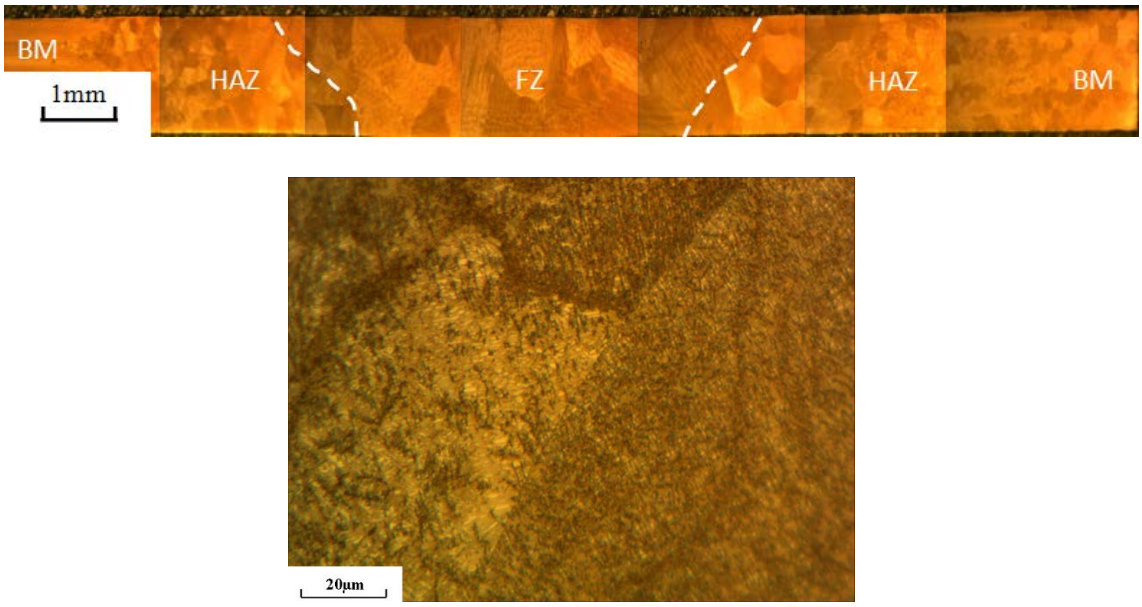

Figure 5.29. Optical micrographs of overall weld profile and FZ of welded Ti5553 aged at 600℃ for 3hrs

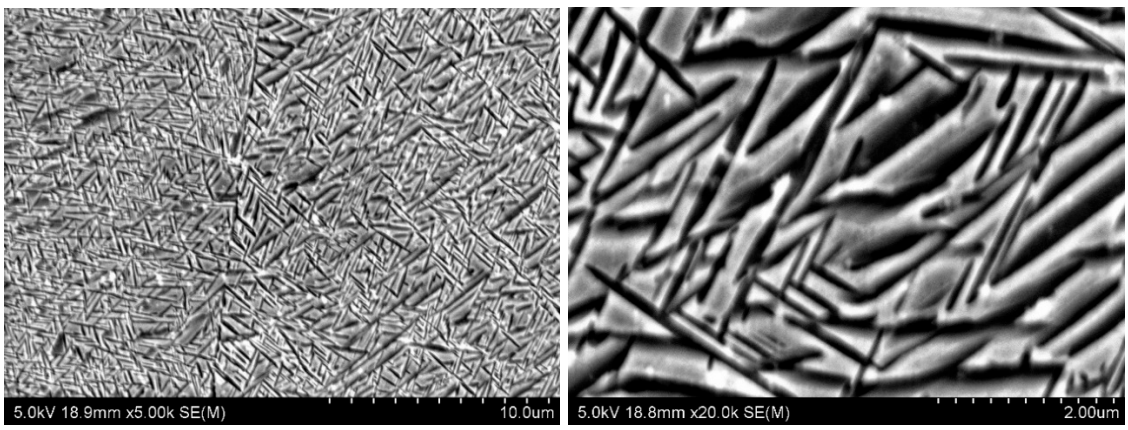

Figure 5.30. SEM micrographs of FZ of welded Ti5553 aged at 600℃ for 3hrs

6) 4 hours at 600℃: no significant changes in microstructure except for a continuous coarsening in α laths growth. The average length of α laths is 3.2μm, and the thickness of the α laths continues to increase with an average value of 0.16μm.

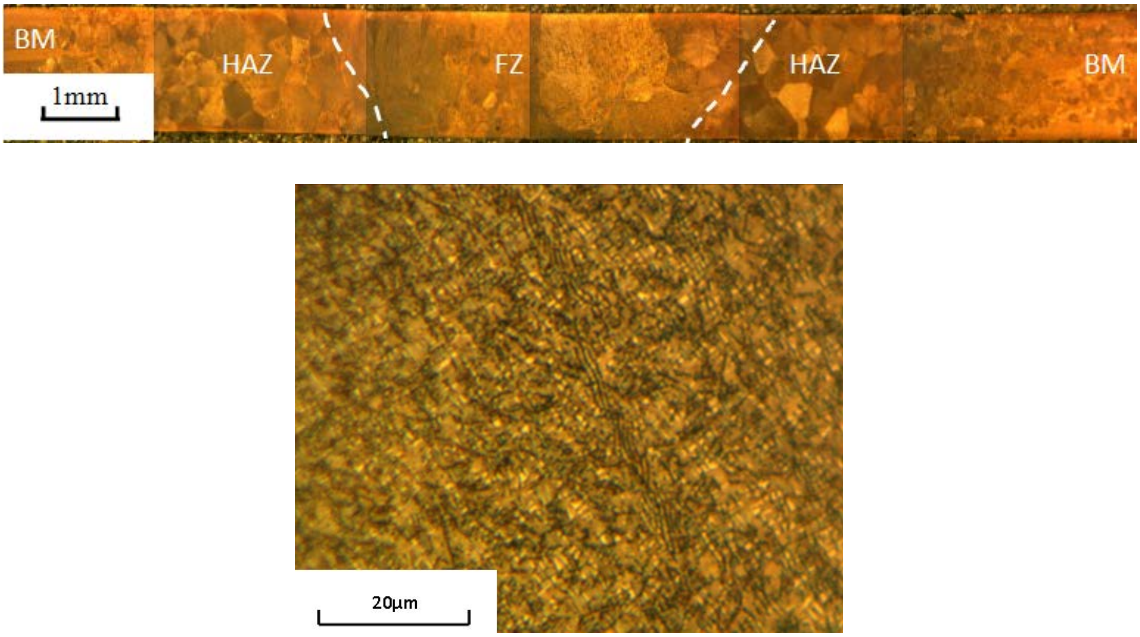

Figure 5.31. Optical micrographs of overall weld profile and FZ of welded Ti5553 aged at 600℃ for 4hrs

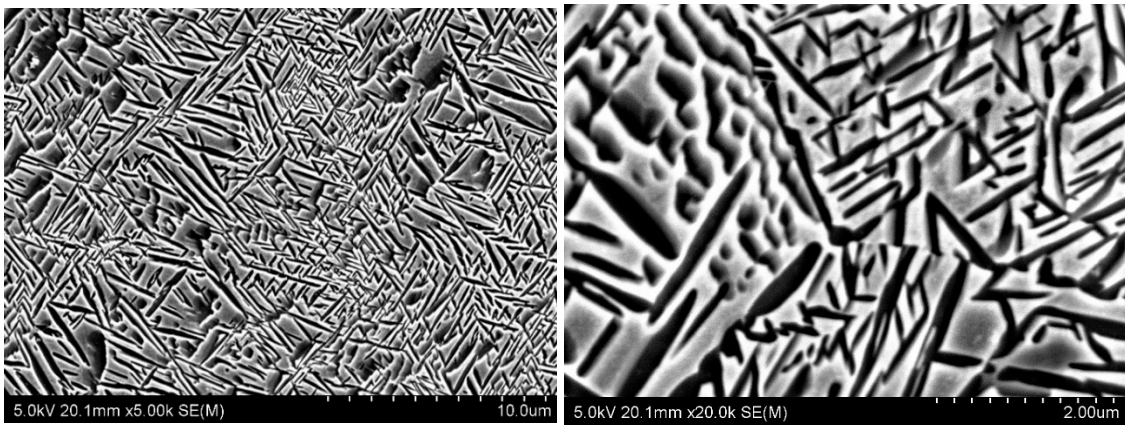

Figure 5.32. SEM micrographs of FZ of welded Ti5553 aged at 600℃ for 4hrs

7) 8 hours at 600℃: the α laths are difficult to observe due to the overlap of α platelets. The average area of α laths is estimated to be 0.5μm^2, which is similar to those aged for 4hrs.

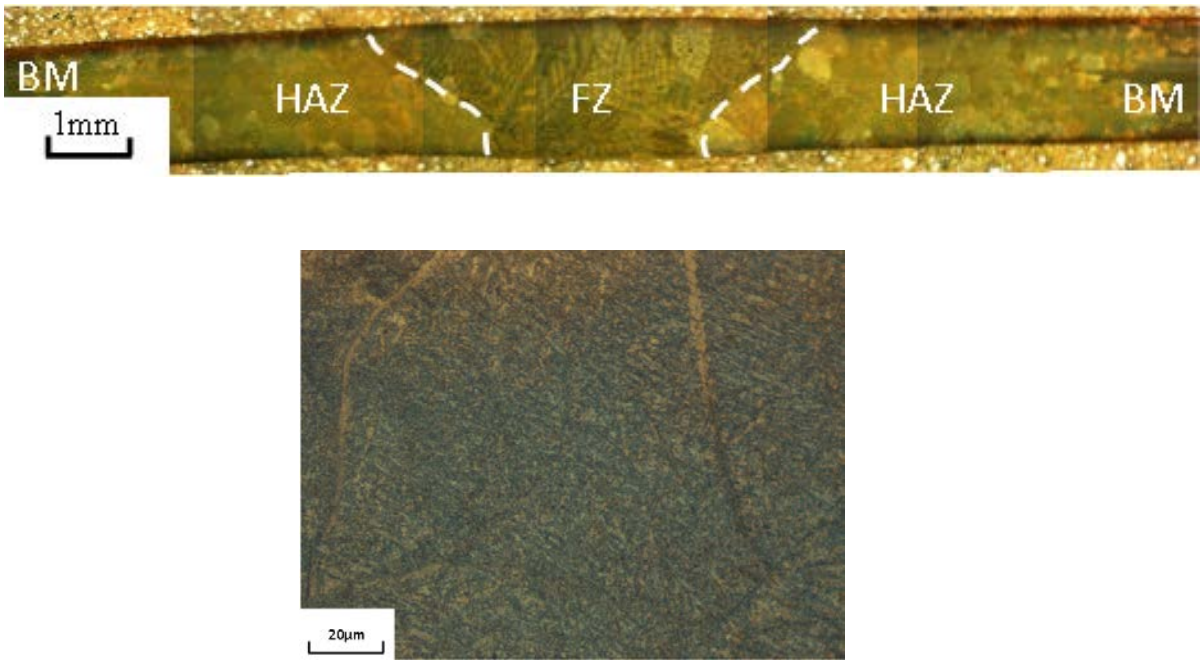

Figure 5.33. Optical micrographs of overall weld profile and FZ of welded Ti5553 aged at 600℃ for 8hrs

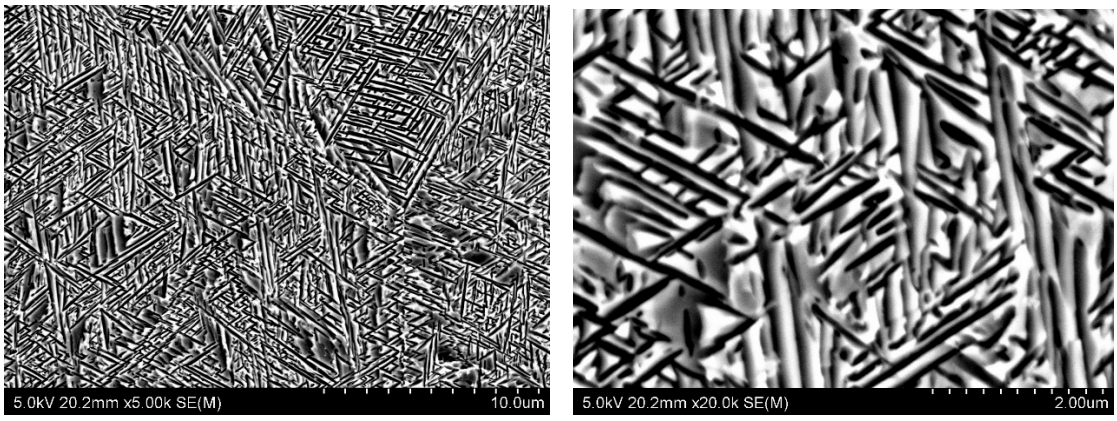

Figure 5.34. SEM micrographs of FZ of welded Ti5553 aged at 600℃ for 8hrs

5.4.3 Metallurgy in two-step ageing

Two-step ageing was carried out to investigate the effects on the hardness profile. The selected specimens were first aged isothermally at 500 ℃ and 600 ℃ for 8hrs then immediately transferred to an 800℃ furnace for an additional 2hrs. The optical and SEM micrographs, as presented in Figure 5.35 and 5.36, showed a disappearance of the α phase after ageing at 800℃ for 2hrs. This is due to a beta transus temperature (856℃) of Ti5553 which is very close to a second ageing condition (800℃). The hardness test also showed a rapid reduction in the hardness profile in the FZ and HAZ which confirmed the dissolution of α precipitates.

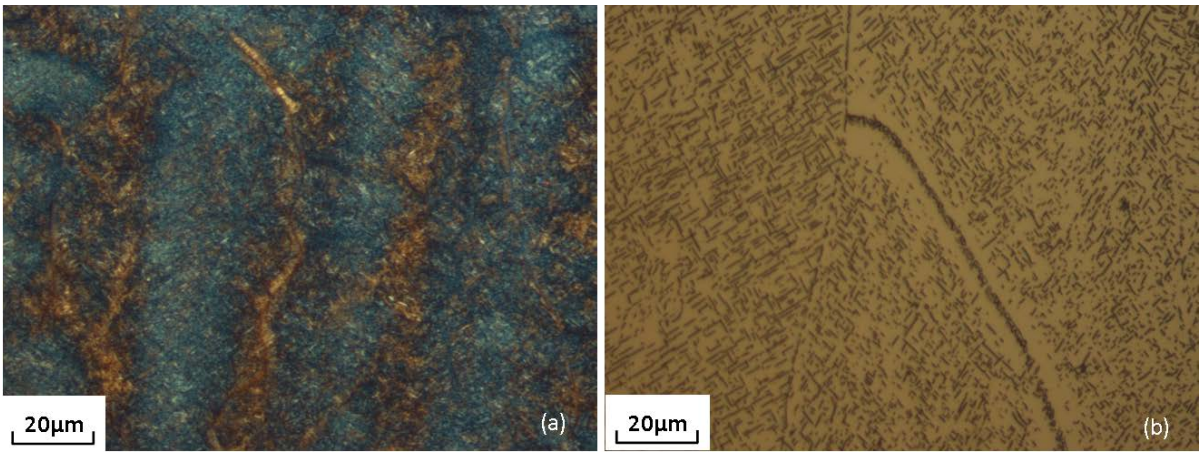

Figure 5.35. Optical micrographs of the FZ in welded Ti5553: (a) sample aged at 500℃ for 8hrs, (b) sample aged at 500℃ for 8hrs followed by addition ageing at 800℃ for 2hrs

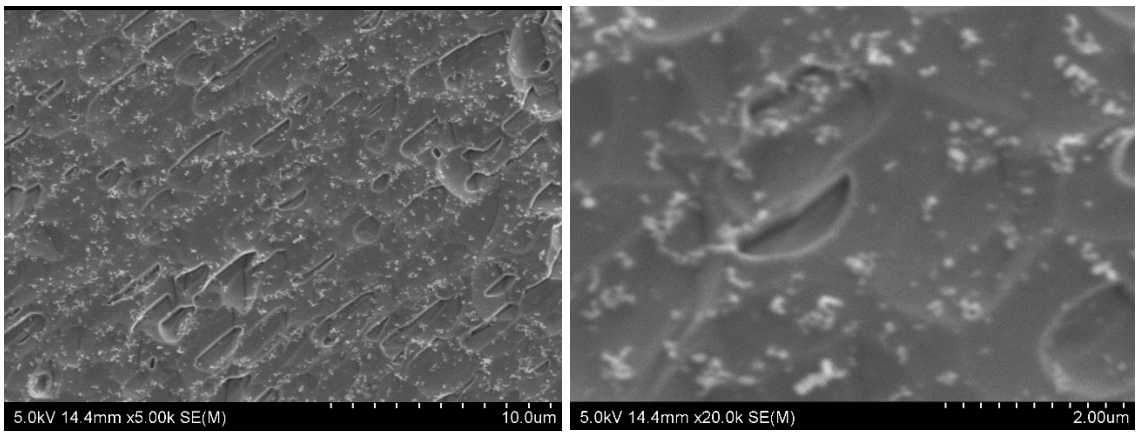

Figure 5.36. SEM micrographs of the FZ of welded Ti5553 that was aged at 500℃ for 8hrs followed by addition ageing at 800℃ for 2hrs

5.5 Average size of α precipitates

The average α size and volume fraction were measured with a SEM image associated with ImageJ image process software. The α size was calculated as the average area of the α lath which means both length and width were considered in this study. The volume fraction was measured using an ImageJ area fraction function. The average size and volume fraction of the α phase as a function of ageing time are displayed in Figure 5.37 and 5.38.

The specimen aged at 500℃ showed a slower precipitation rate than that aged at 600℃ for a short time of ageing. At 30mins ageing time, specimens aged at both 500℃ and 600℃ seemed to have reached their maximum area fraction, hence the equilibrium of α precipitation. At this ageing time, the volume fraction of α has the highest value of 36.6% for that aged at 500 ℃ and 37.2% for that aged at 600℃. These maximum values are similar to what Du et al. (Du Z., et al., 2014) reported on the volume fraction of the secondary α phase which is 35% at 560℃ ageing temperature. With an increased ageing time, samples that were aged at 500℃ showed a small variation in terms of volume fracture. However, samples aged at 600℃ appeared to have a large reduction in the area fraction of α. Associated with the average size of α, as shown in Figure 5.38, this reduction was caused by a distinct α lath coarsening.

As the ageing time increased after reaching the maximum α precipitation, the α laths were growing in both length and width. However, between 2hrs and 8hrs of ageing time, the length of laths showed a small increase with an average value of 2.99μm for 500℃ and 3.16μm for 600℃. However, the width of the α laths had a significant increase during this 6hrs. At 500℃, the α laths width increased from 0.039μm to 1.113μm. Also at 600℃, the α laths width grew from 0.089μm to 0.196μm. These average widths are slightly smaller than what Du et al. reported due to the original specimen and heat treatment conditions not being exactly the same. However, the trend of growth pattern is consistent with that at a higher temperature, where the α laths are coarser.

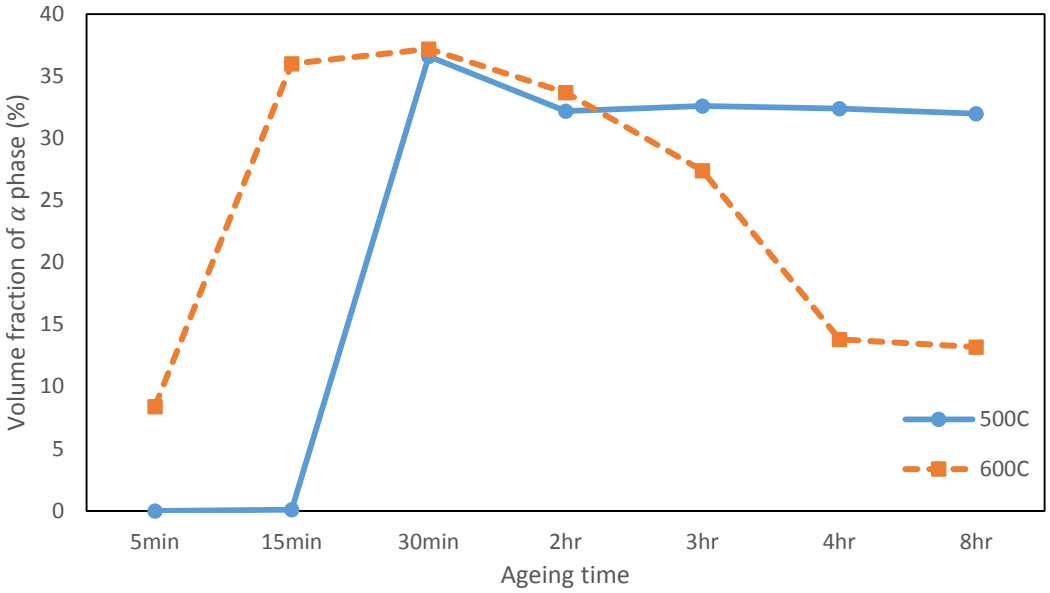

Figure 5.37. Volume fraction of α phase as function of ageing time

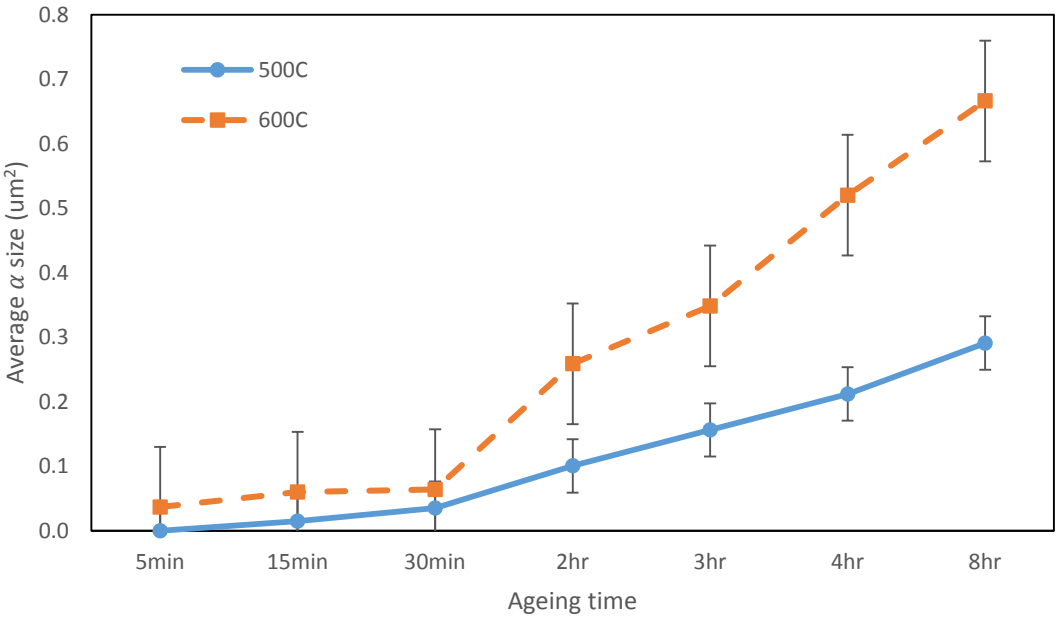

Figure 5.38. Average size of α laths as function of ageing time

5.6 Phase transformation analysis

In order to study the influence of the temperature and ageing time on β to α phase transformation, a TEM was used to analyse the phase transformation upon various PWHT. One of the goals is to identify the existence and role of the metastable ω phase during the α precipitation. From the literature reviews and the current results, particularly hardness and optical microscopy, the following ageing has been chosen: 500℃ for 2hrs, 4hrs, 8hrs; 600℃ for 5mins and 700℃ for 4hrs.

1) Figure 5.39 is a TEM bright field (BF) image of as-received Ti5553 (BM) with the corresponding selected area electron diffraction (SAED) pattern in $[011]\beta$ zone axis. The small primary α particles were located within the β matrix, as illustrated in the BF image. SAED imagery proved the existence of the $\alpha + \beta$ phase. According to the literature (Ahmed et al., 2015; Cotton et al., 2016), the faint spots that show in the SAED image were the reflections of the α phase.

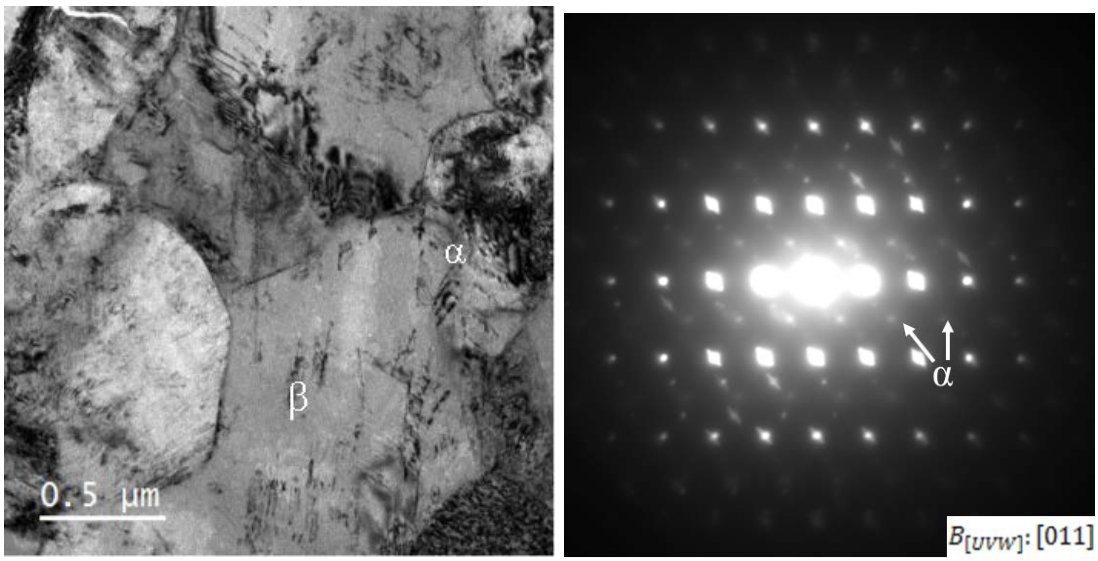

Figure 5.39. TEM bright field (BF) image and corresponding SAED of as-received Ti5553 in [011]β zone axis direction, camera length D=285mm

2) Figure 5.40 is a selected area of FZ under AW Ti5553 conditions. Comparing the diffraction pattern and BF image of the BM, the FZ exhibited single phase microstructure where a large area of clean β matrix was present in the BF image. The corresponding SAED pattern displays BCC reflection in the [011] beam direction and the existence of athermal ω_a precipitates within the β grains. The streaking in the SAED image is due to omega-precursor diffuse scattering (Cotton et al., 2016). The ω reflection overlaps with primary beta at the 1/3 and 2/3 $[\bar{2}1\bar{1}]$ position. Those athermal ω_a particles were produced during welding and retained in the β matrix upon air cooling to room temperature. These pre-existing ω_a promote the α precipitation which explains why the FZ response to heat treatment was faster than that of the BM.

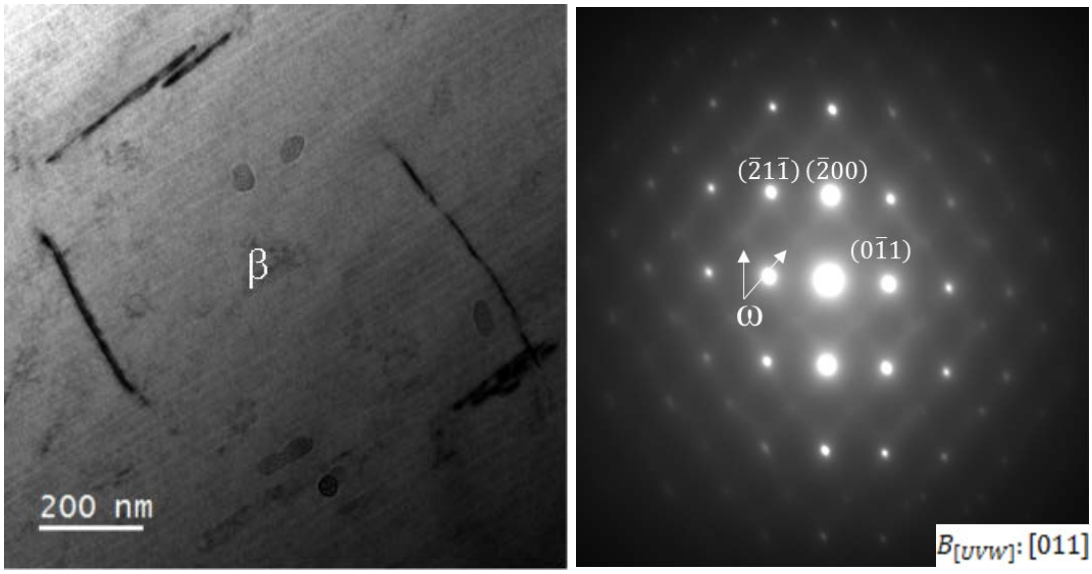

Figure 5.40. TEM BF image and SAED of AW Ti5553 FZ in [011]β zone axis direction, camera length D=285mm

3) TEM result of specimen aged at 500℃ for 2hrs revealed heavily grown thin needle-like α particles, as shown in Figure 5.41. The α precipitation of the FZ region formed a film which covered the prior β matrix. The dark field (DF) image showed no evidence of retained athermal ω_a nor was coarsened isothermal ω_{iso} present at this condition. The width of the α platelet was approximately 25nm. The corresponding SAED pattern indicated a simple HCP index in the [0001] beam direction.

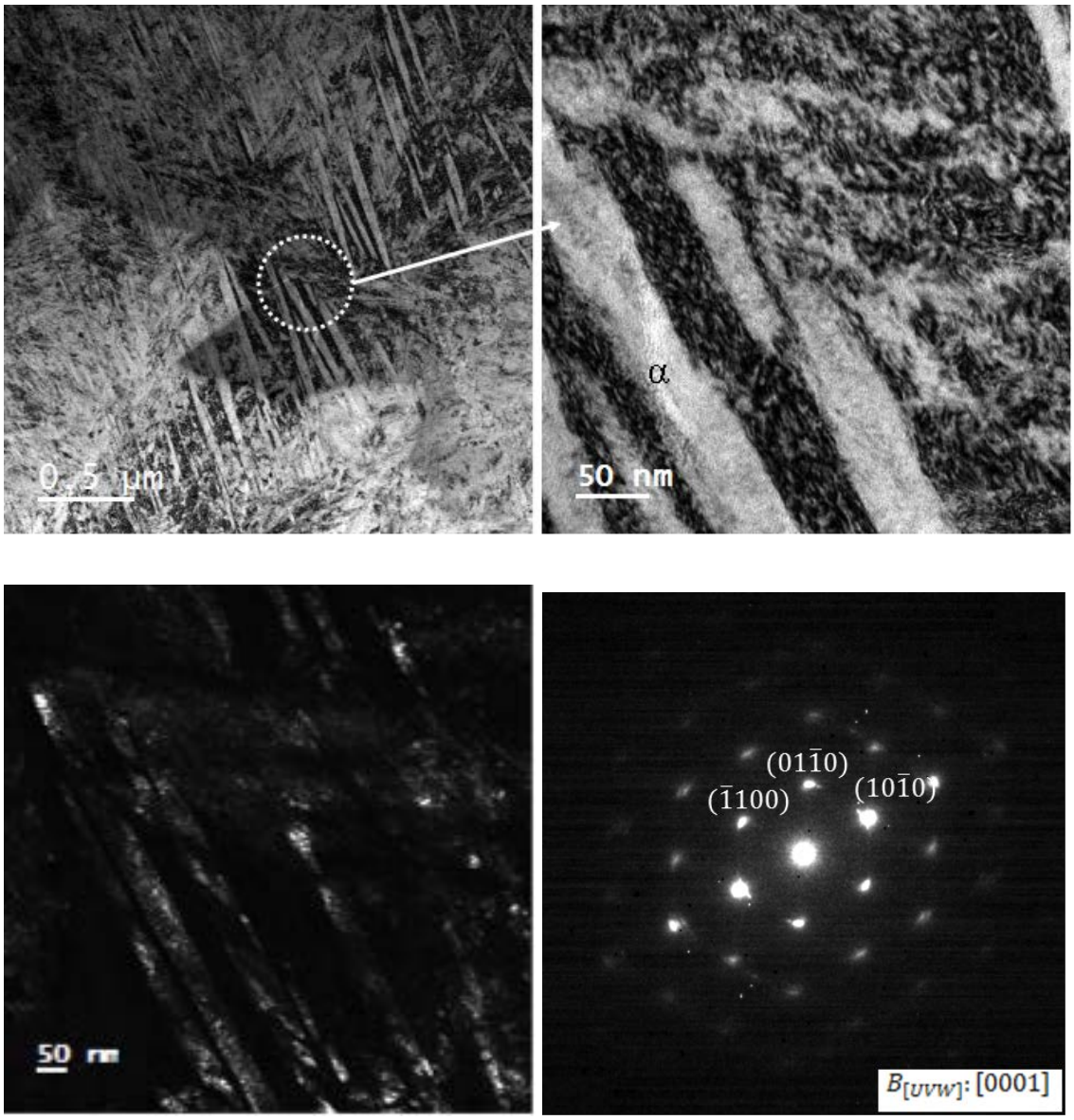

Figure 5.41. TEM BF and DF images, and SAED of Ti5553 FZ aged at 500℃ for 2hrs, camera length D=285mm

4) Ageing at 500℃ for 4hrs; the TEM BF image shows a more compact α film. By doubling the ageing time, the enlarged image indicated that the α particle had coarsened to approximately 100nm in thickness. The BF image along the grain boundary displayed the α growth in a different orientation. The corresponding SAED pattern indicated a simple HCP index in [0001] beam direction.

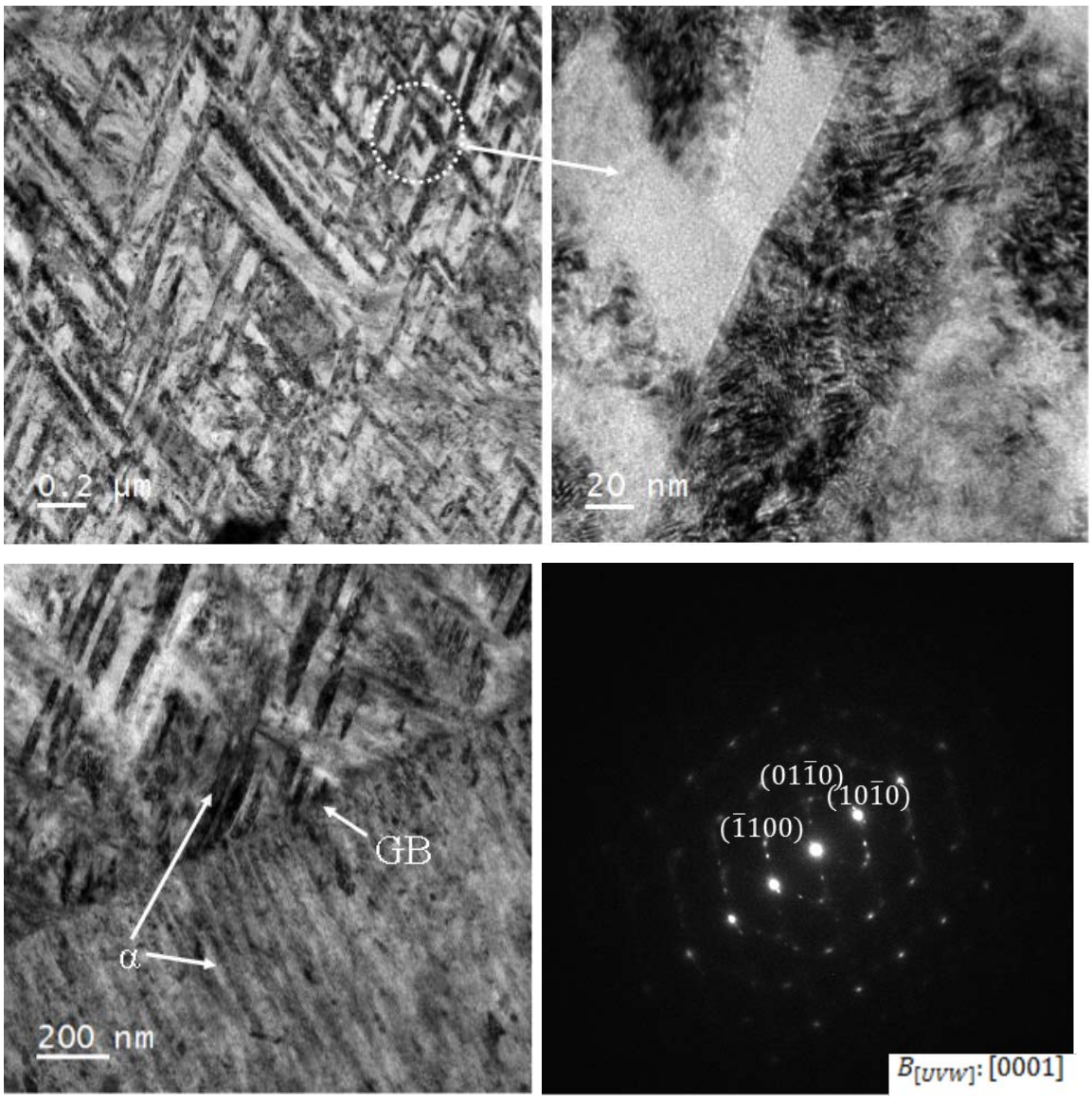

Figure 5.42. TEM BF images and SAED of Ti5553 FZ aged at 500℃ for 4hrs, camera length D=285mm

5) In Figure 5.43, the TEM BF image of a sample aged at 500°C for 8hrs of the FZ region reveals the prior β matrix is almost completely covered by a thickened α film.

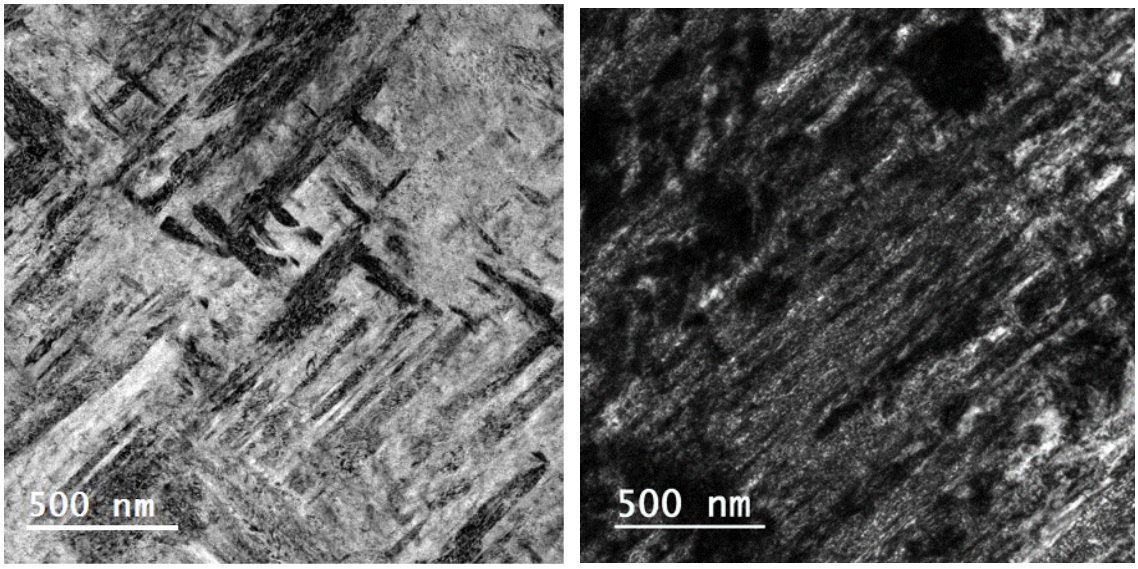

Figure 5.43. TEM BF images of Ti5553 FZ aged at 500℃ for 8hrs, camera length D=285mm

6) Ageing at 600 ℃ for 5mins; the TEM BF image revealed a small amount of α scattered in a large clean area of β-phase matrix which was found in the FZ. The top two images indicated the start of α nucleated near the GB and within the grains. The size of the early stage of an α particle is 0.5-1μm long but only about 0.1 μm wide. The precipitation was non-uniform and heterogeneous. Dislocation due to the strain created by the early stages of the HCP alpha disc formation in the BCC matrix was observed. Similar observation was also made by Giosa (Giosa R. P., 2009). Some of the nearly formed α precipitates were present as a parallel array. The corresponding SAED indicates a simple BCC reflection in the $[\bar{1}11]$ beam direction. There was no evidence of a ω phase at this temperature, that is consistent with the previous study in which the ω phase dissolved at 600 ℃ (Duerig & Williams, 1984; Harper, 2004; Leibovitch & Rabinkin, 1980).

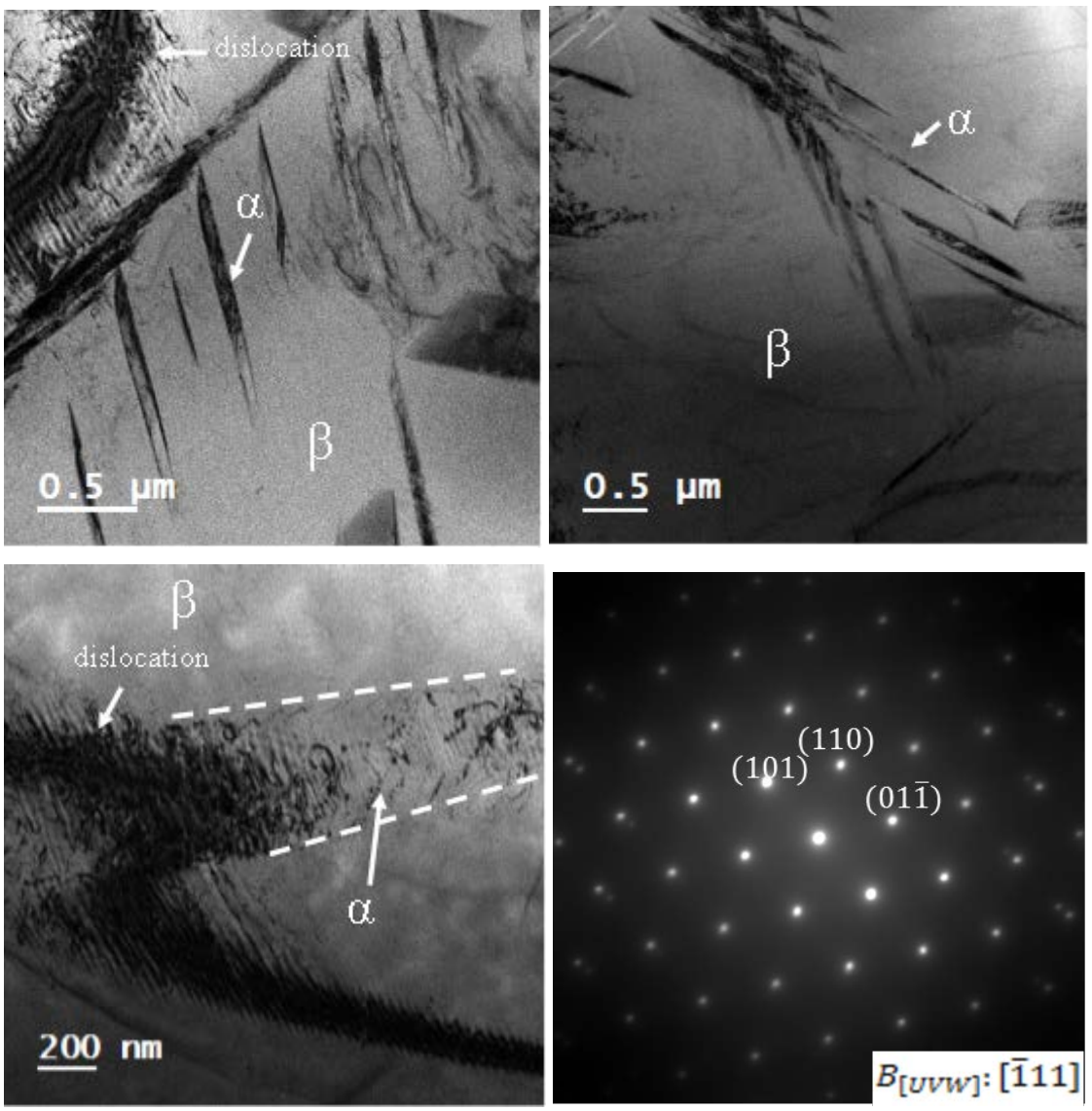

Figure 5.44. TEM BF images and SAED of Ti5553 FZ aged at 600℃ for 5mins, camera length D=285mm

7）As shown in Figure 5.45, the dark area indicated a β-matrix and the light bright area demonstrated the fine acicular α in the FZ region following ageing at 700^{o}C. It is a typical bimodal microstructure (globular + lamellar alpha microstructure) of a lean β titanium alloy which was also described by Duerig et al (Duerig & Williams, 1984).

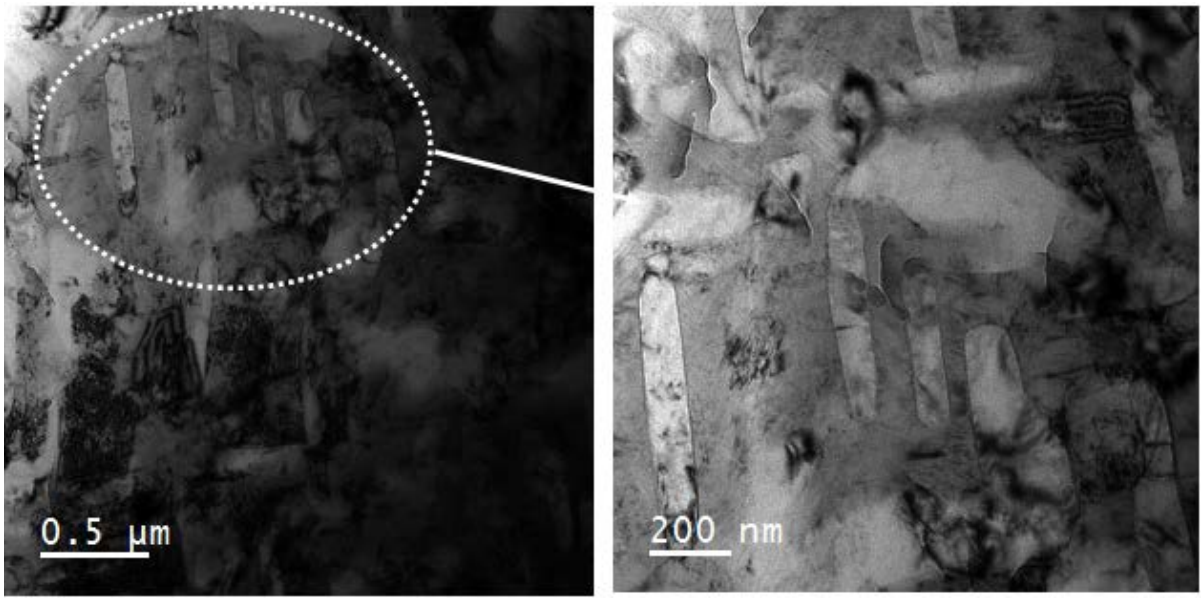

Figure 5.45. TEM BF images of Ti5553 FZ aged at 700 ^{o}C for 4hrs, camera length D=285mm

5.7 Summary

This chapter presented the results from the ageing of welded Ti5553 at various temperatures and times. Microstructure investigation shows Ti5553 can retain its β phase at an AW condition. Thus solution heat treatment is unnecessary before precipitation hardening. However, the different ageing temperatures can affect the α precipitation rate and the size of particles.

It has been reported that for wrought Ti5553, after solution heat treatment and following isothermal ageing, the ω_{iso} phase can be found during the ageing process at 400℃ dissolving at 600℃ (Chen Y. et al., 2014; Fanning, 2005; Wagner et al., 2010). The ω_{iso} phase also provided growth sites for α precipitates. The TEM result of AW Ti5553 FZ confirmed the existence of a ω phase. These ω phases were athermal ω_a particles which were formed and retained in the weld zone during air cooling after the welding process. However, there was no evidence of isothermal ω_{iso} during ageing at 500℃ and 600℃. It can be concluded that ω_a particles have completely transformed to an α. Due to the different reaction rates upon heat treatment between the base material and the weld zone, it proved that ω_a was a precursor to the $\beta \rightarrow \alpha$ diffusion since there was no ω_a in the BM.

As shown in Figure 5.46, a higher temperature certainly shortens the age hardening time. This is based on the results from 5mins to 2hrs of the PWHT at 500℃ and 600℃ as an example. The specimen aged at 600℃ started to precipitate within 5mins. According to Cotton et al. (Cotton et al., 2016), the precipitation at 600℃ started within 1-2mins. The precipitation is heterogeneous where a low angle α array was found near the grain boundary and dislocation sites; and also an intersecting intragranular α needle within the β grains. Nevertheless the specimen aged at 500℃ did not produce any α particles. However, the high magnification micrograph image shows initial sub-grains which may promote α precipitation. The α particles started to precipitate when ageing took place at 15mins for 500℃. The SEM revealed that an α phase was favoured to form near the grain boundary or sub-grains. By the time of 30mins of ageing at 500℃ and 600℃, both conditions appeared to have a similar structure and amount of α precipitates. This result will be further discussed in the mechanical properties section. At 2hrs of ageing, both conditions show different degrees of α particles coarsening. It appeared that at 600℃ α

laths are significantly thicker than at 500°C. A summary of the microstructure upon

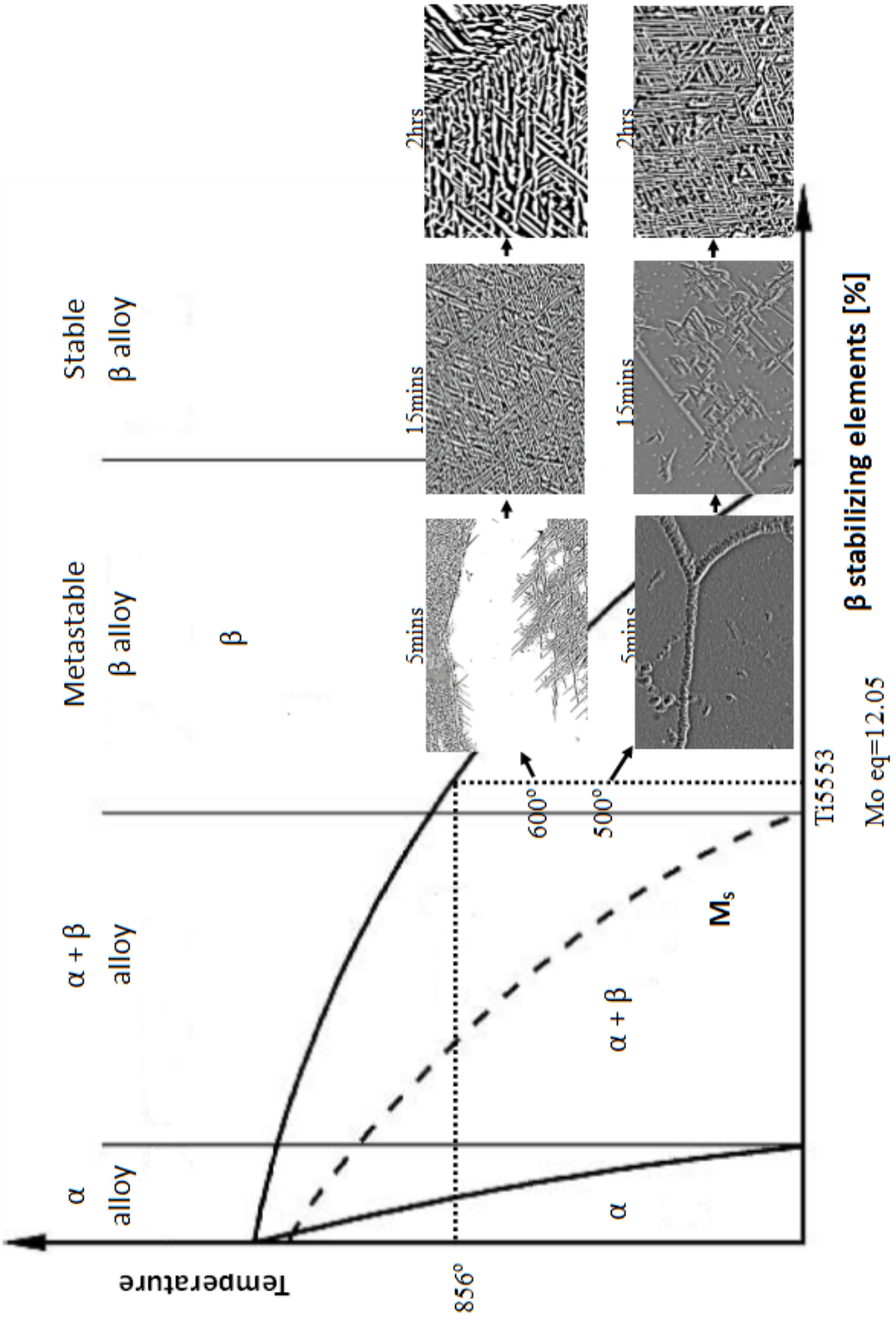

Figure 5. 46. Pseudo phase diagram and microstructure of aged Ti5553 FZ at 500℃ and 600℃ for 5mins, 15mins and 2hrs.

various age times for both temperatures, are shown in Figure 5. 47 and 5.48.

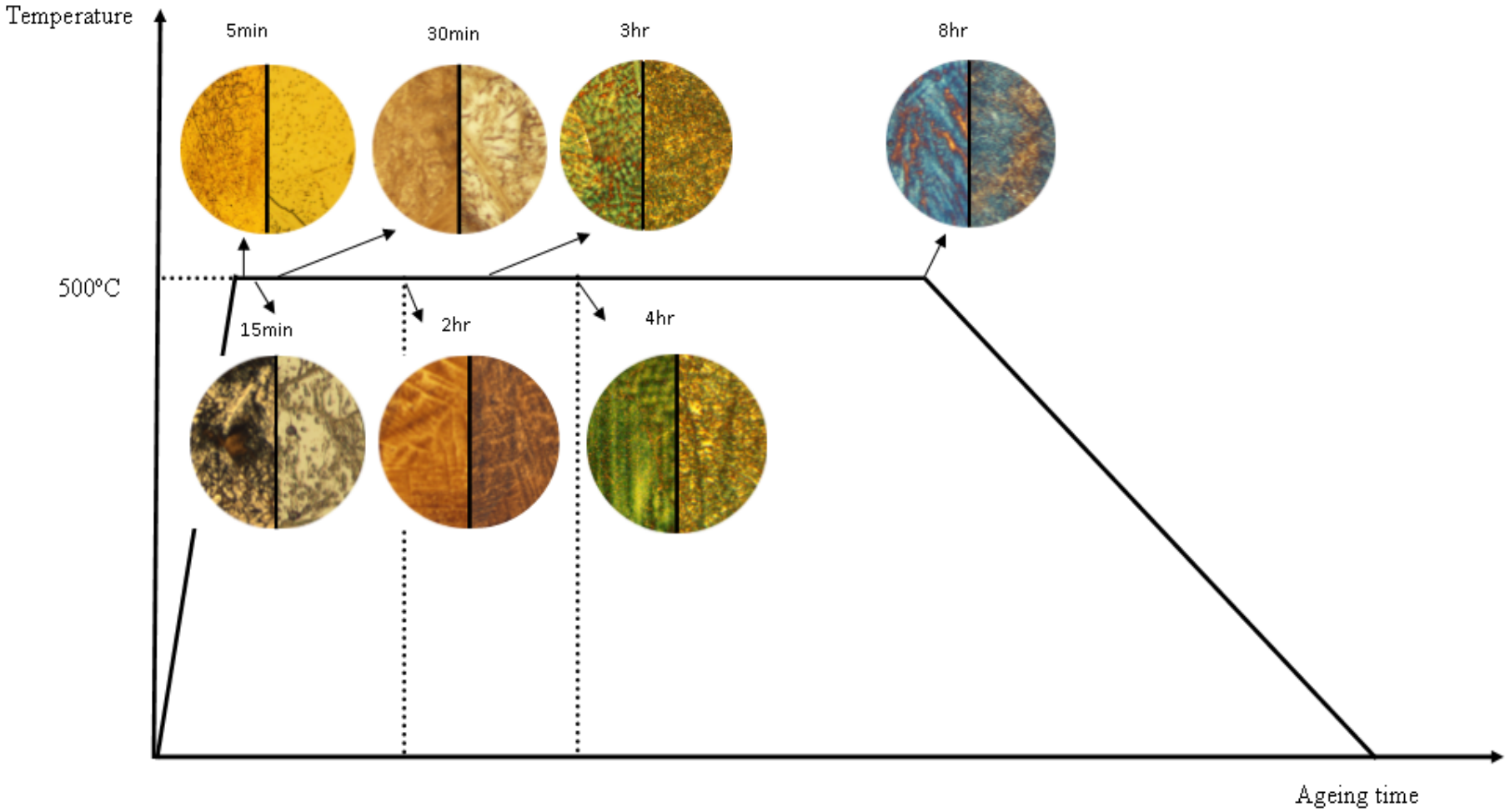

Figure 5. 47. Microstructure of Ti5553 FZ at 500°C with various ageing times. Images were taken after air cooling from ageing temperature at 500°C for the time indicated (5min-8hr)

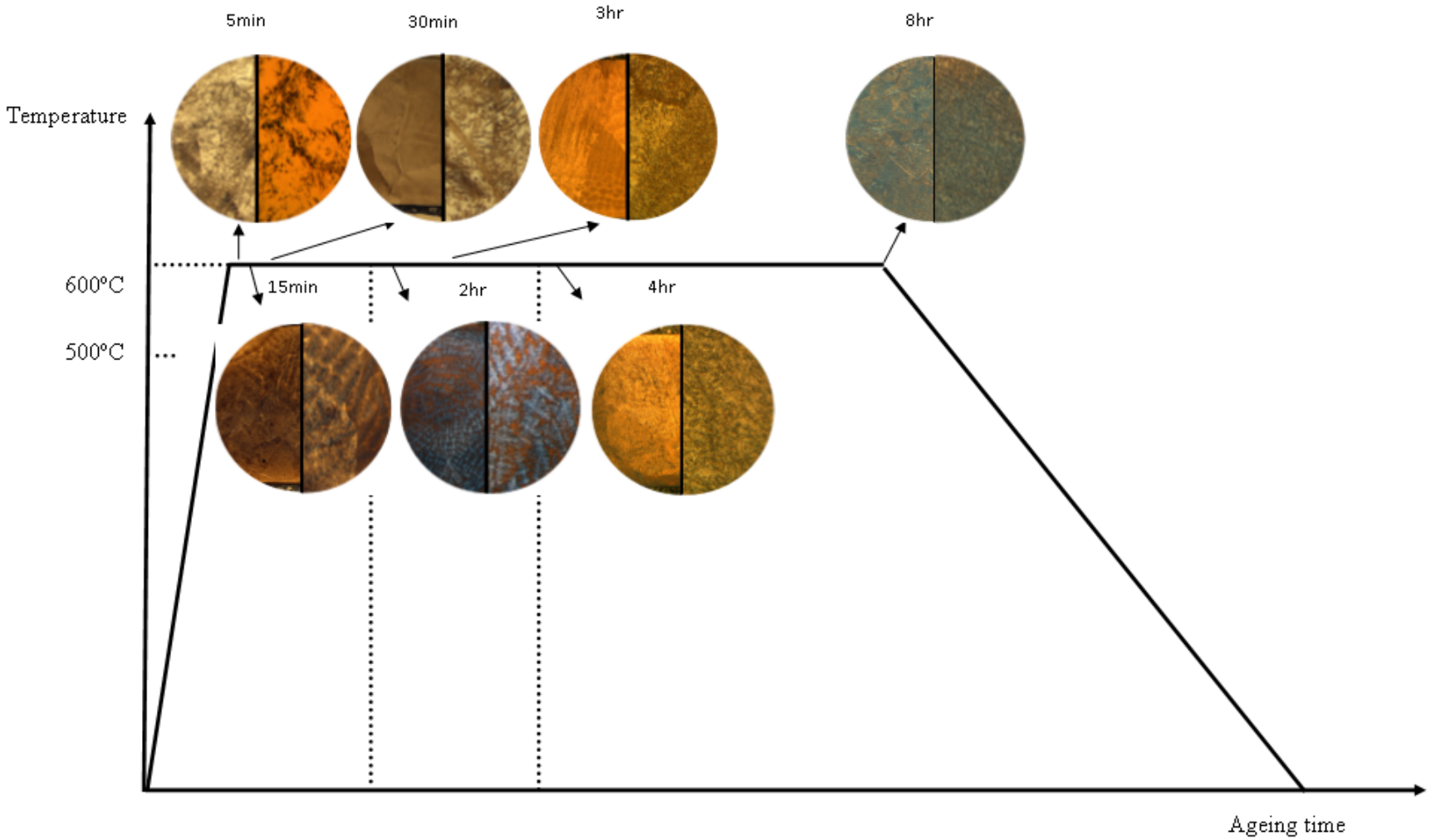

Figure 5.48. Microstructure of Ti5553 FZ at 600°C with various ageing time. Images were taken after air cooling from ageing temperature at 600°C for the time indicated (5min-8hr)

A comparison of the SEM micrographs between specimens aged at 500℃ and 600℃ is demonstrated in Figure 5.49. As discussed earlier, the microstructure at an early stage of the PWHT (first 15mins) showed significant differences. A higher ageing temperature was confirmed to have a faster precipitation rate than a lower temperature. At 30mins of ageing for both temperatures seems to have a similar microstructure in terms of density and distribution. However, high magnification SEM results showed the different morphology of α laths. The α laths at 500℃ are longer but thinner than at 600℃. As the heat treatment continued, α laths coarsening become more obvious at 600℃. The influences of volume fraction and morphology of the α phase will be further discussed in the next chapter.

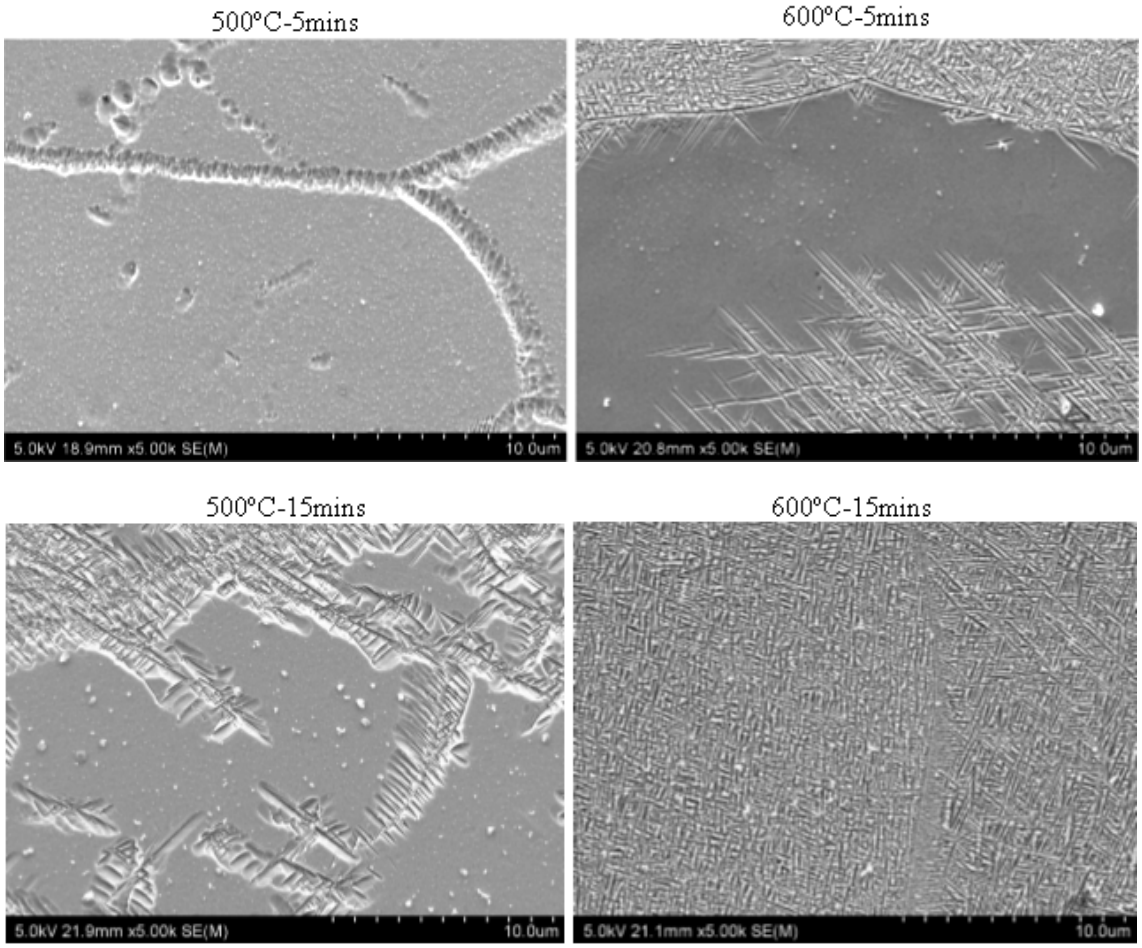

500°C-30mins

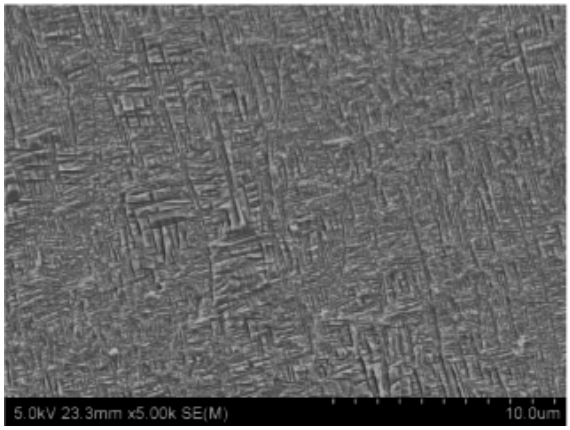

600°C-30mins

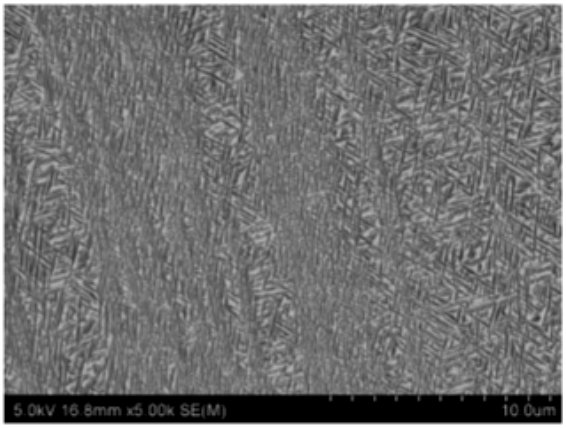

500°C-2hrs

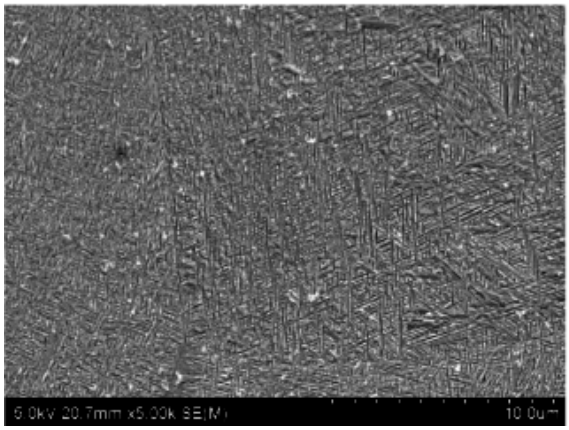

600°C-2hrs

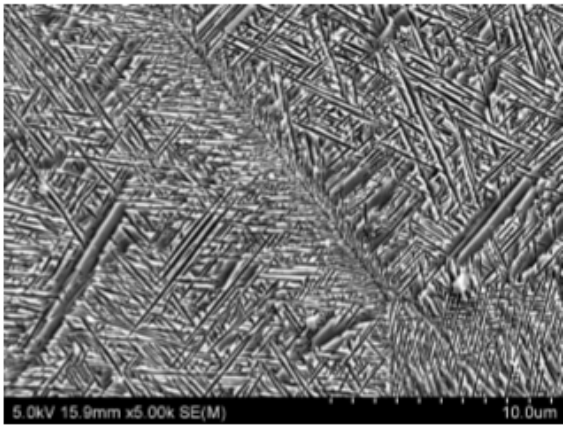

500°C-3hrs

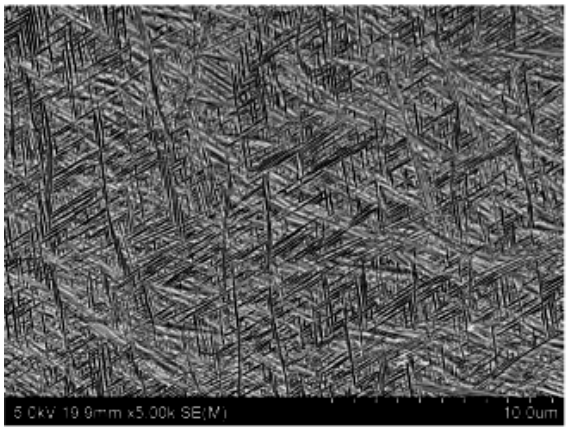

600°C-3hrs

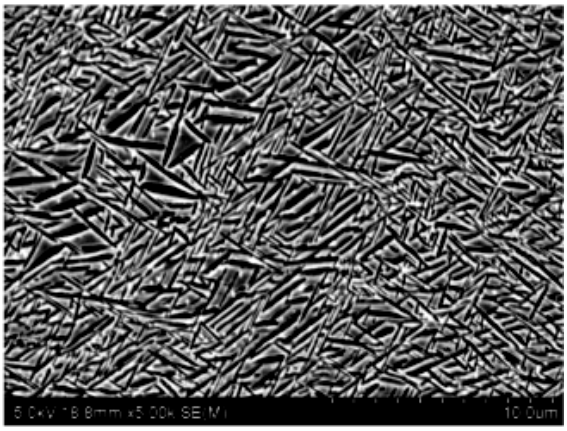

500°C-4hrs

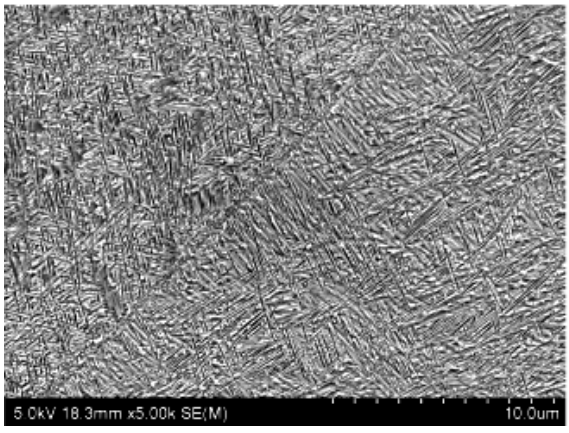

600°C-4hrs

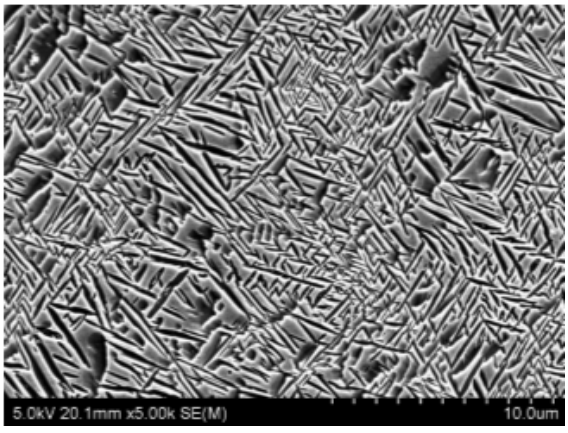

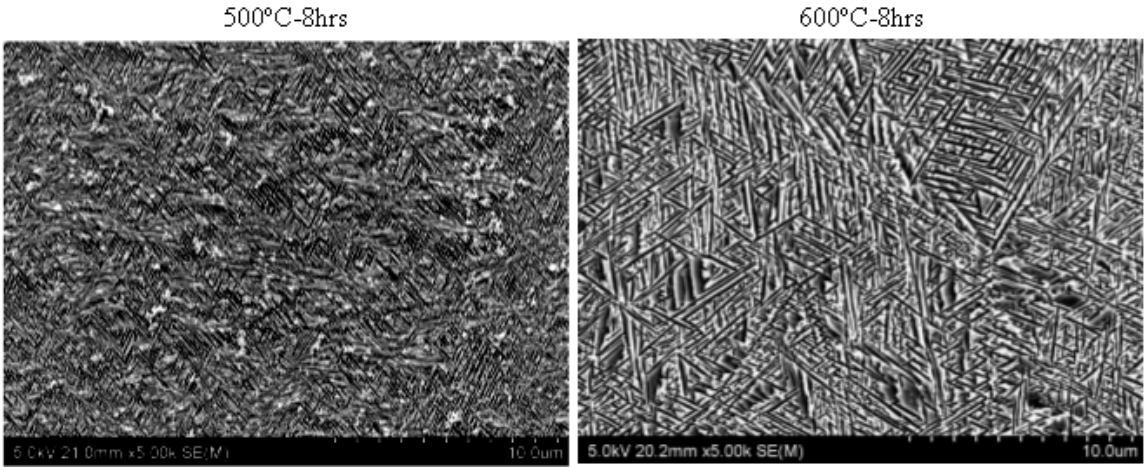

Figure 5.49. SEM micrographs of PWHT welded Ti5553 FZ at ageing temperature of 500℃ and 600℃ with various ageing times

Chapter 6. Mechanical properties in post welded heat treatment of Ti5553

6.1 Introduction

This chapter discusses the mechanical properties of Ti5553-Ti5553 similar welding specimens upon various PWHT which will be compared with the as-welded (AW) condition. The mechanical properties analysis is carried out by comparing micro-hardness and tensile test results. Relating to the previous study of microstructure evolution, this chapter will explain the relationship between precipitation and mechanical properties.

6.2 Hardness testing

Figure 6.1 demonstrates the hardness profiles of Ti5553-Ti5553 similar welding specimens in an AW condition. It shows FZ and HAZ have an average hardness of 289HV which is slightly lower than a BM of 330HV. This phenomenon may be caused by the dissolution of Al in the FZ (Mitchell, Short, Pasang, & Littlefair, 2011). An EDS result of as-welded Ti5553 FZ as shown in Table 6.1, revealed the amount of Al was 2.51wt% where the content of aluminium in the as-received condition was 5.03wt%. EPMA scanning of AW Ti5553 FZ also indicated the average content of aluminium is around 2.5% (Figure 6.2). Relating to the previous chapter, the as-welded Ti5553 can retain its β phase in the weld zone upon air cooling to room temperature, where the BM contains both the α and β grains.

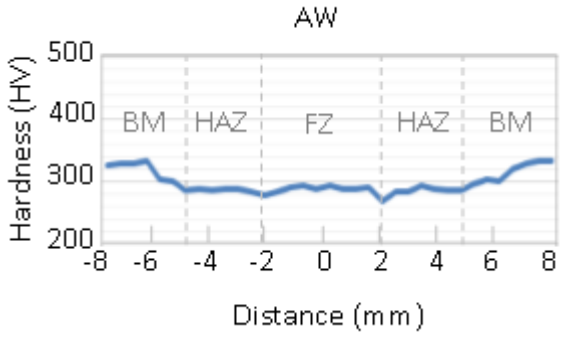

Figure 6.1. Hardness profile of Ti5553 similar welding in the as-welded (AW) condition

Element Line	Net Counts	Weight %	Atom %
O K	0	0.00	0.00
Al K	1219	2.51	4.49
Ti K	19936	84.59	85.23
V K	1277	6.47	6.13
Cr K	371	2.07	1.92
Fe K	16	0.11	0.10
Mo L	1325	4.25	2.14
Total		100.00	100.00

Table 6.1. Energy Dispersive Spectrometer (EDS) result of as-welded Ti5553 FZ

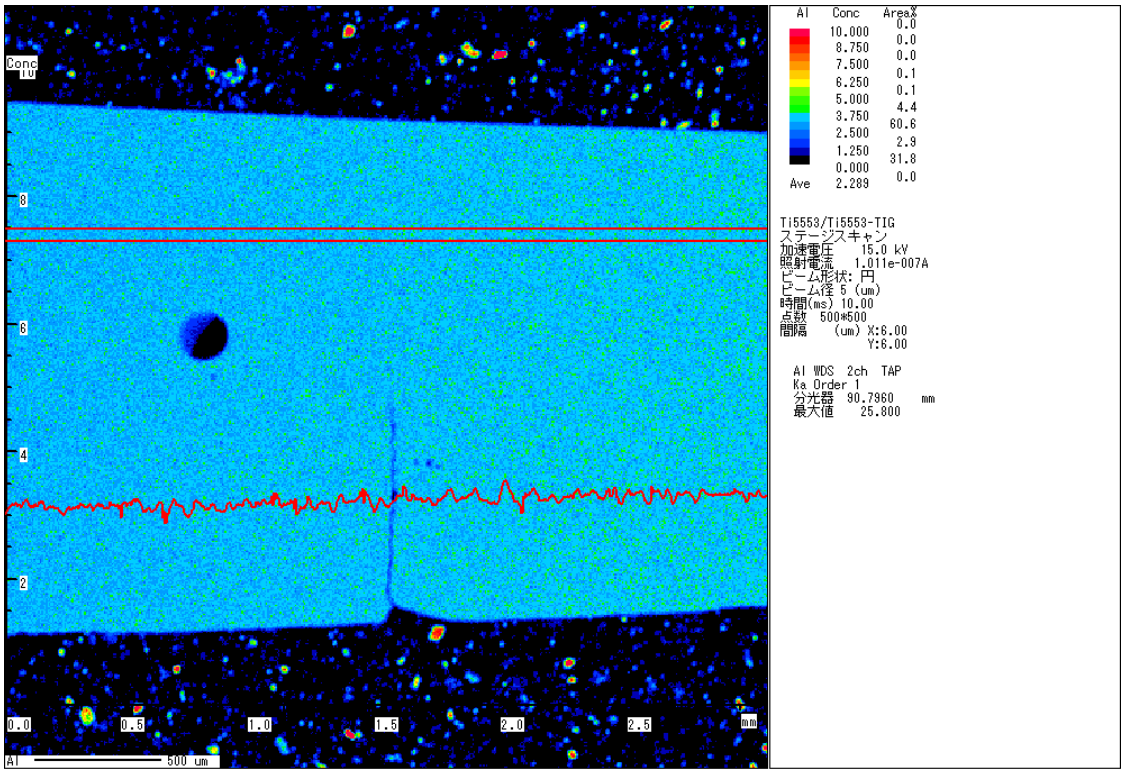

Figure 6.2. Electron Probe Micro-Analysis (EPMA) scan of aluminium across the FZ and HAZ of as-welded Ti5553

Figure 6.3 and 6.4 demonstrate the hardness profiles for individual weldment upon various PWHT. The overall increase in the hardness after PWHT is attributed to the precipitation of α phase particles. For a short time of PWHT, the hardness of specimens aged at 500℃ and 600℃ appear to display a great difference. In the first hardness profiles as shown in Figure 6.3 (a), they were age hardened at 500℃ in the first 5mins, where there was no obvious change in hardness compared to the AW condition. The average

hardness in the FZ and HAZ was approximately 293HV and the BM was around 337HV. It indicates that the initial stage of an α precipitate site has very little or none existing in the weld zone, which has almost no impact on hardness. However, ageing at 600℃ for 5mins as shown in Figure 6.4 (a) displayed local hardening due to the uneven distribution of α particles, where the FZ and HAZ has an average value of 370HV and 343HV for BM. These results are consistent with the microstructure observation which has no α precipitation at 500℃/5min condition, however, the α nucleation started within 5mins at a 600℃ ageing temperature.

At 15mins of ageing the specimen that was heat treated at 500℃ started to get hardened locally due to the randomly distributed α platelets. As displayed in the hardness profile Figure 6.3(b), the average hardness values in the weld zone and BM are almost the same; 324HV and 338HV respectively. While the specimen heat treated at 600℃ for 15mins showed a continuous increase in hardness, as shown in Figure 6.4 (b). At this temperature, hardness of the weld zone was 398HV and BM was 341HV. The reason for this difference in hardness of the weld zone is due to the distribution of the α particles. For 15mins of ageing at 500℃ the precipitations were scattered. The α particles were inclined to precipitate near the grain boundaries (or dislocation) because it helped reduce the activation energy barrier to nucleation (Lampman, 1997). However, ageing at 600℃ for 15mins, the α particles had already uniformly precipitated.

After ageing of 30mins, hardness in the FZ and HAZ has elevated higher than the BM for both temperatures. The hardness profiles of 500℃, as shown in Figure 6.3(c) and 600℃ in Figure 6.4 (c), are very similar; they were approximately 400HV in the weld zone and 340HV in the BM. This can be explained by the microstructure. Comparing the SEM results, the morphology and distribution of the α platelets show a great similarity in both ageing conditions.

Further ageing from 2hrs to 8hrs between the two temperatures leads to significant differences. Ageing at 500℃, as shown in Figure 6.3(d, e, f, and g), resulted in a continuous increase in hardness, reaching the maximum value of 455HV after 4hrs of ageing. The increase of hardness in the weld zone was not significant from 2hrs to 4hrs, and further ageing caused a small drop in the hardness. Meanwhile, hardness in the BM was raised to 378HV at 3hrs and remained the same for further ageing. This means in the

weld zone that the precipitation of α platelets reached its equilibrium at 4hrs. Continuous heat treatment causes coarsening of the α laths in the weld zone. The BM gets hardened slower than the FZ and HAZ. This phenomenon indicated a different growth rate of α precipitation in the unaffected zone. Also the BM has lower maximum hardness than the weld zone. This is because the prior α grain in the BM does not contribute to the precipitation hardening process.

As shown in Figure 6.4 (d, e, f, and g), ageing at 600℃ in the weld zone reached the maximum hardness value of 408HV at 2hrs, which is not so different compared to ageing at 30mins. Further ageing caused a decrease in hardness. Meanwhile, the BM reached its maximum value of hardness of 360HV at 2hrs and started to drop as ageing continued. This observation indicated the equilibrium of an α precipitation in the weld zone which occured at 30mins of age hardening. Further ageing resulted in an increase of volume fraction of coarser α particles due to overageing.

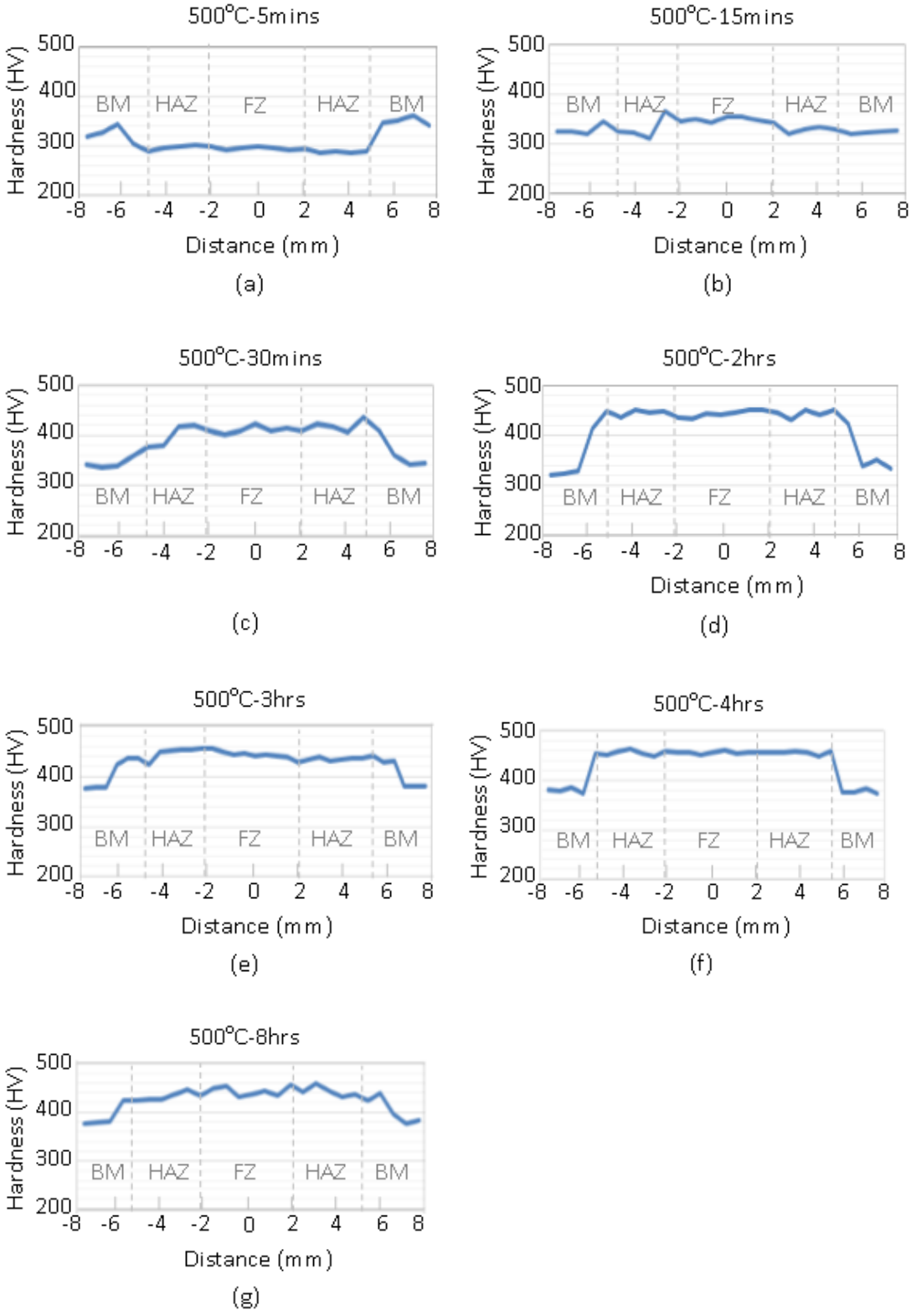

Figure 6.3.Hardness profiles of Ti5553-Ti5553 similar welding specimens aged at 500℃

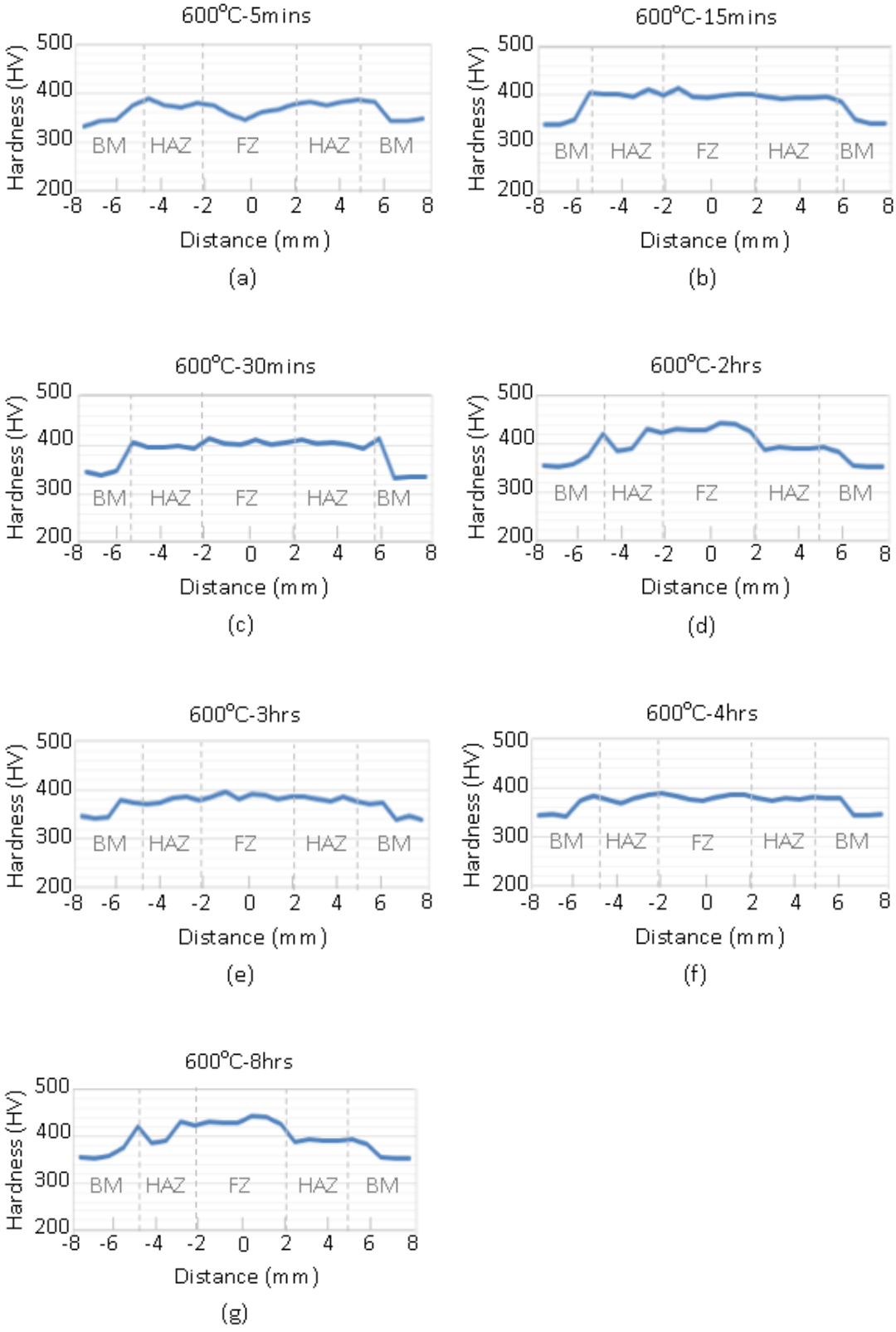

Figure 6.4. Hardness profiles of Ti5553-Ti5553 similar welding specimens aged at 600℃

Comparing the average hardness value in the FZ and the HAZ between 500°C and 600℃, as shown in Figure 6.5, before the first 30mins, the specimen aged at 500℃ showed a higher response than that of 600℃ to heat treatment. The average values of two conditions overlap at 30mins due to the similar microstructure. However, at 600℃, hardness reached its maximum at 2hrs of ageing then started dropping. Although a higher ageing temperature can shorten the age hardening time, the maximum hardness achieved at 600℃ is lower than at 500℃ due to the differences in the volume fraction of fine α platelets (Figure 5.37 and Figure 5.49).

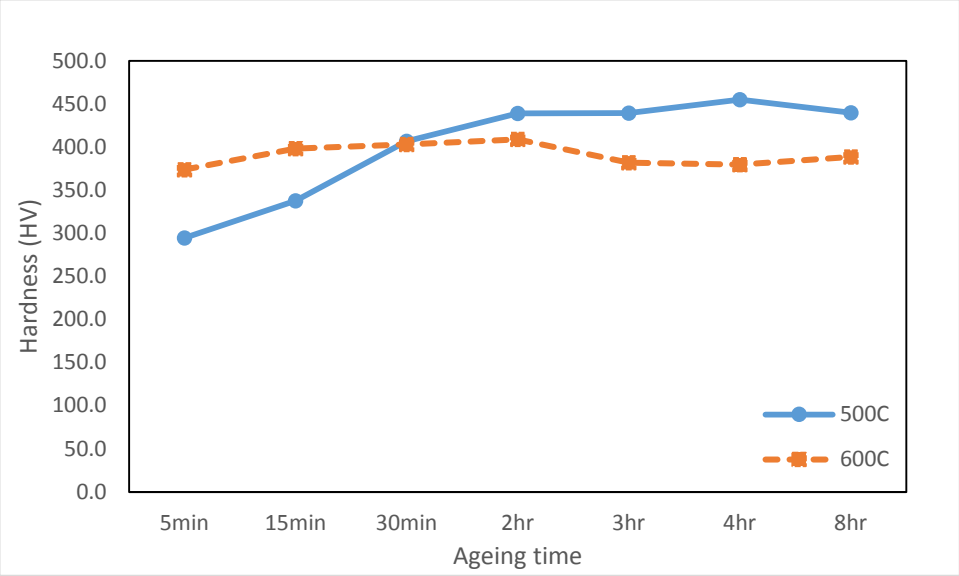

Figure 6.5. Comparison of hardness profiles between two ageing temperatures

Faster age hardening in the weld zone than the BM also indicated that the retained ω_a particles inside the β grains at an AW condition provided nucleation sites for the α particles to precipate. The existence of ω_a particles were verified by a diffraction pattern of an AW TEM result. The lower maximum hardness value in the BM can be explained by the microstructure. Figure 6.6 and 6.7 show SEM images of the BM aged at 500℃ for 2hrs and 3hrs. The circular shapes in those images are prior α grains which have no effect on age hardening. After ageing for 2hrs, a very fine secondary α phase began to precipitate in the retained β matrix. The microstructure was a bimodal structure with primary globular α and newly formed lamellar alpha in a prior β. Following ageing for 3hrs, the amount of the α phase was significantly increased and the size of such acicular α was coarsened. Comparing the precipitation progress in the FZ for the same ageing temperature, the α film was almost completely covered after 30mins of ageing time.

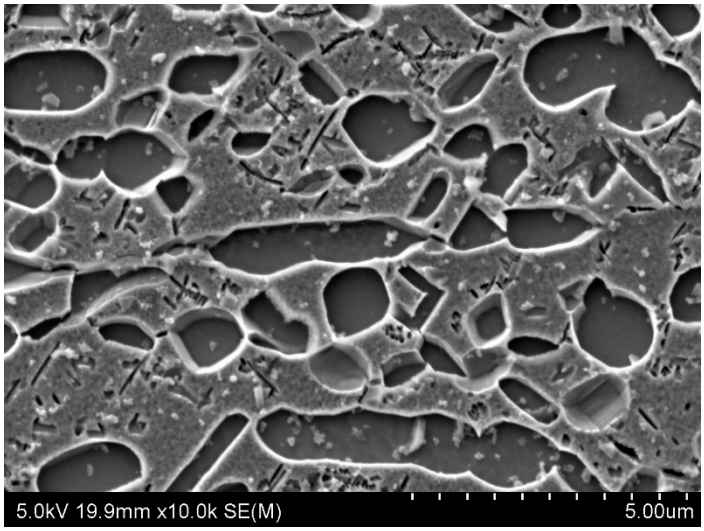

Figure 6.6. SEM micrograph of BM aged at 500℃ for 2hrs

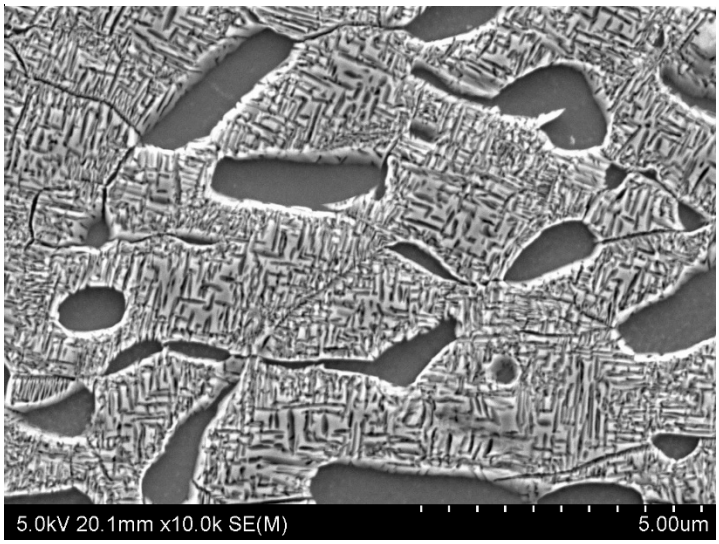

Figure 6.7. SEM micrograph of BM aged at 500℃ for 3hrs

Figure 6. 8 is a comparison of the average hardness in the BM, HAZ, and FZ. The hardness profile showed that the HAZ is slightly softer than the FZ at the corresponding ageing time, however, the differences were very small. It indicated the number of precipitates in the HAZ is less than the FZ but still very smiliar. The change in hardness for short-time ageing (< 30mins) in the BM was slower than the HAZ and FZ. This is due to the retained athermal ω_a in the weld zone promoting an α precipitation, thus producing a faster hardened rate in the HAZ and FZ. After 8hrs of ageing, further ageing at a higher tempearture (800℃) caused a dramatic drop in hardness. The reaction is caused by dissolution of the alpha phase since 800℃ is very close to the Ti5553 beta transus temperature, that is 856℃. This reaction happened very quickly (within 5mins).

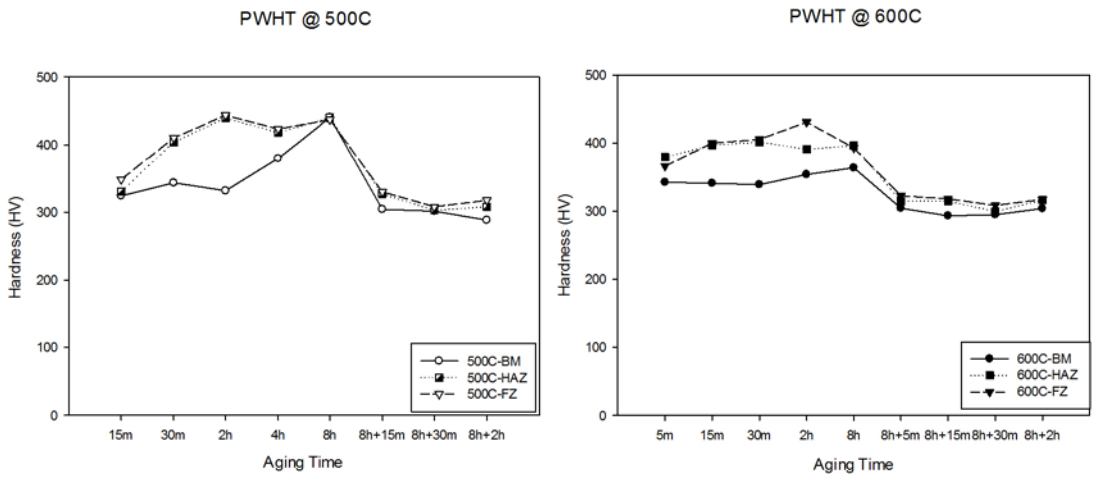

Figure 6. 8. Average micro-hardness (HV) in BM, HAZ, and FZ of samples aged at 500℃, 600℃ followed by ageing at 800℃

6.3 Tensile testing

In order to analyse the relationship between the strength and microstructure, a tensile test was employed. Commonly, there are a few ways to increase the strength such as work hardening, solid solution strengthening, precipitation strengthening and grain boundary strengthening. The corresponding factors for these strengthening mechanisms involved dislocation density ($\Delta\sigma_y = Gb\sqrt{\rho}$), radius and volume fraction of precipitates ($\Delta\tau = \frac{Gb}{l_{interparticle} - 2r_{particle}}$), grain size ($\sigma_y = \sigma_0 + kd^{-1/2}$), and solute atom concentration ($\Delta\tau = Gb\sqrt{C_s}\epsilon^{3/2}$) (Callister, 2007; Giosa.R.P, 2009). The only significant feature that alters strengthening in this study was the presence of a volume fraction of precipitates.

The ultimate tensile strength (UTS) results and location of fractures are presented in Table 6.2. As expected, by precipitating alpha particles, strength has been increased. Specimens aged at a higher temperature have higher UTS to the corresponding ageing time. To ensure the accuracy of test results, a total of three sets of tensile tests were carried out. The average values were used to present the graphs. The elongation (%) was measured with 50mm extensometer and later on verified with a digital Vernier calliper. Figure 6.9 summarises the ultimate tensile strength (UTS) of the Ti5553 weldments that were aged at 500℃ and 600℃ over time. The features of the fractures will be analysed in the next chapter.

Condition	UTS (MPa)	Elongation (%)	Fracture location
As-welded	720	6.72	FZ
500℃-5min	731	6	FZ
500℃-15min	743	3.8	FZ
500℃-30min	809	2.3	FZ
500℃-2hr	714	1	FZ
500℃-3hr	753	1.2	FZ
500℃-4hr	753	0.32	FZ
500℃-8hr	698	0.31	FZ
600℃-5min	741	2	FZ
600℃-15min	910	1	FZ
600℃-30min	983	1.6	FZ
600℃-2hr	889	0.51	FZ
600℃-3hr	914	1	FZ
600℃-4hr	931	0.59	FZ
600℃-8hr	949	0.81	FZ

Table 6.2. Tensile properties after ageing at 500℃ and 600℃

In the first 5mins of ageing, the specimen aged at 500℃ showed no significant increase compared to the AW condition. This result justified the previous microstructure observation where no precipitation was found at this condition. However, there was a small improvement in strength of the sample aged at 600℃ for 5mins (723MPa-741MPa) due to the small amount of secondary α precipitates. Clement et al. also mentioned at precipitation, hardening happens within 1-2mins at 600℃ for Ti5553 (Clement et al., 2007). As the ageing time is increased, the tensile strength increased for both temperatures. It can be observed that for the same amount of ageing time, the specimen aged at 600℃ had higher UTS than at 500℃.

The highest average tensile strength was obtained on the specimen aged at 600℃ for 30mins (983MPa). Nevertheless, the highest UTS for that aged at 500℃ also happened at 30mins (809MPa). Associated with the observation of the microstructure on each age hardening condition, it can be explained by the size and volume fraction of the α phase. Specimens that are aged for 30mins at both temperatures have reached their equilibrium of α precipitation with the highest volume fraction of around 36%. It caused a significant increase in the UTS for the first 30mins of ageing.

When the ageing time was increased (2-8hrs), the tensile strength decreased with an average UTS of 740MPa for samples aged at 500℃. Samples aged at 500℃ for 8hrs had lower UTS than the AW specimen. During this period, additional ageing did not affect the tensile strength significantly. The difference of UTS for samples aged for 2-8hrs was less than 6%. Compared with samples aged at 600℃, the tensile strength showed similar behaviour with the additional ageing time. As shown in Figure 6.9, after reaching the maximum UTS at 30mins, there was a small variance of the UTS. But overall the tensile strength remained at the same level. Also, samples aged at 600℃ had a much higher UTS than those aged at 500℃ for the corresponding ageing time. Based on the findings about the microstructure, an increase in ageing time after 30mins resulted in α laths coarsening significantly. These coarsened α laths caused a decrease in the α phase volume fraction, but they did not have a significant influence on the tensile strength.

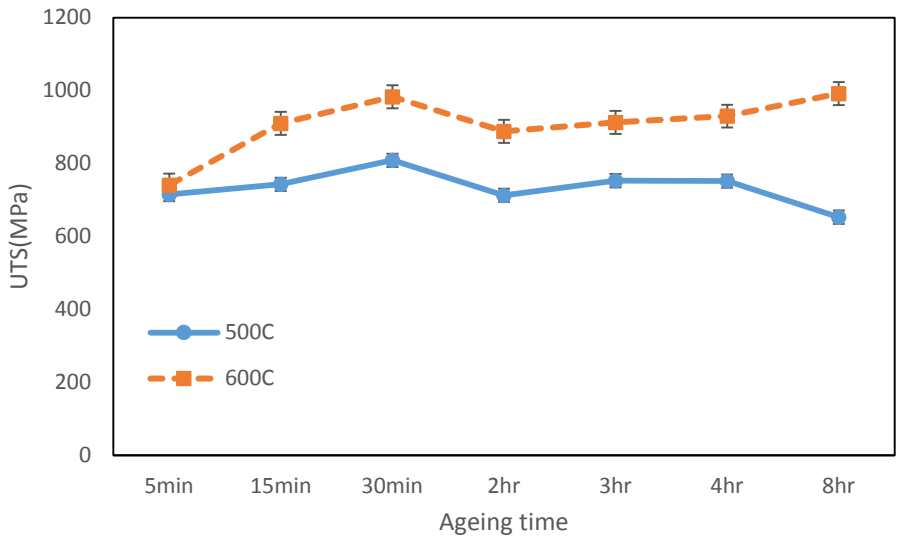

Figure 6.9. Ultimate tensile strength vs. ageing time for samples aged at 500℃ and 600℃

The elongation of tensile test pieces was illustrated in Figure 6.10. As the ageing time increased, test pieces aged at 500℃ showed a rapid reduction in ductility upon heat treatment. However, specimens aged at 600℃ exhibited more brittle behaviour at the early stage of precipitation hardening. Nevertheless, there was a trend of elongation which appeared to be decreasing as the ageing time increased. The variance of elongation for specimens aged at 600℃ is from 0.5% to 2%. The significant difference between samples aged less than 30mins ageing time is due to the different amounts of alpha precipitation.

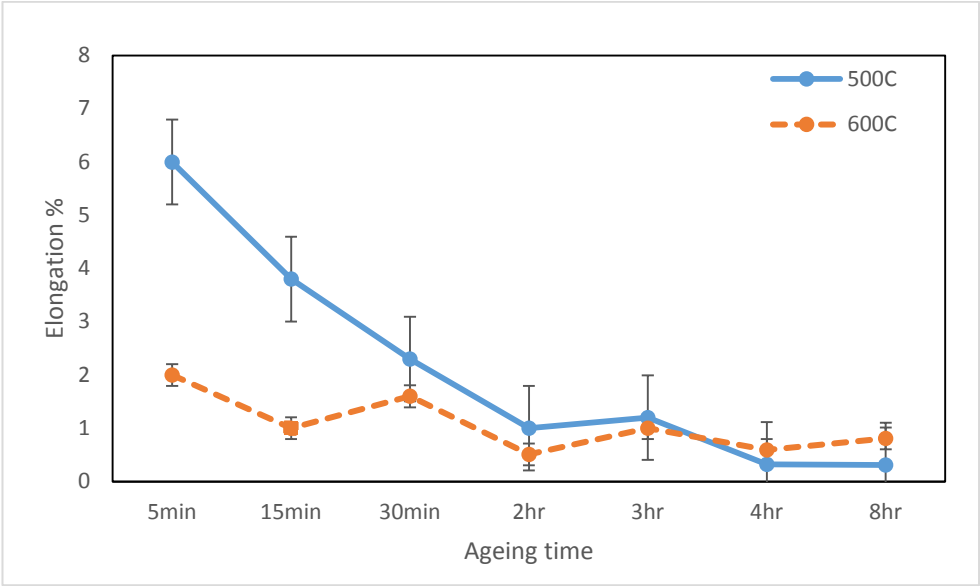

Figure 6.10. Elongation (%) of tensile test pieces vs. ageing time for samples aged at 500℃ and 600℃

Figure 6.11 & 6.12, are graphs showing hardness and elongation against the ageing time for samples aged at 500℃ and 600℃. Samples aged at 500℃ showed typical behaviour of escalation in hardness with a reduction in ductility when increasing the ageing time. However, the changes in samples aged at 600℃ did not show much difference. In comparison between the average size of the α precipitation and elongation are presented in Figure 6.13 & 6.14. The ductility appeared to be reciprocal to the average α lath size for 500℃ aged samples. However, the variation in ductility for 600℃ aged samples is not significant since the precipitation happened very quickly (within 5mins).

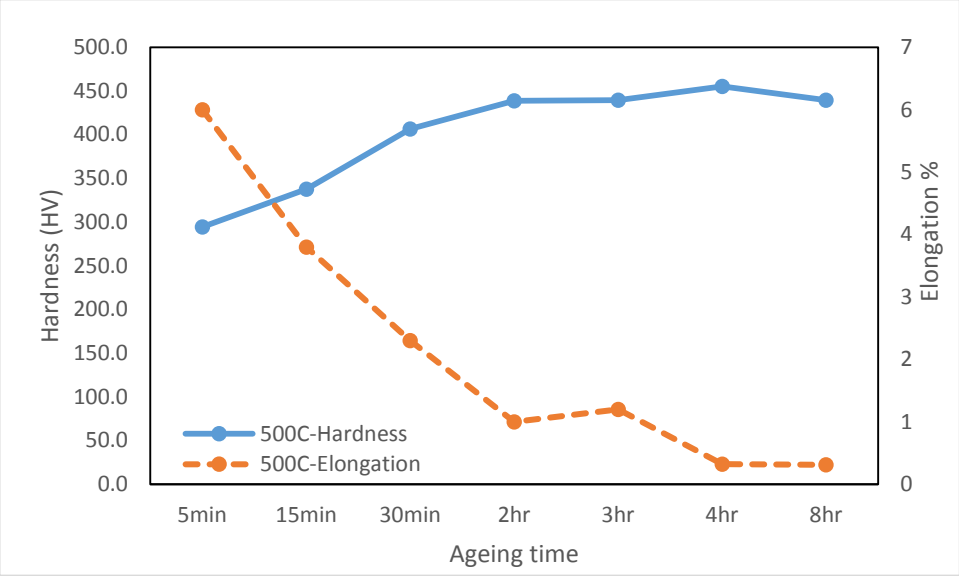

Figure 6.11. Hardness (HV) and Elongation (%) vs. ageing time for samples aged at 500℃

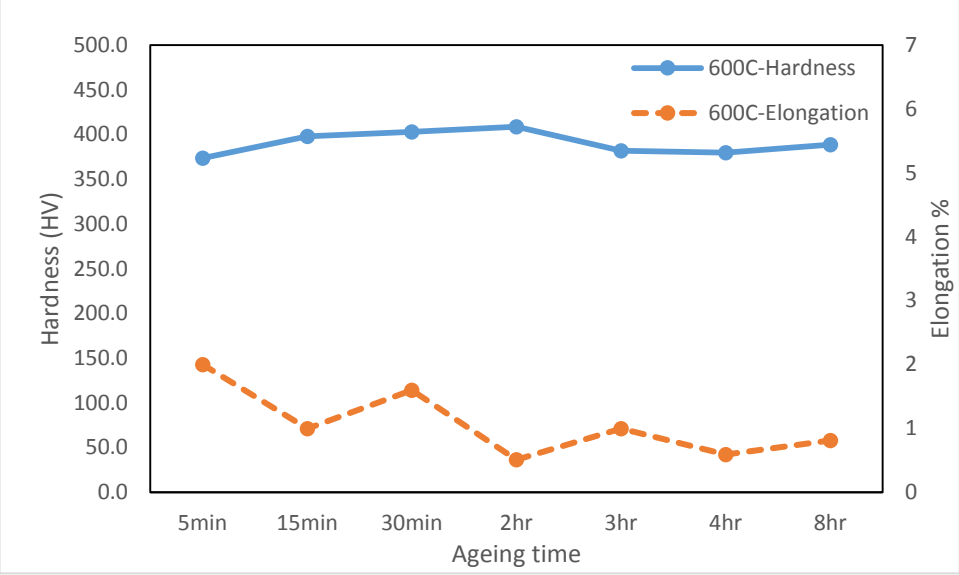

Figure 6. 12. Hardness (HV) and Elongation (%) vs. ageing time for samples aged at 600℃

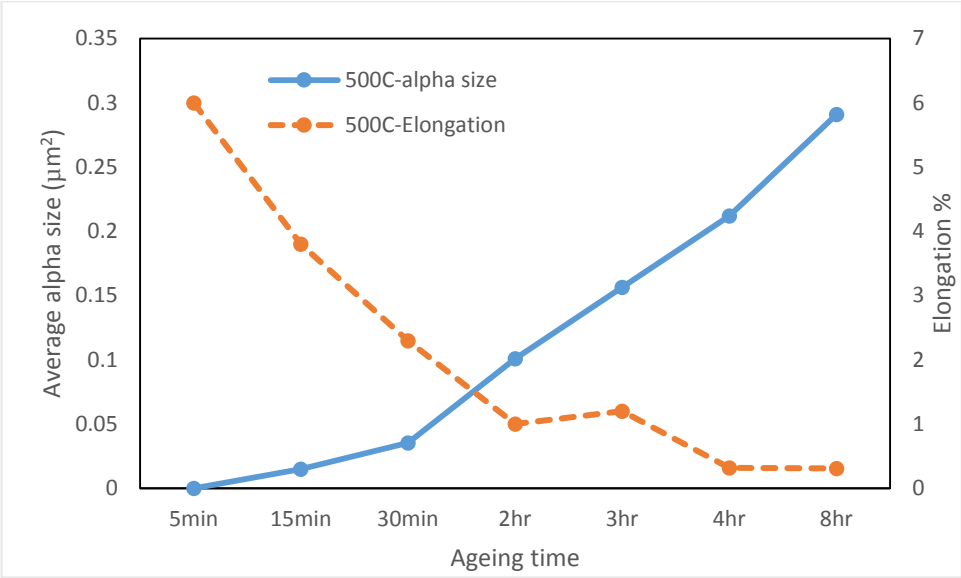

Figure 6.13. Average size of α lath (µm^2) and Elongation (%) vs. ageing time for samples aged at 500℃

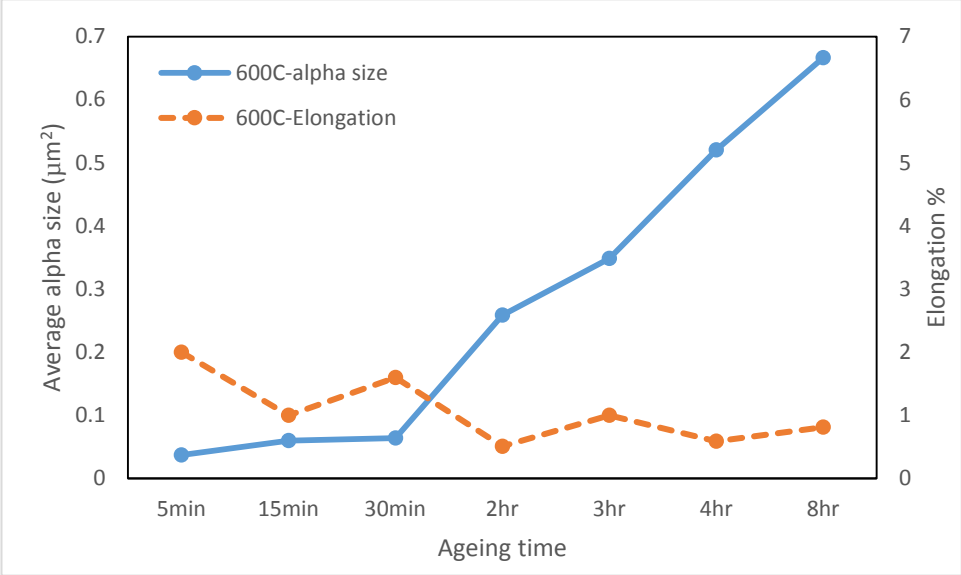

Figure 6.14. Average size of α lath (µm^2) and Elongation (%) vs. ageing time for samples aged at 600℃

6.4 Summary

To analyse the relationship between the morphology of precipitation and mechanical properties, test results were analysed in pairs. They were: UTS-Hardness (Figure 6.15), UTS-Average α size (Figure 6.16), and Hardness-Average α size (Figure 6.19), UTS-Elongation (Figure 6.20).

For the same ageing temperature, there seems not enough evidence to relate tensile strength with hardness. However, comparing the results between the two ageing temperatures (Figure 6.15), the samples aged at 500℃ had a lower UTS but a higher hardness than samples aged at 600℃. For a short ageing time (less than 30mins), the tensile strength for samples aged at both temperatures had increased. These escalations reached their maximum value when aged at 30mins then remained at a specific range. There were slight increases for the longer ageing time, but the differences were fairly small. Nevertheless, the maximum hardness value for ageing at 600℃ occurred between 30mins and 2hrs ageing time. Further ageing caused a slight decrease in hardness of approximately 6%. The maximum hardness value for ageing at 500℃ occurred after 2hrs of ageing time and was about 8% higher than the maximum hardness for ageing at 600℃. The behaviours of tensile strength and hardness can be explained by the size of the α phase.

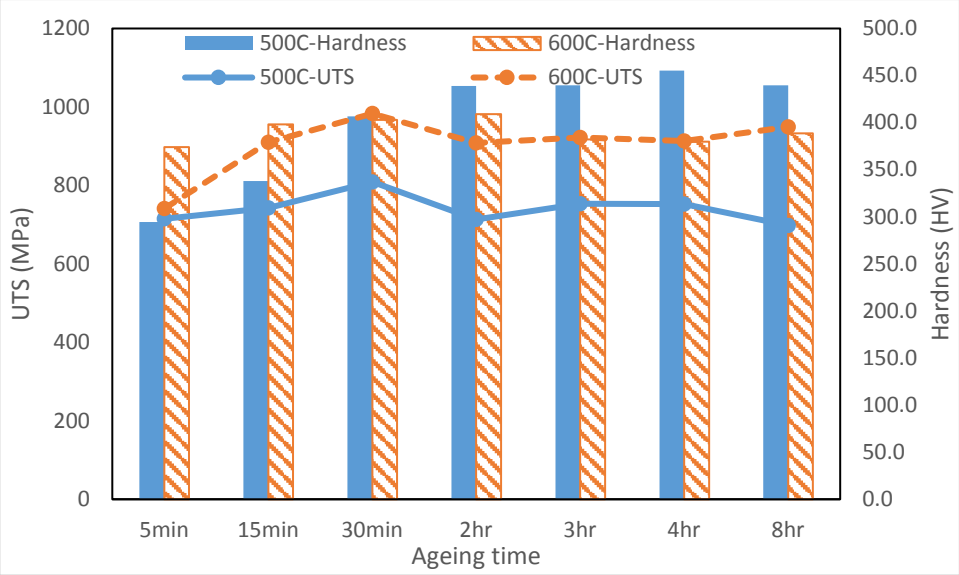

Figure 6.15. Tensile strength (MPa) and microhardness (HV) of samples aged at 500℃ and 600℃ vs. ageing time

Figure 6.16 demonstrated the relationship between tensile strength with an average size of the α laths. In relation to the observation of the precipitation microstructure, after 30mins of age hardening, specimens were covered by α laths homogenously. The volume fraction of the α phase also reached its maximum of 36-37%. At this condition, the tensile strength had its maximum UTS for both ageing temperatures. After 30mins of ageing, the α laths continued growing. This α growth was not only in length but also in width. At a certain ageing time, the α laths reached their maximum length but continued coarsening for both ageing temperatures. The coarsened α laths caused a decrease in volume fraction and also a slight drop in tensile strength. However, the influence on tensile strength was fairly small. Nevertheless, Figure 6.16 showed that sample aged at 600℃ with a larger α size had a much higher average tensile strength than samples aged at 500℃ with a corresponding ageing time.

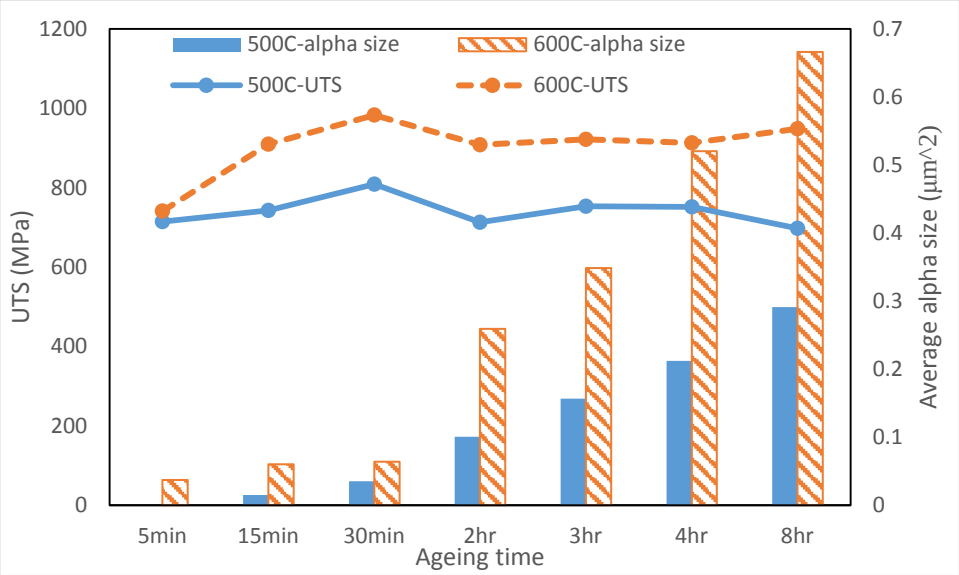

Figure 6.16. Tensile strength UTS (MPa) and average alpha size (µm2) of samples aged at 500℃ and 600℃ vs. ageing time

On the contrary, during the α phase coarsening, a larger α size resulted in a lower hardness value. The summary of hardness profiles for ageing at 500℃ and 600℃ are presented as Figure 6.17 & 6.18. The relationship between hardness in the weld zone and the α size is shown in Figure 6.19. Hardness increases with a decreasing particle size after reaching its critical grain size. This can also be described as a Hall-Patch relationship (Bhattacharjee et al., 2008).

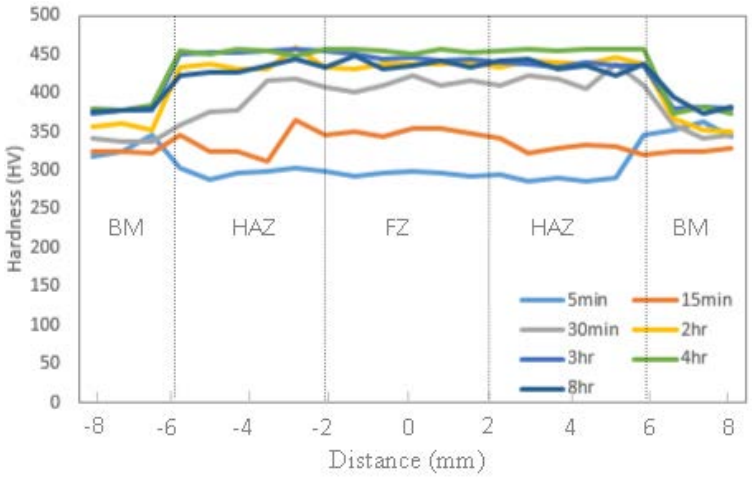

Figure 6.17. Hardness profile for samples aged at 500℃

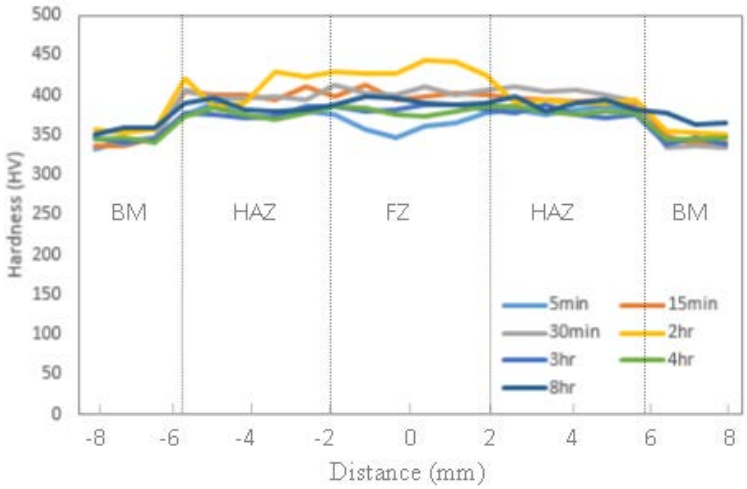

Figure 6.18. Hardness profile for samples aged at 600℃

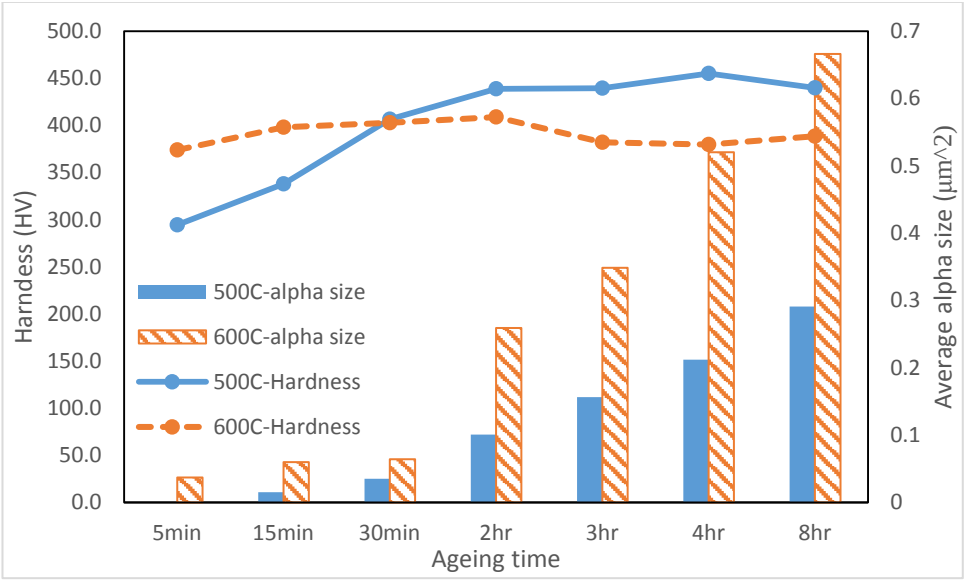

Figure 6.19. Microhardness (HV) and average alpha size (µm^2) of samples aged at 500℃ and 600℃ vs. ageing time

In the literature review of Du et al. about the effect of heat treatment on microstructure and mechanical properties of Ti-3.5Al-5Mo-6V-3Cr-2Sn-0.5Fe, they pointed out that an increase in the ageing temperature lead to a decrease in strength and an increase in ductility, with a corresponding higher ageing temperature which had higher ductility (Du Z. et al., 2014). In other words, increasing the volume fraction of precipitated α or decreasing the α size would improve the yield strength (Du Z. et al., 2014). Their work showed that an increase in the ageing temperature causing a larger width of secondary α and lower volume fraction of α, was similar to my results. Clement et al. also said the lower ageing temperature (400℃) had less yield strength compared to ageing at 500℃ due to the brittle behaviour of lower temperatures (Clement et al., 2007). However, as shown in Figure 6.20, it is not necessarily true. For instance, with ageing at 600℃ it had low ductility in general but still had much higher tensile strength than ageing at 500℃. But for the same temperature, with an increase in ageing time, the brittleness was one of the factors that lead to failure.

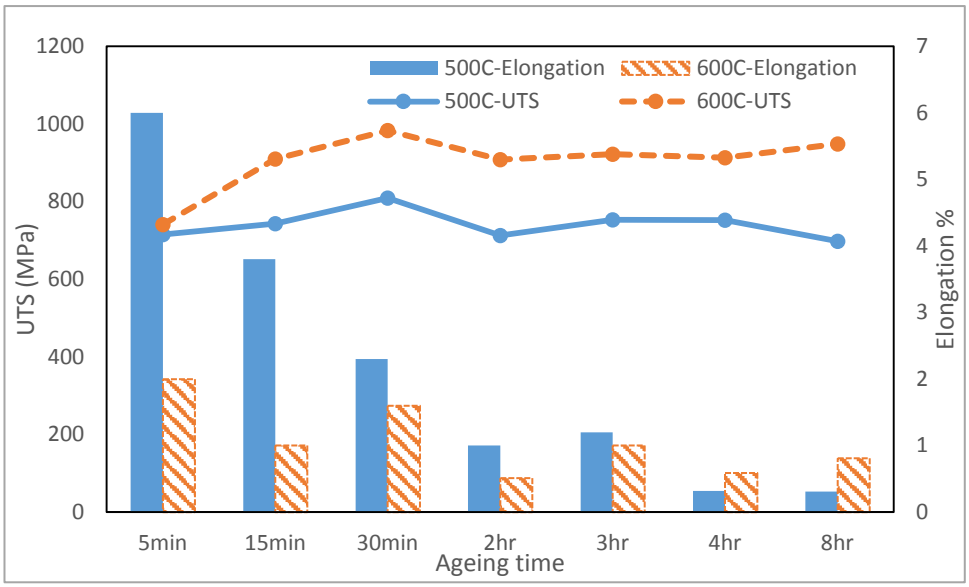

Figure 6.20. Tensile strength (MPa) and Elongation (%) of samples aged at 500℃ and 600℃ vs. ageing time

Chapter 7. Fractography

7.1 Introduction

This chapter reports the fractography which includes crack propagation and fracture analysis of Ti5553-Ti5553 similar welding specimens following tensile testing in the as-welded (AW) condition and after post welding heat treatment (PWHT). The purpose is to understand the mechanism of fracture and the cause of fracture features by studying the fracture surfaces. The samples were examined using a Scanning Electron Microscope (SEM).

7.2 Crack propagation analysis

Based on the microstructure evolution and mechanical properties described in the previous chapters, AW and six PWHT specimens were selected for crack propagation analysis. In order to compare the results between short-time and long-time PWHT, and since most of the α precipitation happens within first 30mins, the chosen specimens for crack propagation analysis were samples aged at 500℃ and 600℃ for 5min, 30min and 8hr. Since the fractures were caused by tensile testing, Mode I (opening) and II (shearing) fracture loading modes were involved. All selected samples were lightly etched with Kroll's reagent for microstructure examination. Based on literature reviews, there are two types of cracks; (i) transgranular, whose cracks propagate through the grains and (ii) intergranular, where the fracture path is along the grain boundaries (Handbook, 1987).

(1) As-welded (AW) specimen

Figures 7.1 and 7.2 show the optical macrograph and SEM image of the top surface of the AW tensile test specimen. The specimen was reserved from tensile testing before the fracture. As shown in Figure 7.2, a long discontinuous transgranular crack was observed across the FZ of the test piece. The discontinuous location likely occurred at the grain boundary. The direction of this crack changed with altered crystallographic orientation.

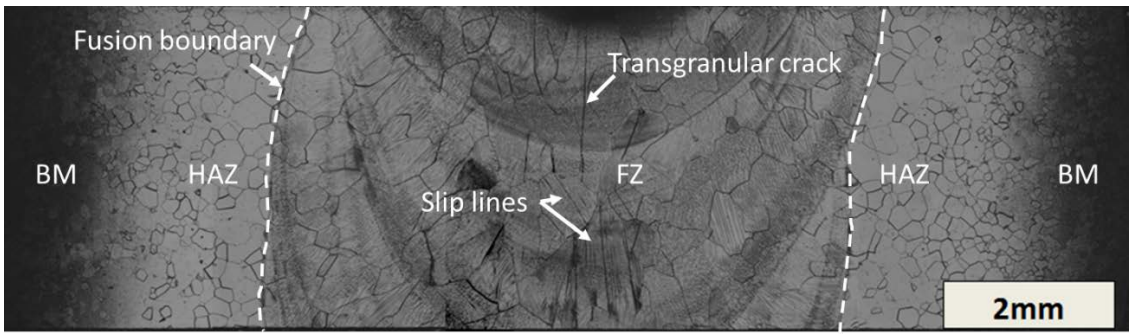

Figure 7.1. Optical micrograph showing slip lines and transgranular crack propagated along the top surface of AW tensile test piece. Specimen was reserved from tensile testing prior to fracture

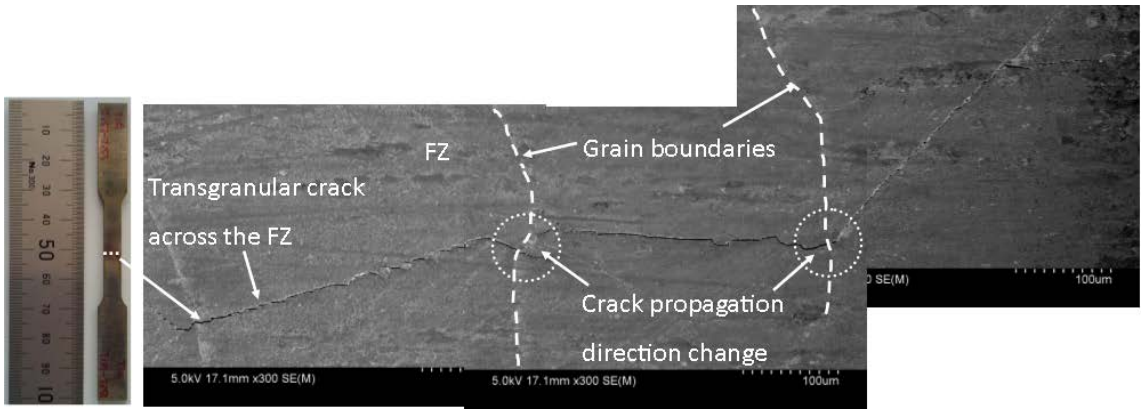

Figure 7.2. SEM image of a transgranular crack propagated along FZ. Specimen was reserved from tensile testing before fracture

Higher magnification SEM images of cracks at various locations near the fracture surface are shown in Figure 7.3. Crack (a) had formed on the side of the sheet specimen and with a planar growth form had propagated towards a grain boundary. After reaching the grain boundary, this crack changed direction and continued growing on a new crystallographic plane until it reached the second grain boundary. In a second case (b), the crack also formed on the edge and reaching a grain boundary it failed to penetrate the grain boundary and instead bounced along the boundary three times before the crack stopped growing. Crack type (c) formed in the middle of this specimen; its opening displacement was much less than the other two cracks and grew along the grain boundary. Type (a) and (b) are both transgranular cracks, type (c) is an intergranular crack.

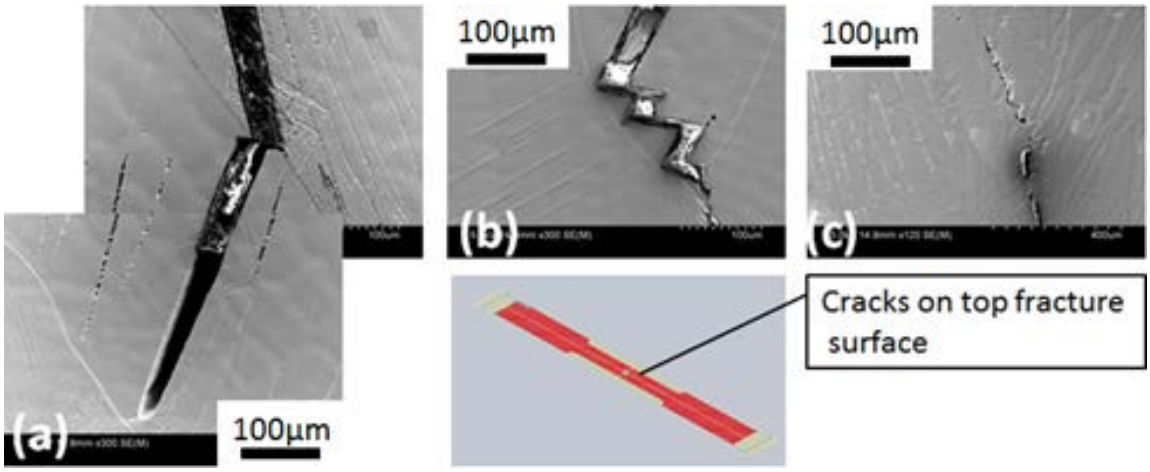

Figure 7.3. SEM images of cracks on AW Ti5553 FZ

(2) Post weld heat treatment (PWHT)

Fracture locations of most tensile specimens from PWHT conditions occurred in the fusion zone (FZ). A few samples were fractured in the base metal (BM) and heat affected zone (HAZ). Macrographs of the broken test pieces and the locations of fracture are shown in Figure 7.4 and 7.5.

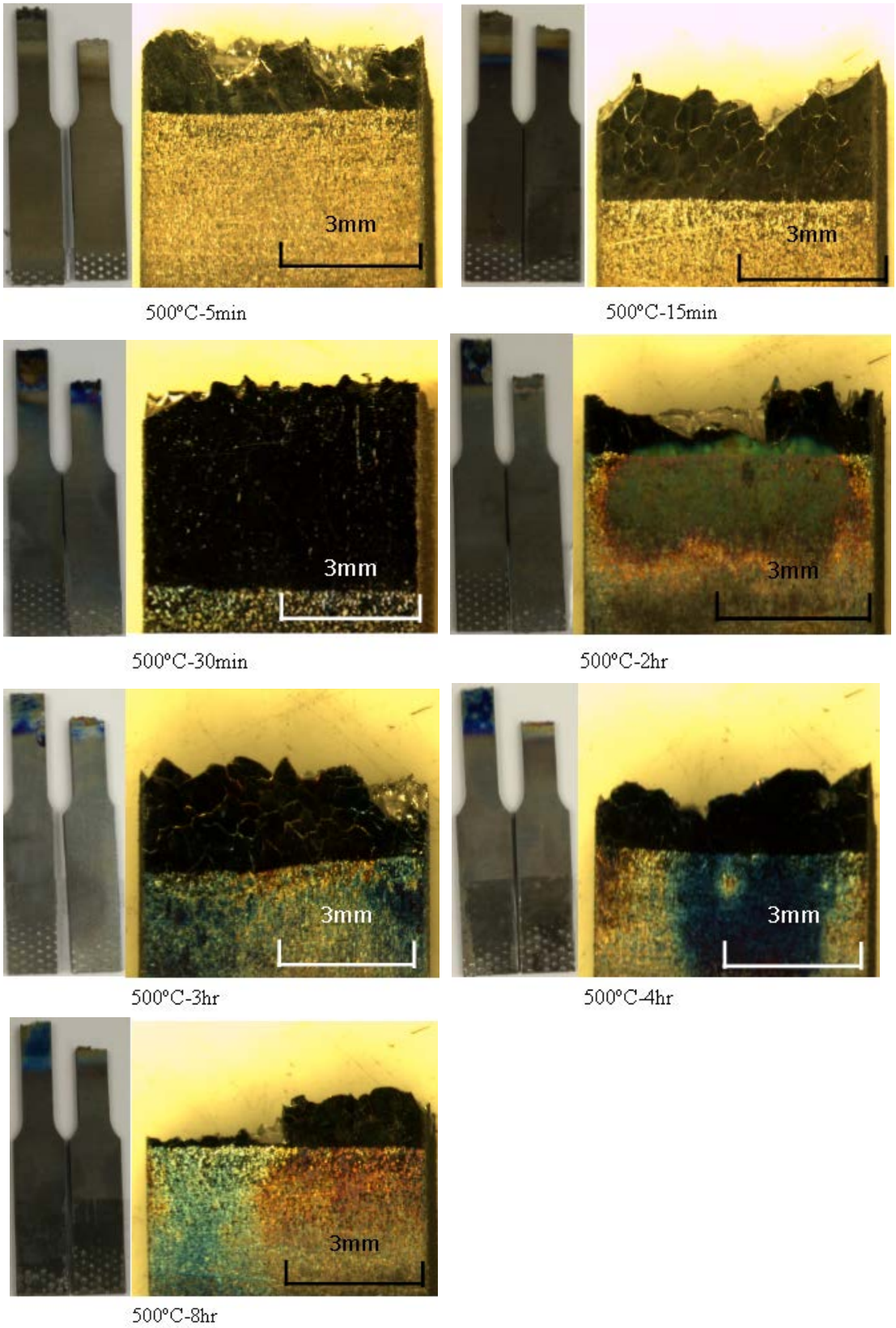

Figure 7.4. Macrographs of the broken test pieces and the fracture locations of specimens aged at 500℃ after tensile test

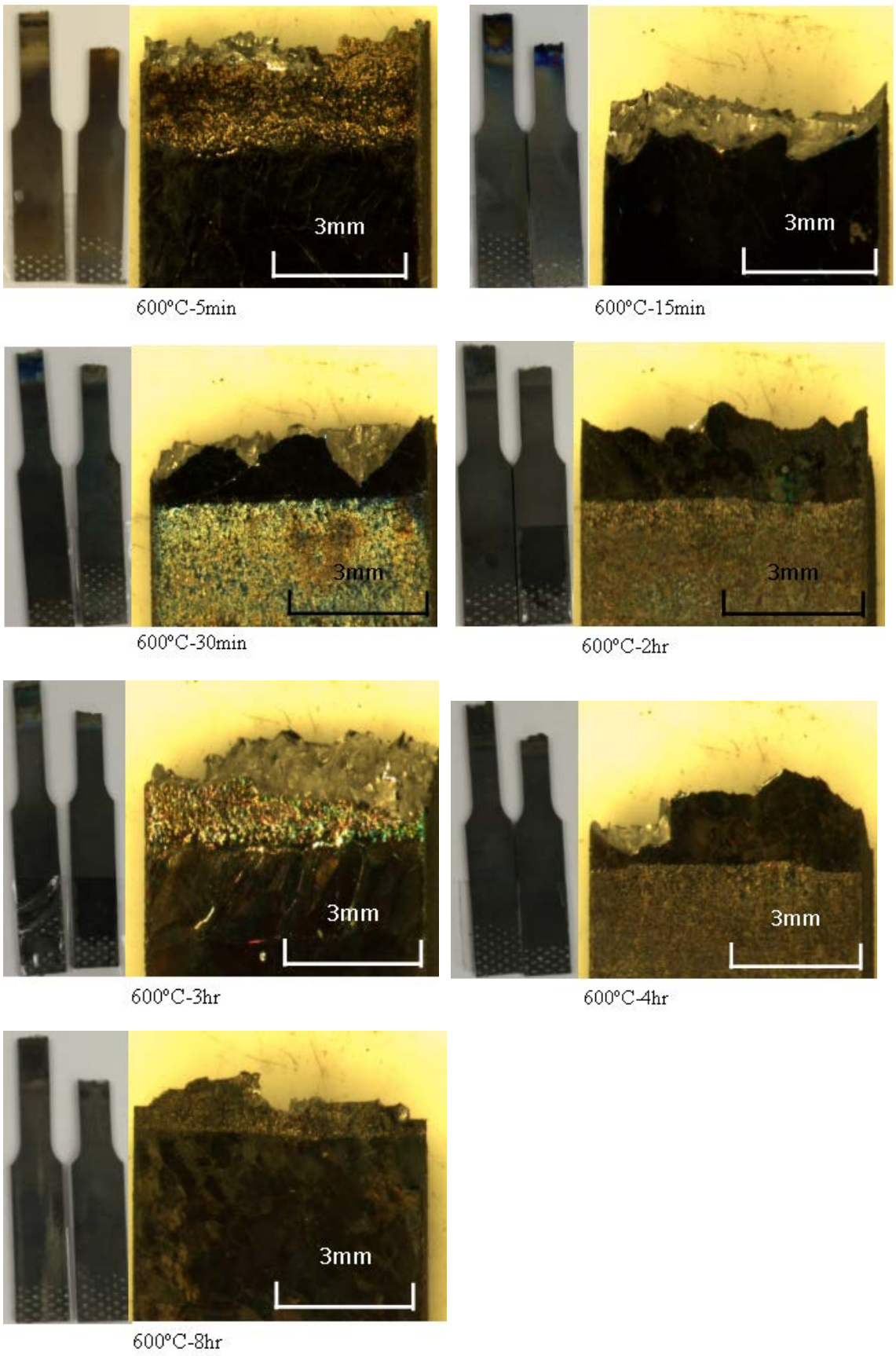

Figure 7.5. Macrographs of the broken test pieces and the fracture locations of specimens aged at 600℃ after tensile test

Sample aged at 500℃ for 5min had a very similar microstructure as the AW condition. As shown in Figure 7.6 on the top surface of the tensile test piece, the slip lines are visible in the low magnification optical microscopy (OM) image. Multiple transgranular cracks in the HAZ can be seen clearly near the fusion boundary. The top view of the fracture surface indicated a transgranular fracture. The weld area of both the AW and the sample aged at 500℃ for 5min conditions were covered by the BCC β phase.

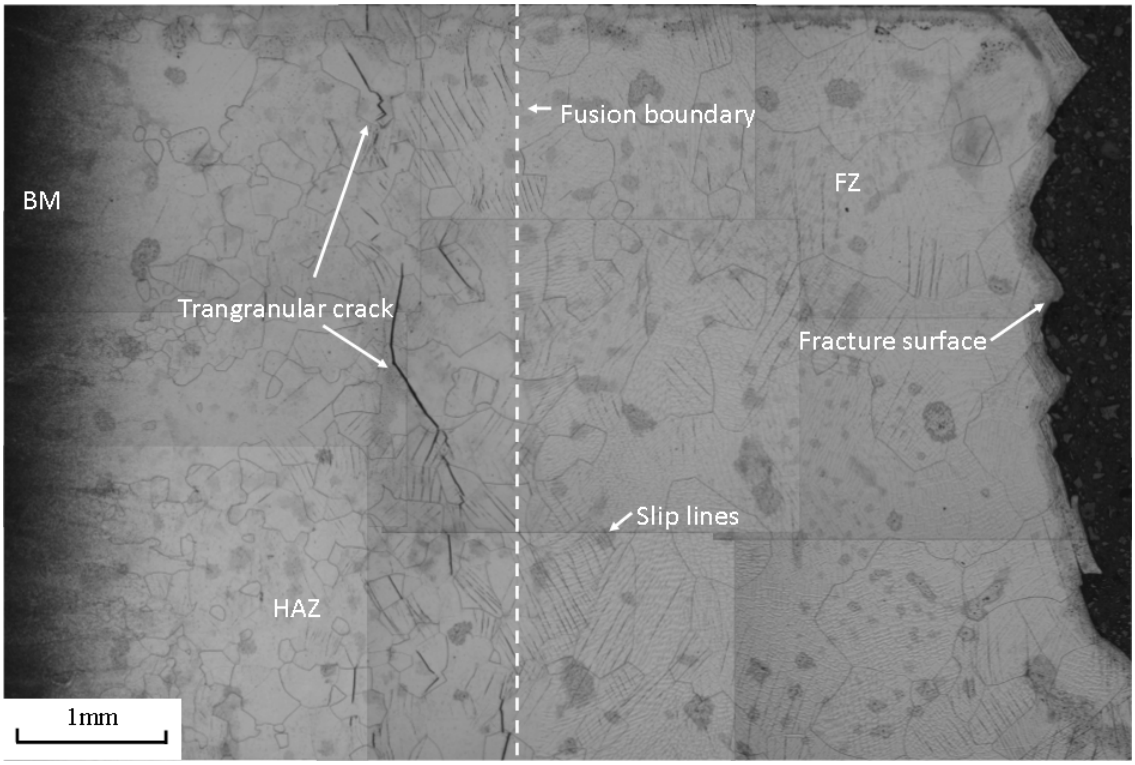

Figure 7.6. Top surface optical microscopy image of the fractured sample aged at 500℃ for 5mins

For the sample aged at 600℃ for 5min, the slip lines were much more difficult to observe, as shown in Figure 7.7. This is due to the etching effect on the α phase and also more importantly, fewer slip systems were in the HCP crystal structure than the BCC structure. As mentioned in the literature review, the titanium HCP structure only has 3 slip systems. Nevertheless, similar to the sample aged at 500℃ for 5min, large transgranular cracks were found in the HAZ approximately 500μm near the fusion boundary. The fracture surface showed a transgranular fracture mode where it took place in the FZ.

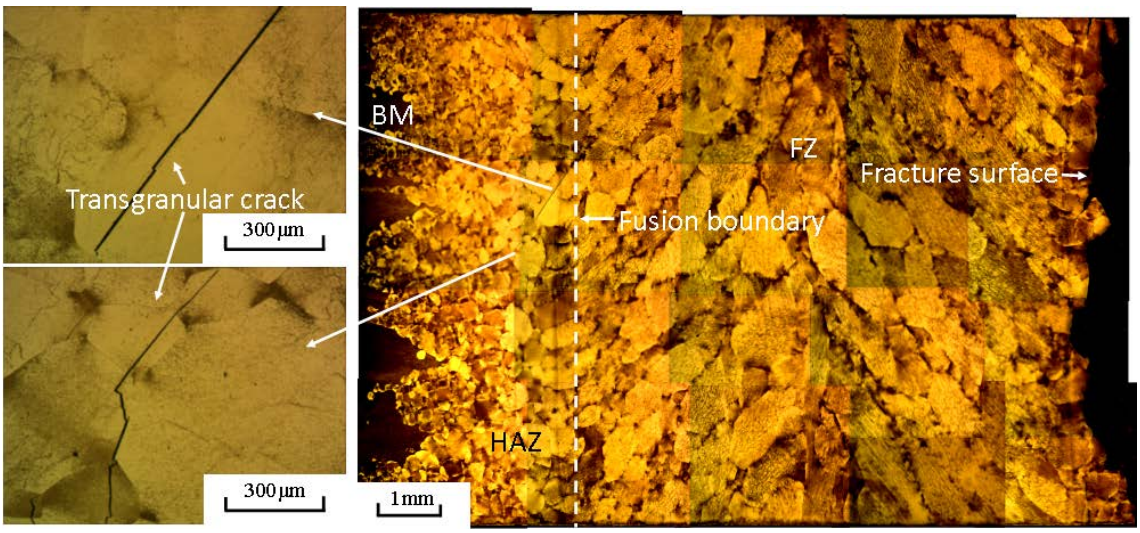

Figure 7.7. Top surface optical image of the fractured sample aged at 600℃ for 5mins

Figure 7.8 and 7.9 are the optical images of the fractured sample aged for 30mins at 500℃ and 600℃, respectively. As mentioned in previous chapters, α precipitates had covered the prior β phase on PWHT samples aged for 30mins for both ageing temperatures. The average size of the α precipitates was comparable, indicating that equilibrium in the state of precipitation had been reached. Hardness test and tensile test results also showed similarity of these ageing conditions. The transgranular cracks were found in the optical image of a fractured top surface. Those large and easily observed cracks were located in the HAZ near the fusion boundary within 500µm. Slip lines were hardly observed.

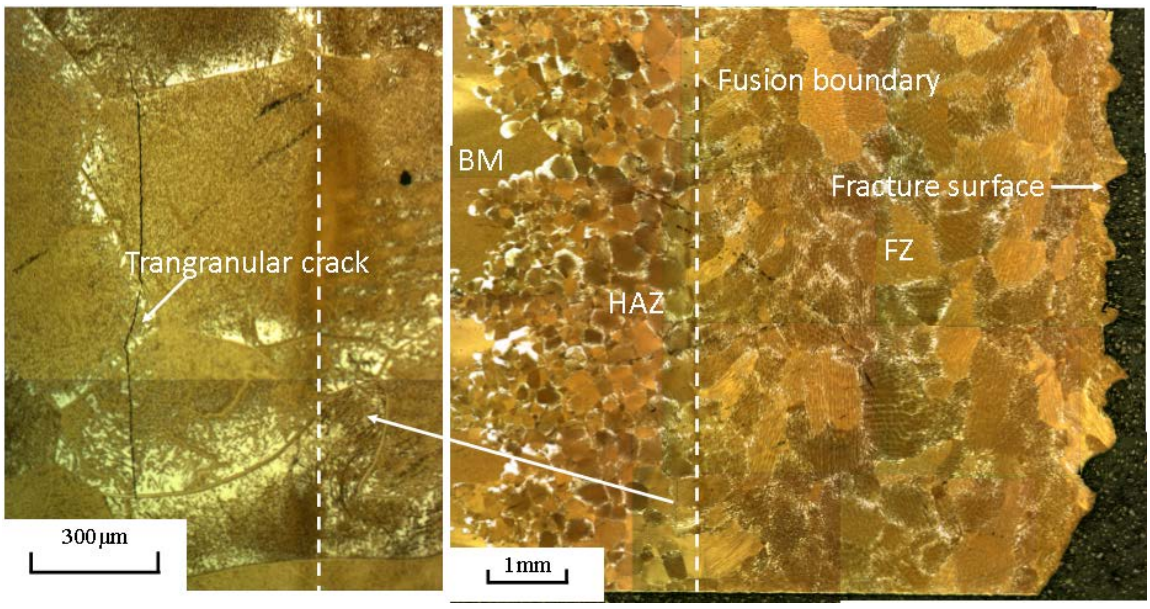

Figure 7.8. Top surface optical image of the fractured sample aged at 500℃ for 30mins

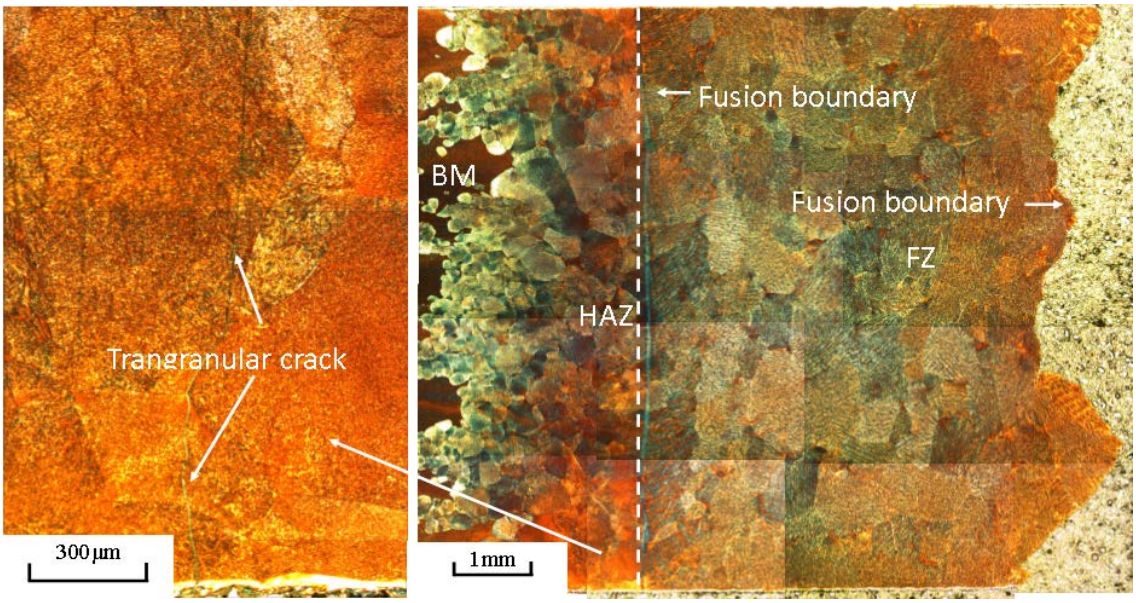

Figure 7.9. Top surface optical image of the fractured sample aged at 600℃ for 30mins

Figure 7.10 and 7.11 are the optical images of the fractured sample ageing for 8hrs at 500℃ and 600℃ respectively. The fracture surface showed a much flatter transgranular fracture feature which indicated a more brittle fracture.

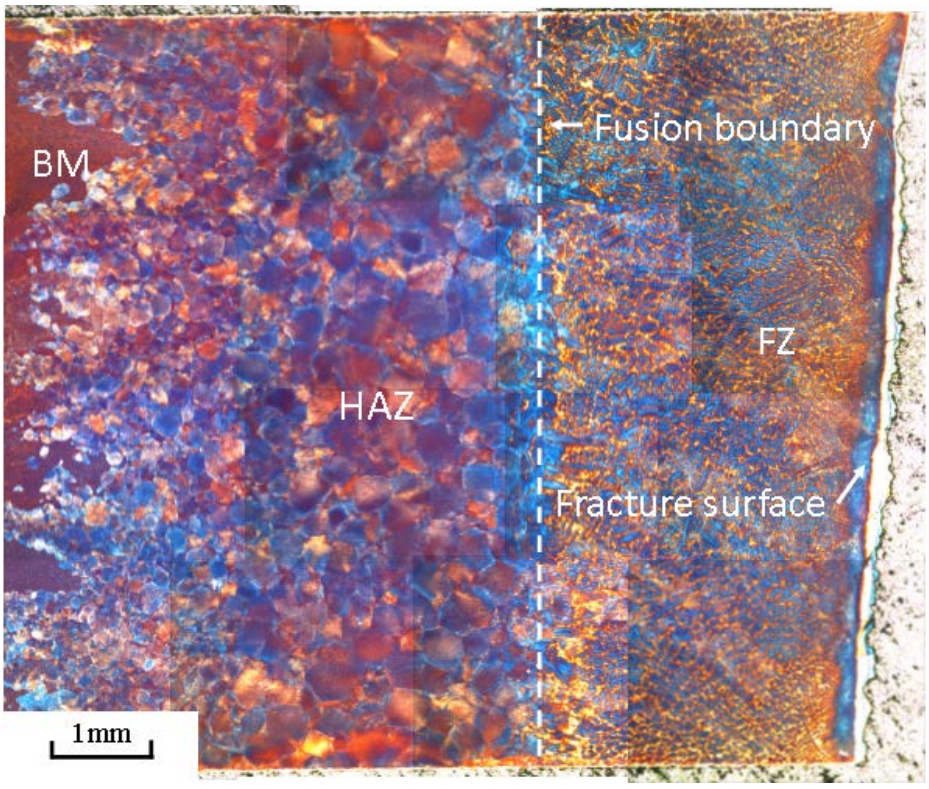

Figure 7.10. Top surface optical image of the fractured sample aged at 600℃ for 30mins

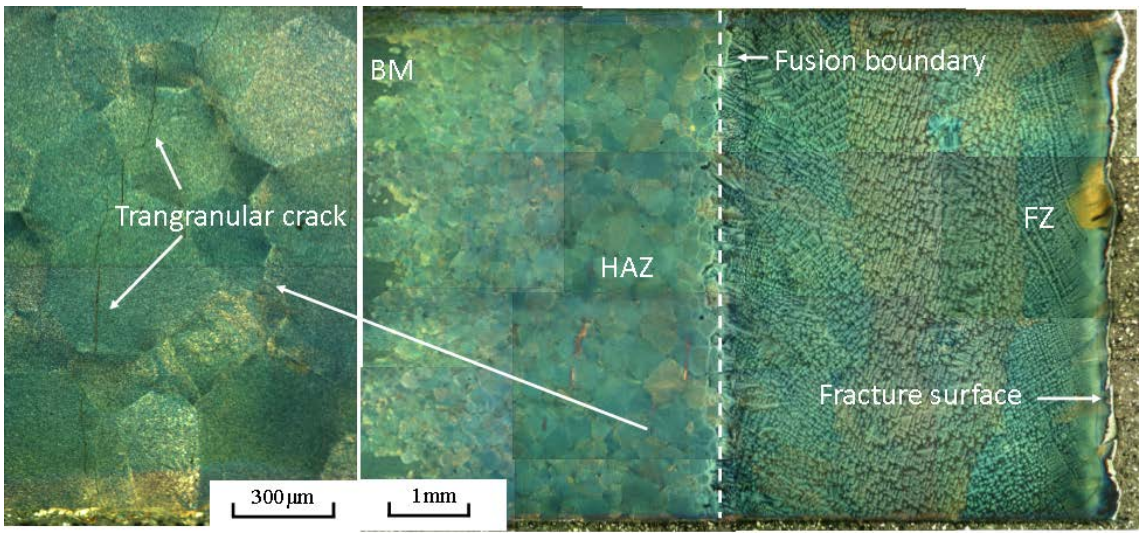

Figure 7.11. Top surface optical image of the fractured sample aged at 600℃ for 30mins

7.3 Fracture modes

As mentioned in the literature review, there are two basic paths that a fracture can take: transgranular and intergranular. The observation of the top fractured surface was dominated by a transgranular crack. The cross section of the fracture surface indicated the behaviour of a mixed mode of fracture. Regardless of the fracture path, there are four principle fracture modes: a dimple rupture, cleavage, fatigue, and decohesive rupture. On a macroscopic scale, the overall structure of the fracture surface of the tensile test specimen contained brittle planar facets which consisted of shallow dimples. Some of these facets were parallel to each other, yet others had different orientations and intersected each other. A typical example is demonstrated in Figure 7.12. The fractured sample was aged at 500℃ for 5mins. At high magnification, the surface of the facet plane contained clearly defined slip lines and shallow dimple structures. These large flat facet planes were separated by more ductile and larger size dimple rupture on the side of the planes. Nevertheless, the SEM observation of all fractured samples indicated a 100% dimple rupture via a microvoid coalescence. The complete SEM images of the fracture surface are presented in the appendix.

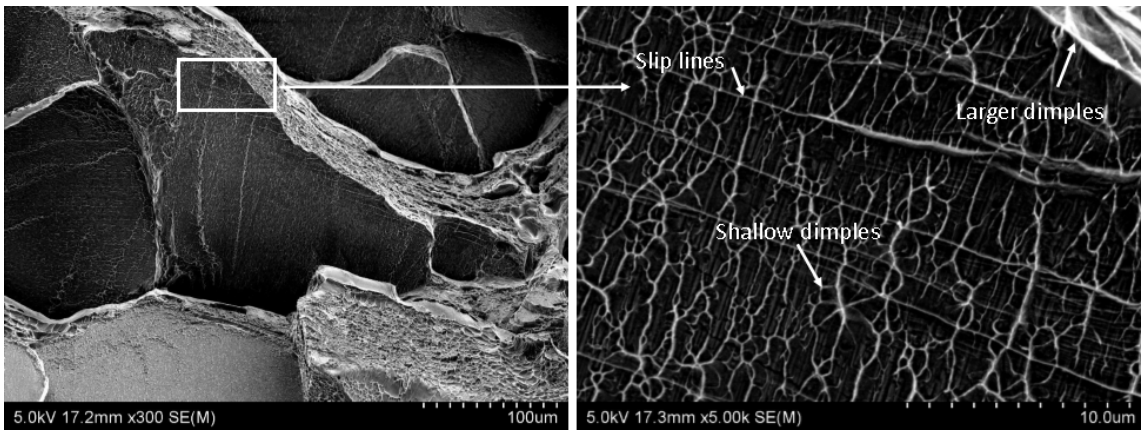

Figure 7.12. SEM images of the fracture surface for sample aged at 500℃ for 5mins. High magnification SEM image indicated slip lines

Figure 7.13 showed a typical equiaxed dimple rupture via microvoid coalescence. This image was taken near the edge of the fracture surface of the sample that was aged at 600℃ for 15mins. The size of the dimples was approximately between 1.5 to 8.5μm in diameter. Such features suggested a relatively ductile fracture and the tensile load was applied in a normal direction to the fracture surface.

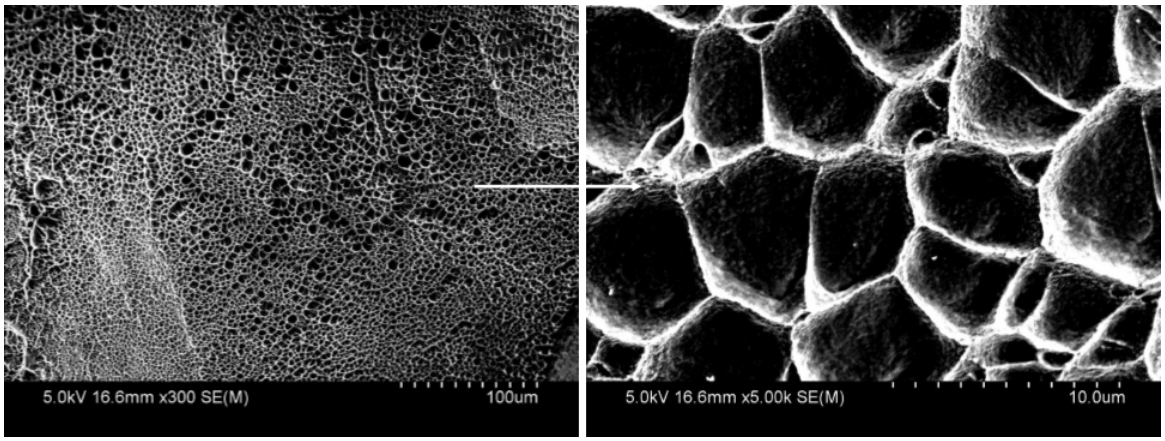

Figure 7.13. Fractured sample aged at 600℃ for 15mins, equiaxed dimples structure near the edge of fracture surface

On the same specimen (15mins at 600ºC), Figure 7.14 demonstrated a relatively flat surface containing an array of grooves and a side view of the columnar grain structure fracture. The two were indicated in the location of the overall fracture cross section (top image of Figure 7.14). The grain boundary was clearly observed in the middle of the flat fracture cross section. The fracture path cut through the columnar structure and failed via a transgranular crack. The surface of grooves appeared to be covered by a shallow dimple rupture.

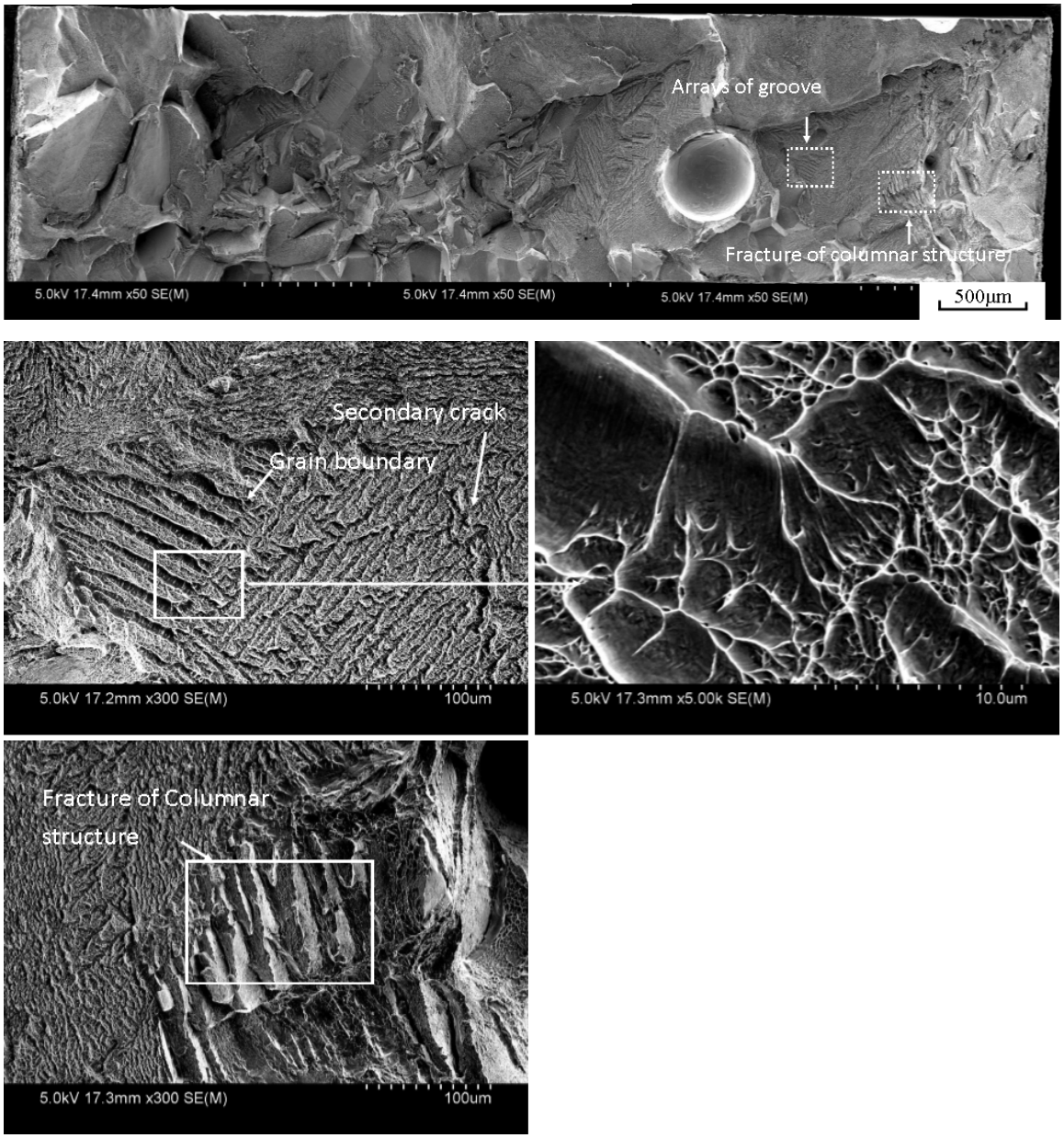

Figure 7.14. Evidence of fractured columnar structure. Sample was aged at 600℃ for 15mins

Although it was observed that the top surface of fractured samples showed only transgranular cracks, the cross section of the fracture surface contained both transgranular and intergranular cracks. As shown in Figure 7.15, such intergranular cracks often occurred on the boundaries of facet planes. The densely packed slip lines within the grain developed into transgranular cracks, while the boundary of this facet was separated by an intergranular crack path. For many of the facet planes, the fracture path initiated and propagated through the low resistance grain boundaries and eventually failed in the transgranular mode via overload (Lippold, 2015). Figure 7.16 is another example of a typical facet plane that was separated via a shallow dimple rupture.

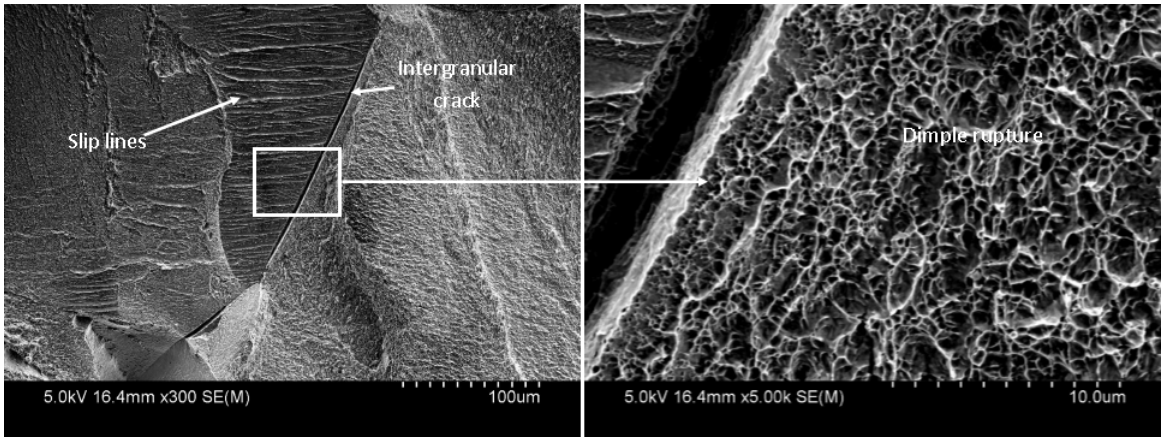

Figure 7.15. An intergranular crack along the grain boundary between the two facets. High magnification SEM image indicated a dimple rupture fracture feature. Fractured sample was aged at 600℃ for 30mins

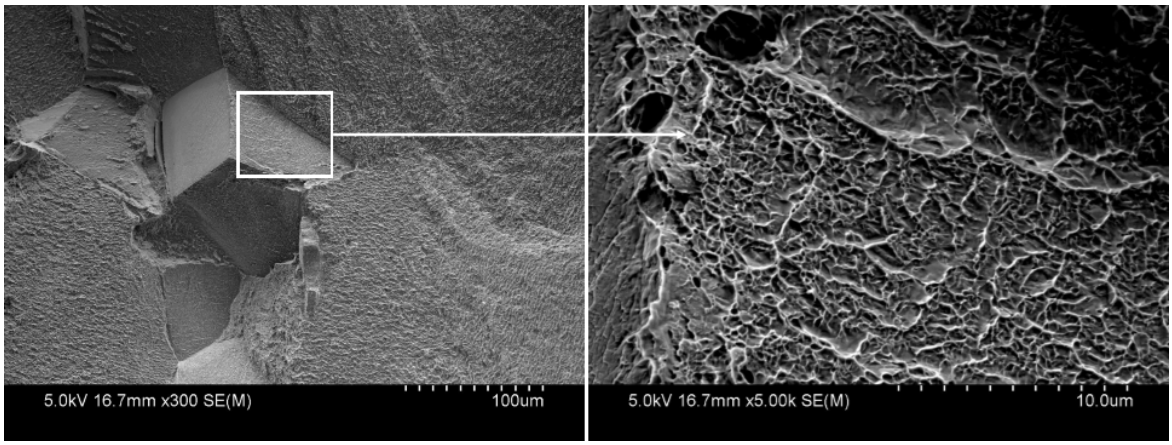

Figure 7.16. Example of a facet plane of sample aged at 600℃ for 2hrs. It demonstrated a typical example of facet plane with a flat surface. The high magnification SEM image showed shallow dimple structure

Figure 7.17 is an example of fracture surface with an acicular α lath. Such a feature is normally devoid of dimple structure and has a relatively flat surface.

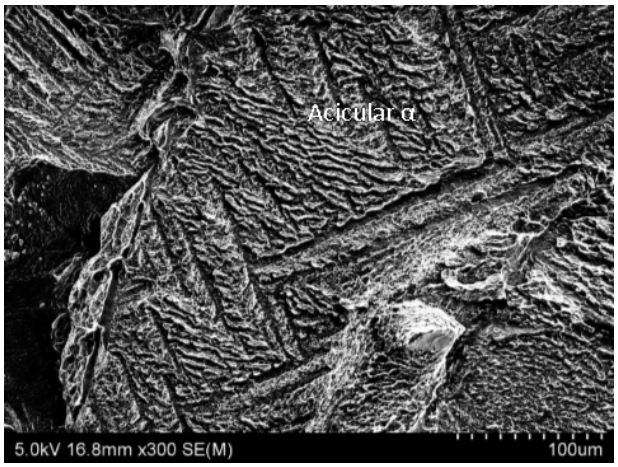

Figure 7.17. Acicular α lath on fractured surface of sample aged at 500℃ for 3hrs

7.4 Summary

For most of the tensile test pieces the fracture took place in the FZ. The top surface OM observation showed a large amount of transgranular cracks in the HAZ near the fusion boundary. Slip lines could easily be seen on the top surface of the AW and sample aged at 500℃ for 5min due to its BCC β phase. It is further evidence proving that α phase precipitation does not start at 500℃ for 5min. The OM fracture surface analysis showed that all the failure was transgranular. For 8hrs ageing time, the sample aged at both 500℃ and 600℃ had rather a flat fracture surface, which suggested a brittle failure.

The fractography results of the cross section of the fracture surface revealed a dimple rupture via microvoid coalescence. This was the major fracture mode for all tensile tested pieces. Equiaxed and elongated dimples were observed which means both tension and shear was involved (loading Mode I and II). The dimple size was difficult to measure due to different orientations. However, the large equiaxed dimple structure was more likely to be found near the surface. The centre of fracture was formed by many facets separated by shallow dimples. These facets sometimes intersected with each other, while some were parallel to each other. Although a transgranular crack path dominated the fracture surface, a small amount of intergranularity could be found in the centre of the fracture. Despite the elongation, results of the mechanical testing were fairly low; the fractography

examination showed the PWHT Ti5553 had reasonable ductility even for a low strain sample such as that aged at 600℃ for 8hr (Figure 7.18).

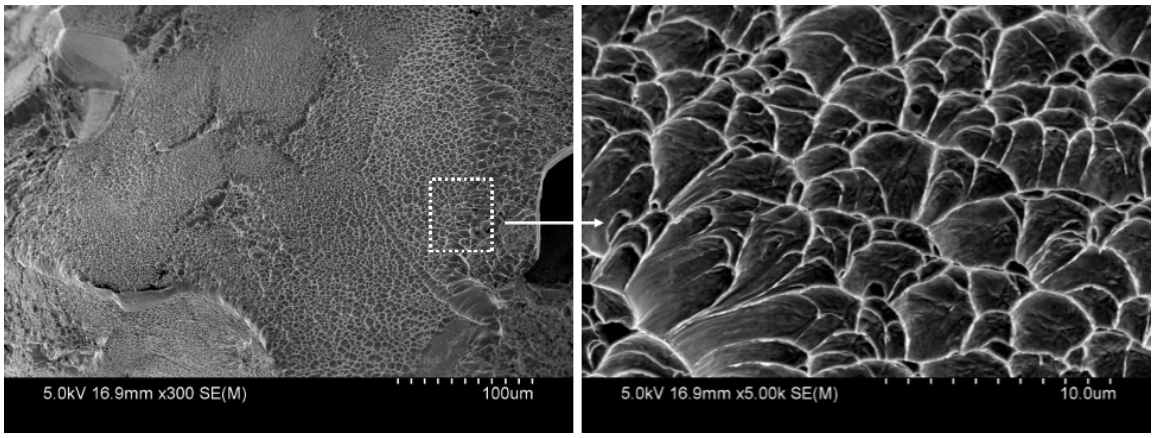

Figure 7.18. Dimple rupture on fracture surface of sample aged at 600℃ for 8hrs

Chapter 8. Dissimilar welding of Ti5553-Ti64 & Ti5553-CPTi

8.1 Introduction

In this chapter, the results from the as-welded dissimilar welding of Ti5553-Ti64 and Ti5553-CPTi are presented. The purpose of this experiment is to investigate the weldability of these new alloys, Ti5553, with the existing and very common titanium such as Ti64 (Ti6Al4V) and CP Ti (Commercially Pure Titanium). The workpieces were welded autogenously along longitudinal planes. Tensile tests and hardness tests were carried out for mechanical properties in comparison to Ti5553-Ti5553 similar welding. Energy dispersive spectroscopy (EDS) and electron probe micro-analysis (EPMA) were employed to investigate the material flow in the melt pool.

8.2 Microstructure of as-received Ti64 and CPTi

The microstructure of as-received Ti64 and CPTi are demonstrated as in the horizontal, longitudinal and transverse planes, as shown in Figure 8.1 and 8.2. The welding direction is the same as the horizontal direction. The OM images indicated both Ti64 and CPTi were in the as-rolled condition. High magnification images revealed equiaxed α grains with intergranular β microstructure.

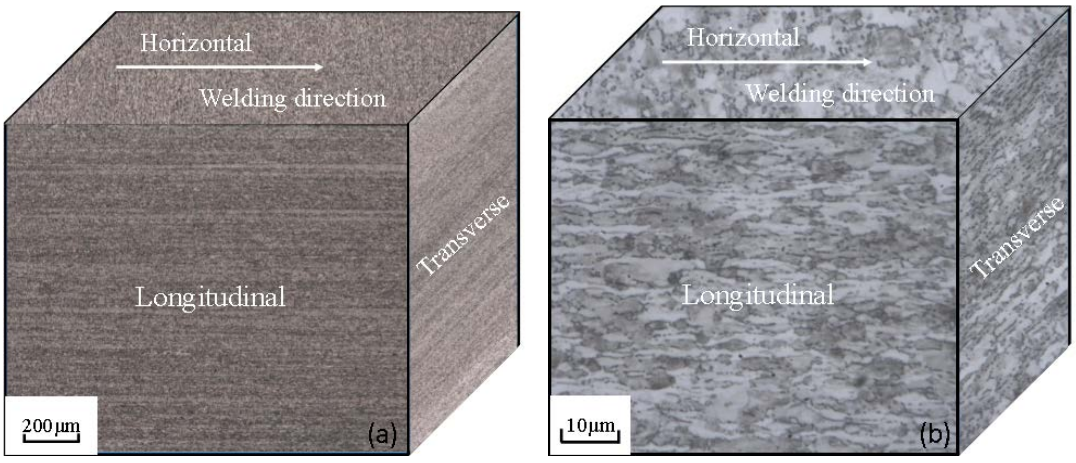

Figure 8.1. Microstructure of Ti64 in (a) 50x and (b) 1000x magnification of horizontal, longitudinal and transverse planes

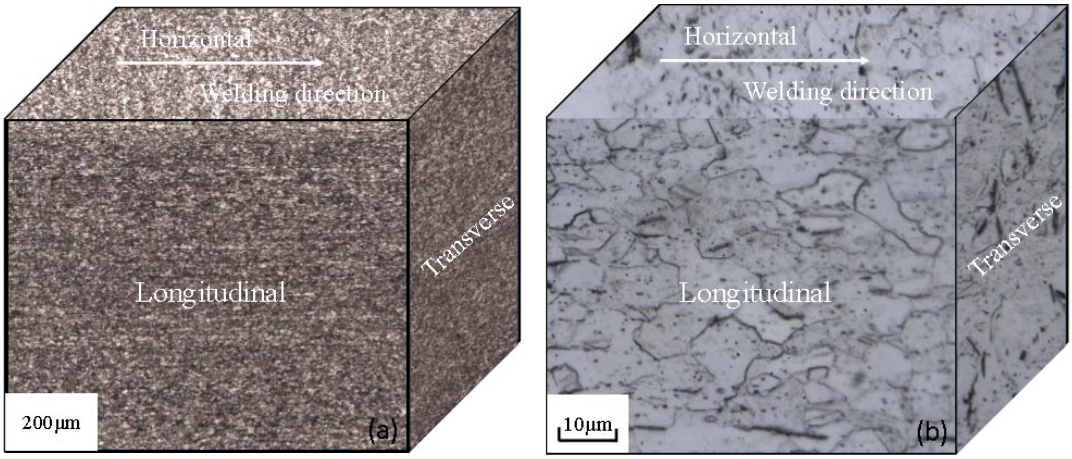

Figure 8.2. Microstructure of CPTi in (a) 50x and (b) 1000x magnification of horizontal, longitudinal and transverse planes

8.3 Metallurgy of as-welded dissimilar welding

In this section, a few microstructure observations in the as-welded (AW) condition are discussed. The workpieces are butt joint welded autogenously, which means the fusion zone is formed by the melting and re-solidification of the base metal, only without any filler metals. The welding methods employed were gas tungsten arc welding (GTAW) and laser beam welding (LBW). The welding parameters are shown in Table 8.1. EPMA results are also presented in this chapter for chemical composition analysis.

Welding method	**Power**	**Welding speed**	**Shielding gas**	**Gas flow**
GTAW	700W	3mm/s	Pure Argon	15LPM
LBW	2kW	15-20mm/s	Pure Argon	20LPM

Table 8.1. Welding parameters for GTAW and LBW

8.3.1 Microstructure of as-welded Ti5553-Ti64

Figure 8.3 and 8.4 show the overall microstructure of AW Ti5553-Ti64 carried out by GTAW and LBW respectively. As presented in these images, all weldments exhibited a relatively small equiaxed grain structure in the HAZ. The grain size was prone to grow larger towards the centre of the weld zone. Epitaxial grain growth was found at the fusion boundary in GTAW and LBW Ti5553-Ti64 specimens (Figure 8.5). For the LBW specimen, epitaxial growth extended from the grain boundary to the top of the weld crown, which is shown in Figure 8.5 (c). Extensive dendritic structure was scattered near the Ti5553 side in dissimilar welds. Epitaxial growth in the GTAW Ti5553-Ti64 weld zone was found to be favoured towards the Ti5553 base material (BM). Macrosegregation was found in the form of transverse solute banding in both GTAW and LBW etched weldment surfaces which appeared as curvilinear contours. Macrosegregation is related to changes in the solid-liquid interface velocity during solidification (Donachie, 2000; Liu, Baeslack III, Hurley, & Baeslack, 1994). In Ti5553-Ti64 weldments, the transverse solute banding affected the tendency for local martensitic transformation, i.e. $\beta \rightarrow \alpha^{"}$ transformation (Liu et al., 1994). Such macrosegregation can also be found in similar welding with filler material (Kou & Yang, 2007).

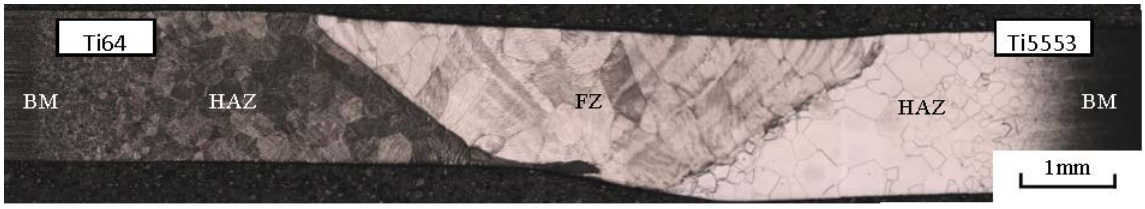

Figure 8.3. Microstructure of as-welded Ti5553-Ti64: GTAW

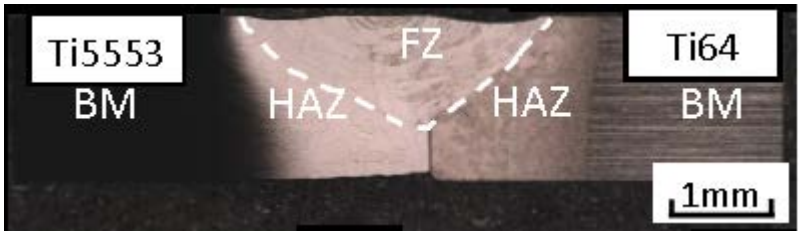

Figure 8.4. Microstructure of as-welded Ti5553-Ti64: LBW

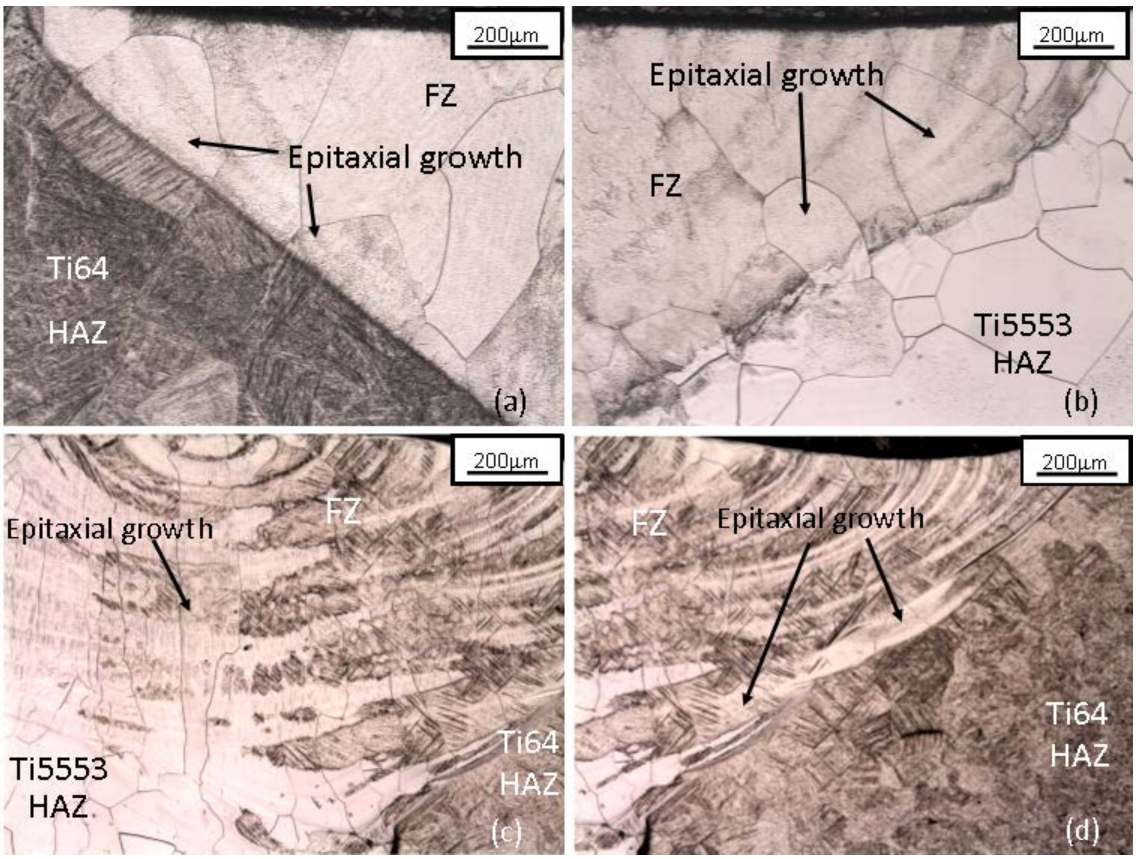

Figure 8.5. Microstructure near fusion boundary of as-welded Ti5553-Ti64 weldments: (a) GTAW near Ti64 HAZ, (b) GTAW near Ti5553 HAZ, (c) LBW mid of FZ, and (c) LBW near Ti64 HAZ

Energy Dispersive Spectrometry (EDS) (Figure 8.6) in the SEM was employed to understand the composition of the semi-elliptical bands inside the dissimilar weld pool. The result showed that in the selected location where the arrow indicated, there was a sudden drop of Mo (shown in yellow) in the scanned area. EPMA results (Figure 8.7) show chemical compositions across the as-welded HAZ and FZ for LBW Ti5553-Ti64. The declining line of Mo, Cr in the FZ revealed a poor mixing of Ti5553 and Ti64 base metal which resulted in uneven volumetric proportions.

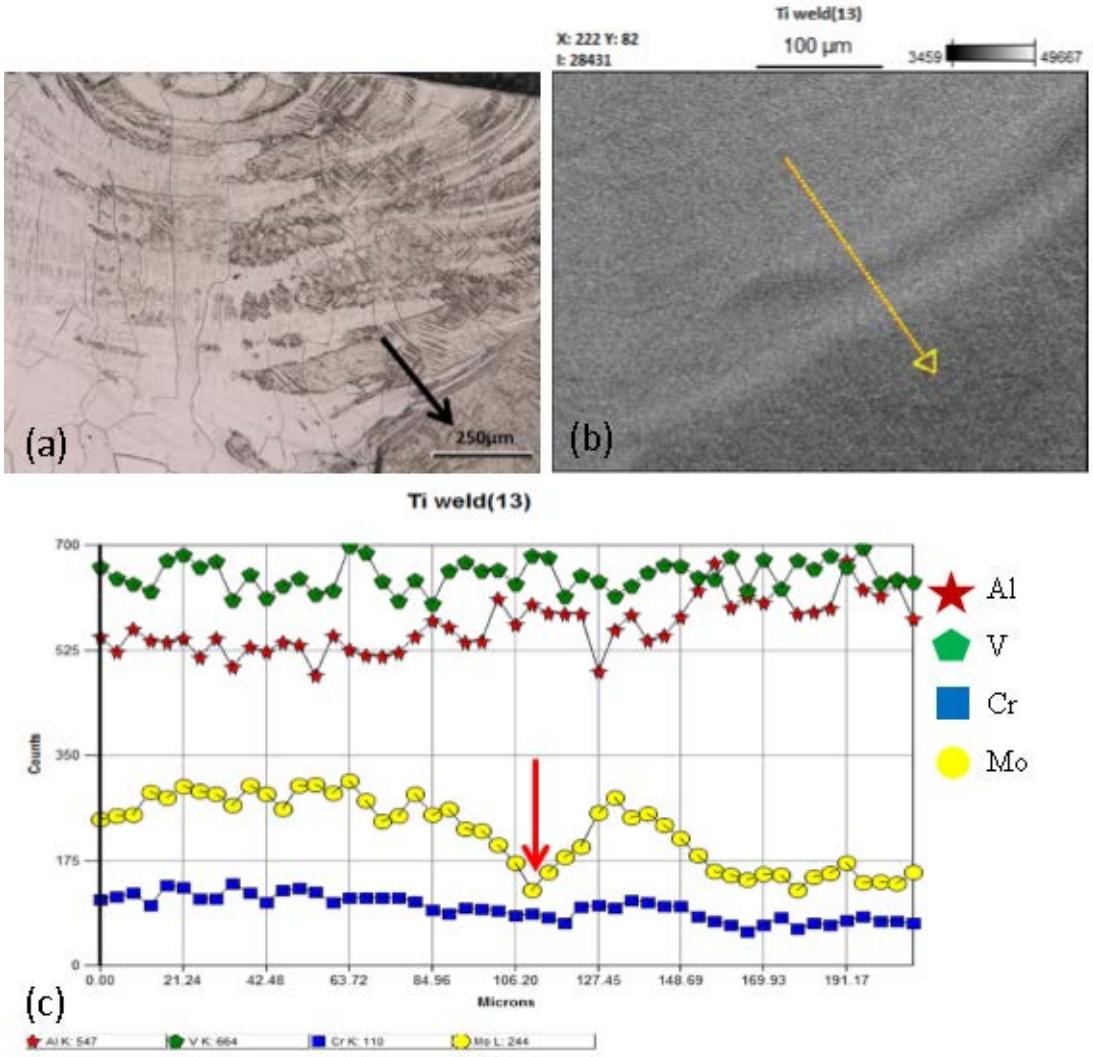

Figure 8.6. EDS results of Ti5553-Ti64 LBW specimen, arrows indicated the EDS scan location: (a) optical micrograph of FZ, (b) SEM image, (c) EDS line scan

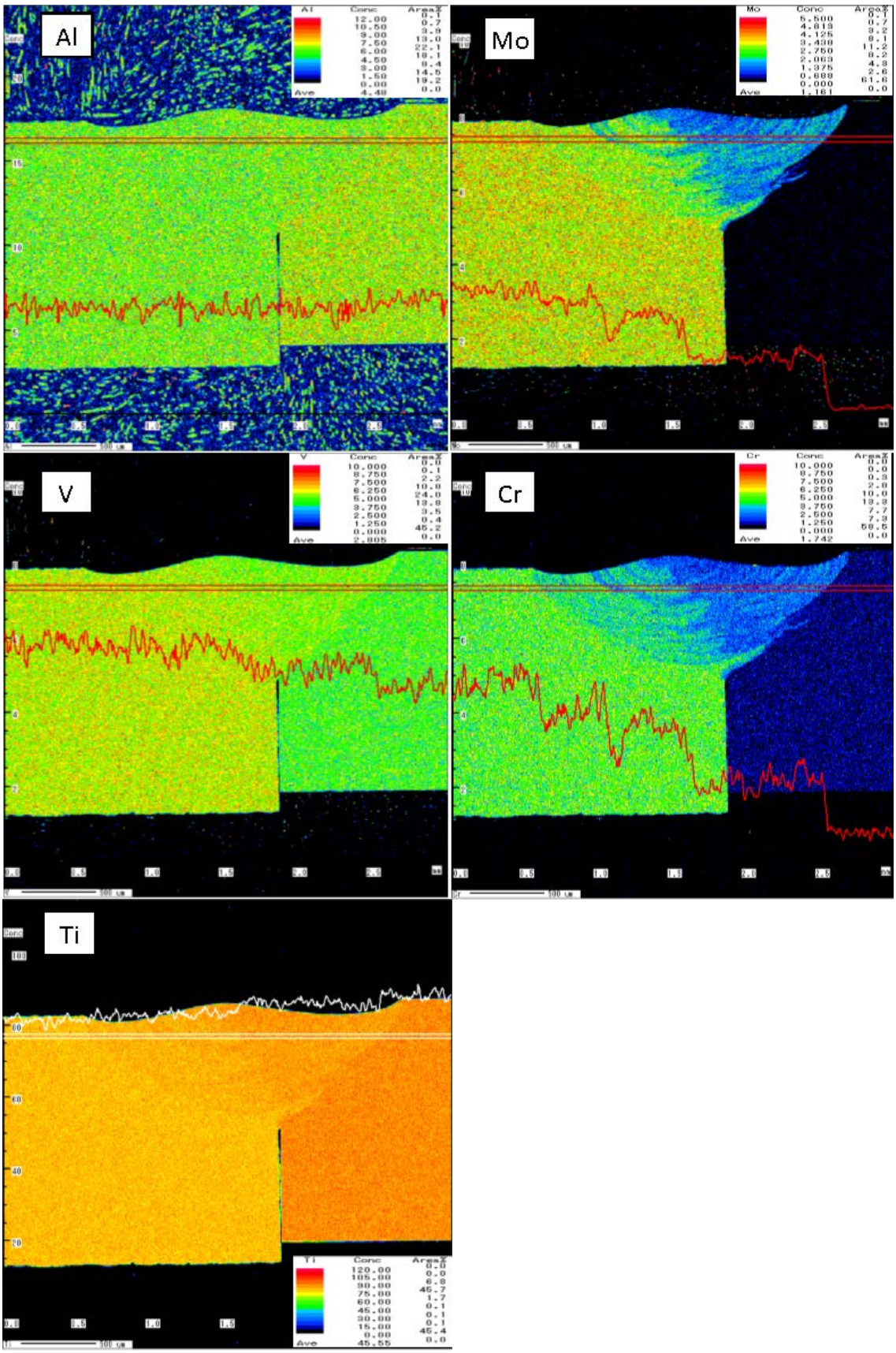

Figure 8.7. EPMA results of AW Ti5553-Ti64 across the HAZ and FZ

8.3.2 Microstructure of as-welded Ti5553-CPTi

Figure 8.8 and 8.9 show the overall microstructure of AW Ti5553-CPTi carried out by GTAW and LBW respectively. Epitaxial grain growth was only found near the fusion boundary towards Ti5553 BM as shown in Figure 8.10 (a). Transverse solute banding was found in both the GTAW and LBW etched weldment surfaces. The proportion of martensite was higher in the FZ which was near the CPTi fusion boundary. However, compared with the EPMA results of Ti5553-Ti64, as shown in Figure 8.11, the flat lines of Mo, V and Cr indicate an equal base metal mixture.

Figure 8.8. Microstructure of as-welded Ti5553-CPTi: GTAW

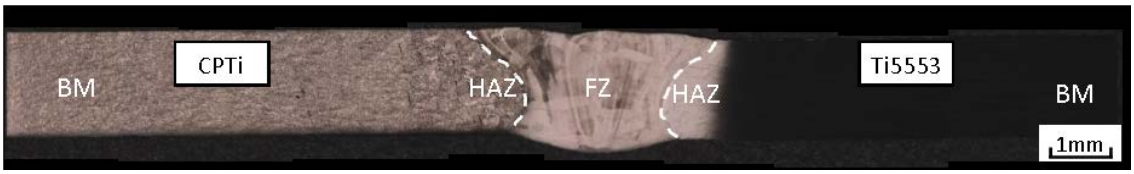

Figure 8.9. Microstructure of as-welded Ti5553-CPTi: LBW

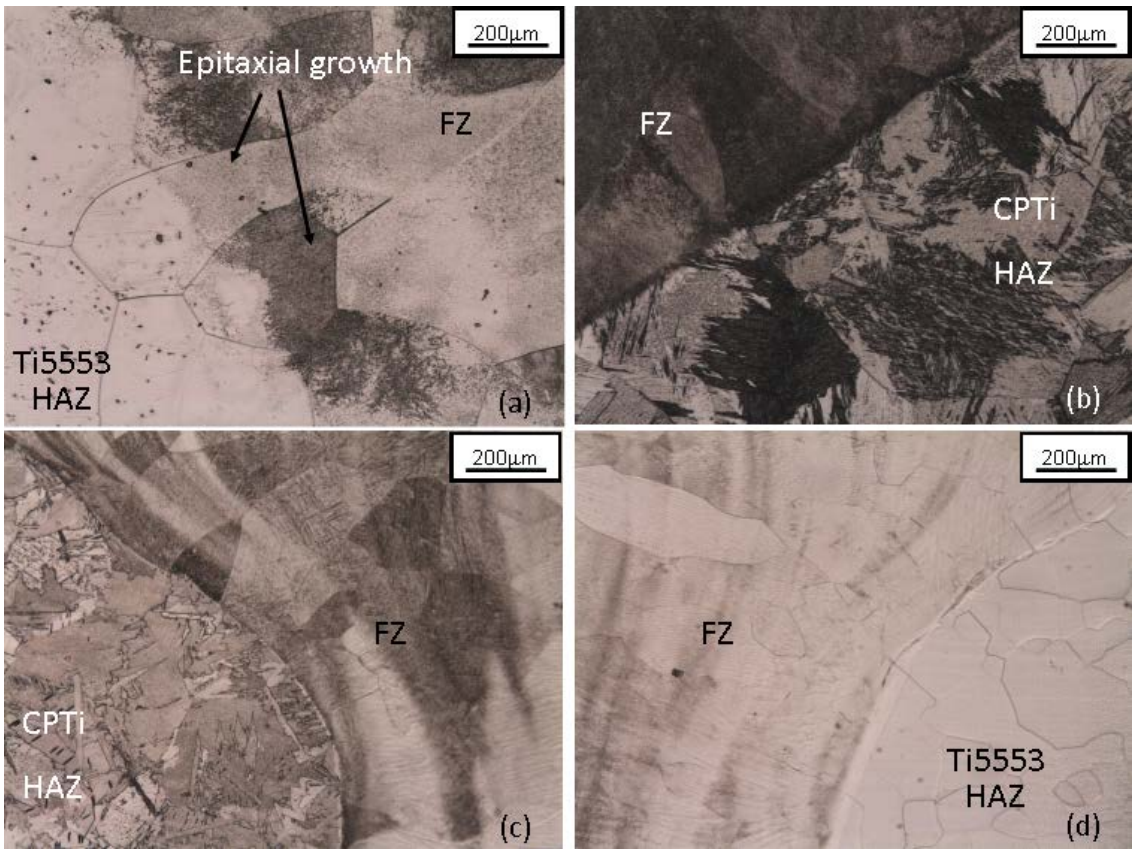

Figure 8.10. Microstructure near fusion boundary of as-welded Ti5553-CPTi weldment: (a) GTAW near Ti5553 HAZ, (b) GTAW near CPTi HAZ, (c) LBW near CPTi HAZ, and (d) LBW near Ti5553 HAZ

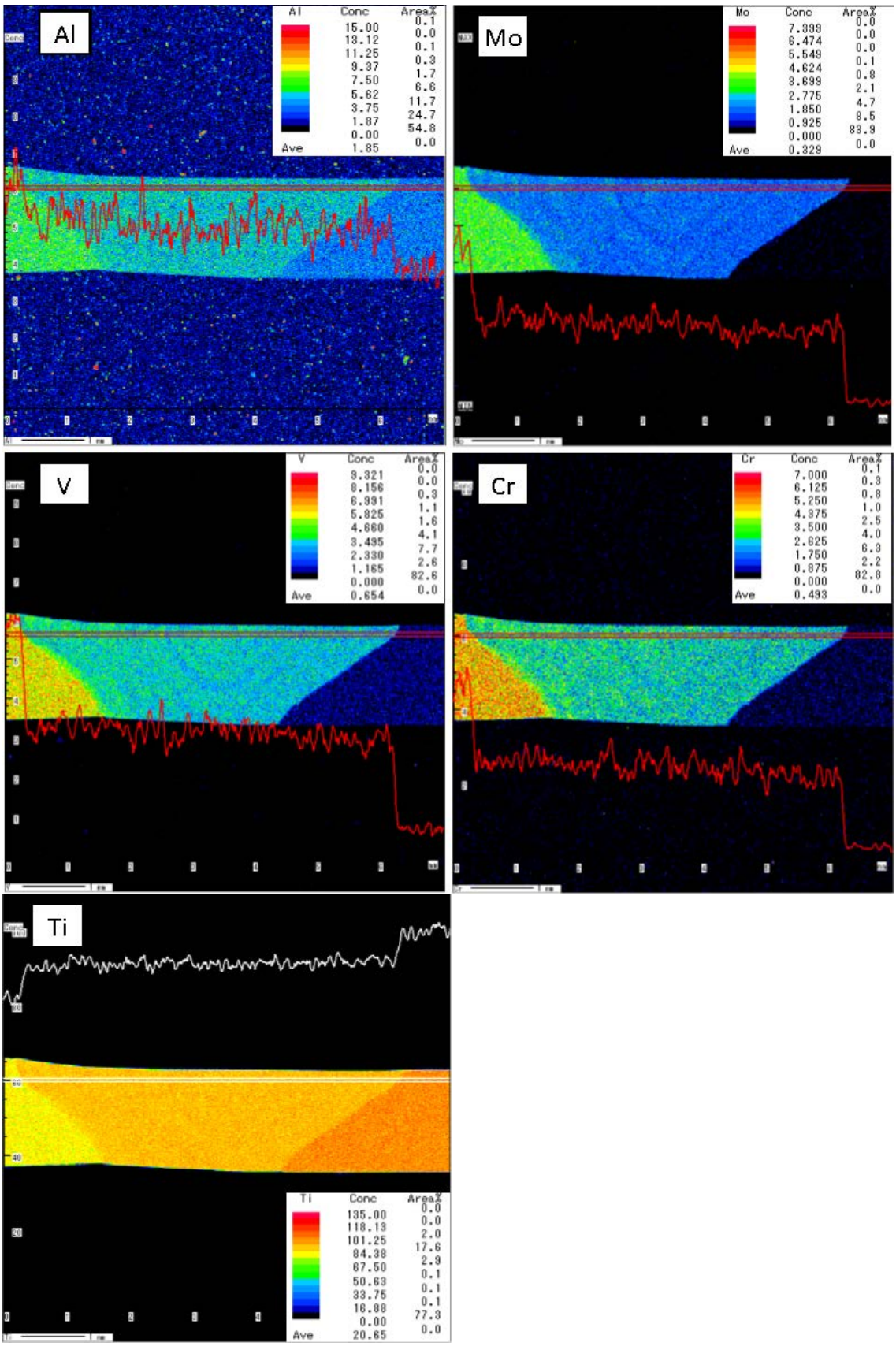

Figure 8.11. EPMA results of AW Ti5553-CPTi across the HAZ and FZ

8.4 Mechanical properties of as-welded Ti5553-Ti64 & Ti5553-CPTi

Figure 8.12 demonstrates the hardness profile of GTAW dissimilar welding: (a) Ti5553-Ti64, (b) Ti5553-CPTi. Both workpieces were examined in the AW condition. Hardness profiles indicated that the FZ had greater hardness than both the BM and HAZ specimens. The hardness profile of dissimilar joints indicated the existent of martensite in the FZ area. The martensitic structure was observed in optical microscopy images. Tensile test results for AW specimens are shown in Table 8.2. Compared with the Ti5553-Ti5553 AW specimen, Ti5553-Ti64 has higher tensile strength and "reasonable" ductility (dimple rupture). The fracture location for Ti5553-Ti64 was located in the FZ but near the Ti5553 boundary. The fracture location for Ti5553-CPTi occurred in the CPTi base metal and this specimen had the highest strain (~ 11%) but lower tensile strength than the Ti5553-Ti5553 similar weldment. It is worth noting that fracture locations took place at the Ti5553 (for Ti5553-Ti64 welds) and at the CPTi (for Ti5553-CPTi welds) due to their lower strength/hardness.

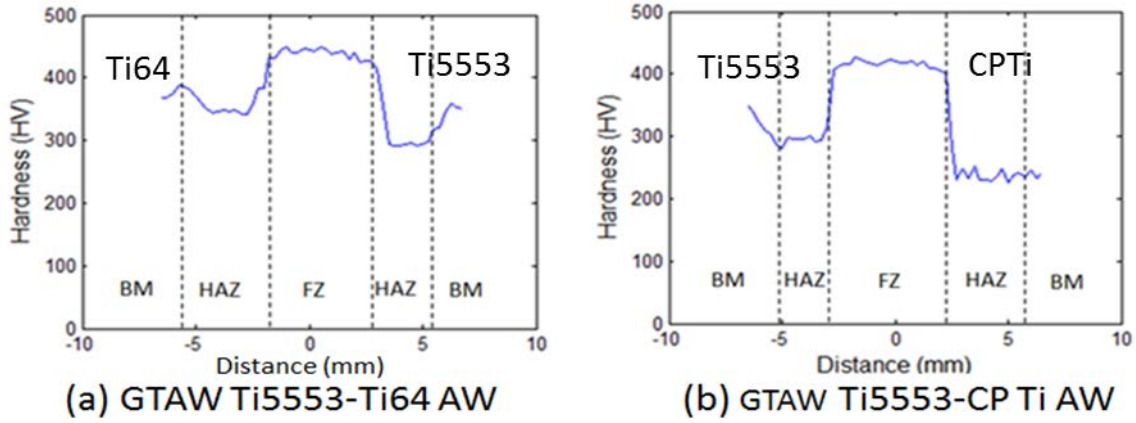

Figure 8.12. Hardness profile of GTAW dissimilar welding in the AW condition; (a) Ti5553-Ti64, (b) Ti5553-CPTi

Weld joint	Strain (%)	UTS (MPa)	Fracture location
GTAW Ti5553-Ti5553	7	720	FZ
GTAW Ti5553-Ti64	1	853	FZ near Ti5553 fusion boundary
GTAW Ti5553-CPTi	11	654	CPTi BM

Table 8.2. Tensile test results of AW GTAW Ti5553-Ti5553, Ti5553-Ti64 and Ti5553-CPTi

8.5 Fractography of AW Ti5553-Ti64, Ti5553-CPTi

The fracture location of AW Ti5553-Ti64 and Ti5553-CPTi are displayed in Figure 8.13. All fractures occurred at the low-strength area, such as the fusion boundary near Ti5553 for Ti5553-Ti64 as shown in Figure 8.13 (a), and BM of CPTi for Ti5553-CPTi as shown in Figure 8.13 (b). Low magnification SEM images are shown in Figure A3 in the Appendix.

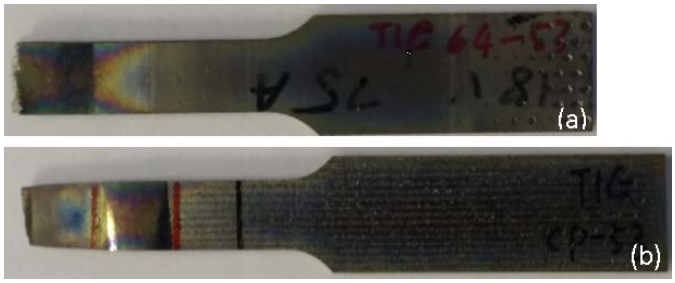

Figure 8.13. Broken pieces after tensile testing: (a) Ti5553-Ti64, fractured at the FZ near Ti5553 fusion boundary, and (b) Ti5553-CPTi, fractured in BM of CPTi

The fracture surface of Ti5553-Ti64 is shown in Figure 8.14. The overall structure of the fracture surface contained many brittle planar facets. The high magnification SEM image showed the facet surface was separated by shallow dimples. Also the boundaries of facet planes were surrounded by large dimple structures. Overall, since the fracture location was in the FZ and very close to the Ti5553 side fusion boundary, the fracture had similar features to AW Ti5553-Ti5553 (Figure A.3) and PWHT Ti5553 for 5mins (Figure 7.12).

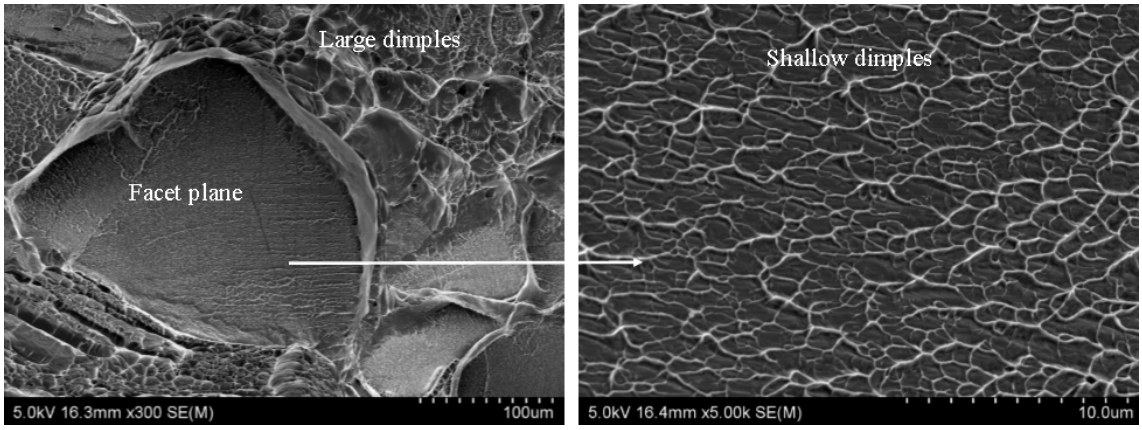

Figure 8.14. SEM images of fracture surface for AW Ti5553-Ti64

Figure 8.15 shows the fracture surface of Ti5553-CPTi. Since the fracture happened in the BM of CPTi, the fracture was ductile compared to other specimens. There was

obvious necking at the fracture edge as shown in Figure 8.13 (b). Unlike the fracturing in the FZ, the fracture surface did not have facet structures. However, the overall surface was formed by large dimples. Small transgranular cracks were found in the centre of the fracture, as shown in Figure 8.15 (c).

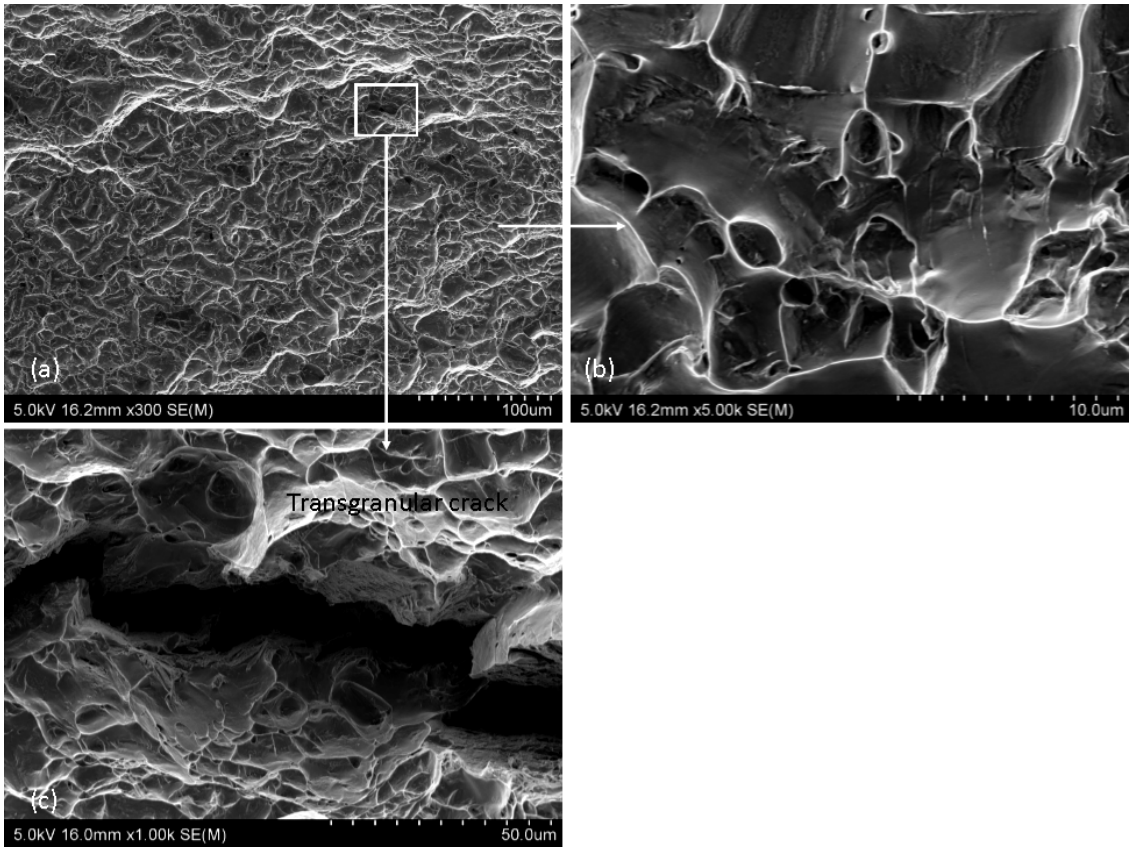

Figure 8.15. SEM images of fracture surface for AW Ti5553-CPTi. The fracture location was in the BM of CPTi

Chapter 9. Conclusions and future work

In this PhD study, the major work was carried out using microstructure observation and mechanical testing for Ti5553-Ti5553 similar weldments isothermally aged at 500℃ and 600 ℃. The relationship between microstructures and mechanical properties were analysed and a few conclusions have been made.

- Precipitation hardening happened within 5mins at a 600℃ ageing temperature which is much quicker than that aged at 500℃. Around 30mins of ageing time, the α platelets seemed to reach the equilibrium of precipitation and hence had the highest volume fraction (approximately 36%-37%). Optical microscopy (OM) and scanning optical microscopy (SEM) observations showed that at this ageing time, the weldment surfaces were covered by a secondary α phase. This was also proved by mechanical testing later on. An extended ageing time resulted in the α laths coarsening in terms of growing in length and width. The length of the α lath grew, seeming to slow down after 2hrs of ageing and stopped growing after 4hrs. The width of alpha laths continued to coarsen as the ageing time increased. At 600℃ ageing temperature, this coarsening was correspondingly faster and the size of the α laths bigger than samples aged at 500℃.
- TEM results in the FZ area of an AW specimen showed the diffraction patterns of the ω phase. This ω phase had retained athermal ω_a which was formed during cooling from the welding process. All this evidence proved that the ω phase in the weld zone improved the precipitation rate, that is, the ω phase provided nucleation sites for the α phase. However, the TEM investigation of specimens aged at 500℃ did not discover any ω particles. Thus a 500℃ temperature was too high for welded Ti5553 to form isothermal ω_s.
- Apart from studying the precipitation in the FZ and HAZ, some observations in the BM were made. The BM responded to heat treatment but was slower than in the FZ and HAZ. Micro-hardness in the BM for either 500℃ or 600℃ did not increase until 2hrs of ageing time.
- Hardness test results showed that for short ageing times (e.g. 5-15 minutes), samples aged at 600℃ responded to heat treatment faster than samples aged at 500℃ for the corresponding ageing time. However, after 30mins of ageing at 500℃, the hardness values in the weld zones were almost the same as the one aged at 600℃. As the ageing time extended, hardness in the weld zone of the sample

aged at 500℃ continued to increase and had higher hardness values than those aged at 600℃ for the same ageing time. Nevertheless, samples aged at 500℃ reached the maximum value after 4hrs. In relation to the microstructure observation, it can be concluded that the main factor affecting hardness was the volume fraction of the α platelets. A longer ageing time resulted in the α laths coarsening and caused a reduction in the volume fraction. In the weld zone, the average hardness of 600℃ aged samples reached the maximum value around 2hrs of ageing time. Then as the heat treatment continued, the average hardness value showed a slight drop. Thus, samples aged at 600℃ for a long ageing time with a larger α laths area, had a lower hardness value.

- Tensile results showed that for both temperatures 500℃ and 600℃, the average maximum tensile strength was those specimens that were aged for 30mins. Longer ageing times caused a slight drop in tensile strength for samples aged at 500℃, but no significant effects were observed on samples aged at 600℃. Comparing each tensile strength to the corresponding ageing time, samples aged at 600℃ had a higher value than the ones aged at 500 ℃. From the microstructure and morphology of the α phase point of view, it was revealed that for 30mins of ageing time, when the α phase reached its highest volume fraction, the tensile strength had the highest value. However, for samples aged 600℃, changes of the α phase size did not affect its tensile strength. The samples appeared however, to be more brittle with longer ageing times.
- For most of the PWHT tensile test pieces, the fracture took place in the FZ. Fracture observation showed 100% dimple rupture via microvoid coalescence in the fracture surface. Even for a longer ageing time with little elongation, such as samples aged for 8hrs, the high magnification SEM images showed a dimple-like structure which indicated reasonable ductility. Transgranular cracks were formed on the major crack path. Only a few intergranular cracks were found in the centre of the fracture cross section on the boundaries of the facet planes. Typically the facet planes were separated by shallow dimple ruptures.
- Preliminary findings from dissimilar welding experiments suggested that Ti5553 alloy is weldable to the most common titanium alloys, Ti6Al4V (Ti64) and the commercially pure titanium (CP Ti). Hardness profiles indicated that the fusion zone (FZ) had higher hardness than both the heat affected zone (HAZ) and the base metal (BM). Tensile results suggested that the dissimilar weld Ti5553-Ti64

had a higher strength than both Ti5553-Ti5553 and Ti5553-CPTi. This is due to the formation of martensite (α") in the FZ upon solidification, particularly on the Ti5553-Ti64 welds. All fractures occurred at the low-strength area, that is the fusion boundary near Ti5553 (for Ti5553-Ti64 welds), and the base metal of CP Ti (for Ti5553-CP Ti welds).

From these studies it is clear that further studies are needed including:

- More studies need to be done to ensure the ω phase is responsible for α nucleation. Due to the incapability of the TEM machine at high magnification, the ω particle in the AW FZ was unable to be seen in the DF image. Since there was no evidence to prove the existence of isothermal ω_s at 500℃, a lower ageing temperature such as 400℃ can be conducted for ω_s investigation.
- Electron backscatter diffraction (EBSD) can be used to analyse the crystal orientation and investigate the crack propagation. A few attempts were performed but it was unsuccessful due to the lack of dedicated facilities and time.
- A lot more research about PWHT of dissimilar welding Ti5553-Ti64 and Ti5553-CPTi needs to be done in the future where the mechanical properties need to be carried out.

References

Ahmed, M., Li, T., Casillas, G., Cairney, J. M., Wexler, D., & Pereloma, E. V. (2015). The evolution of microstructure and mechanical properties of Ti-5Al-5Mo-5V-2Cr-1Fe during ageing. *Journal of Alloys and Compounds*, *629*, 260–273. https://doi.org/10.1016/j.jallcom.2015.01.005

Ardell, A. J. (1985). Precipitation hardening. *Metallurgical and Materials Transactions A*, *16*(12), 2131-2165.

Baeslack, W. A., Liu, P. S., & Paskell, T. (1993). Weld solidification and HAZ liquation in a metastable-beta titanium alloy-Beta-21S. *Materials Characterization*, *30*(2), 147–154. https://doi.org/10.1016/1044-5803(93)90018-Q

Baeslack III, W. A., Liu, P., Barbis, D., Schley, J., & Wood, J. (1993). Postweld heat treatment of CTA welds in a high-strength metastable-beta titanium alloy-Beta-CTM. *The Minerals, Metals & Materials Scociety*, 1469–1476.

Bania, P. J. (1994). Beta titanium alloys and their role in the titanium industry. *JoM*. https://doi.org/10.1007/BF03220742

Bhattacharjee, A., Ghosal, P., Nandy, T., Kamat, S., Gogia, A., & Bhargava, S. (2008). Effect of grain size on the tensile behaviour and fracture toughness of Ti-10V-4.5Fe-3Al beta titanium alloy. *Trans.Indian Inst.Met.*, *61*, 399–405.

Branch, P. M., & Section, M. S. (1995). Sympathetic nucleation : An overview. *5107*(95).

Callister, W. (2007). *Materials science and engineering: An introduction* (7th ed.). New York, NY: John Wiley & Sons.

Callister, W., & Rethwisch, D. (2013). *Fundamentals of materials science and engineering.* (Vol. 21). New York, NY: John Wiley & Sons.

Caron, R., & Staley, J. (1997). Effects of composition, processing, and structure on properties of nonferrous alloys. *Materials Selection and Design*, *20*, 383–415.

Chandler, H. (1996). *Heat treater's guide: Practices and procedures for nonferrous alloys*. ASM International.

Chen, Y., Du, Z., Xiao, S., Xu, L., & Tian, J. (2014). Effect of aging heat treatment on microstructure and tensile properties of a new β high strength titanium alloy. *Journal of Alloys and Compounds*, *586: 588-5*.

Clement, N., Lenain, A., & Jacques, P. (2007). Mechanical property optimization via microstructural control of new metastable beta titanium alloys. *JoM*, 50–53.

Corbacho, J., Suarez, J., & Molleda, F. (1998). Grain coarsening and boundary migration during welding of Invar Fe-36Ni alloy. *Material Characterization*, *41*, 27–34.

Cotton, J. D., Boyer, R. R., Briggs, R. D., Baggerly, R. G., Meyer, C. A., Matt, D., Yao, X. (2016). Phase transformations in Ti-5Al-5Mo-5V-3Cr-, (June 2007), 0–4.

Davis, J. R. (2012). *Alloying: Understanding the basics*. ASM International.

Donachie, M. J. (2000). *Titanium: A technical guide*. ASM International.

Du Z., Xiao, S., Xu, L., Tian, J., Kong, F., & Chen.Y. (2014). Effect of heat treatment on microstructure and mechanical properties of new β high strength titanium alloy. *Materials and Design*, *55*, 183–190.

Duerig, T. W., & Williams, J. C. (1984). Overview: Microstructure and properties of beta titanium alloys. *Beta Titanium Alloys in the 1980's, TMS*.

Fanning, J. C. (2005). Properties of TIMETAL 555 (Ti-5Al-5Mo-5V-3Cr-0.6Fe). *Journal of Materials Engineering and Performance*, 14:788-791.

Froes, F. (2015). *Titanium-Physical Metallurgy, Processing and Applications*. ASM International.

Giosa, R. P. (2009). *The effect of heat treatment on the microstructure evolution and mechanical properties of Ti5-Al-5V-5Mo-3Cr, and its potential application in landing gears*. McMaster University.

Grote, K., & Antonsson, E. (2009). *Springer handbook of mechanical engineering. Volume 10*. Springer Science & Business Media.

Handbook, M. (1987). *Vol.12: Fractography*. *ASM Metals Handbook*. Ohio, OH: ASM International Metals Park.

Harmon, E., & Troiano, A. (1961). Beta transformation characteristics of titanium alloyed with vanadium and aluminum. *Trans.ASM*, *53*, 43–53.

Harper, M. (2004). *A study of the microstructural and phase evolution in TIMETAL 555*. Ohio, OH: Ohio State University.

Hickman, B. S. (1969). The formation of omega phase in titanium and zirconium alloys: A review. *Journal of Materials Science*, *4*(6), 554–563. https://doi.org/10.1007/BF00550217

Kou, S. (2003). *Welding metallurgy* (2nd ed.). New York, NY: John Wiley & Sons.

Kou, S., & Yang, Y. (2007). Fusion-boundary macrosegregation in dissimilar-filler welds. *Welding Journal*. *86*(10), 303.

Kuroda, T., Matsuda, F., & Iwagi, I. (2017). Effects of two-step ageing and thermomechanical treatments on age-hardening properties of welded β titanium alloy effects of two-step ageing and thermomechanical treatments on age-hardening properties of welded β titanium alloy, *7116*(April). https://doi.org/10.1080/09507119409548536

Leibovitch, C., & Rabinkin, A. (1980). Metastable diffusionless equilibria in Ti-Mo and Ti-V systems under high pressure conditions. *Calphad*, *4*(1), 13–26.

Leyens, C., & Peters, M. (2003). *Titanium an titanium alloys*. *Titanium and Titanium Alloys*. https://doi.org/10.1002/3527602119

Lippold, J. (2015). *Welding metallurgy and weldability*. New York, NY: John Wiley & Sons.

Liu, P. S., Baeslack III, W. A., Hurley, J., & Baeslack, W. A. (1994). Dissimilar alloy laser beam welding of titanium: Ti-6AI-4V to Beta-C^{TM} The results from welding the dissimilar alloys with a C0 2 laser indicate it to be an attractive alternative to GTA welding. *Welding Journal*, 175–181.

Lütjering, G., & Williams, J. C. (2007). *Titanium* (2nd ed.). Berlin, Germany: Springer-Verlag.

Lampman, S. (1997). Weld integrity and performance. *ASM International*.

Menon, E. S. K., & Aaronson, H I. (1987). Overview no. 57 Morphology, crystallography and kinetics of sympathetic nucleation. *Acta Metall.*, *35*(3), 549–563.

Messler, R. W. (2004). *Principles of welding processes: Physics, chemistry and metallurgy*. New York, NY: John Wiley and Sons.

Mitchell, R., Short, A., Pasang, T., & Littlefair, G. (2011). Characteristics of electron beam welded Ti & Ti Alloys. *Advanced Materials Research*, *275*, 81–84. https://doi.org/10.4028/www.scientific.net/AMR.275.81

Nag, S. (2008). *Iinfluence of beta instabilities on the early stages of nucleation and growth of alpha in beta titanium alloys*. Ohio, OH: Ohio State University.

Nag, S., Banerjee, R., Srinivasan, R., Hwang, J. Y., Harper, M., & Fraser, H. L. (2009). ω-Assisted nucleation and growth of α precipitates in the Ti–5Al–5Mo–5V–3Cr–0.5Fe b titanium alloy. *Acta Materialia*, *57*(7), 2136–2147. https://doi.org/10.1016/j.actamat.2009.01.007

Nyakana, S., Fanning, J., & Boyer, R. (2005). Quick reference guide for β titanium alloys in the 00s. *JMEPEG 14*, 799–811.

Ohmori, Y., Ogo, T., Nakai, K., & Kobayashi, S. (2001). Effects of ω-phase precipitation on β → α, α″ transformations in a metastable β titanium alloy. *Materials Science and Engineering A*, *312*(1–2), 182–188. https://doi.org/10.1016/S0921-5093(00)01891-8

Sabol, J. C., Pasang, T., Misiolek, W. Z., & Williams, J. C. (2012). Localized tensile strain distribution and metallurgy of electron beam welded Ti-5Al-5V-5Mo-3Cr titanium alloys. *Journal of Materials Processing Technology*, *212*(11), 2380–2385. https://doi.org/10.1016/j.jmatprotec.2012.06.023

Shariff, T, Cao, X, Chromik, R, Wanjara, P, Cuddy, J. & Birur, A. (2012). Effect of joint gap on the quality of laser beam welded near-β Ti-5553 alloy with the addition of Ti-6Al-4V filler wire. *J. Mater Sci.*, 47:866-875.

Sukedai, E., Yoshimitsu, D., Matsumoto, H., Hashimoto, H., & Kiritani, M. (2003). β to ω phase transformation due to aging in a Ti-Mo alloy deformed in impact compression. *Materials Science and Engineering A*, *350*(1–2), 133–138. https://doi.org/10.1016/S0921-5093(02)00714-1

Sun, Z., Rao, Q., & Chen, F. (2013). An analysis of distinction between loading mode and fracture mode. In *In ICF11, Italy 2005*.

Vander Voort, G. (1999). Metallographic preparation of titanium and its alloys. Retrieved

from https://vacaero.com/information-resources/metallography-with-george-vander-voort/1397-metallographic-preparation-of-titanium-and-its-alloys.html

Wagner, V., Baili, M., Dessein, G., & Lallement, D. (2010). Experimental characterization of behavior laws for titanium alloys: Application to Ti5553. *Key Engineering Materials*, *446*, 147–155. https://doi.org/10.4028/www.scientific.net/KEM.446.147

APPENDIX A – Cross section SEM images of PWHT Ti5553 fracture surface

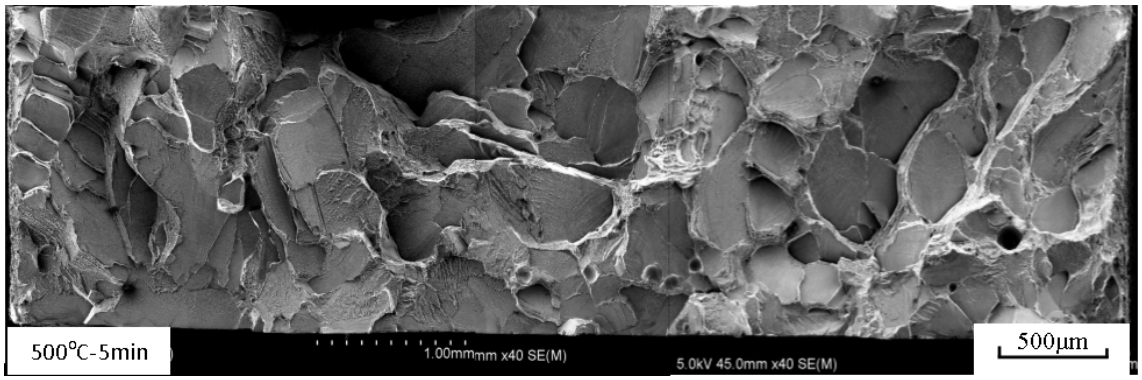

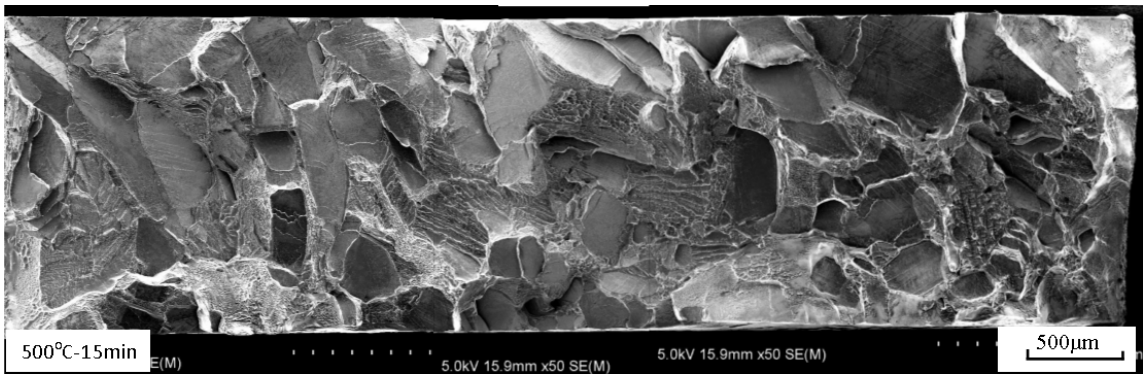

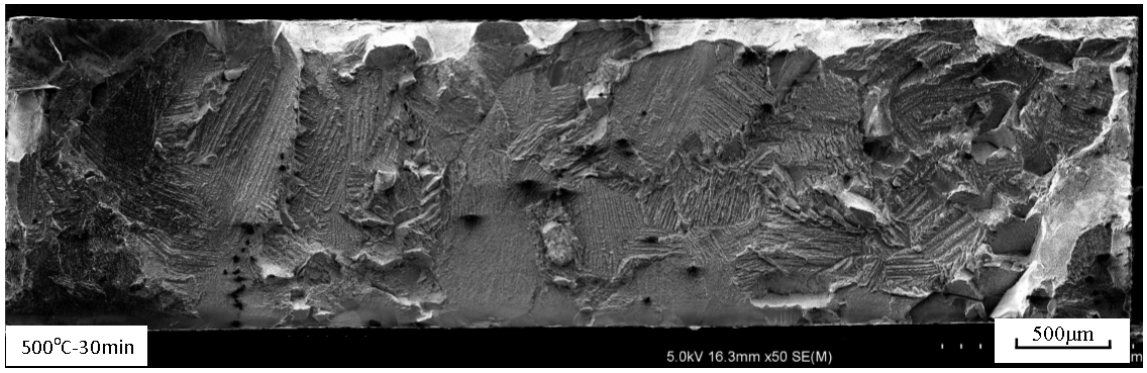

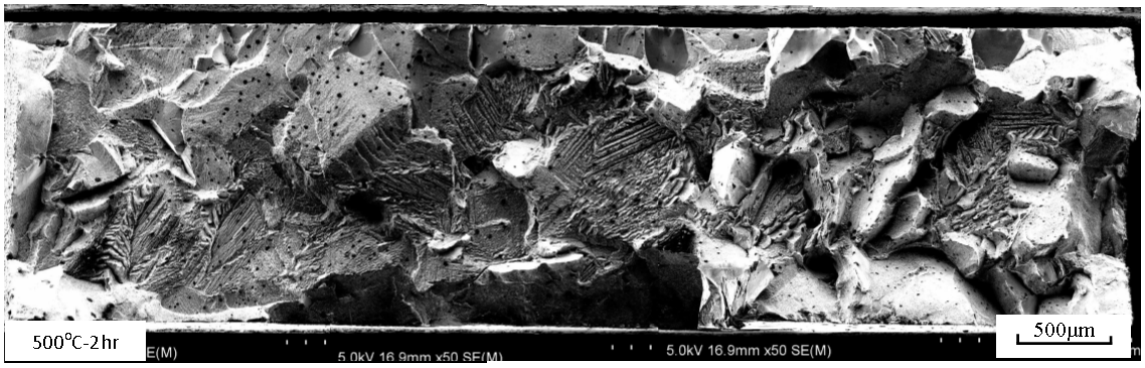

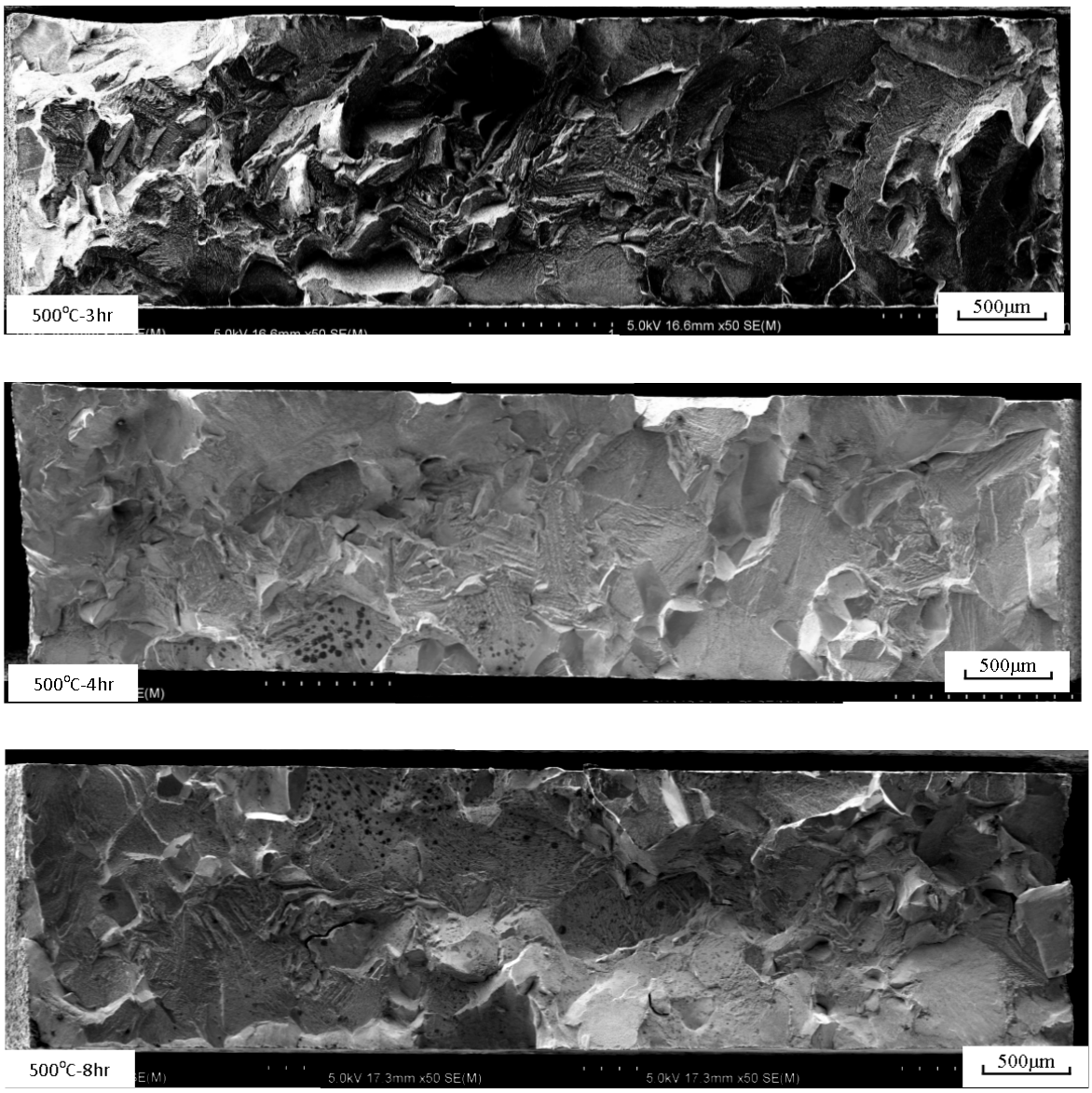

Figure A.1. SEM images of fracture surface for samples aged at 500℃

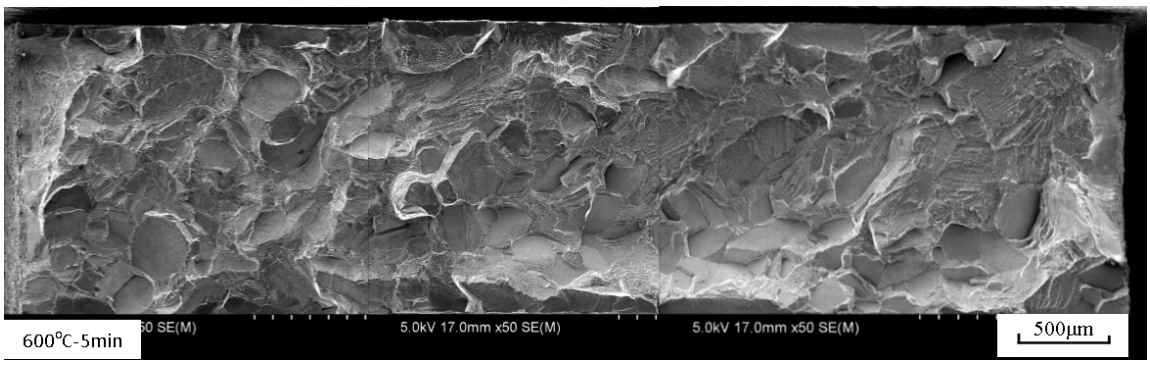
600°C-5min
5.0kV 17.0mm x50 SE(M)
5.0kV 17.0mm x50 SE(M)
500µm

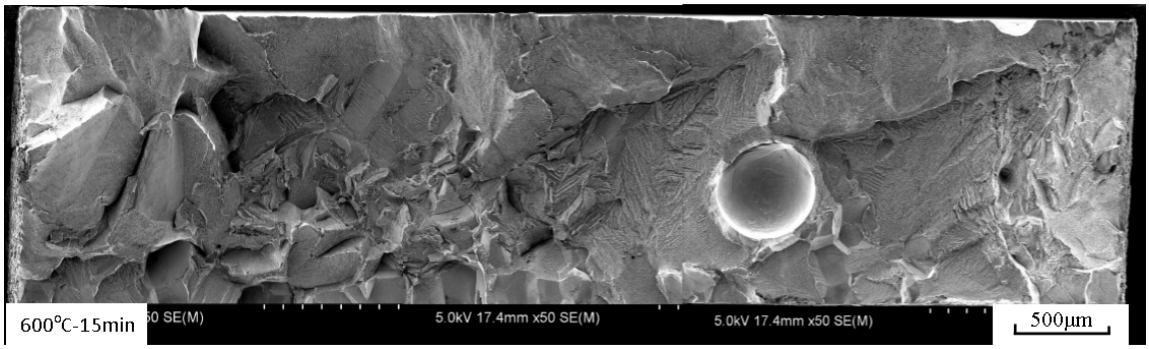
600°C-15min
5.0kV 17.4mm x50 SE(M)
5.0kV 17.4mm x50 SE(M)
500µm

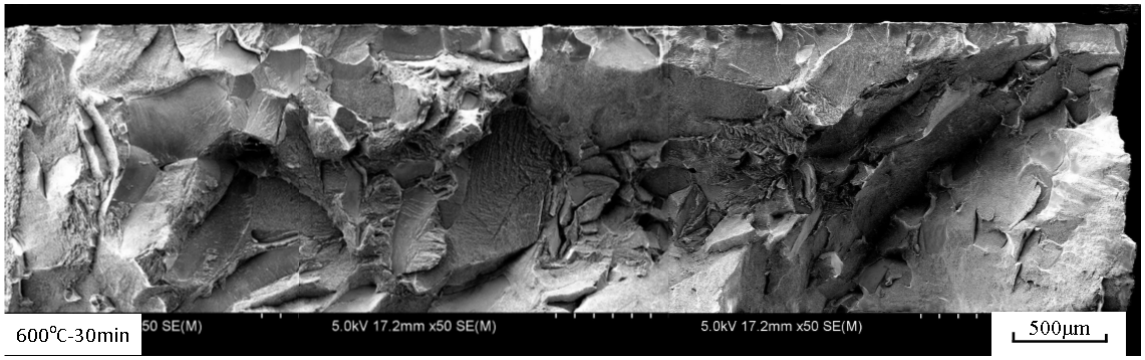
600°C-30min
5.0kV 17.2mm x50 SE(M)
5.0kV 17.2mm x50 SE(M)
500µm

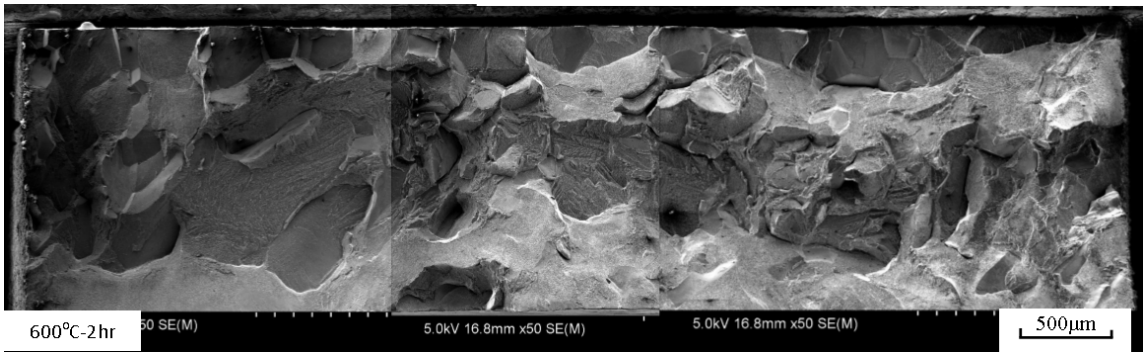
600°C-2hr
5.0kV 16.8mm x50 SE(M)
5.0kV 16.8mm x50 SE(M)
500µm

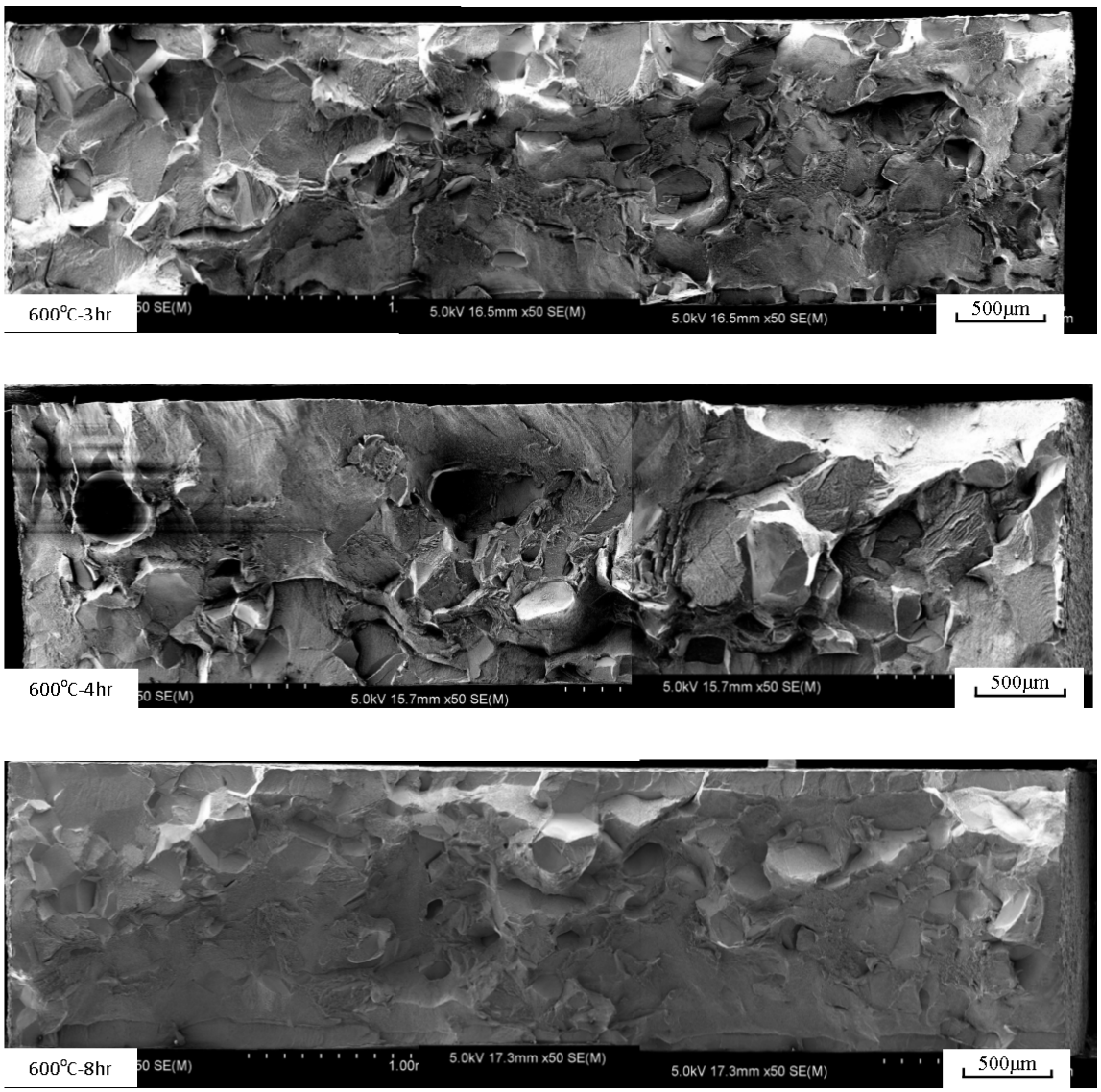

Figure A.2. SEM images of fracture surface for samples aged at 600℃

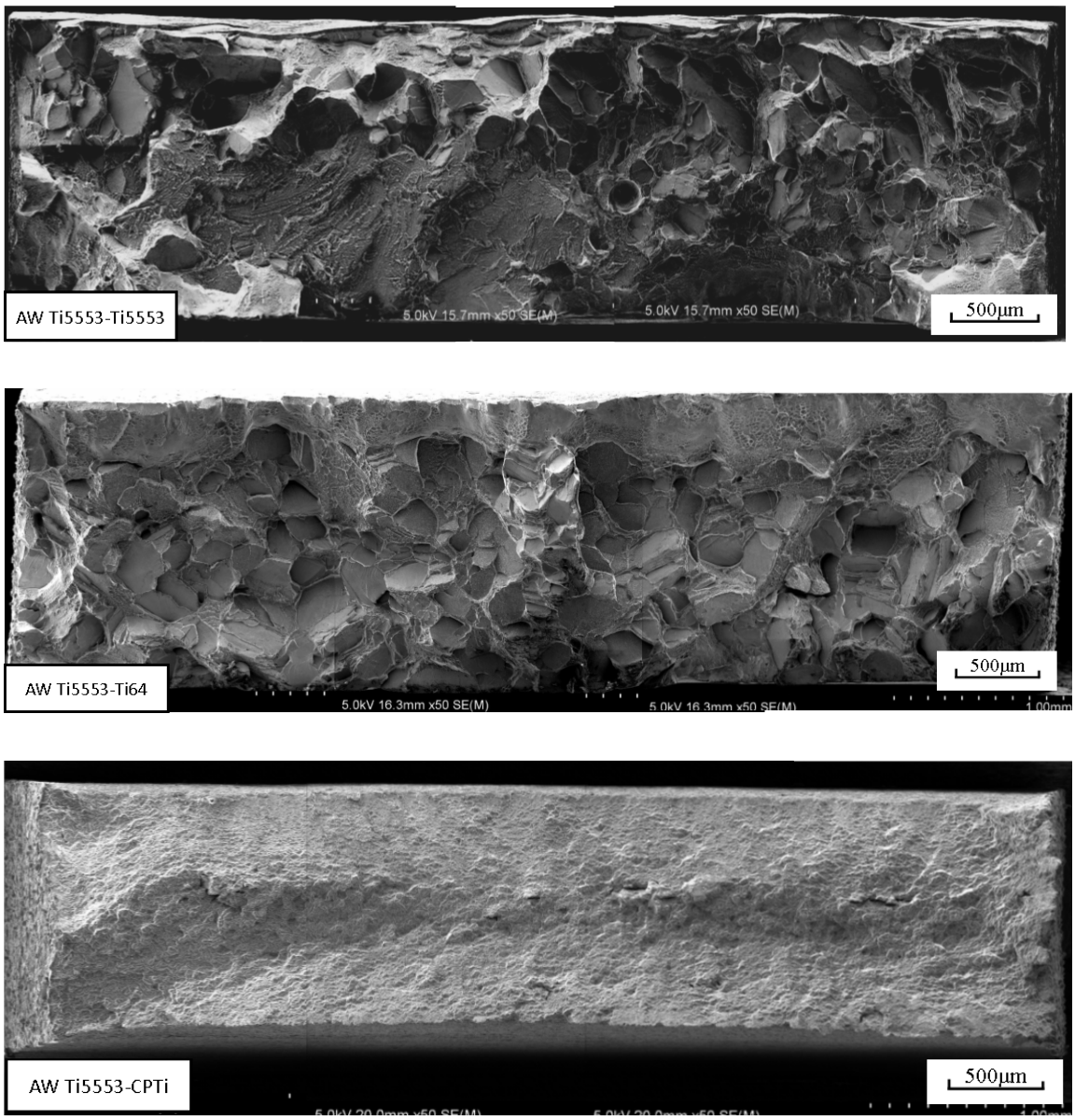

Figure A.3. SEM images of fracture surface for AW: Ti5553-Ti5553, Ti5553-Ti64, and Ti5553-CPTi

APPENDIX B – Calculations of d-spacing

$$r * d = \lambda * L$$

$$200KV\ e\ beam:\ \ \lambda = 0.00251nm$$

Camera length calibration

Displaying on screen	Real value L
120mm	153mm
150mm	196mm
200mm	264mm
285mm	368mm
320mm	422mm

Fusion zone of as-welded Ti5553

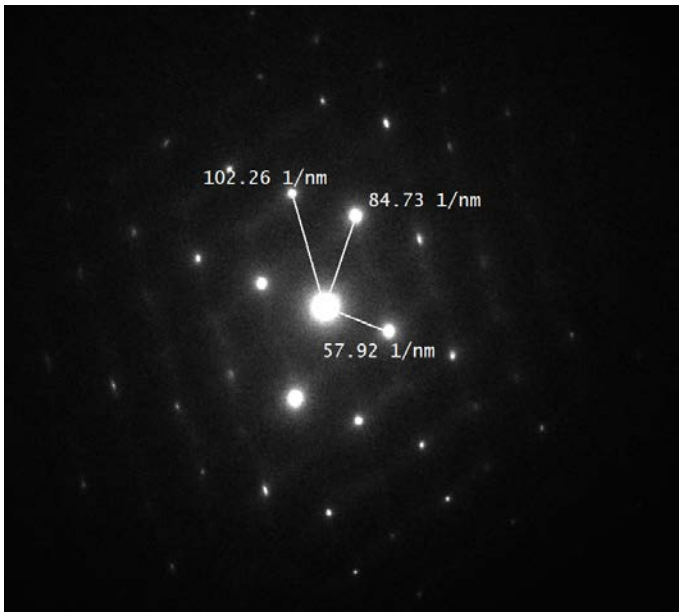

Figure B.1. SAED of AW Ti5553 FZ, camera length displayed on screen D=285mm

Info

Data type:	Integer 4 Signed
Size in pixels:	2048 x 2048
Size in bytes:	16393K
Dimensions:	952.64 1/nm x 952.64 1/nm
Pixel Size:	0.47 1/nm x 0.47 1/nm

$$R_1 = 57.92 \;\; 1/nm \quad R_2 = 84.73 \;\; 1/nm \quad R_3 = 102.26 \;\; 1/nm$$

$$Dimension = 952.64 \; 1/nm$$

$$D = 285mm, therefore \; L = 368mm$$

$$\frac{1}{d_1} = \frac{2048 \times 14(\mu m) 57.92 \left(\frac{1}{nm}\right)}{952.64 \left(\frac{1}{nm}\right)} \times \frac{1}{0.00251nm \times 368mm}$$

$$d_1 = 0.530nm = 5.3\text{Å}$$

$$\frac{1}{d_2} = \frac{2048 \times 14(\mu m) 84.73 \left(\frac{1}{nm}\right)}{952.64 \left(\frac{1}{nm}\right)} \times \frac{1}{0.00251nm \times 368mm}$$

$$d_2 = 0.362nm = 3.62\text{Å}$$

$$\frac{1}{d_3} = \frac{2048 \times 14(\mu m) 102.26 \left(\frac{1}{nm}\right)}{952.64 \left(\frac{1}{nm}\right)} \times \frac{1}{0.00251nm \times 368mm}$$

$$d_3 = 0.300nm = 3\text{Å}$$

$$\frac{d_1}{d_2} = \frac{R_2}{R_1} = \frac{84.73}{57.92} = 1.4629; \qquad \frac{d_1}{d_3} = \frac{R_3}{R_1} = \frac{102.26}{57.92} = 1.7655;$$

Interplanar angle measured from image

$$angle \; between \; g_1 and \; g_2, \qquad \emptyset_1 = 94°$$

$$angle \; between \; g_1 and \; g_3, \qquad \emptyset_2 = \; 129°$$

$\sqrt{N_1}/\sqrt{N_2}$ (hkl / hkl)	110	200	211	220
110	1.0000	1.4142	1.7321	2.0000
200	0.7071	1.0000	1.2247	1.4142

Possible indices: d_1: {110} d_2: {200} d_3: {211}

Calculated angle between g_1 and g_2: $\Phi = 90°$

Calculated angle between g_1 and g_3: $\Phi = 125°$

APPENDIX C – Publications

1. Welding Metallurgy of a Beta Titanium Alloy for Aerospace applications

T. Pasang[1], Y. Tao[1], J.C. Sabol[2], W.Z. Misiolek[2], O. Kamiya[3] and G. Kudo[3],

[1]Department. of Mechanical Engineering, AUT University, Auckland, New Zealand

[2]Institute for Metal Forming, Lehigh University, Bethlehem, PA, USA

[3]Department of Mechanical Engineering, Akita University, Akita, Japan

1 Introduction

Titanium and its alloys are used in many different areas such as aerospace, automotive, medical, sporting equipment and chemical industries. Such wide areas of applications are associated with the excellent high strength to weight ratio, good creep resistance, excellent corrosion resistance and good biocompatibility. A number new titanium alloys with comparable, if not better, properties were introduced in the last decade or so. One of them is a metastable β titanium alloy known as Ti-5Al-5V-5Mo-3Cr (Ti5553). This alloy offers high strength, excellent hardenability and fracture toughness, and also high fatigue resistance. The landing gear of Boeing 787 has been forged from this alloy. Many other forged aircraft structures and a few other niche applications in the aerospace area have been specified [1] which may involve welding.

Most titanium alloys have excellent weldabilty in the annealed condition, and relatively lim- ited weldability in the solution treated and aged conditions [2]. Commercially pure titanium (CP Ti), α-titanium and α/β titanium alloys have better weldability compared with metastable β titanium alloys. In other words, as the amount of beta-stabilizer elements increase the ductility decreases [2]. CP Ti welds, typically, have coarse columnar grains in the fusion zones (FZ) compared with the head affected zones (HAZ) and the base metal (BM) [3]. The HAZ consists of equiaxed transformed β grains which increase in size as the FZ is approached. Within these grains, colonies of α-phases are present. The FZ of α/β alloys contains coarse, columnar prior beta grains. The grain structures of Ti6Al4V (Ti64) welds showed the presence of a small amount of acicular α, a larger amount of α-prime (martensite) in the HAZ and α-prime covering the entire FZ with increased hardness in FZs [4]. For metastable β titanium alloys, the FZ is comprised of coarse columnar β grains from solidification while the HAZ is characterized by retained β structure. Both, the FZ and HAZ are low in strength (low hardness) but have

good ductility. Various welding studies on β titanium alloys, e.g. on Beta-21S, Ti-15V-3Cr-3Al-3Sn and Beta-CTM have been reported [5,6,7]. They reported that the FZ and HAZ contained re- tained β grain structures. Epitaxial grain growth was observed to form in the HAZ through the fusion boundary into the FZ. The FZ had transitioned from a solidification mode of a cellular- type along the fusion boundary to a completely cellular-dendritic (or columnar dendritic) solidi- fication mode at the weld centreline.

The most common welding techniques to joint titanium and its alloys are gas tungsten arc welding (GTAW), gas metal arc welding (GMAW), plasma arc welding (PAW), laser beam welding (LBW) and electron beam welding (EBW) [2,12]. Two of the above welding methods, i.e. LBW and GTAW were employed in this study. Similar and dissimilar titanium weld joints were made and the microstructures and mechanical properties are presented in this paper.

2 Experimental Procedures

2.1 Materials and Welding Procedures

Three different types of titanium were used in this investigation. They were commercially pure titanium (CP Ti), α/β alloy Ti6Al4V (Ti64) and β alloy Ti-5Al-5V-5Mo-3Cr (Ti5553), all in the annealed condition. Their chemical compositions are shown in Table 1.

Table 1. Chemical composition of the titanium alloys (wt.%)

	Ti	Al	V	Mo	Cr	Fe	C	O	N
CP Ti	Bal.	0.16	<0.01	<0.01	<0.01	0.22	0.01	0.28	0.01
Ti64	Bal.	6.08	3.85	<0.01	0.02	0.17	0.02	0.05	<0.01
Ti5553	Bal.	5.03	5.10	5.06	2.64	0.38	0.01	0.14	<0.01

Full penetration butt joints were made without filler metal (autogeneous) by LBW and GTAW on sheets with a thickness of 1.6 mm. Note that the Ti5553 alloy samples were sliced from a 8 mm thick plate. The welding joints combinations were (i) Ti5555-Ti5553, (ii) Ti5553-CP Ti, and (iii) Ti5553-Ti64. The welding conditions are presented in Table 2. Before welding, the samples were cleaned according to ASTM B 600-91 standard. The welding di- rection was perpendicular to the rolling direction.

Table 2. Welding parameters for LBW and GTAW

LBW	Power = 2 kW; speed = 15 mm/sec; continuous argon gas flow of 20L/min
GTAW	Current = 50 Amp DCEN; voltage 10V; continuous argon gas flow of 1-16L/min

2.2 Metallography and Mechanical Testing

The metallographic sample preparation consisted of grinding from 120 grit to 2400 grit SiC paper, polishing to 0.3 µm colloidal alumina, followed by final polishing with 0.05 µm colloidal silica suspension. Kroll's reagent with a composition of 100 mL water + 2 mL HF + 5 mL HNO3 was used to etch the samples to reveal the weld profiles and grain structures. Optical microscopy and scanning electron microscopy (SEM) were employed to characterize and study the microstructures of the etched samples.

Vickers hardness with a load of 300g (HV300g) was used to investigate the hardness profile of the welds. Hardness indentations were placed about 0.2 mm from the top surface. Two sub- size tensile tests samples were taken from the welded sheets (Figure 1) in accordance with ASTM E 8M – 04, with the weld located perpendicular to the tensile axis. The tensile tests were conducted at room temperature with a crosshead speed of 3 mm/min.

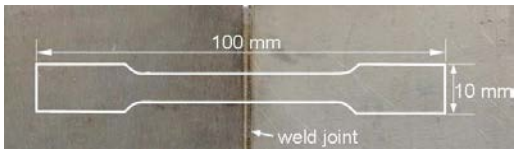

Figure 1: Schematic diagram showing a tensile test sample position on the LBW material.

3 Results and Discussions

Microstructures of the Ti5553, CP Ti and Ti64 base metals (BM) are presented in Figure 2. The Ti5553 alloy showed a typical α/β microstructure with globular α particles distributed within the β matrix. These α particles have an average size of less than 5 µm. The CP Ti had nearly equiaxed α grains with an average size of 20 µm in the longitudinal direction. It also contained disperse β phase (dark). The presence of β phase is associated with the addition of small amounts of Fe in CP Ti. The Ti64 alloy had elongated primary α grains in the α/β ma- trix. General weld profiles from LBW and GTAW are presented

in Figure 3. It can be seen that the weld zone widths of LBW and GTAW are markedly different, being fairly narrow in the former and could be up to five times wider in the latter. The grain sizes in the FZ for all welds were up to a few hundred microns. In the HAZ, large grains were observed at the near HAZ (along the fusion boundary) of up to 200 μm in the LBW samples, and up to 600 μm for GTAW samples. The larger grain sizes in the near HAZ are associated with intermediate peak temperature during welding that facilitates grain growth. The grains became gradually smaller towards the BM. More specifically the characteristics of each weld joint are described below:

1. Ti5553-Ti5553 (Figs. 4a, 4b, 5a and 5b): (i) the FZ consisted of a columnar dendritic-typed grain morphology indicating a high concentration of β-stabilizing elements, (ii) the HAZ is decorated with retained, equiaxed β grains with larger grains at the fusion boundary and smaller grains towards BM, and (iii) grains from the HAZs grew epitaxially into the FZs.
2. Ti5553-CP Ti (Figs. 4c, 4d, 5c and 5d): (i) dendritic grains were observed on the Ti5553 side and lamellar type-grains were present on the CP Ti side (Figs. 4d and 5d), (ii) α-prime (martensite) was clearly present in the FZ adjacent to the CP Ti side (not in the HAZ) and decreasing towards the Ti5553 side, (iii) epitaxial grain growth was clearly observed on the Ti5553 side but not very clear on the CP Ti side.
3. Ti5553-Ti64 (Figs. 4e, 4f, 5e and 5f): (i) dendritic grains were observed on the Ti5553 side and lamellar type-grains were present on the Ti64 side, (ii) α-prime (martensite) was clearly present at the Ti64 side from FZ through far HAZ. The presence of martensite was decreasing towards the Ti5553 side, (iii) epitaxial grain growth was observed on the Ti5553 side but not as obvious on the Ti64 side.

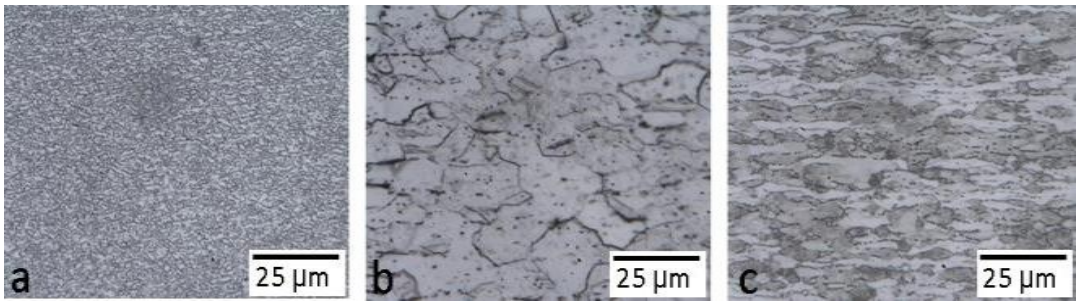

Figure 2: Micrographs showing microstructures of the base metals for (a) Ti5553, (b) CP Ti and (c) Ti6Al4V.

SEM micrographs showed dendritic-typed structures throughout the FZ of Ti5553-Ti5553 (Fig. 6a). The extent of dendritic structures became less obvious on the FZ of

Ti5553-CP Ti and Ti5553-Ti64 perhaps due to the formation of the martensitic phase (Fig. 6b). Epitaxial grain growth from the near HAZ into the FZ is very clearly observed (Fig. 6). Fig. 6b also indicates the formation of α-prime (martensite) in the Ti5553-Ti64 sample from the HAZ on Ti5553 side to the fusion boundary. The formation of both the dendritic-typed structures and α-prime (martensite) are compositional-driven. The higher the β stabilizing elements the more likely it is to form dendritic structures [8] while the α-prime (martensite) formation could take place if the Molybdenum equivalent - Moeq (generally used to see the effects of β stabilizing elements) is less than 10 [9]. Note that the Ti5553 alloy has Moeq ~ 12.

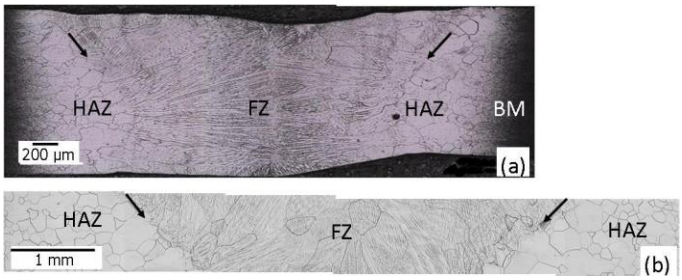

Figure 3: Micrographs showing examples weld profiles of (a) LBW and (b) GTAW for Ti5553-Ti5553 welds. BM = base metal; FZ = fusion zone; HAZ = heat affected zone; arrows indicate fusion boundary.

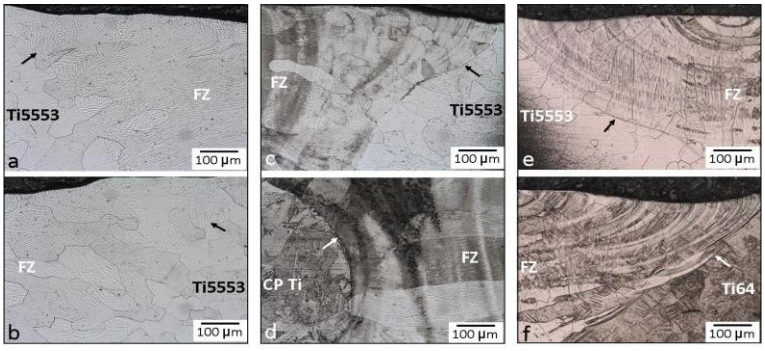

Figure 4: Microstructures around the LBW weld zones for welding combinations of Ti5553-Ti5553 (a,b), CP Ti-Ti5553 (c,d), and Ti5553-Ti64 (e,f). FZ = fusion zone; arrows indicate fusion boundary.

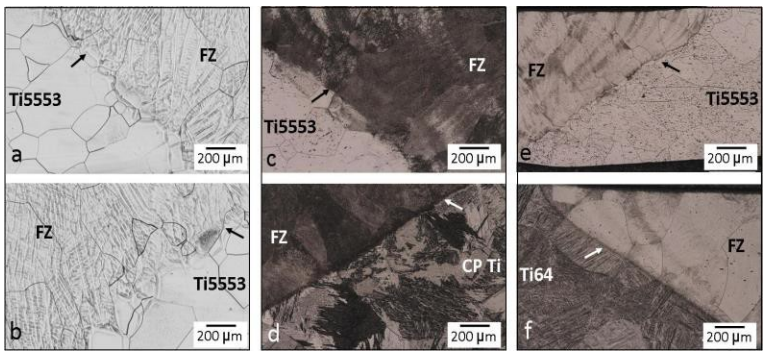

Figure 5: Microstructures around the GTAW weld zones for welding combinations of Ti5553-Ti5553 (a and b), CP Ti-Ti5553 (c and d), and Ti5553-Ti64 (e and f). FZ = fusion zone, and arrows indicate fusion boundary.

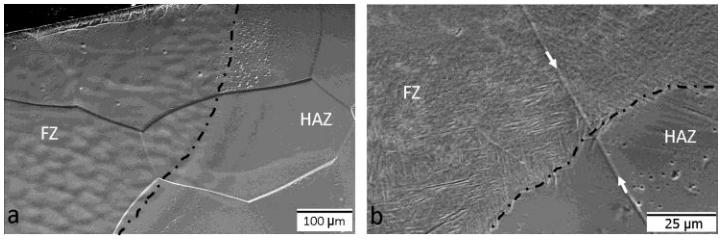

Figure 6: SEM micrographs showing the fusion line area of (a) Ti5553-Ti5553, and (b) Ti5553-Ti64 at the near HAZ of Ti5553 side. White arrows indicate epitaxial grain boundary; dashed line represents fusion boundary.

For mechanical properties, the hardness profiles were similar except for the GTAW weld that has a wider FZ and HAZ due to its wider weld zones associated with the high heat input. Typical hardness profiles in the as-welded (AW) condition are given in Figs. 7 and 8. For the Ti5553-Ti5553 welds, lower hardness values were observed in the HAZ and FZ area for both LBW and GTAW. Similar observations were reported earlier by Mitchell et al. [10] and Sabol et al. [11]. A possible explanation for the lower hardness found in the fusion zone is the disso- lution of α in the FZ and part of the HAZ, leaving only retained β. Retained β phase is softer than both α as well as precipitation strengthened β alloys [11].

The dissimilar joints showed the opposite phenomenon with high hardness values in HAZ and FZ compared with the BM. The plausible explanation for this is the formation of α-prime (martensite) in the FZ and partially in the HAZ area where the Moeq would be less than 10.

The results from tensile testing are summarized in Table 3. The data showed a reduction in strengths if compared to the strengths of BM. The tensile tests involving CP Ti, wherein sam- ples fractured in the CP Ti BM corresponds to its annealed microstructure which is

softer to all other areas. All other samples fractured at the weld zones. The relatively low in strengths for the GTAW Ti5553-Ti5553 weldment were related to slightly lack of penetration at the root in addition to the presence of retained β phase.

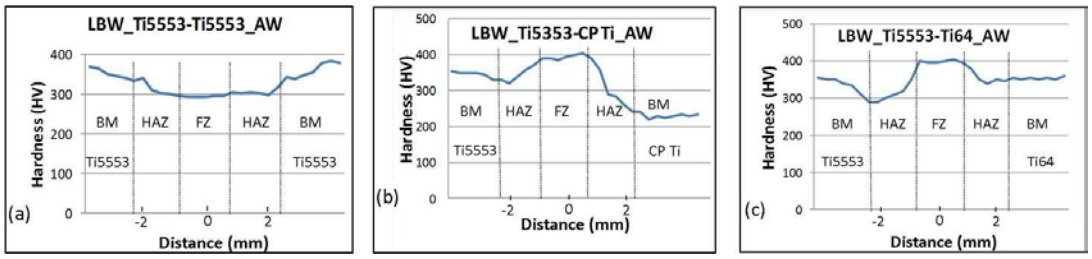

Figure 7: Hardness profiles of various weld joint combinations using LBW.

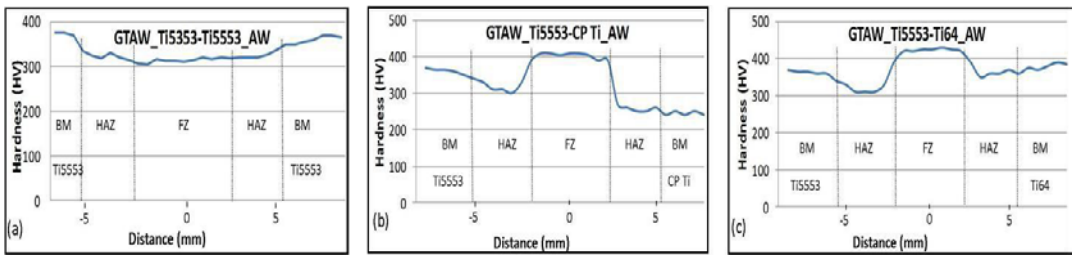

Figure 8: Hardness profiles of various weld joint combinations using GTAW.

Table 3. Tensile test data of base metals (BM) and various welding combinations

Welding combinations	Yield Strength (MPa)	Tensile Strength (MPa)
BM: Ti5553	1030	1050
BM: CP Ti	630	690
BM: Ti64	940	980
LBW: Ti5553-Ti5553	814	814
LBW: Ti5553-CP Ti	372	475
LBW: Ti5553-Ti64	870*	870*
GTAW: Ti5553-Ti5553	613	613
GTAW: Ti5553-CP Ti	560	654
GTAW: Ti5553-Ti64	853	853

*only one sample tested

4 Summary

Investigations on welding characteristics of a new metastable β titanium alloy Ti-5Al-5V- 5Mo-3Cr (Ti5553) were conducted. A similar (Ti5553-Ti5553) and two dissimilar (Ti5553- CP Ti and Ti5553-Ti64) weld joints were made. The results indicated that this new metastable β titanium alloy is weldable either by LBW or GTAW. On the similar

weld, it had dendritic- type structure in the FZ and retained beta in the HAZ. It also showed low hardness, hence, low strength in the HAZ and FZ. The dissimilar welds had higher hardness on the HAZs and FZs. The plausible explanation for this phenomenon is related to the absence of α-prime (mar- tensite) on the similar welds and its presence in the dissimilar joints.

5 Acknowledgement

The authors would like to thank the Loewy Family Foundation, Lehigh University, and the Engineering Research Institute (ERI), AUT University. Assistance from Mr. Rodney Boyer of the Boeing Company who provided the Ti5553 alloy is greatly appreciated. Thank you also to Mr. Kimura of the Akita Prefecture Research Center for performing LBW and Mr. Makirai Henry of AUT for performing GTAW.

6 References

[1] Fanning, J.C., "Properties of Timetal 555 (Ti-5Al-5Mo-5V-3Cr-0.5Fe)", Journal of Ma- terials and Performance, pp. 788-791, 2005.

[2] Donachie, M.J., "Titanium: A Technical Guide", second Edition, ASM Int'l, 2000.

[3] Lathabai, S., Jarvis, B.L and Barton, K.J., "Comparison of Keyhole and Conventional Gas Tungsten Arc Welds in Commercially Pure Titanium", Materials Science and Eng., A299, pp. 81-93, 2001.

[4] Irisarri, A.M., Barreda, J.L. and Azpiroz, X.,"Influence of the Filler Metal on the Properties of Ti-6Al-4V Electron Beam Weldments. Part I: Welding Procedures and Microstructural Characterization", Vacuum 84, pp. 393-399, 2010.

[5] Becker, D. and Baeslack III, W.A., "Property-Microstructure Relationships in Metastable-Beta Titanium Alloy Weldments", Welding Journal 59, pp. 85-93, 1980.

[6] Liu P.S., Hou K. H, Baeslack III, W.A. and Hurley, J., "Laser Welding of an Oxidation Resistant Metastable-Beta Titanium Alloy – Beta-21S". Titanium '92 (Froes F.H. and Caplan I, editors), TMS, pp. 1477, 1993.

[7] Baeslack III W.A., Liu, P.S., Barbis, D.P., Schley, J.R. and Wood, J.R." Postweld Heat Treatment of GTA Welds in a High-Strength Metastable Titanium Alloy – Beta-CTM", Titanium'92, Science & Tech., F.H. Froes & I. Chaplan (eds), pp. 1469-1476, 1993.

[8] Sindo, K., "Welding Metallurgy", John Wiley and Sons, second edition, 2003.

[9] Bania P.J., “Beta titanium alloys in the 1990’s”, In: Eylon D., Boyer R.R., Koss D.A (Eds.), TMS, Warrendale, PA, pp. 3-14, 1993.
[10] Mitchell, R., Short, A., Pasang, T. and Littlefair, G., “Characteristics of EBW Ti Alloys”, Structural Integrity and Failure - SIF, University of Auckland, 2010.
[11] Sabol, J.C., Pasang, T., Misiolek, W.Z. and Williams, J.C., “Localized tensile strain dis- tribution and metallurgy of electron beam welded Ti–5Al–5V–5Mo–3Cr titanium alloys”, Journal of Materials Processing Technology 212, pp. 2380– 2385, 2012.

2. Comparison of Ti-5Al-5V-5Mo-3Cr Welds Performed by Laser Beam, electron Beam and Gas Tungsten Arc Welding

T. Pasang[a],*, J.M.Sánchez Amaya[b], Y. Tao[a], M.R. Amaya-Vazquez[b], F.J. Botana[b], J.C Sabol[c], W.Z. Misiolek[c], O. Kamiya[d]

[a]*Dept. of Mechanical Eng., AUT University, Auckland 1020, New Zealand*

[b]*Universidad de Cádiz. Departamento de Ciencia de los Materiales e Ingeniería Metalúrgica y Química Inorgánica. Avda. República Saharaui s/n, 11510-Puerto Real, Cádiz, Spain*

[c]*Institute for Metal Forming, Lehigh University, 5 East Packer Avenue, Bethlehem, PA 18015, USA*

[d]*Department of Mechanical Engineering, Akita University, Akita City, Japan*

Abstract

Welding characteristics of Ti-5Al-5V-5Mo-3Cr (Ti5553) alloy has been investigated. The weld joints were performed by laser beam (LBW), electron beam (EBW) and gas tungsten arc welding (GTAW). Regardless of the welding method used, the welds showed low hardness values with coarse columnar grains in the fusion zone (FZ) and retained equiaxed beta phase within the heat affected zone (HAZ). Larger grains were present at the near HAZ compared with far HAZ (near base metal). The strengths of the welded samples were lower than the base metal. Fracture occurred at the weld zones with transgranular and microvoid coalescence fracture mechanism.

Keywords: Laser beam welding; electron beam welding; tungsten inert gas welding; titanium alloys; Ti-5Al-5V-5Mo-3Cr

1. Introduction

It is generally known that commercially pure titanium, α-titanium, and α/β- titanium have excellent weldability. Metastable titanium alloys, however, may have limited weldability due to the high content ofstabilizing elements [Donachie, 2000]. Some of the weldability studies on metastable titanium are summarized in the following. In general, in the as-welded (AW) condition the weld fusion zone (FZ) is comprised of coarse columnar grains from solidification while the heat affected zone (HAZ) adjacent to the fusion lines are characterized by retained structure. In this condition, they are low in strength (low hardness) but have good ductility. Becker and Baeslack (1980) conducted weldability studies on three different types of metastable titanium alloys (Ti-15V- 3Cr-

3Al-3Sn; Ti-8V-7Cr-3Al-4Sn-1Zr and Ti-8V-4Cr-2Mo-2Fe-3Al) and showed that the alloys are readily weldable. Their findings confirmed the above explanations. For all three alloys, the strengths were increased with post weld heat treatment at, however, the expense of ductility. Weldability of Beta-21S sheet using laser welding technique was investigated by Liu at al. (1993). Both the FZ and HAZ were narrow with fine retained grain structure. The FZ had a "crown-shaped" (more literatures refer to as an hour glass-shaped, hence, used in this paper) with wider top and bottom surfaces compared with the mid-thickness area. Epitaxial grain growth was observed to form from the narrow HAZ through the fusion boundary into the FZ. The FZ had a transitioned from a solidification mode of a cellular-type along the fusion boundary to a complete cellular-dendritic (or columnar dendritic) solidification mode at the weld centreline. Baeslack et al. (1993a) conducted welding investigations on Beta-CTM implementing gas tungsten arc welding (GTAW or TIG). The as-welded samples showed epitaxial growth from the near-HAZ into the FZ, solidified with a cellular mode and progressively formed a complete columnar-dendritic grain structure at the weld centreline.

In the early 2000s, a new metastable titanium alloy known as Ti-5Al-5V-5Mo-3Cr (Ti5553) was introduced. Apart from its high strength, excellent hardenability and fracture toughness, it also offers high fatigue resistance. The potential applications of this alloy are in the high-strength related areas such as landing gear and pylon/nacelle areas. Note that the landing gear beam truck of Boeing 787 has been successfully manufactured using this alloy (Fanning and Boyer, 2003). To find more applications in different areas, a number of factors are to be investigated, and one of them is the weldability. According to Donachie (2000), Leyens and Peters (2003), the most common welding techniques to joint titanium and its alloys are GTAW, gas metal arc welding (GMAW/MIG), plasma arc welding (PAW), laser beam welding (LBW) and electron beam welding (EBW). The first three methods fall in the arc welding category with high heat input and low power density of heat source, while the last two techniques belong to high-energy beam group.

This paper presents findings from a recent investigation with the objective of comparing the microstructures and properties of the Ti5553 welds following different types of welding methods. Three of the above five methods were employed, i.e. LBW, EBW and GTAW.

2. Experimental Procedures

2.1. Materials

The alloy used in this investigation was provided by the Boeing Aircraft Company, and that is a new metastable titanium, Ti-5Al-5V-5Mo-3Cr (Ti5553). The alloy was in the

annealed condition with a typical α/β microstructure. The chemical composition of the material is shown in Table 1.

Table 1. Chemical composition wt.% of the Ti-5553 alloy used in this study

Material	O	N	Al	V	Mo	Cr	Fe	Ti
Ti5553	0.14	<0.01	5.03	5.10	5.06	2.64	0.38	Bal.

1.1. Welding Procedures

Autogeneous (no filler metal added) full penetration butt welding joints Ti5553 were obtained by LBW, EBW and GTAW. The welding conditions were as follows.

1. LBW: the weld joints were performed using an Nd:YAG welding machine under a continuous flow of argon (as shielding gas) of 20L/min, a laser power of 2kW with welding speed of 15 mm/sec.
2. EBW: the weld joints were made in the down-hand position using 150kV welding voltage, a traverse speed of 8.5mm/s and welding currents of around 3mA. The details have been reported by Mitchell et al. (2011) and Sabol et al. (2012).
3. GTAW: the weld joints were obtained with a DCEN 50Amp current, a voltage of 10V and with a flow of argon (shielding gas) of 12-16 L/min.

Regardless of the welding procedure, the sizes of samples were always 50x50x1.6mm. Before welding, the samples were cleaned according to ASTM B 600-91 standard. The welding direction was perpendicular to rolling direction (Figure 1).

1.2. Metallography

Metallographic samples for grain structure investigation and for hardness tests were prepared from the welded sheets (as shown in Figure 1). The metallography preparation steps consisted of grinding from 120 grit to 2400 grit SiC paper, polishing to 0.3 μm colloidal alumina, followed by final polishing with 0.05 μm colloidal silica suspension. The samples were etched with Kroll's reagent with a composition of 100 mL water + 2 mL HF + 5 mL HNO3. An optical microscope was used to characterize the microstructures of the welds.

1.3. Mechanical Testing

Hardness tests on the metallographically-prepared samples were conducted across the weld to produce the hardness profiles. The load used was 300g (HV300g). Tensile tests samples were taken from the welded sheets (Figure 1) in accordance with ASTM E 8M – 04, with the weld located perpendicular to the tensile axis. The tensile tests were conducted at room temperature with a crosshead speed of 3 mm/min.

1.4. Fracture Surface Analysis

Following tensile tests, the fracture surfaces were cleaned with an ultrasonic cleaner, and were examined using a Scanning Electron Microscope (SEM) at relatively low and high magnifications.

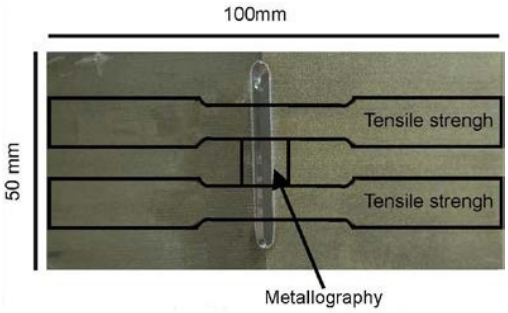

Fig. 1. Schematic diagram indicating the weld joint and locations of samples

1. Results and Discussions

Microstructure of the base metal is given in Figure 2 showing the α/β microstructure where α particles with an average size of less than 5μm are distributed within the β matrix. The shapes of the FZ were identical between LBW and EBW, i.e. an hour glass-shaped (Figures 3 and 4), while the GTAW welds showed a V-shaped profile (Figure 5). The presence of hour glass-shaped FZ on the LBW titanium welds and the absence of this shape in the GTAW has been observed earlier. Liu et al. (1993) and Baeslack et al. (1993b) performed LBW and GTAW, respectively, on a metastable titanium alloy Beta-21S, 1.5 mm thick sheet. Liu et al. (1993) reported a weld zone like hour glass-shaped FZ, while Baeslack et al. (1993b) reported a V-shaped FZ. Odabashi et al. (2010) observed that the hour glass-shaped FZ of LBW Inconel 718 with low amount of heat input, i.e. with high welding speed and power. The explanations on these differences are relatively unclear, although it is believed that the flow of the molten metal and the heat in the molten zone (i.e. later become FZ) are crucial in determining the shape and the size of FZ. According to Rai et al. (2009) the widening top and bottom surface, hence, hour glass-shaped is due to the presence of Marangoni convective currents which drives away the molten metal from the location of heat source. Therefore, the weld pools at the top and bottom surfaces are wide compared to the center of the FZ. Liu et al. (1993) suggested that the hour glass- shaped was due to heat flow in 3D and 2D on the surfaces and the mid-thickness, respectively. In a review by Walsh (2012), it was pointed out that the weld pool geometry is greatly affected by focus/defocus beam which may create a surface tension which is responsible for the metal flow, and hence, the weld zone shape. The V-shaped in the GTAW is conduction dominated where the width of the weld is 2.5x the material thickness.

The widths of the FZ and the HAZ of the GTAW welds were much wider compared with those of LBW and EBW. The FZ created by GTAW was as wide as 5.4 mm compared with 2.6 mm and 1.7 mm made by LBW and EBM, respectively. The HAZ of the GTAW sample reached 3mm and up to 800µm for both LBM and EBW samples. The wider weld zones in the GTAW samples compared with EBW and LBW samples is associated with the high heat input into the workpiece on the GTAW process.

The grain sizes in the FZ for all welds were up to a few hundred microns. In the HAZ, large grains were observed at the near HAZ (along the fusion boundary) of up to 200µm in the EBW and LBW samples, and up to 600µm for GTAW samples. The grains became gradually smaller towards the BM. The larger grain sizes in the near HAZ are associated with intermediate peak temperature during welding that facilitates grain growth.

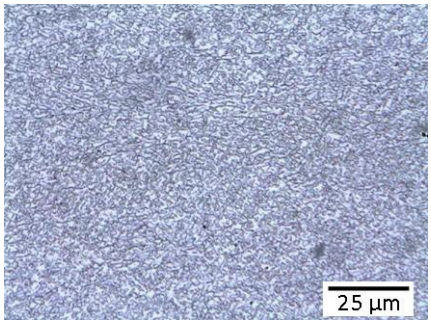

Fig. 2. Microstructure of the base metal showing the α/β microstructure. Note α particles (white).

Some similarities were observed in the weldments' microstructure regardless of the welding method used as described in the followings:

1. The FZ contained a columnar dendritic-typed grain morphology including a high concentrated β-stabilizing elements,
2. The HAZ is decorated with retained, equiaxed grains with larger grains at the fusion boundary and smaller grains towards BM,
3. Epitaxial growth from the HAZ into the FZ was clearly observed.

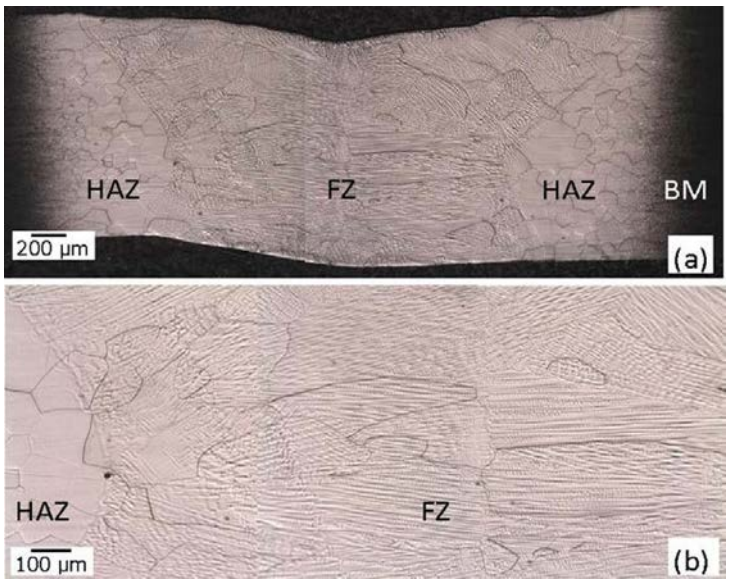

Fig. 3. Weld profile of LBW sample showing the (a) low magnification micrograph of the FZ, HAZ and BM and (b) higher magnification micrograph at the FZ and near HAZ/fusion boundary. Note that the BM is dark due to fast etching rates compared with HAZ and FZ areas

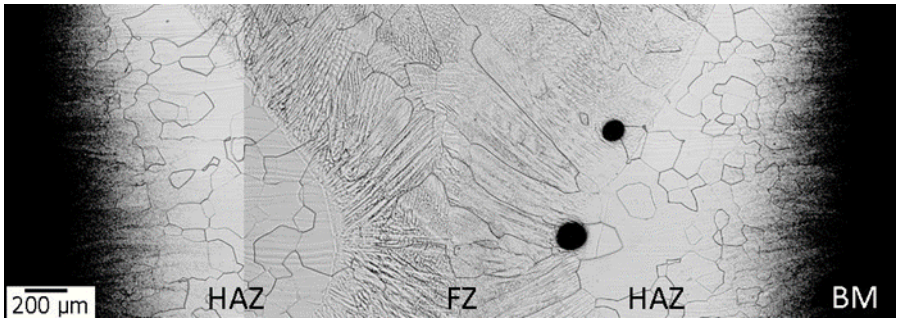

Fig. 4. Weld profile of the EBW samples showing the microstructures in the FZ, HAZ. Note that BM is dark due to fast etching rates compared with HAZ and FZ areas

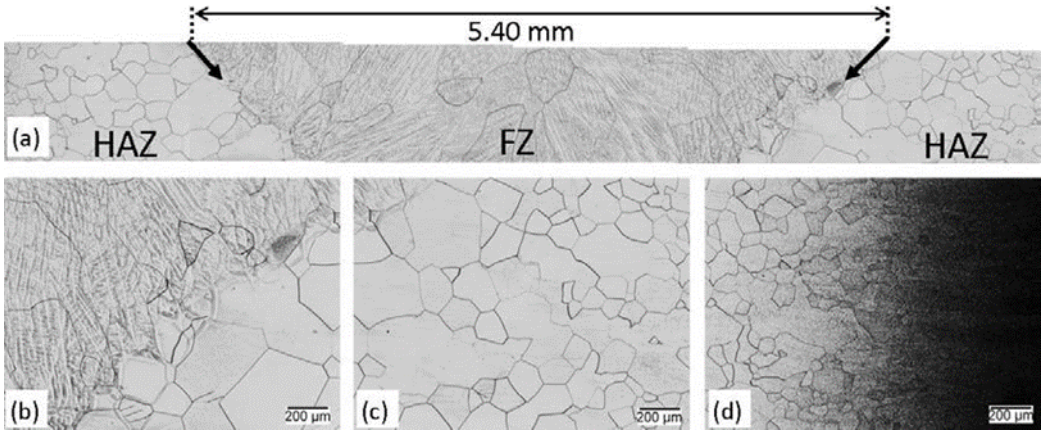

Fig. 5. GTAW weld profile showing the (a) HAZ, FZ and fusion boundary (thick arrows), (b) FZ, fusion boundary and near HAZ, (c) HAZ, and (d) far HAZ and BM. Note that the BM is dark due to fast etching rates compared with HAZ and FZ areas

Hardness profiles for all weldments were similar except for the GTAW weld that has a wider FZ and HAZ due to its wider weld zones. Typical hardness profiles in the as-welded condition are given in Figure 6. Regardless of the welding method used, the hardness values were typically comparable, i.e. 290-320HV in the FZ, 300-360HV in the HAZ and 370-390HV for BM. The weld zones (FZ and HAZ) had lower hardness values compared with that of the base metals. It is noteworthy that the hardness profiles of metastable β titanium alloys are different than those of $\alpha\ or\ \alpha/\beta$ alloys. Hardness values of the $\alpha\ or\ \alpha/\beta$ alloys in the weld zones are generally comparable or higher than that of the BM, due to the formation of α' (alpha prime) or martensite (Amaya-Vazquez et al. 2012). In the metastable β titanium alloy, the formation of these strengthening precipitates is suppressed because of the overwhelming amount of β stabilizing elements leading to a $[Mo]_{eq}$ around 12. According to Bania (1993), α' (alpha prime) or martensite will not form if the $[Mo]_{eq}$ is greater than 10.

Table 2 summarizes the results obtained from tensile testing. The data showed a reduction in strengths, but the elongation was relatively comparable to that of the un-welded samples.

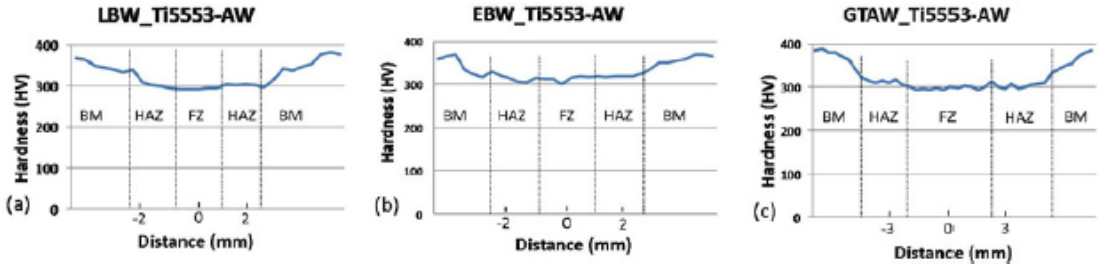

Figure 6. Typical hardness profiles across the weld for (a) LBW, (b) EBW [8] and (c) GTAW/TIG. Note a wider weld zones of GTAW/TIG compared with LBW and EBW.

Table 2. Mechanical properties of Ti5553 on various conditions.

Conditions	YS (MPa)	UTS (MPa)	Elongation (%)	Ref.
Un-welded	1028	1053	12	Mitchell et al. (2011)
As-welded: LBW	N/A	757	9	-
As-welded: EBW	680	680-780	11	Mitchell et al. (2011), Sabol et. al. (2012)
As-welded: GTAW	N/A	591*	N/A	-

*Fractured prematurely

Fracture surfaces from the tensile test samples are given in Figure 7. All samples fractured in the weld zones, and exhibited transgranular fracture modes with microvoid coalescence (dimples) mechanism. This implies that a relatively ductile weld zone results from each of the three welding methods.

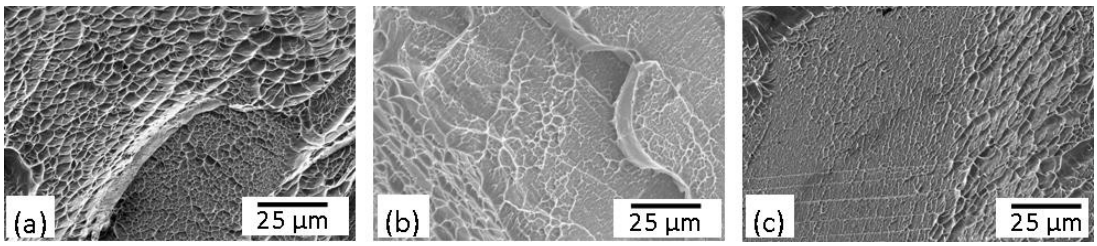

Fig. 7. SEM images showing transgranular fracture with microvoid-coalescence mechanism on (a) LBW, (b) EBW and (c) GTAW.

4. Summary

Ti-5Al-5V-5Mo-3Cr butt welds obtained by LBW, EBW and GTAW have been compared. It has been shown that this new metastable β titanium alloy is weldable. The morphology, the microstructure and the mechanical properties of the welds have been investigated and reported in this paper. The weld profiles due to LBW and EBW showed an hour glass-like appearance, while those from GTAW had a common V-liked shape. From the tensile testing, it is shown that, in the as-welded condition, the strength of the welded specimen is lower than that of the BM (also shown by the lower hardness); however, some ductility was maintained in terms of elongation.

Acknowledgements

The authors (JMSA, MSAV & FJB) would like to thank the financial support of the projects SOLDATIA, Ref. TEP 6180 (Junta de Andalucía, Spain). TP would like to thank The Loewy Family Foundation for sponsoring his research leave at Lehigh University.

References

Amaya-Vazquez, M.R., Sánchez-Amaya, J.M., Boukha, Z., Botana, F.J.. 2012. Microstructure, microhardness and corrosion resistance of remelted TiG2 and Ti6Al4V by a high power diode laser. Corrosion Science Vol. 56, pp. 36-48.

Baeslack III, W.A., Liu, P.S., Barbis, D.P., Schley, J.R., Wood, J.R. 1993 a. Postweld Heat Treatment of GTA Welds in a High-Strength Metastable Titanium Alloy – Beta-CTM. Titanium ’92, Science & Tech., F.H. Froes and I. Chaplan (eds), TMS, pp. 1469-1476.

Baeslack III, W.A., Liu P.S. and Paskell T. 1993 b. Weld Solidification and HAZ Liquiation in a Metastable-Beta Titanium Alloy – Beta-21S. Materials Characterization 30, pp.147-54.

Bania P.J., 1993. Beta titanium alloys in the 1990's. In: Eylon D., Boyer R.R., Koss D.A (Eds.), TMS, Warrendale, PA, pp. 3-14

Becker, D.W., Baeslack III, W.A., 1980. Property-microstructure relationships in metastable-beta titanium alloy weldments. Welding Journal, 59, Research Suppl.,pp. 85s-92s

Donachie Jr, M.J., 2000. Titanium – A Technical Guide, ASM International 2nd edition, pp. 70.

Fanning, J.C., Boyer, R.R. 2003. Properties of TIMETAL 555 – A New Near- Beta Alloy for Airframe Components, Proceedings of the10th World Conference on Titanium, Vol. IV, pp. 2643-2650.

Leyens, C., Peters M. (editors). 2003. Titanium and Titanium Alloys: Fundamentals and Applications. Willey-VCH Verlag GmbH & Co, Weinhamm.

Liu, P.S., Hou, K.H., Baeslack III,W.A., Hurley, J. 1993. Laser Welding of an Oxidation Resistant Metastable-Beta Titanium Alloy – Beta-21S. Titanium '92 (Froes F.H. and Caplan I, editors), TMS, pp. 1477.

Mitchell, R. Short, A., Pasang, T., Littlefair, G. 2011. Characteristics of Electron Beam Welded Ti and Ti Alloys, Advanced Materials Research Vol. 275, pp. 81-84.

Odabashi, A., Unclu, N., Goller, G., Eruslu, M.N. 2010. A Study on Laser Beam Welding (LBW) Technique: Effect of Heat Input on the Microstructural Evolution of Superalloy Inconel 718. Metall Trans., Vol.41A, pp. 2357-2365.

Rai, R., Burgardt, P., Milewski, J.O., Lienert, T.J., DebRoy, T. 2009. Heat transfer and fluid flow during electron beam welding of 21Cr–6Ni– 9Mn Steel and Ti–6Al–4V alloy. J. Phys. D: Appl. Phys. 42**,** pp. 1-12.

Sabol, J.C., Pasang, T., Misiolek, W.Z., Williams, J.C. 2012. Localized tensile strain distribution and metallurgy of electron beam welded Ti– 5Al–5V–5Mo–3Cr titanium alloys. Journal of Materials Processing Technology 212, pp. 2380– 2385.

Walsh, C.A. 2012. Laser Welding – Literature Review. Materials Science and Metallurgy Department, University of Cambridge, England.

3. Microstructure evolution and phase transformation of welded metastable beta-Titanium alloy (Ti-5Al-5V-5Mo-3Cr-0.5Fe)

Tao, Y*, Pasang, T, Chen, ZW, and Conor. P

Dept of Mechanical Engineering, AUT University, Auckland, New Zealand,

* yuan.tao@aut.ac.nz

INTRODUCTION

Titanium alloys have high strength to weight ratio, relatively high melting point, and excellent corrosion resistance which makes titanium alloys excellent choice for aerospace industry. [1] According to the data provided by Prima Industry, the material usage of titanium for the next generation aircraft on B787 is 15% and A350 is 14% [2]. Ti-5Al-5V-5Mo-3Cr-0.5Fe (Ti5553, in wt%) is a recently developed metastable β titanium alloy which was specifically designed to replace Ti-10V-2Fe-3Al (Ti1023) for large airplane components [3]. As comparing to Ti1023, Ti5553 has high strength, good cycle fatigue properties, and is applicable for thick section due to its deep hardenablility [3]. The β-stabilizers in Ti5553 depress the β transus temperature to an average value of 856^{o}C [3].

So far, the weldability of alloy Ti5553 to Ti64 and Ti5553 to CP Ti has not been well understood. In our previous studies, a few findings have drawn our attention. Firstly, in typical Ti5553-Ti5553 weld joints, some dendrites arms are crossed by the grain boundaries. This phenomenon was also discovered in LBW Ti5553-Ti64 specimen. There is a small amount of epitaxial grain growth has been found in Ti5553-Ti64 and Ti5553-CP Ti fusion zone boundary. In this research, a series of microstructure examinations and mechanical testing were carried out in order to reveal the grain boundaries where the cross boundary dendrites occurred and the uncommon epitaxial growth in dissimilar welding.

METHODS

The titanium alloys used in this research include: metastable beta Ti5Al5V5Mn3Cr (Ti5553), alpha-beta Ti6Al4V (Ti64), and commercial pure titanium (CP Ti). The combination of welded titanium alloys included: (i) similar welding Ti5553/Ti5553, (ii) dissimilar welding Ti5553/Ti64 and (iii) Ti5553/CP Ti. Full penetration butt weld joints were performed using Gas Tungsten Arc Welding (GTAW/TIG), Laser Beam Welding (LBW), and Electron Beam Welding (EBW)

Following welding, some coupons were prepared for microstructure examination, tensile test, and hardness test, according to standard procedure. An optical microscope and scanning electron microscope (SEM) were used to evaluate the grain structure.

RESULTS

(i) Microstructure

Microstructures of similar and dissimilar weld zones are shown in Figs. 1, 2 & 3. Ti5553, exhibited relatively smaller equiaxed grains structure in heat affected zones (HAZ) and larger grains in fusion zones (FZ). Epitaxial grain growth was found extensing from the fusion boundary in all three types of Ti5553-Ti5553 weld and in also some Ti5553-Ti64 specimens indicated as dashed line in Fig 2. Extensive dendritic structure was evident in Ti5553-Ti5553 FZ, but was scattered near the Ti5553 side in dissimilar welds. Epitaxial growth in Ti5553-Ti64 weld zone was also favoured towards Ti5553 base material (BM).

A small amount of dendritic structure in Ti5553-Ti5553 FZ exhibited transecting boundaries (Fig 3(a)). Some of columnar grains extended from the top to bottom of the weld zone. Fig 3 (b) shows an example, in Ti5553-Ti64 LBW FZ.

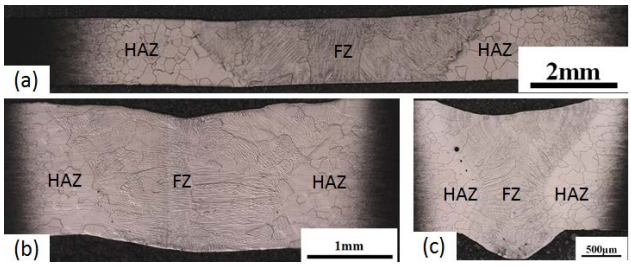

Fig. 1: Etched Ti5553-Ti5553 weld zone: (a) Gas Tungsten Arc Welding (b) Laser Beam Welding, (c) Electron Beam Welding,

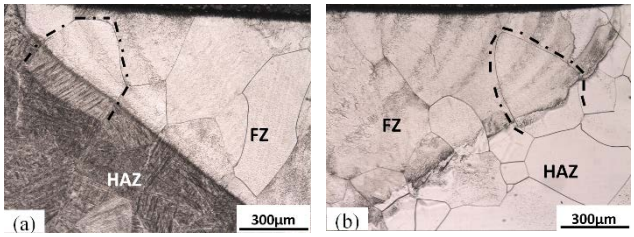

Fig. 2: Etched GTAW Ti5553-Ti64 weld zone, red dash line indicates epitaxial growth: (a) near Ti64 HAZ (b) near Ti5553 HAZ

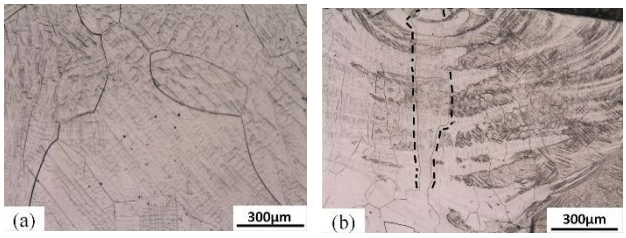

Fig. 3: Cross boundary dendrite growth: (a) GTAW Ti5553 (b) LBW Ti5553-Ti64

(ii) Tensile testing and hardness profile

The results from tensile testing of several of welding combination are presented in Table 1. The failure locations varied among the different weld types.

Sample Name	Strain (%)	UTS (MPa)	Yield (MPa)	Failure location
GTAW Ti5553-T i5553	0.682	613	613	FZ
GTAW Ti5553-Ti64	1.041	853	853	Ti5553 FZ/HAZ
GTAW Ti5553-CPTi	10.98	654	560	CPTi BM
LBW Ti5553-Ti5553	1.508	814	814	FZ
LBW Ti5553-CPTi	15.72	475	372	CPTi BM
EBW Ti5553-Ti5553*	0.83	778	-	FZ
EBW Ti5553-Ti64*	0.87	899	-	FZ
EBW Ti5553-CPTi*	15.48	655	566	CPTi BM

*Table 1 Tensile test data of various welding combination, *[6]*

The SEM results demonstrate that fracture of Ti5553-Ti5553 welds happened at the fusion zone. Evidence of porosity was found on some fractures. On a macroscopic scale the fractures showed planar facets but SEM examination showed widespread microvoid coalescence (dimple-like) structures indicating some ductility during fracture.

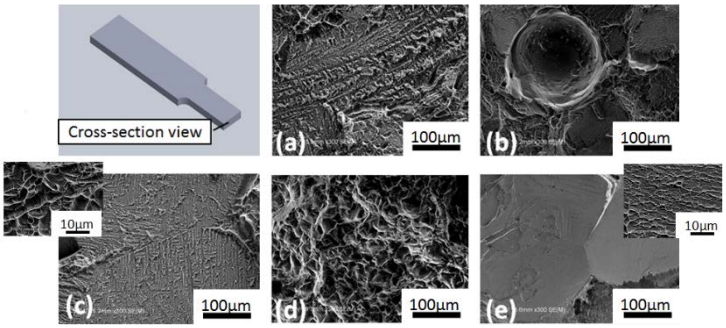

Fig. 4: SEM results of fracture cross-section surface: (a) & (b) LBW Ti5553-Ti5553, (c) GTAW Ti5553-Ti5553, (d) LBW Ti5553-CPTi, (e) GTAW Ti5553-Ti64

Inspection of the Ti5553-Ti5553 GTAW tensile specimens showed the presence of cracks near the fracture surface, as shown in Fig. 5. Crack (a) had formed on the side of the sheet specimen and with a planar growth form had propagated towards a grain boundary. After reaching grain boundary, this crack changed direction and continued

growing on new crystallographic plane till reached the second grain boundary. In a second case (b), the crack also formed on edge and reaching a grain boundary it had failed to penetrated grain boundary and instead bouncing along the boundary three times before crack growth stopped. Crack type (c) formed in the middle of this specimen; its opening displacement was much less than the other two cracks and grew along grain boundary.

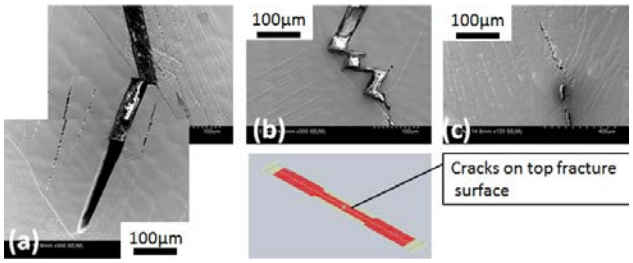

Fig 5: SEM images of cracks on GTAW Ti5553-Ti5553

Fig 6, compares GTAW hardness profiles, for Ti5553-Ti5553, FZ and HAZ have slightly lower hardness value than BM. This phenomenon may be caused by the dissolution of α in the FZ. [4] For dissimilar joints, FZ has higher value than BM, the softest area is in HAZ. The hardness profile of dissimilar joints indicates the possible existent of martensite

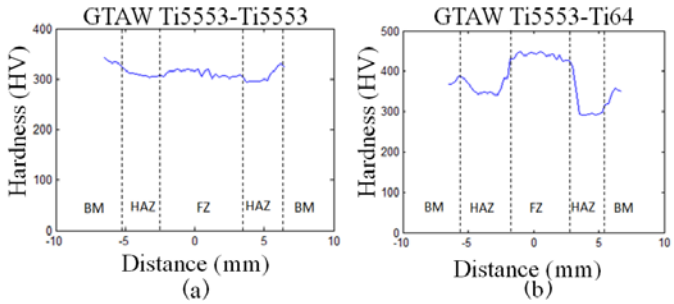

Fig. 6 Hardness profile of GTAW: (a) Ti5553-Ti5553; (b) Ti5553-Ti64.

DISCUSSION

During phase transformation the BCC β phase transforms to the HCP α phase undergoing conventional nucleation and growth, or martensitic structure [1]. For CP Ti (α-alloy) and Ti64 (α+β-alloy) similar welding, dendritic structure normally disappears after phase transformation. However, in our experiment, dendritic structure was visible in dissimilar welding, especially towards Ti5553 side. The reason for this phenomenon may be related to its high content of β-stabilizer elements. The distribution of dendrites is more obvious towards Ti5553 side.

In our study, epitaxial growth was found in both GTAW and LBW Ti5553-Ti64 weld zone. Some dendrites in Ti5553-Ti5553 FZ were intersected by the large grain boundary. Microstructure investigation and hardness profile of dissimilar weld zone can prove the existent of martensitic structure.

ACKNOWLEDGEMNTS

The authors would like to thank Mr. Makirai Henry (AUT) and Prof. Kamiya (Akita University) for access to welding facilities.

REFERENCES

[1] G. Lütjering & J.C.Williams. (2002). “Titanium”. Springer USA.

[2] Prima industrie, “Titanium laser beam welding: a breakthrough technology for next-gen aircrafts”.

[3] T.Shariff., X.Cao., R.R.Chromik., P.Wanjara., J.Cuddy., A.Birur., (2011). “Effect of joint gap on the quality of laser beam welded near-β Ti-5553 alloy with the addition of Ti-6Al-4V filler wire”. J Mater Sci. DOI 10.1007/s10853-011-5866-0.

[4] Mitchell, R., Short, A., Pasang, T. and Littlefair, G., (2010) “Characteristics of EBW Ti Alloys”, Structural Integrity and Failure - SIF, University of Auckland.

[5] Sindo Kou, (2003). “WELDING METALLURGY”. John Wiley & Sons, Inc., Hoboken, New Jersey.

[6]R. Mitchell, A. Short, T.Pasang, G.Littlefair, (2010). “Characteristics of Electron Beam Welded Ti & Ti alloys” AUT.

4. Research on Various Welding Methods on Aerospace Titanium Alloys: collaboration between Akita University and AUT University

Timotius Pasang*, Yuan Tao*, Osamu Kamiya**, Yasuyuki Miyano**, Gakuya Kudo**
* Department of Mechanical Engineering, AUT University, Auckland, New Zealand 1020
**Department of Mechanical Engineering, Faculty of Engineering and Resource Science, Akita University, 1-1 Tegatagakuen-machi, Akita, 010-8502, Japan
tpasang@aut.ac.nz

Abstract: In the past two decades or so, titanium and its alloys have found a significant increase in the aerospace applications. One of the reasons is associated with the introduction of various new titanium alloys. Ti-5Al-5V-5Mo-3Cr (Ti5553) is one of the most notable new titanium alloys. This alloy has a high strength, excellent hardenability and good fracture toughness. Landing gear beam truck of aircraft has been successfully manufactured using this alloy. In order to find more applications in various areas, a number of factors are to be investigated, and one of them is its weldability. Three types of welding methods were used in this investigation, i.e. Laser Beam Welding (LBW), Electron Beam Welding and Gas Tungsten Arc Welding (GTAW). The results showed that it is possible to perform similar Ti5553 alloy weld as well as dissimilar titanium welds. It was observed that the (i) strength at the weld zones was lower compared with the base metal, and (ii) grains grew epitaxially from the near heat affected zone into the fusion zones. This study is part of a strong on-going collaboration projects between Akita University and AUT University.

Key words: Titanium alloys, electron beam welding, laser beam welding, gas tungsten arc welding

1 INTRODUCTION

Titanium and its alloys are used in many different areas such as aerospace, automotive, medical, sporting equipment and chemical industries. Such wide areas of applications are associated with the excellent high strength to weight ratio, good creep resistance, excellent corrosion resistance and good biocompatibility. A number new titanium alloys with comparable, if not better, properties were introduced in the last two decades or so.

One of them is a metastable β titanium alloy known as Ti-5Al-5V-5Mo-3Cr (Ti5553) primarily for aircraft landing gear application [1]. Apart from its high strength, excellent hardenability and fracture toughness, this alloy also offers high fatigue resistance. A few other niche applications in the aerospace area have, since, been specified. For these applications, there may be a need to join them, e.g. by welding, and therefore its weldability needs to be investigated.

Depending on alloy classification, titanium and its alloys have moderate to excellent weldability [2]. Most titanium alloys have excellent weldabilty in the annealed condition, and relatively limited weldability in the solution treated and aged conditions [2]. In general, commercially pure titanium (CP Ti), α-titanium and α/β titanium alloys have better weldability compared with metastable β titanium alloys. These facts imply the effects of composition of the material and their conditions (e.g. strength). Aside from the materials, welding methods may have different influences on the weldability of titanium and its alloys [2]. It is generally accepted that fusion welding of titanium can successfully be performed in completely inert or vacuum environments either through arc or high-energy beam welding. Arc welding provides a high heat input into workpiece (and low power density of heat source), while the high-energy beam welding methods impart the opposite [3]. For this reason, the latter has the advantage of deeper penetration and much narrower weld zones, hence, thicker welds are possible compared with the former [2,3].

A summary of the microstructural features following welding of titanium and its alloys representing CP Ti, α/β alloys such as Ti6Al4V and metastable β titanium alloys are briefly presented below. Typically, CP Ti welds have coarse columnar grains in the fusion zone (FZ) compared with the heat affected zones (HAZ) and the base metal (BM) [4]. The HAZ consists of equiaxed transformed β grains which increase in size as the FZ is approached. Within these grains, colonies of α-phases are present. The FZ of α/β alloys contains coarse, columnar prior beta grains. These grains may have originated from the near HAZ adjacent to the fusion line during solidification [2]. The grain structures of Ti6Al4V (Ti64) welds showed the presence of a small amount of acicular α, a larger amount of α-prime (martensite) in the HAZ and α-prime covering the entire FZ [5]. Huiquang et al. [8] reported columnar grains in the FZ. They also observed an increase in hardness due to the presence of α-prime in the FZ compared with the BM [6]. For metastable β titanium alloys, the FZ is comprised of coarse columnar β grains from solidification while the heat affected zone (HAZ) adjacent to the fusion lines are characterized by retained β structure. In this condition, they are low in strength (low hardness) but have good ductility. Becker and Baeslack [7] conducted weldability studies

on three different types of metastable β titanium alloys (Ti-15V-3Cr-3Al-3Sn; Ti-8V-7Cr-3Al-4Sn-1Zr and Ti-8V-4Cr-2Mo-2Fe-3Al) and confirmed the above explanations. They also suggested that the alloys were weldable [7]. Liu et al. [8] studied the weldability of Beta-21S sheet using laser welding technique. They reported that the FZ and HAZ were narrow with fine retained β grain structures. Epitaxial grain growth was observed to form in the narrow HAZ through the fusion line into the FZ. The FZ had transitioned from a solidification mode of a cellular-type along the fusion line to a completely cellular-dendritic (or columnar dendritic) solidification mode at the weld centreline. Baeslack et al. [9] investigated Beta-CTM alloy by implementing gas tungsten arc welding (GTAW) and observed epitaxial growth from the near-HAZ into the FZ, which solidified with a cellular mode and progressively formed a complete columnar-dendritic grain structure at the weld centreline. From the above summary, it can be seen that titanium may or may not be able to produce α-prime (martensite) upon cooling. This phenomenon is governed by the so called Molybdenum equivalent (Moeq). α-prime (martensite) could form if the Moeq is less than 10 [10].

The most common welding techniques to joint titanium and its alloys are gas tungsten arc welding (GTAW), gas metal arc welding (GMAW), plasma arc welding (PAW), laser beam welding (LBW) and electron beam welding (EBW) [2,11]. The first three methods fall in the arc welding category with high heat/energy input and low power density of the heat source, while the last two techniques belong to the high-energy beam group. In this study, similar and dissimilar titanium weld joints were made using EBW, LBW and GTAW methods. The results in terms of microstructures and mechanical properties are presented. However, due to the limit of this paper, only Ti5553/Ti5553 weld joints will be discussed in detail and the other types of weld joints are briefly explained.

1 EXPERIMENTAL

1.1 Materials

The main alloy studied was the new Ti-5Al-5V-5Mo-3Cr (Ti5553). Two other alloys, i.e. commercially pure titanium (CP Ti), Ti-6Al-4V (Ti64) were also used for comparison. These materials represent three different classes of titanium, namely unalloyed (CP Ti), α/β alloy (Ti64) and β-alloy (Ti5553), respectively. Their chemical compositions are shown in Table 1. CP Ti and Ti64 alloys were commercially purchased, while the Ti5553 alloy was provided by the Boeing Commercial Airplanes.

Table 1. Chemical composition of the titanium alloys (wt.%)

Elements	**CP Ti**	**Ti64**	**Ti5553**
Ti	Bal.	Bal.	Bal.
Al	0.16	6.08	5.03
V	<0.01	3.85	5.1
Mo	<0.01	<0.01	5.06
Cr	<0.01	0.02	2.64
Fe	0.22	0.17	0.38
C	0.01	0.02	0.01
O	0.28	0.05	0.14
N	0.01	<0.01	<0.01

1.2 Welding Procedures

Full penetration butt joints were performed without filler metal (autogeneous) by LBW, EBW and GTAW. LBW was conducted at the Akita Research Institute of Advanced Technology (ARIAT), Akita - Japan, EBW was performed at the Air New Zealand Gas and Turbine facilities in Auckland, New Zealand, while GTAW was done at the Department of Mechanical Engineering, AUT University, Auckland, - New Zealand. The welding conditions are presented in Table 2. Various welding combination were made for similar titanium i.e. Ti5553/Ti5553, Ti64/Ti64 and CP Ti/CP Ti, and dissimilar titanium including Ti5553/Ti64, Ti5553/CP Ti, and Ti64/CP Ti.

Table 2. Welding parameters

Welding Methods	Parameters
LBW - Nd: YAG	Power = 2 kW; speed = 15 mm/sec; continuous argon gas flow of 20L/min
EBW	Voltage = 150kV; speed = 8.5 mm/sec; current = 3mA
GTAW	Current = 50 Amp DCEN; voltage 10V; continuous argon gas flow of 1-16L/min

1.3 Metallography and Microscopy

Metallographic samples were prepared according to the standard procedures. The steps consisted of grinding from 120 grit to 2400 grit SiC paper, polishing to 0.3 µm colloidal alumina, followed by final polishing with 0.05 µm colloidal silica suspension. Kroll's reagent with a composition of 100 mL water + 2 mL HF + 5 mL HNO3 was used to etch the metallographically-prepared samples to reveal the weld profiles and grain structures. Both optical microscope and scanning elecgtron microscope (SEM) were employed to characterize and study the microstructures of the etched samples.

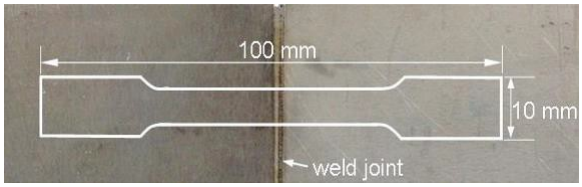

Figure 1: Schematic diagram showing a tensile test sample position on the laser beam welded (LBW) material.

1.4 Mechanical Testing

Mechanical testing performed including hardness and tensile tests. Vickers hardness method with a load of 300g (HV300g) was used to investigate the hardness profile of the welds. Hardness indentations were placed about 0.2 mm from the top surface. Tensile tests samples were taken from the welded sheets (Fig.1) in accordance with ASTM E 8M – 04, with the weld located perpendicular to the tensile axis. Tensile tests were conducted at room temperature with a crosshead speed of 3 mm/min.

1.5 Post Welding Heat Treatment (PWHT)

Post welding heat treatment (PWHT) was performed on some of the welded samples at 700oC for 4h and air cooled. The specimens were then prepared metallographically, analysed and mechanically tested for comparison with the as-welded samples.

2 RESULTS AND DISCUSSION

Microstructures of the base materials of Ti5553, CP Ti and Ti64 are presented in Fig.2.The Ti5553 alloy showed a typical α/β microstructure with globular α particles distributed within the β matrix. These α particles have an average size of less than 5 μm. The CP Ti had nearly equiaxed α grains with an average size of 20 μm in the longitudinal direction. It also contained disperse β phase (dark). The presence of β phase is associated with the addition of small amounts of Fe in CP Ti. The Ti64 alloy had elongated primary α grains in the α/β matrix.

General weld profiles from EBW, LBW and GTAW are presented in Figs.3-7. It can be seen that the width of the weld zones of LBW and GTAW are markedly different, being fairly narrow in the former and could be up to five times wider in the latter. The grain sizes in the FZs for all welds were up to a few hundred microns. In the HAZ, large grains were observed at the near HAZ (along the fusion line) of up to 200 μm in the LBW samples, and up to 600 μm for GTAW samples. The larger grain sizes in the near HAZ

are associated with intermediate peak temperature during welding that facilitates grain growth. The grains became gradually smaller towards the BM.

For Ti5553-Ti5553 weld joints (Figs.3-5), some similarities were observed in the weldments' microstructures regardless of the welding method used as described in the followings

1. The FZ contained a columnar dendritic-typed grain morphology indicating a high concentration of β-stabilizing elements,
2. The HAZ is decorated with retained, equiaxed β grains with larger grains at the fusion line and smaller grains towards BM,
3. Epitaxial grain growth from the HAZ into the FZ was clearly observed.

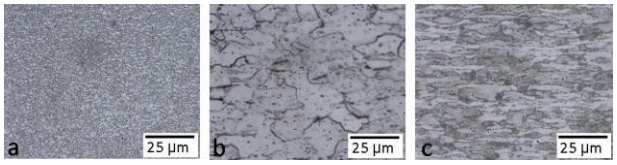

Figure 2: Micrographs showing microstructures of the BM for (a) Ti5553, (b) CP Ti and (c) Ti6Al4V.

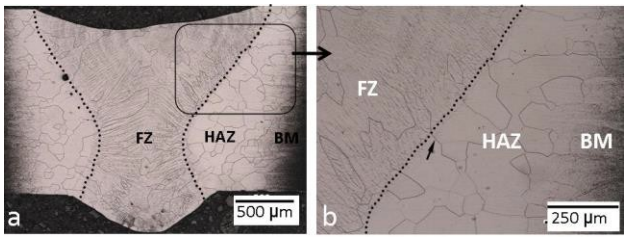

Figure 3: Micrographs showing examples weld profiles of Ti5553-Ti5553 EBW; dotted lines indicate fusion line, and small arrow indicate epitaxial grains

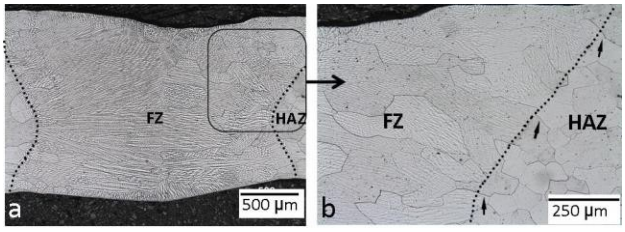

Figure 4: Micrographs showing examples weld profiles of Ti5553-Ti5553 LBW; dotted lines indicate fusion line, and small arrows indicate epitaxial grains.

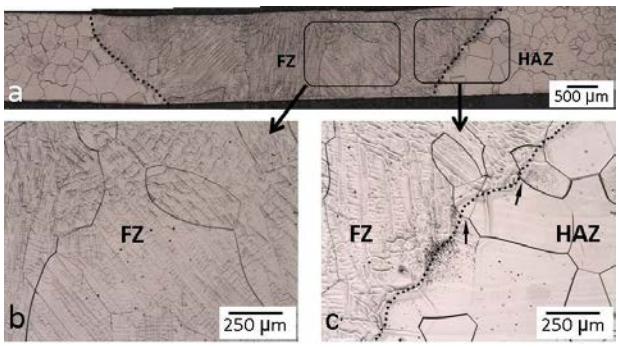

Figure 5: Micrographs showing examples weld profiles of Ti5553-Ti5553 GTAW; dotted lines indicate fusion line, and small arrows indicate epitaxial grains.

On the CP Ti-CP Ti weld joint, acicular α phases were observed from the HAZ to the FZ with larger grain size compared with the BM. In the FZ, with grain size of up to 200 µm, fine acicular α were evident. Note that fine acicular alpha can be mistaken for α-prime (martensite). For Ti64-Ti64 weldment, grains in the HAZ were slightly larger than those in the BM, and the grain size increased significantly in the FZ. α-prime (martensite) was faintly observed in the HAZ and is very clear in the FZ. The formation of martensite in Ti64 is associated with fast cooling rates from melting.

The microstructures for the dissimilar weld joints (Ti5553-CP Ti, Ti5553-Ti64 and CP Ti-Ti64) are summarised below: Ti5553-CP Ti, shown in Fig.6, for example, the presence of α-prime (martensite) at the FZ adjacent to the CP Ti side (not in the HAZ) is associated with the alloying elements coming from Ti5553. It was also observed that the amount of α-prime was decreasing towards the Ti5553; dendritic grains were observed on the Ti5553 side and lamellar type-grains were present on the CP Ti side; epitaxial grain growth was clearly observed on the Ti5553 side and less obvious on the CP Ti side.

On the Ti5553-Ti64 weld, α-prime (martensite) was clearly present at the Ti64 side from FZ through far HAZ. The presence of α-prime (martensite) was decreasing towards the Ti5553 side with the increase of the Moeq as explained later; dendritic grains were observed on the Ti5553 side and lamellar type-grains were present on the Ti64 side; epitaxial grain growth was observed on the Ti5553 side but not on the Ti64 side (Fig.7).

For CP Ti-Ti64 weld joint, the locations of the fusion boundaries were not very clear due to the similar microstructural features in the HAZ and FZ as well as the significant grain coarsening in the HAZ (which results in large β grains in this region). The presence of α-prime (martensite) was very clear on the Ti64 side but not on the CP Ti side.

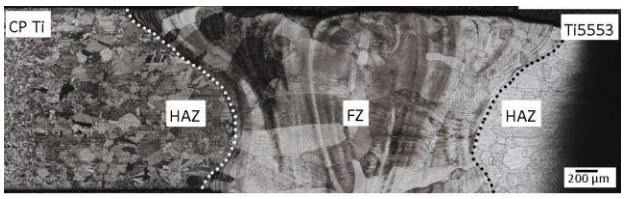

Figure 6: Micrographs showing an example of CP Ti-Ti5553 joint by LBW; dotted lines indicate fusion line.

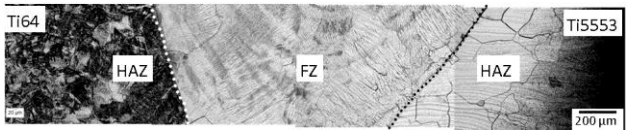

Figure 7: Micrographs showing examples of Ti64-Ti5553 weld joint by EBW; dotted lines indicate fusion line.

SEM micrographs showed dendritic-typed structures throughout the FZ of Ti5553-Ti5553. The extent of dendritic structures became less obvious on the FZ of Ti5553-CP Ti and Ti5553-Ti64 perhaps due to the formation of the martensitic phase. Epitaxial grain growth from the near HAZ into the FZ is very clearly observed (Fig.8). Figure 8b also indicates the presence of α-prime (martensite) in the Ti5553-Ti64 sample from the HAZ on Ti5553 side to the fusion line. The formation of both the dendritic-typed structures and α-prime (martensite) are compositional-driven. On the one hand, the higher the β stabilizing elements the more likely it is to form dendritic structures [3]. On the other hand, if the β stabilizing elements istoo high, it will raise the Moeq which will inhibit the formation of α-prime (martensite) [10]. Ti5553 has Moeq of around 12.

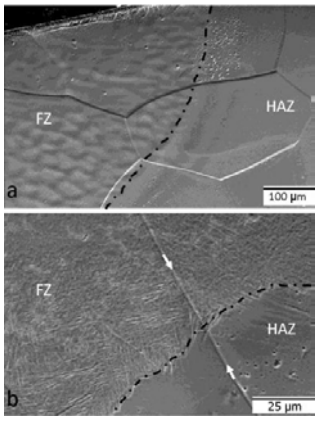

Figure 8: SEM micrographs showing fusion line area of (a) Ti5553-Ti5553, and (b) Ti5553-Ti64 at the near HAZ of Ti5553 side. White arrows indicate epitaxial grain boundary; dashed line represents fusion lines.

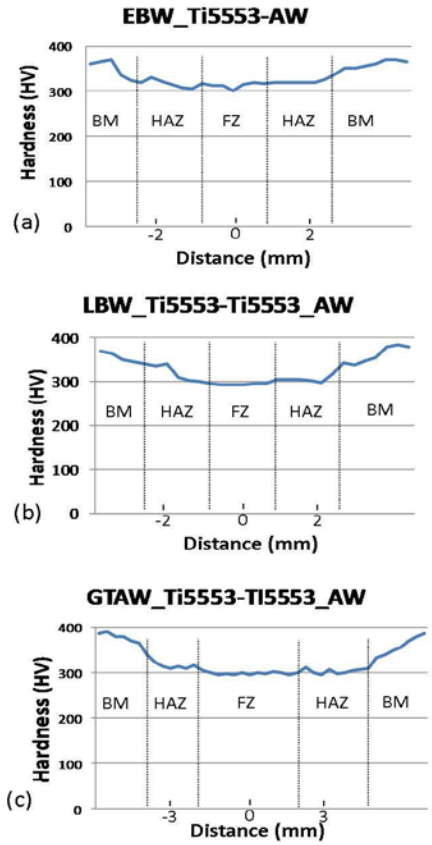

Figure 9: Hardness profiles of Ti5553-Ti5553 weld joints of EBW, LBW and GTAW

Hardness profiles of Ti5553-Ti5553 weld joints for EBW

LBW and GTAW are given in Fig.9. They showed a similar pattern i.e. lower hardness in the weld zones (both FZ and HAZ) compared with BM. The lower hardness in the weld zone is associated with the presence of retained β phase. Figure 10 shows an example of fracture surface from GTAW Ti5553-Ti5553 weld joint. Macroscopically, the fracture surface appears to be fairly brittle. However, at higher magnification, microvoid coalescence fracture mechanism (dimples) was obvious. This indicated a relative ductility at the weld zone.

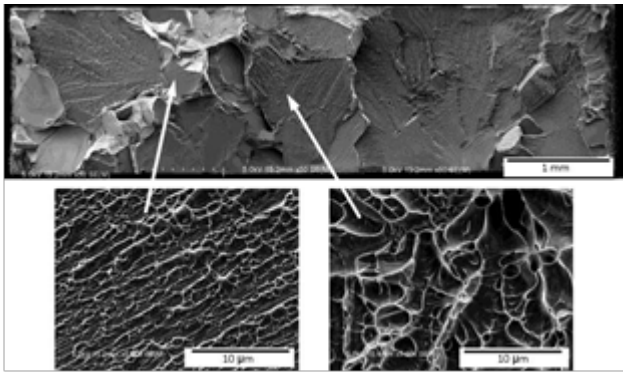

Figure 10: SEM images showing an example of fracture surface from GTAW Ti5553-Ti5553 weld joint

The effect of PWHT can be seen on Figs.11 and 12. Upon heating at 700oC/4h and air cooled, the microstructure had completely changed with the presence of homogeneous α precipitates in the BM, HAZ and the FZ (Fig.11). The fusion line is barely seen, but the grain structures are relatively obvious particularly the area between HAZ with equiaxed grains and BM with elongated grain structures (Fig.11).

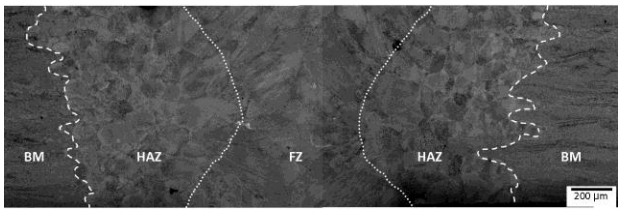

Figure 11: Micrographs showing an EBW profile after PWHT at 700oC/4h and air cooled.

Hardness values of the PWHT samples were constant across the BM to the HAZ and FZ (Fig.12). It also showed that hardness values of PWHT samples were comparable to that of BM in the as-received condition. Furthermore, the strength, both yield and ultimate, showed an increased by about 15 and 10%, respectively (Table 3).

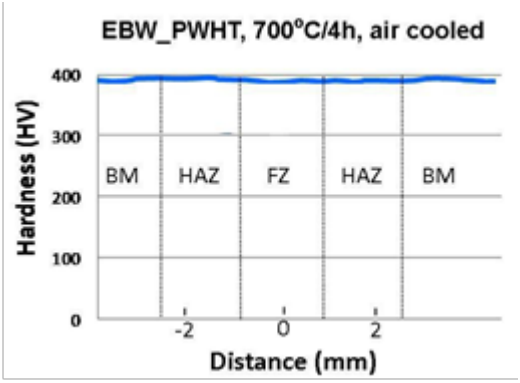

Figure 12: Hardness profiles of EBW sample following PWHT at 700oC/4h and air cooled.

Table 3. Tensile testing data of Ti5553-Ti5553 weld joints

Welding Methods	Yield Strength (MPa)	Tensile Strength (MPa)	Elongation (%)
EBW_AW	680	780	9
LBW_AW	1028	1053	12
GTAW_AW	785	785	8
EBW_PWHT	815	858	13

AW = as-welded; PWHT = post-weld heat treatment

Acknowledgement – The authors would like to thank Mr Richard Ison and Barry Able from the Air New Zealand for supporting the EBW, Mr. Kimura of the Akita Prefecture Research Center for performing the LBW and Mr. Makirai Henry for performing GTAW.

References

[1] Fanning, J.C., "Properties of Timetal 555 (Ti-5Al-5Mo- 5V-3Cr-0.6Fe)", Journal of Materials Engineering and Perfo rmance, 14(6), 788-791, (2005).

[2] Donachie, M.J., "Titanium: A Technical Guide", second edition, ASM International, (2000).

[3] Sindo, K., "Welding Metallurgy", John Wiley and Sons, second edition, (2003).

[4] Lathabai, S., Jarvis, B.L and Barton, K.J., "Comparison of Keyhole and Conventional Gas Tungsten Arc Welds in Commercially Pure Titanium", Materials Science & Eng, A 299, 81-93, (2001).

[5] Irisarri, A.M., Barreda, J.L. and Azpiroz, X.,"Influence of the Filler Metal on the Properties of Ti-6Al-4V Electron Beam Weldments. Part I: Welding Procedures & Microstructural Charac.", Vacuum 84, 393-399, (2010).

[6] Huiqiang, W., Jicai, F. and Jingshan, H.,"Microstructure Evolution & Frac. Behaviour for Electron Beam Welding of Ti-6Al-4V", Bulletin of Materials Science 27, 387-392, (2001).

[7] Becker, D. and Baeslack III, W.A., "Property - Microstructure Relationships in Metastable-Beta Titanium Alloy Weldments", Welding Journal 59, 85-93, (1980).

[8] Liu P.S., Hou K. H, Baeslack III, W.A. and Hurley,J., "Laser Welding of an Oxidation Resistant Metastable-Beta Titanium Alloy – Beta-21S". Titanium '92 (Froes F.H. & Caplan I, editors), TMS, 1477-1485, (1993).

[9] Baeslack III W.A., Liu, P.S., Barbis, D.P., Schley, J.R. and Wood, J.R.,"Postweld Heat Treatment of GTA Welds in a High-Strength Metastable Titanium Alloy-Beta-CTM", Titanium '92, Science & Tech., F.H. Froes and I. Chaplan (eds), TMS, 1469-1476, (1993).

[10] Bania P.J., "Beta titanium alloys in the 1990's", In: Eylon D., Boyer R.R., Koss D.A (Eds.), TMS, Warrendale, PA, 3-14, (1993).

[11] Lütjering, G. and Williams J.C., "Titanium", Berlin Springer, 23-42, (2003).